ABSTRACT

Title of Document: ULTRASOUND THERMAL THERAPHY: PATIENT-SPECIFIC PLANNING FOR INTRALUMINAL AND EXTERNAL DELIVERY

Danica Stefannie Gordon, M.S., 2012

Directed By: Dr. Chandrasekhar Thamire, Department of Mechanical Engineering

Thermal therapy can be regarded as one of the promising emerging technologies for cancer treatment. In the current study, proof-of concept patient-specific treatment protocols are formulated for high frequency ultrasound thermal therapy for intramural and external delivery. Propagation of ultrasound waves in biological tissue is first determined using the finite difference method, which generates the temperature histories from the bioheat transfer model. Thermal coagulation contours are determined by thermal dose information. From an analysis of the results for a range of parameters, treatment protocols for prostate and breast cancers are developed for a broad spectrum of patients. Results indicate tumors varying in size and location can be targeted effectively using the designs employed. To further improve simulations, thermal damage data for breast cancer is determined through pilot *in vitro* experiments. The algorithms developed can help optimize the design of delivery equipment and generate accurate patient-specific US clinical protocols.

ULTRASOUND THERMAL THERAPY: PATIENT-SPECIFIC PLANNING FOR INTRALUMINAL AND EXTERNAL DELIVERY

By

Danica Stefannie Gordon

Thesis submitted to the Faculty of the Graduate School of the
University of Maryland, College Park, in partial fulfillment
of the requirements for the degree of
Master of Science
2012

Advisory Committee:
Dr. Chandrasekhar Thamire, Chair
Dr. Kenneth Kiger
Dr. Jungho Kim

Dedication

I'd like to dedicate this thesis firstly to my parents, all three of them ☺ My mother, Ms. Stella Varnavas Gordon, my father, Mr. Bruce Gordon, and my stepmother, Mrs. Lauranne Klyce Gordon, have all given me incredible support through my schooling, made learning a priority, and created amazing examples for me to follow that makes me want to always strive to be all that I can.

Also, I'd like to thank my brother Jason Aris Gordon, who helped foster my interest in math and science and inspired me to become an engineer five and a half years ago.

And finally, I want to dedicate this work to my twin sister Carly Nicolette Gordon, who I admire every day for her intellect and hard work, and uses her amazing abilities to do good in the world. Throughout my graduate degree she supported me and was always available to listen to me, no matter how busy she was.

.

Acknowledgements

I'd first and foremost like to acknowledge my advisor, Dr. Chandrasekhar Thamire, who has taught me so much in the three years I have known him. His patience is unsurpassed, and I was fortunate to have such an extended period of time to learn from his wealth of knowledge. I have learned invaluable lessons from my research with him, and I'd like to thank him for how it will help me thrive in the future.

Next, I'd like to acknowledge Dr. Wei-Sing Chu and everyone at BioQuick Corporation for their facilities and assistance on performing the cell studies.

And finally, I'd like to acknowledge all of my lab mates, who each had a hand in the completion of this research. Mr. Esteban Echeverria started in this research area prior to myself, and was always willing to share his knowledge on the subject and help me get through my work. Mr. Babak Eslami, Mr. Karim Najjar, and Mr. Shreyas Parameshwaran always offered support and advice when I needed it, and Mr. Eslami along with Mr. Aleksandr Gorbashev taught me hand machining, which was necessary for my physical experiments. Mr. Andrew Oles helped me to look at my problems from different perspectives, especially when I was having coding difficulties. Mr. Erik Levin and Mr. Mayank Bhalla helped greatly in the last semester to allow this project to come to completion on time, and I'd like to acknowledge Mr. Rabee Zuberi for helping establish the numerical simulations side of our lab.

Finally, I'd like to thank two high school interns who worked on this project with me, Mr. Samir Durvasula and Ms. Teju Peesay, who were always willing to learn and help out in any way that I needed.

Table of Contents

List of Tables

List of Figures

Chapter 1: Introduction

Fighting cancer can be stressful and uncertain, and side effects from traditional treatment methods such as radiation, open surgery, and chemotherapy can further compound the patient’s stress. Thermal therapy provides an attractive alternative treatment option. It offers advantages of being minimally invasive, less expensive, and posing less risk of post-procedural complications, while possessing the potential to be effective. The ultimate goal of the research conducted in this project is to increase the efficacy and accuracy of thermal therapy by ultrasound (US) thermal therapy, so that it can become a common cancer treatment.

Prostate and Breast Cancers

Prostate and breast cancers are two of the most prevalent cancers among men and women, respectively. One in six male Americans is diagnosed with prostate cancer [1], while one in eight women in the U.S. will receive a breast cancer diagnosis [2]. The large disparity between the number of cases of prostate and breast cancer when compared to other cancer types is depicted in Figure 1 (for men) and Figure 2 (for women), from the *Cancer Statistics* report (reprinted with permission). The plots display the number of diagnoses per 100,000 people from 1975 to 2008, and prove how these cancers have consistently dwarfed the prevalence of other cancer throughout the years.

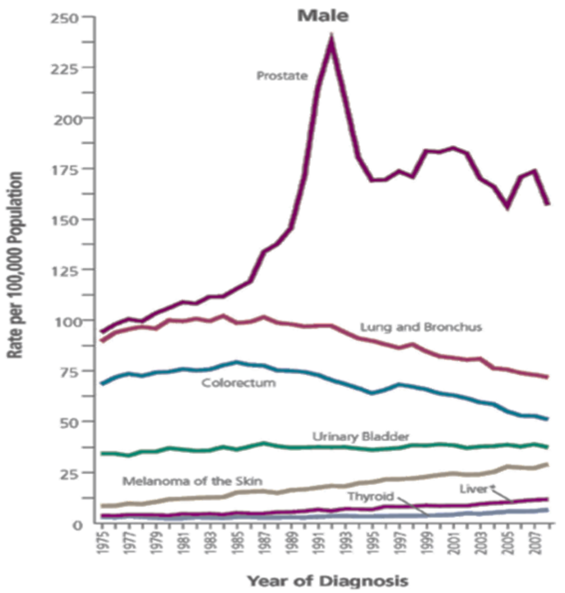

Figure 1 The number of men who are diagnosed with different types of cancer for every 100,000 men from 1975 – 2008 (with permission) [3].

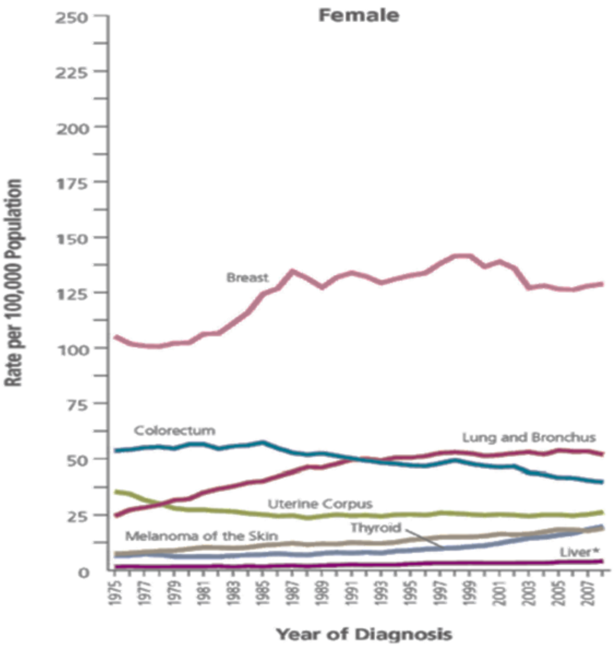

Figure 2 The number of women who are diagnosed with different types of cancer for every 100,000 women from 1975 – 2008 (with permission) [3].

Treatment Problems

The current cancer modalities often are associated with a great deal of discomfort and health damage; also, these treatments often incur long patient recoveries in and out of the hospital. Prostate cancer is usually treated with surgery, hormone therapy, chemotherapy, or radiation treatments [4]. These treatments are often associated with problems such as urinary incontinence, sexual dysfunction, urinary tract infections, and rectal damage [5, 6]. Trans-urethral resection of the prostate (TURP) is considered the “gold-standard” for treating BPH and prostate cancer, but it is not acceptable for all patients (especially those who are older or of poor health) [7, 8].

Breast cancer is also primarily treated with surgery, along with chemotherapy, radiation treatment, and hormone therapy [9]. A mastectomy can have a negative social impact and degrade the quality-of-life for females, while a lumpectomy, although not as severe, still leaves a scar [7]. Chemotherapy can be a problem because there are a finite number of chemotherapy treatments that patients can receive because, while becoming more focused in its targeting capabilities, it is still a toxin that adversely affects many different body systems. [7]. Radiation treatments harm the tissue surrounding tumors because the harmful rays spread throughout more than just the tumor volume [7].

Thermal Ablation by Ultrasound Thermal therapy

Thermal treatment is an innovative cancer treatment option which is potentially superior to other methods because it destroys the malignant cells without the harmful side-effects of radiation or chemotherapy. Thermal therapy involves heating cancerous cells to supraphysiological temperatures with the goal of inducing cell death. Thermal therapy refers to heating cells in the temperature range of 41 to 46°C; if temperatures above 46°C are used in treatments then it is considered thermal ablation [10, 11].

Currently microwave, radio-frequency (RF), and laser ablation are in use for local thermal therapy; however, they have limitations that warrant better methods be examined. For example, microwave therapy lacks the ability to focus heat into the target zones effectively, i.e., to treat tumors without affecting the surrounding healthy tissue, and RF therapy tends to be more invasive compared to other methods and may require multiple applications in smaller bursts to avoid damage to healthy surrounding tissue [12].

In the present study, high frequency ultrasound (US) ablation is utilized as a treatment option because of its ability to focus heat more effectively and less invasively compared to the other minimally invasive methods. Additionally, delivery of US can be interstitial, intraluminal, or extracorporeal [7]. High intensity ultrasound for medical therapy was proposed back in 1942, but it was not until 1960 that it was sufficiently validated to attempt human treatment [13].

Ultrasound thermal therapy has the potential to be superior to traditional cancer treatments mainly because its non- or minimally-invasive nature results in less disruption to the patient’s life. There is little pain, no dosage limit, and it allows for a quick recovery with no scars [7]. Also, it has the ability to treat deep-set tumors from an extracorporeal transducer when the US beams are effectively located and steered [14]. US thermal therapy has been proven effective on cancers of the liver, prostate, breast, kidney, bone, bladder, and non-cancerous diseases such as benign prostatic thermal therapy (BPH), uterine fibroids, and acoustic hemostasis [14, 15, 16, 17].

Most importantly to this research, the potential and efficacy of US thermal therapy has been proven for prostate treatment (both for cancer and non-cancerous BPH) [13] and breast cancer [18]. This this study will focus on the improvement of treatment planning and device design for ultrasound thermal therapy for prostate and breast cancers.

Objective

There are three main objectives of this study: (1) to simulate and design a device for prostate cancer ablation from US thermal therapy, (2) to simulate and design a device for breast cancer ablation from US thermal therapy, and (3) to develop thermal-damage models for breast cancer cells to improve the simulations. The devices designed will also have an associated treatment planning protocol so the physicians can design patient-specific treatments.

This thesis will first provide the necessary background information, then detail the numerical technique used to simulate tissue necrosis and device design for prostate cancer, explain the steps for simulation and design of breast cancer treatment devices, and finally describe how cell thermal damage information is determined.

Chapter 2: Background

The process of tumor ablation by ultrasound thermal therapy begins with an ultrasonic wave created by a transducer. This wave heats up the tissue, which will cause cell death after a lethal heat dose is administered. An understanding of the science behind ultrasound and cellular death from thermal therapy is important for the choices made during this study. The following chapter will first discuss prostate and breast cancer, and then it will explain the general principles behind ultrasound thermal therapy, the physics of ultrasound propagation and generation, the physics of heat transfer through biological tissue, and finally the currently-available ultrasound thermal therapy devices.

Prostate and Breast Cancer

It is important to understand the anatomy of the parts of the body which are to be modeled to create an accurate simulation. This section details the anatomy of the prostate and breast.

Prostate Anatomy

The prostate gland is a male reproductive organ which adds a nourishing fluid to semen. A healthy prostate should be about the size of a walnut, and surrounds the top of the urethra (passes urine from the bladder outside of the body). During ejaculation, sperm flows from the testes to the prostate gland, where it becomes semen after combining with fluid in the prostate. The semen flows into the urethra and exits the body. The prostate gland grows continuously after puberty, and if the prostate becomes too large it is called Benign Prostatic Hyperplasia, which can cause urinary disorders [19].

Benign Prostatic Hyperplasia (BPH) is a non-cancerous growth of the prostate gland. The enlarged prostate will block the bladder exit and the top of the urethra, which greatly impacts the urine flow rate (Figure 3). This disease is very common, and mostly begins when the patient is in his middle ages (Figure 4). Almost 100% of the males aged 90 or older are affected by BPH [20]. BPH results from a combination of normal prostate growth and the formation of nodules [20].

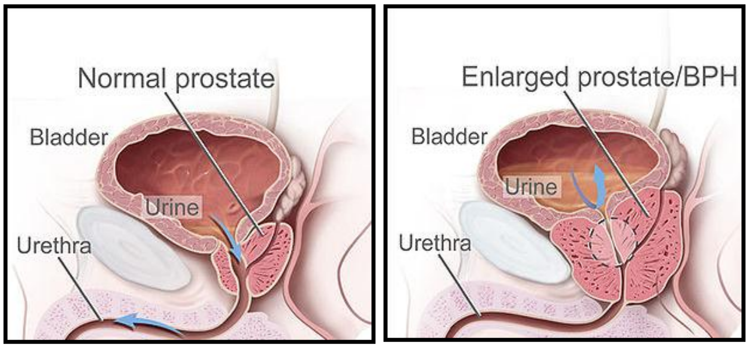

Figure 3. The enlarged prostate blocks the bladder exit and the top of the urethra [21].

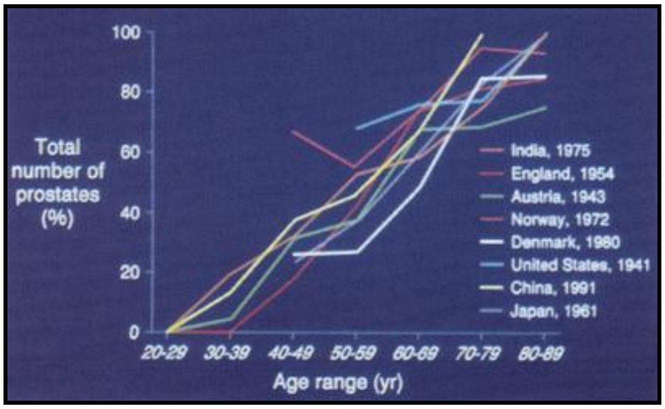

Figure 4. Number of men with enlarged prostates versus age, demonstrating the increase of BPH prevalence during aging [20].

BPH is not cancer and does not cause cancer, however it can be indicative of prostate cancer in the future. Prostate cancer usually occurs in patients with an enlarged prostate and years after the development of BPH. About ten percent of the prostates that are surgically removed for BPH are found to have a cancerous growth [20].

Breast Anatomy

The breast is mostly consisting of fat tissue with hollow lobules surrounding and connected to the nipple which bring the milk to the breast during nursing [22, 23, 24]. The pectoralis muscle lies behind the breast on the chest [23, 24]. The vasculature and lymph ducts mostly propagate in the radial direction away from the nipple. Figure 5 is a diagram of the anatomy of the breast.

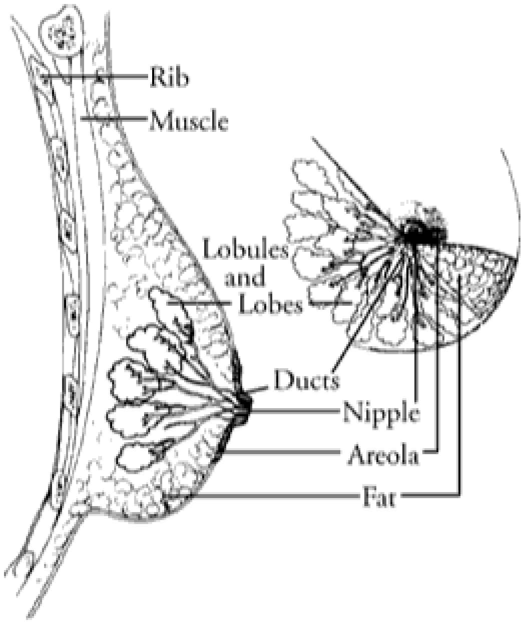

Figure 5 Anatomy of the breast [22].

The Principles of Ultrasound Thermal therapy

When cells are heated, there are two mechanisms which contribute to cell death: thermal stress from the absorption of heat energy and mechanical stress from acoustic streaming and cavitation effects [7, 25]. Cavitation can occur from either highly negative pressures caused by the US wave which create an air pocket in the tissue, or the phase change of the water inside the tissue into gas at temperatures exceeding 100^oC [13, 17].

When the ultrasound wave is generated into the body, it causes a vibration of the tissue molecules [26]. This leads to friction in the tissue, which turns the ultrasonic energy into thermal energy [13]. Thermal therapy (41 to 46°C) causes cell death by inducing apoptosis (programmed cell death [27]), whereas thermal ablation (> 46°C) directly kills the cells by necrosis (lysis formation and membrane degradation [27]) [10]. Thermal ablation requires a much shorter heating time, usually on the scale of seconds to a few minutes, but thermal therapy needs anywhere from thirty minutes to a few hours to be successful [10]. Another difference is that higher temperature treatments usually require only one dose, while at moderate temperatures multiple treatments may be necessary: this adds to the appeal of thermal ablation, so recently further research has been conducted to fully understand the associated cell death to make it a more reliable option [28].

US thermal therapy can be monitored in real-time during treatments through use of magnetic resonance imaging (MRI) or ultrasonic imaging [13, 26]. This allows for control of the procedure by observing the temperature in the treatment area because it is impossible to perfectly predict the thermal gradients since each body has slightly different geometry of vasculatures. This study does not research thermal monitoring of treatments, but it is important to be kept in mind during device design.

Ultrasonic waves have a higher intensity close to the transducer than at a distance away [26] (see Ultrasound Physics section); this is advantageous for tumors close to the edge of the body because a transducer can be nearby and then the tissue past the tumor location will be spared the high treatment temperatures. However, if the tumor is deeper set, then it may be necessary to use high-intensity focused ultrasound (HIFU) to move the location of highest temperature further from the US source. The ultrasonic wave can be focused by using a focusing transducer (explained in Ultrasound Physics section), and causes a very small volume of necrosed tissue (roughly an ellipsoid shape, with center diameter usually around 2-3 mm with a length of 8-10 mm [17]). There is a very distinct boundary created between the dead cells and non-disrupted tissue cells, which makes this treatment ideal for sparing healthy tissue surrounding a tumor [7]. Adding to this advantage is the increased toxicity of thermal therapy to tumors as opposed to healthy tissue because there is a lack of perfusion inside tumors, and perfusion cools the tissue during treatment [7]. An image depicting this is displayed in Figure 6.

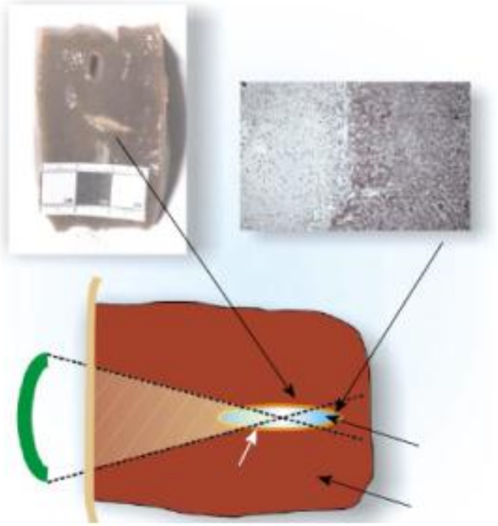

Figure 6 Schematic of HIFU transducer focusing on a small volume of tissue. The photo on the upper left shows the geometry of this necrosed region, and the image to its right displays the distinct boundary between the necrosed and unharmed tissue [7].

This study focuses on the use of ultrasound thermal therapy for treating tumors in the prostate gland or the breast. The anatomy and geometry of these body parts dictate the most-effective US treatment methods. The prostate's proximity to the urethra and the rectum allow for an intraluminal transducer to get very close to its surface. It is especially useful in curing the non-cancerous prostate growth (BPH) because a total destruction of affected area is not crucial [5]. The breast works well with extracorporeal devices because of its convex shape, and since there are no bones and small vasculature, there is little blocking the ultrasonic waves from their predicted propagation path [15, 29].

Ultrasound Physics

Ultrasound refers to an acoustic wave with a frequency above audible human levels, about 20 kHz, but it is usually only used medically at frequencies between 200 kHz and 45 MHz [30]. In order to understand how US creates a hyperthermic effect in the body, the physics behind US propagation must be understood.

Single Wave Propagation

Sound is a compression wave, which has its peaks and valleys in the direction of propagation (longitudinally), shown in Figure 7. This wave is created because the speed of the particles oscillates, so when they move slower compression of the particles occurs, and faster motion creates rarefaction. The distance between two compression or two rarefaction locations is called the wavelength (λ).

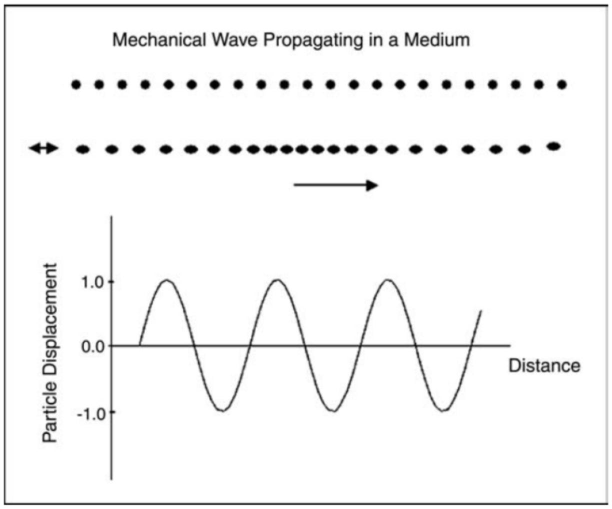

Figure 7 Sound waves travel by compression and expansion of particles [26].

The time it takes for one wavelength to pass a fixed location defines the wave period, which is the inverse of the wave frequency (f). The wavelength and frequency are related by Equation 1

$$f = \frac{c}{\lambda} \qquad \text{Equation 1}$$

where c is the speed of sound propagation. This speed is highly dependent on the medium through which the wave travels, and some common values for biological materials are given in Table 1.

Table 1 Speed of sound through different biological materials [26].

Type of Biological Material	Speed of Sound (c)
Soft Tissue (except lung)	**1550 m/s**
Fatty Tissue	**1480 m/s**
Lung	**600 m/s**
Bone	**1800 – 3700 m/s**

The intensity of the ultrasonic wave will be very high in close proximity to the source, but then rapidly decreases past the "near-field" [26]. The near-field, also known as the Fresnel zone, is characterized by Equation 2 [26]

$$d_F = \frac{a^2}{\lambda} \qquad \text{Equation 2}$$

where d_F is the distance to the edge of the Fresnel zone and a is the radius of the planar, circular ultrasound transducer which created the wave. A graphical representation of this decay in intensity is displayed in Figure 8.

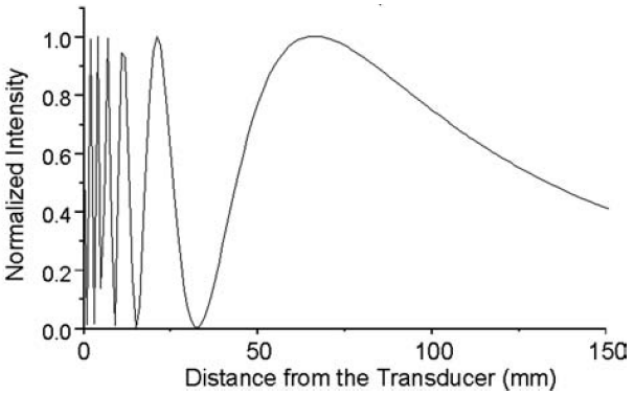

Figure 8 The normalized intensity of an ultrasonic wave as it travels axially away from the transducer source [26].

The amplitude is half of the difference in magnitude between the points of compression and rarefaction in the sound wave. During its travel, the wave amplitude does not necessarily remain constant; dispersion, attenuation, and scattering contribute to the decrease of a wave's amplitude. Dispersion is the spreading out of the wave into different frequencies as it travels through a medium [31]. The US wave dispersion is neglected in this study because it has minimal effect on the energy losses [32].

Also, as the wave travels energy is transferred from the sound wave to the medium in the form of heat absorption (as mentioned in The Principles of Ultrasound section). Some of the wave energy is also scattered in directions other than the direction of propagation. This absorption and scattering result in an attenuation of the wave's intensity, characterized for travel through a homogenous material by Equation 3 [13, 30, 33, 34]

$$I = I_o e^{-2\alpha x} \qquad \text{Equation 3}$$

where I is the intensity of the wave, I_o is the initial intensity, α is the attenuation coefficient, and x is the propagation distance. The attenuation coefficient is a material constant, and its value for different biological materials is displayed in Table 2.

Table 2 Acoustic attenuation coefficient of different biological materials [35].

Biological Material	Acoustic Attenuation (Np/cm at f = 1MHz)
Water	**2.5e-4**
Blood	**0.02**
Mycardium (perpendicular to fibers)	**0.10**
Liver	**0.08**
Kidney	**0.11**
Skull Bone	**1.3**

These values are both frequency and temperature dependent. The frequency dependence of the attenuation coefficient is approximately characterized by Equation 4 [13, 36, 33]

$$\alpha = \alpha_o f^n \qquad \text{Equation 4}$$

where α_o is the temperature-dependent factor, f is the frequency, and n is between 1 and 2 for biological tissues. In biological tissues, there is a large increase in acoustic attenuation as the tissue temperature increases [14]. For the purpose of this paper, the attenuation coefficient is defined by Equation 5 [32]

$$\begin{aligned} &for\ thermal\ dose < 100, \quad \alpha = 5 \\ &for\ thermal\ dose \geq 100, \quad \alpha = 5 + log\big((thermal\ dose) - 2\big) \end{aligned} \qquad \text{Equation 5}$$

where the *thermal dose* is a value defining the time and temperature exposure of the tissue, which will be discussed in the Thermal Damage to Cells section. No frequency term is included in this equation because the thermal dose is dependent on the frequency.

Wave diffraction is the diversion of the wave particles from their linear propagation direction [20]. This phenomenon was first reported by Francesco Grimaldi, and was claimed by Christiaan Huygens [20]. Huygens' principle states that a wave-front is the result of the combination of many spherical wave point sources (shown in Figure 9), which can be proven experimentally by the diffraction pattern created from a light source shining through a thin slit.

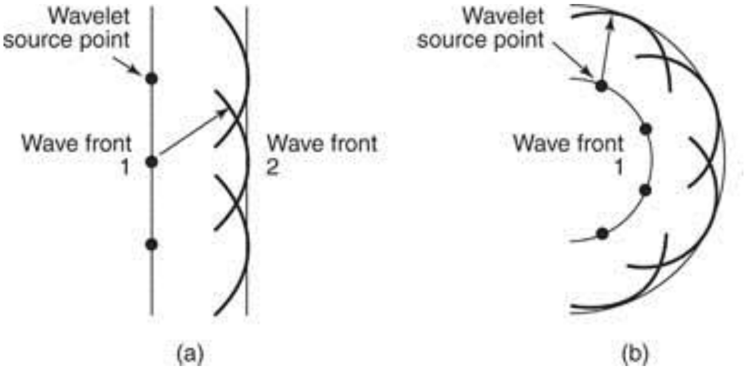

Figure 9 (a) Flat and (b) curved wavefronts resulting from multiple point sources, according to Huygens' principle [37].

Each spherical wave creates its own pressure along its propagation path, and the summation of each pressure determines the pressure profile within the tissue volume.

Each wave reaches a local maximum pressure every wavelength.

If two waves of the same frequency are in phase (their peaks coincide), then constructive interference is created and the amplitude of the wave is the sum of each wave's amplitude. If two waves are out of phase (the peak from one wave coincides with the valley from the second), then it is completely destructive interference, and the amplitudes are subtracted from one another (Figure 10). If constructive interference occurs in one location from multiple waves, then a focal point with a high relative intensity is created.

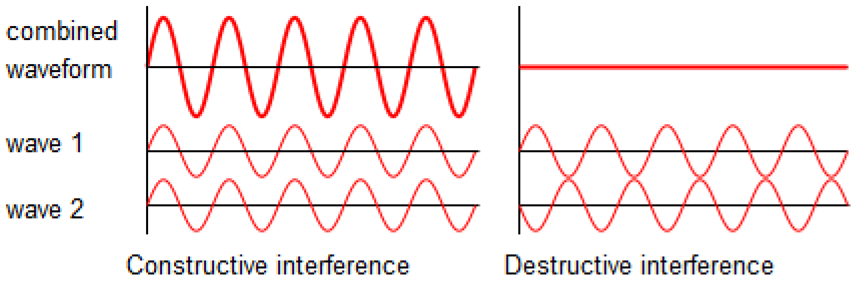

Figure 10 Two in-phase waves combine to create (a) constructive interference; two out-of-phase waves combine to create (b) destructive interference [38].

This focal point can be created mechanically or electronically. If it is mechanical, either a curved transducer is used or multiple wave sources are placed in locations where their peaks will all intersect at a specified point (Figure 11). Electronic focal points are created by timing the US emission of multiple sources so that the delays cause the peaks to coincide (Figure 12).

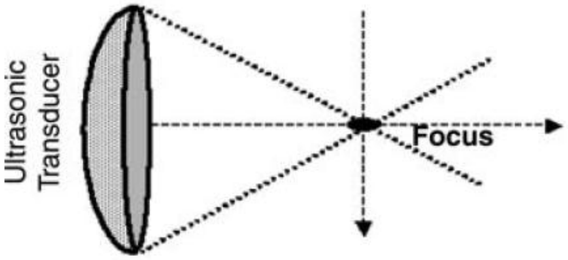

Figure 11 An ultrasound transducer with a curved lens to focus the wave [26].

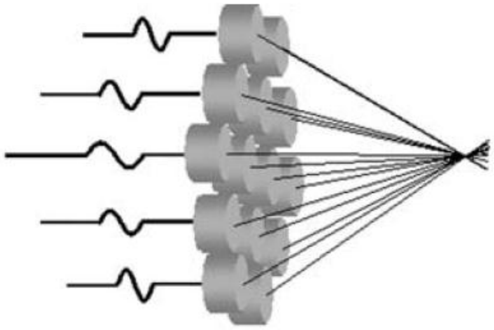

Figure 12 An ultrasound transducer with a planar array of elements to focus the wave [26].

The phase difference between any two point sources with the same frequency waves for complete constructive interference will occur according to Equation 6 [39]

$$\Delta\phi = \frac{d_2 - d_1}{\lambda} * 2\pi \qquad \text{Equation 6}$$

where $\Delta\varphi$ is the phase difference, and d_1 is the distance from the first source to the specified point, and d_2 is the distance from the second source to the specified point (d_1 and d_2 are depicted in Figure 13), and λ is the wavelength of the waves. This calculation is performed for every transducer to determine the phase difference to create this peak. However, it must also be considered that there will be secondary peaks where other wavelengths intersect with each other.

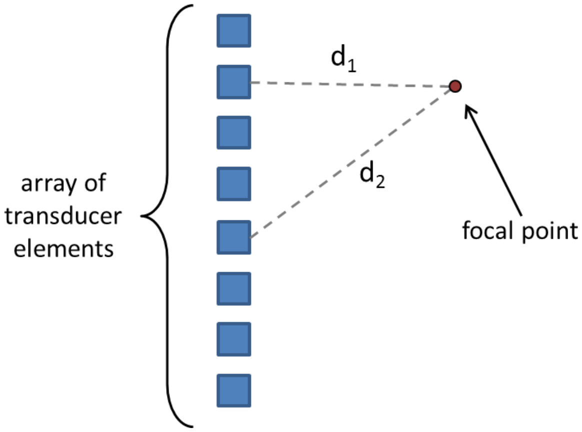

Figure 13 Array of transducer elements (blue squares) and a focal point (red circle) are shown, where the distance between the focal point and two representative elements is shown with the distances d_1 and d_2.

Ultrasound Transducers

This ultrasonic wave is created from the vibration of a piezoelectric crystal. A piezoelectric material is one which generates an electric charge upon deformation, or inversely it deforms from an electrical stimulation [30, 33]. Therefore, the application of an alternating electrical current to a piezoelectric crystal will cause the crystal to vibrate: if oscillated at the appropriate frequency, the vibration will be in the ultrasonic range. If this crystal is placed against a backing material which has the same acoustic impedance as itself, then the wave generated by the vibration will propagate away from that backing [30]. The crystal is protected by a lens, and maximum energy transferal is ensured by minimizing air resistance with a coupling medium at the interface of the lens and the material into which the US will propagate [30].

The shape and configuration of the transducer will change the manner of US propagation, so its choice depends on the application. If the highest ultrasonic energy needs to be close to the transducer, then a single flat transducer can create the necessary field; it generates a wave perpendicular to the surface, so the attenuation will cause the highest heat at the transducer interface [30]. However, for situations where the highest US intensity must be far from the transducer, a single flat transducer will no longer suffice [30]. As was described in the US Focal Point section, a focus far from the US source can be created by a curved transducer, an array of flat transducers arranged in a curved configuration, or an array in a flat configuration which is subjected to electronic focusing. Also, a curved lens in front of a planar transducer can create the same effect. When ultrasonic energy is focused to create thermal ablation, it is considered high-intensity focused ultrasound (HIFU).

Heat Generation

Ultrasonic heat is generated within the tissue from the heat absorption. Heat generation in one dimension is related to the wave intensity by Equation 7

$$q''' = -\nabla \mathrm{I} \qquad \text{Equation 7}$$

where q''' is the heat generation and I is the wave intensity. For the planar transducers, Equation 3 accurately describes the intensity propagation through the tissue, so in one dimension the final heat generation is calculated by Equation 8

$$q''' = 2\alpha I_o e^{-2\alpha x} \qquad \text{Equation 8}$$

However, for HIFU the changes in intensity are not solely a factor of acoustic attenuation (as they are in Equation 3) – since the transducer is not flat, the interference between waves also contributes greatly. To determine the intensity from created by HIFU, the heat generation is calculated from the pressure profile created by the ultrasound in the tissue. The pressure created at each point in the tissue by an individual element in a transducer array can be calculated with Equation 9 [8]

$$p_i(x, y, z) = \sqrt{\frac{2W\rho}{cA}}\left(\frac{fS}{d}\right)e^{\left(\phi - \frac{2\pi d}{\lambda}\right)i - d\alpha} \qquad \text{Equation 9}$$

where p_i is the pressure profile in the volume, x, y, and z are the spatial coordinates of that point, W is the power of the ultrasound source, ρ is the density of the medium, c is the speed of sound, A is the total surface area of the ultrasound source, f is the frequency, S is the area of the individual element, d is the distance from the source to the current point, and φ is the phase of the wave. The final pressure at each point is the sum of the pressure from each element at that point, as shown in Equation 10 [8]

$$P(x, y, z) = \sum_{i=1}^{n} p_i(x, y, z) \qquad \text{Equation 10}$$

where P is the total pressure. The resulting heat generation is calculated by

$$q'''(x,y,z) = \frac{\alpha P^2(x,y,z)}{\rho c} \qquad \text{Equation 11}$$

The heat generation determines the temperature distribution throughout the tissue.

Heat Transfer in Biological Tissues

Once the heat generation in the tissue is known, the temperature at those locations can be determined. Biological tissues are a porous medium consisting of a matrix of collagen fibers, cells, and proteins, with an interstitial fluid running through its cavities (containing blood and plasma) (Figure 14) [40]. This results in a combination of conduction and convection which transfer the generated heat throughout the volume.

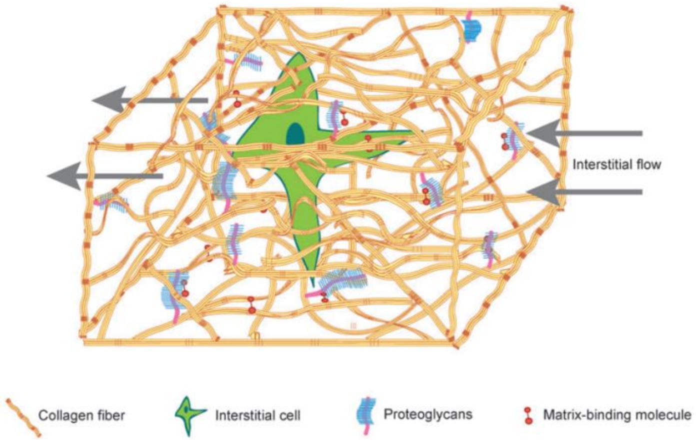

Figure 14 Biological tissues consist of a solid matrix through which interstitial fluid flows [40].

Energy Balance

Each finite volume of tissue has the same amount of heat which exits it as the summation of the heat which enters, is generated, and is stored within the volume (Figure 15). Every node in a simulation must adhere to this energy balance.

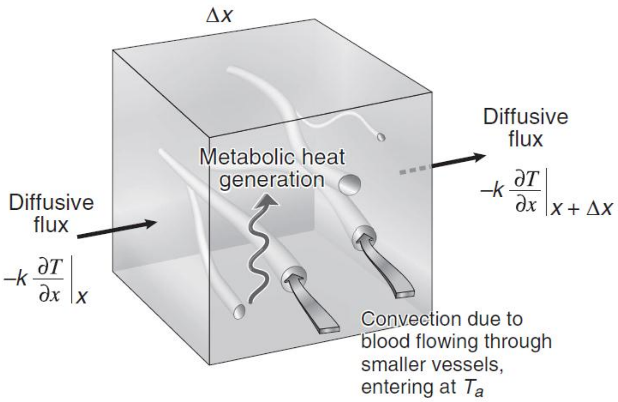

Figure 15 Depiction of energy balance through a finite tissue volume [41].

Conduction is governed by Fourier's Law [42], which states that the heat flux is proportional to the thermal gradient, shown by Equation 12 for one dimension

$$q'' = -k\frac{dT}{dx} \qquad \text{Equation 12}$$

where q'' is the heat flux, k is the heat transfer coefficient, and x is the propagation distance. The heat flux at the entrance of the control volume is equal to the heat flux at the exit minus the change in flux along the length Δx (Equation 13) [42].

$$q''_x = q''_{x+\Delta x} - \frac{\partial q''_x}{\partial x}\Delta x \qquad \text{Equation 13}$$

where q''_x is the heat flux at the entrance and $q''_{x+\Delta x}$ is the heat flux at the exit. Rearranging this equation results in Equation 14

$$q''_{x+\Delta x} - q''_x = \frac{\partial q''_x}{\partial x}\Delta x \qquad \text{Equation 14}$$

In three dimensions, the resulting energy gain by conduction is shown in Equation 15

$$\Delta q_{conduction} = \left(\frac{\partial q''_x}{\partial x} + \frac{\partial q''_y}{\partial y} + \frac{\partial q''_z}{\partial z}\right)\Delta x\Delta y\Delta z \qquad \text{Equation 15}$$

Substituting q'' with Fourier's Law (Equation 12) results in Equation 16

$$q_{conduction} = \left\{\frac{\partial}{\partial x}\left(k\frac{\partial T}{\partial x}\right) + \frac{\partial}{\partial y}\left(k\frac{\partial T}{\partial y}\right) + \frac{\partial}{\partial z}\left(k\frac{\partial T}{\partial z}\right)\right\}\Delta x\Delta y\Delta \mathrm{z}$$

$$= k\left\{\frac{\partial^2 T}{\partial x^2} + \frac{\partial^2 T}{\partial y^2} + \frac{\partial^2 T}{\partial z^2}\right\}\Delta x\Delta y\Delta z \qquad \text{Equation 16}$$

The second equation, with the conduction coefficient outside of the derivative, is obtained only with the assumption that heat conduction coefficient is constant through space. The validity of assumption will be discussed in more detail in the Bioheat Model Assumptions section.

To account for the heat transferred by the interstitial fluid, the heat flux from a fluid moving through a body must be considered. The equation defining this is shown in Equation 17 [41]

$$q_{fluid} = \dot{m}c_p\Delta T \qquad \text{Equation 17}$$

where $\dot{m}$ is the mass flow rate of the fluid, c_p is the fluid's specific heat capacity, and ΔT is the temperature difference between the fluid and the body. For bioheat transfer, the fluid is blood, so the specific heat and temperature of the fluid are represented by c_{pb} and T_b, respectively.

Also, any heat generated within the control volume affects the final temperature of that volume. In the case of biological tissue, without the presence of any external forces this is considered the metabolic heat generation per unit volume, q'''_m. To express this in terms of a heat flux, it must be multiplied by the volume element $(q'''_m * \Delta x\Delta y\Delta z)$.

Heat storage within a volume is the product of the mass (density times volume), specific heat, and rate of temperature change, displayed in Equation 18 [42].

$$q_{stored} = (\rho * \Delta x \Delta y \Delta z) * c_p * \frac{\partial T}{\partial t} \qquad \text{Equation 18}$$

Summing the terms in Equation 16 – Equation 18 and dividing by the control volume results in Equation 19

$$\rho c_p \frac{\partial T}{\partial t} = k\nabla^2 T + c_{pb}\mathrm{w}(T_b - T) + q'''_m \qquad \text{Equation 19}$$

where $w = \dot{m}/(\Delta x \Delta y \Delta z)$ is the blood perfusion rate. This equation is known as the Pennes Bioheat Transfer Equation (BHTE), and is widely used an accepted as an accurate model for energy transport through biological tissue [41, 42].

Bioheat Model Assumptions

It is important to note the assumptions which are taken into consideration for heat transfer through these tissues. The BHTE assumes the tissue vascularization has a negligible influence on the heat transfer, and that the effect of the interstitial fluid flow can be simplified to the isotropic blood perfusion term (the second term on the right side of Equation 19). However, it was found that there can be a significant difference in the heat transfer around very small, counter current blood vessels (two parallel vessels with blood flow in opposite directions) [43]. Also, it assumes that the fluid temperature, T_b, is a constant value through space and time (the value of T_b is given in Table 3). Khaled [43] describes various forms of porous media heat transfer equations which have been developed to more accurately describe this relationship; however, most models for thermal ablation have utilized Pennes and found their results matching well with *in vivo* and *ex vivo* experimentation (see Previous Studies with Ultrasound Thermal therapy section for details on these simulations).

Another set of assumptions for the values of the tissue and blood properties (ρ, c_p, k, c_{pb}, w, and T_b), which are given in Table 3. The tissue density and specific heat are determined by the relationship displayed in Equation 20 [44].

$$\rho c_p = \frac{k}{th_{diff}} \qquad \text{Equation 20}$$

where th_{diff} is the thermal diffusivity, given by 1.80 x 10^{-7} [44]. Thermal conductivity, k, has been found to increase as temperature increases, but it is widely accepted to use a constant value [14]. Blood specific heat is a known constant, given in Table 3. Blood perfusion has also been shown to change with changing temperature, where it rises with increasing temperature before it decreases to about zero at very high heats [14]. Liang [45] observed a change in blood perfusion with different heating powers; this experimentally-determined relationship was used for this research study.

Table 3 Values of tissue and blood properties used during this study.

Property	Value	
T_b	**37 ^{o}C [14]**	
k	**0.499 W/m^{o}C [46]**	
ρc_p	**2.77e6 J/m^{3}K [44]**	
c_{pb}	**4200 J/ kg^{o}C [47]**	
	for Q range	Value
w	0 – 7.5 W	**0.0040 kg/m^{3}s [48]**
	7.5 – 12.5 W	**0.0075 kg/m^{3}s [48]**
	12.5 – 17.5 W	**0.0085 kg/m^{3}s [48]**
	> 17.5 W	**0.0100 kg/m^{3}s [48]**

For this study the metabolic heat generation term (q'''_m) is neglected. This value is relatively small in comparison to the heat generated by the ultrasound input energy, so it has been proven that its contribution to the overall tissue temperature is insignificant during thermal ablation [49]. This results in a replacement of the metabolic generation with the ultrasonic heat generation, so the BHTE is rewritten as Equation 21.

$$\rho c_p \frac{\partial T}{\partial t} = k\nabla^2 T + c_{pb}\mathrm{w}(T_b - T) + q'''$$

Equation 21

Thermal Damage to Cells

To effectively create a device to ablate tumors, knowing the temperature reached within the tissue is not enough; the thermal dose which results in cell death must be determined. The thermal dose refers to the time and temperature combination of the treatment, to be discussed in this section [50].

Cell Death Considerations

Before determining the necessary thermal dose, it is important to note a couple of important considerations for thermal therapy treatment. This section will first explain thermotolerance because it affects the outcome of multiple hyperthermic treatments, and then will describe the role of thermal therapy in combined treatments because it may not be necessary to result in 100% cell death just from heat.

Thermotolerance

After long time periods and multiple doses which are needed for lower temperature hyperthermic treatments (<43°C), the tissue cells start to develop a thermotolerance [27]. The cells adjust to the supraphysiological temperature due to the expression of heat-shock proteins [51, 52, 27], which reduces the efficacy of future rounds of treatment. Thermotolerance is acquired more readily through treatments with a slower heating rate, a lower hyperthermic temperature, and a longer exposure time [53]. To cause the same amount of damage for treatment after thermotolerance is acquired, it is necessary to either increase the treatment time up to twice as long or to increase the temperature by as much as one to two degrees Celsius [53] [54]. Thermal ablation lessens this problem because it greatly reduces the treatment time when compared with conventional thermal therapy; however, the difficulty of sustaining such high temperatures and ensuring that only cancerous cells are adversely affected create complications that are not present with the lower thermal therapy treatments [27]. Another solution to combat thermotolerance is to combine a low temperature thermal therapy with another cancer treatment.

Thermal Therapy in Combination with Chemotherapy

Thermal therapy can also be used with other treatments such as chemotherapy and radiation for cancer therapy [51, 27, 55, 56, 57, 58]. In combination with other treatments, a lower thermal dose of thermal therapy can be used (<43°C [55]). This is because it is not the goal to kill the cancer cells directly from heat exposure, but to enhance the effects of the other treatment methods [51]. Specifically for chemotherapy, a reduced dose of these drugs has been proven to provide the same results as a normal dosage when administered with a hyperthermic treatment [51, 27, 55, 57, 59]. The most affective temperature range for adding to the cytotoxic effects of chemotherapy was found to be between 40.5 and 43°C; above that any enhanced effect of chemotherapy may also be due to thermal therapy-induced cell death [56].

The effect of heat treatment combined with chemotherapeutic treatment is highly dependent on the type of drug. There is a linearly increasing effect of the medication with increasing temperature for alkylating agents and platinum compounds, while antimetabolites are not at all affected by the increased temperature [51, 60, 61]. There are some drugs, such as doxorubicin, which have a more complicated combined effect – their efficacy is not improved before the temperature reaches a specific threshold value (around 42.5°C for doxorubicin) [60, 61].

A problem encountered during chemotherapy is the drug resistance acquired by the cancer cells. After the start of drug treatments, cancer cells lose sensitivity to not only the particular chemotherapy drug used, but other drugs as well (multidrug resistance) [27]. Adding thermal therapy to chemotherapy can help prevent this resistance [27, 60]. However, if the temperature treatments are not hot enough (>42°C), then they may add to the drug resistance because of the introduction of thermotolerance [27, 60].

Thermal Damage Models

Mathematical models have been derived from experimental data to theoretically determine the cell death that occurs at each time-temperature combination. The one-step Arrhenius equation is the most-widely accepted model (it is a two-state model, where the cells are assumed either viable or dead [52]); however, there has been recent research to describe hyperthermic cell death using a different process. Feng [62] fit thermal therapy test data on prostate cancer cells to a different two-state model, which also describes the cells as either alive or dead. This model was designed to fix the major problems of the Arrhenius model, specifically its difficulty with fitting the full range of temperature data and its large fluctuations from small changes in kinetic parameters. Feng's model was able to better describe the data at the lower temperatures. O'Neill [63] developed a three-state model which contained a middle state where the cells were not yet dead but vulnerable. These vulnerable cells could either reverse back to the alive state or continue on to irreversible damage, depending on the environmental conditions at that middle state.

This model fit the data well and was also able to describe not only the fast cell death rate during thermal therapy treatment, but also the continuing slow cell death in the time following treatment, where the cells are at normal physiological temperatures.

Although there is ongoing work to find a better-fitting model, the Arrhenius is used for the majority of cell studies because it works well for most experiments. Also, if it has trouble accurately fitting the whole temperature range, then the tests can be split into different regions (at break points), where each region has its own set of kinetic parameters [52]. The kinetic parameters (A and E_a in Equation 22) define the Arrhenius equation, which relates the rate of cell death, k, to the prescribed temperature (T) by Equation 22 [64],

$$k(T) = Ae^{-E_a/RT} \qquad \text{Equation 22}$$

where A is the frequency factor, E_a is the activation energy, and R is the universal gas constant. Finding a combination of the frequency factor (A) and activation energy (E_a) for a certain cell type allows for optimal thermal doses to be determined. The reaction rate k is related to cell survival by Equation 23 [52],

$$S = e^{-\int_0^t k dt} \qquad \text{Equation 23}$$

where S is the survival fraction.

An equation introduced by He [52] to correlate E_a and A (Equation 24) works well for many recent studies [10, 11, 65, 66, 67]. However, this relationship cannot solely determine the kinetic parameters: both still need to be found experimentally to be accurate [28].

$$ln(A) = 0.38E_a - 9.36 \qquad \text{Equation 24 [52]}$$

Thermal Isoeffective Dose

Another method of predicting cell damage at specified time-temperature combinations is called the "Thermal Isoeffective Dose" (TID), which is a simplification of the Arrhenius equation [28]. With this method, once the injury at one reference isothermal temperature is known, the injury for any range of times and temperatures can be determined. The TID is based on an equation determined by Dewey [68], where from the graph of the Arrhenius relationship of cell death rate, the inverse of the slope is defined as $\widetilde{D}_0$. For any given cell survival, the time of the thermal treatment is proportional to $\widetilde{D}_0$, so it can be written as shown in Equation 25

$$\widetilde{D}_0(T) = C * t(T) \qquad \text{Equation 25}$$

Dewey [68] defined R as the relative decrease in the rate of cell death for a 1°C increase in temperature, which becomes

$$R = \frac{\widetilde{D}_0(T+1)}{\widetilde{D}_0(T)} = \frac{C * t(T+1)}{C * t(T)} = \frac{t(T+1)}{t(T)} \qquad \text{Equation 26}$$

Sapareto and Dewey [69] rearranged Equation 26 to create a conversion of treatment times for any two isothermal temperatures (Equation 27).

$$t_1 = t_2 R^{(T_2 - T_1)} \qquad \text{Equation 27}$$

Sapareto and Dewey [69] then proposed the TID conversion to be specific to 43°C, where the time it takes to inflict a certain amount of damage at any temperature can be converted into the time it takes to cause that same amount of damage at 43°C, using Equation 28

$$CEM43°\mathrm{C} = tR^{43-T} \qquad \text{Equation 28}$$

where CEM43°C is the cumulative number of equivalent minutes at 43°C, t is time (min), T is the average temperature during that time interval (°C), and R is the number of minutes that are needed to compensate for a 1°C temperature difference [28, 53]. R is assumed to be 0.5 for temperatures above 43°C, and 0.25 for temperatures below 43°C [69] (however these are just assumptions, the values are actually different for every type of cell/tissue [53]).

It can be difficult to have a single constant temperature throughout the entire treatment time, so the TID can be used for non-isothermal temperature profiles as well. Transient profiles can be converted into one CEM43°C value by summing together sufficiently small intervals of time, shown by Equation 29 [70, 53, 69].

$$CEM43°\mathrm{C} = \sum_{t=0}^{t_{final}} R^{43-\bar{T}_i}\Delta t \qquad \text{Equation 29}$$

where t_{final} is the last time interval, $\bar{T}$ is the average temperature at the specified time interval, and Δt is the time interval. The TID and Arrhenius approaches give very similar results until the hold temperature exceeds 50°C, where the TID predicts a longer time needed to incur cell death [28]. An important distinction between these two models is that the TID is the same for all cell and tissue types, while the Arrhenius equation is specific to the type of cell in question.

Previous Studies with Ultrasound Thermal therapy

Ultrasound thermal therapy has been considered for many years as a viable option for cancer treatment; however it is not yet implemented in a wide-spread manner because more research is needed to better predict treatment outcomes. There are two main types of devices studied for this thesis: intraluminal cylindrical ultrasound transducers for use on prostate cancer, and external focused ultrasound transducers for breast cancer. Intraluminal devices are designed to be inserted either through the urethra or rectum of the patient for close access of the prostate gland. There is more flexibility with the external focused transducer for breast cancer because there are less geometric limitations than with an intraluminal device.

Performing numerical simulations on the ultrasonic and heat propagation through the biological tissues is important for device design and treatment planning [71]. This section will discuss the current simulation studies and devices designed for ultrasound thermal therapy, including devices which are being currently-tested for use on patients.

Simulations

Many numerical simulations using a finite difference method [6, 29, 49, 71, 72, 73, 74, 75, 76] have been performed which determine the resulting tissue necrosis for ultrasound thermal therapy. Ensuring the accuracy of the simulation model is important because the results will be invalid if the setup is incorrect or simplified too much. However, a model which is too complex will increase the computational expense, so a tradeoff between accuracy and computation time is created. The setup geometry, boundary and initial conditions, and governing equations are all involved in creating an accurate model of heat transfer through the breast and prostate.

Setup geometry

The geometry of the volume to be ablated is usually a simplified version of the actual anatomical shape. However in some cases, prostate volumes were derived from CT or MRI images taken from actual patients [5, 71]. Cubical shapes have been tested as computational domains to solely experiment with the pressure and heat propagation within the tissue [34, 73]. The prostate was often modeled as a hollow cylinder of outer radius 3 cm with the transducers in its center [75]. Tyréus did not use a 3D model but instead split the problem into two 2D models in cylindrical coordinates, r-θ and r-z planes, as shown in Figure 16 [75].

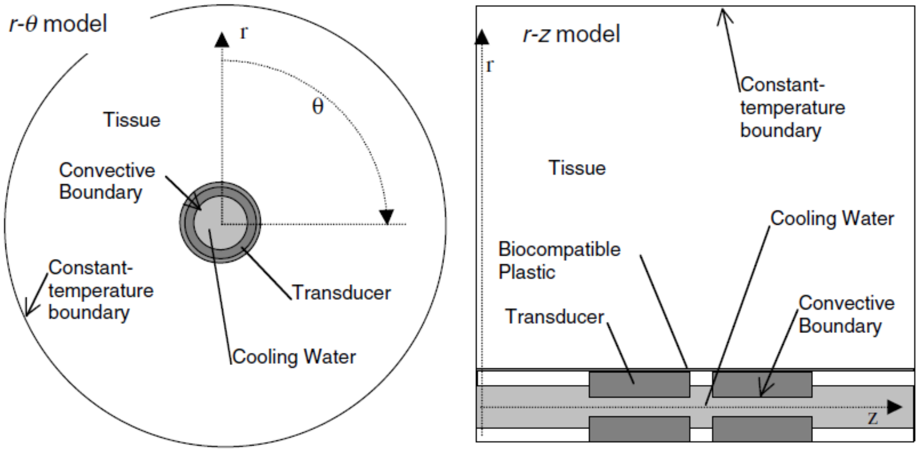

Figure 16 Model setup of intraluminal transducer inside of cylindrical prostate, used by [75]. Two 2D simulations were used in the r-θ (left) and r-z (right) planes.

The breast was modeled as a 6 cm radius hemisphere by Ho [15], Huang [77], Cheng [72], and Ju [29]. Lin [78] modeled the breast as a bell-shape, shown in Figure 17. Most studies used water as a coupling medium between the transducer and breast since it has similar acoustical properties to tissue, so interface attenuation was not included in the model [15, 29, 72]. Malinen included different thermal properties for the external skin, the healthy breast tissue, and the tumorous breast tissue [18].

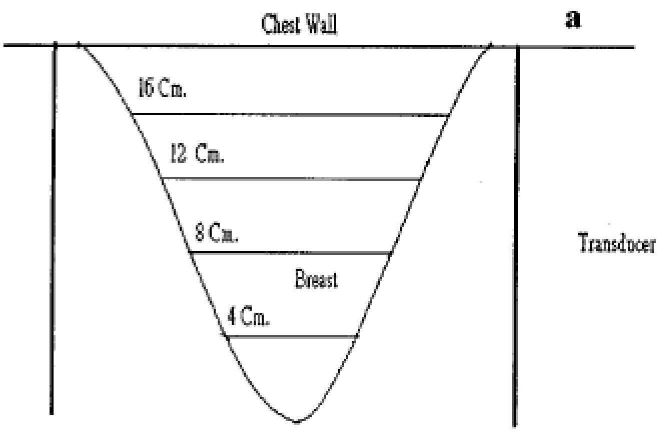

Figure 17 Lin modeled the breast as a bell shape, with the cylindrical transducer coaxially surrounding it [78].

Simulation Parameters and Boundary/Initial Conditions

Most simulations set the boundary and initial conditions to normal body temperature, 37^{o}C [6, 8, 14, 15, 29, 71, 72, 73, 76, 79]. Wan [49] used a Neumann boundary condition instead of the Dirichlet condition because his computation volume was small. For intraluminal simulations where cooling water was involved, a convective boundary condition was used in the center of the cavity, where the water temperature was set to either 5^{o}C [75], 10^{o}C [74], 25^{o}C [14], or 30^{o}C [71], or different temperatures were compared in the study ranging from 5 – 42^{o}C [76]. Ho [15] also tested the use of cooling water external to the breast at 20^{o}C.

The cylindrical transducers will produce heat generation by the gradient of intensity as was shown in Equation 7, but instead of the one-dimension result in Equation 8, the heat generation is described by cylindrical coordinates, resulting in Equation 30 [74] [80] [75] [76] [48] [14]

$$q''' = 2\eta\alpha I_o r_o e^{-2\alpha^{r-r_o}/r} \qquad \text{Equation 30}$$

where η is the applicator efficiency, r_o is the radius of the applicator, and r is the current radius.

The studies which tested phased array transducers modeled them as individual point sources. Huygen’s Principle determined the summation of the individual sources, and Saleh [6] and Hutchinson [8] used Equation 9 – Equation 11 (in Ultrasound Physics section) to calculate the final pressure field. The Rayleigh-Sommerfeld integral was used in many studies to combine the pressure created by each individual element [15] [77] [72] [73] [79] [18] [5], written as

$$p(x,y,z) = \frac{i\rho ck}{2\pi}\int_S u\frac{e^{-(\alpha+ik)(|r-r\prime|)}}{|r-r'|}dS \qquad \text{Equation 31}$$

where p(x,y,z) is the acoustic pressure, ρ is the medium’s density, c is the speed of sound, k is the wave number, u is the surface velocity, α is the attenuation coefficient, r is the location of the point where the pressure is being calculated, and r’ is location of the transducer element. The heat generation produced from this pressure is calculated using Equation 11 [15] [6] [29] [79] [18] [8] [49] [5].

For most studies, the acoustic absorption was considered to be solely a function of the attenuation of the wave [15] [72] [29] [48]. A constant attenuation was considered by most studies, at 5.3 Np/mMHz for Chen [71], 8.3 Np/mMHz for Prakash [80], 0.5 dB/cmMHz for Chopra [5], 5.01/mMHz for Diederich [76], and different values from 2.5 – 30 Np/m were tested by Lin [81]. Instead of using either a constant value for attenuation, or varying it with frequency, Liu [79] and Tyréus [74] [75] varied the ultrasonic absorption with respect to the thermal dose by

$$\alpha(x,y,z) = \begin{cases} \alpha_1, & log(TD) \le 2 \\ \alpha_1 + (\alpha_2 - \alpha_1)\dfrac{log(TD)-2}{7-2}, & 2 < log(TD) \le 7 \\ \alpha_2, & log(TD) > 7 \end{cases} \qquad \text{Equation 32}$$

where $\alpha_1 = 4.1$ Np/mMHz, $\alpha_2 = 9$ Np/mMHz, and TD is the thermal dose at the (x,y,z) coordinate.

The blood perfusion in the tissue was also mostly held constant through time and space, where Lin [81] and Liang [48] used 6 kg/m^{3}s, Chopra [5] simulated 5.3 kg/m^{3}s until the temperature reach 55^{o}C when it became 0, Prakash [80] used a value of 2.5 kg/m^{3}s at temperatures less than 60^{o}C and 0 kg/m^{3}s at higher temperatures, Diederich [76] tested values of constant perfusion from 0.5 – 10.0 kg/m^{3}s, and Chen [71] tested different constant values of attenuation at 0.5, 2.5, 3.5, and 5.0 kg/m^{3}s. However, a more accurate model was created when it was varied. Tyréus [74] [75] modeled it with a constant value (2 kg/m^{3}s for prostate tissue) until the thermal dose reached CEM43^{o}C = 300 minutes, when the perfusion dropped to 0. In a recent study, Prakash [14] compared different combinations of functions which described the blood perfusion and acoustic absorption as a function of an Arrhenius equation defined by Schutt and Haemmerich [82], thermal damage thresholds, or temperature, in order to determine an accurate combination of parameters.

All simulations used Pennes' BHTE (Equation 19) to describe the heat transfer through the tissue [15] [77] [72] [73] [6] [29] [79] [18] [8] [49] [71] [74] [80] [75] [5] [76] [48] [14]. Also, to find the tissue necrosis from the thermal doses, Sapareto and Dewey's thermal isoeffective dose (Equation 28) was used. For necrosis to occur, the studies set CEM43^{o}C to equal 120 minutes [49], 240 minutes [15] [73] [79] [8] [80] [14], 300 minutes [72] [18], or a conservative 600 minutes [74] [75]. Some simulations restricted the computations to temperatures below 100^{o}C [18] [8].

Transducer Configurations

Intraluminal devices often consist of multiple cylindrical transducers axially arranged, which are segmented angularly so different segments can be tuned to different power levels (schematic displayed in Figure 18) [71] [74] [80] [81] [75] [76] [14]. Chopra [5] placed 4 mm x 20 mm planar transducers end-to-end inside of a 6mm diameter catheter. Chen's [71] intraluminal design consisted of a 3 mm radius catheter, 1.75 radius transducer, and individual transducer length of 10 mm (R, Re, and Le in Figure 18, respectively). Tyréus tested interstitial cylindrical transducers with outer diameter 2.2 mm and length 10 mm in one study [75], and outer diameters ranging from 1.5 – 4.0 mm with lengths 5 – 10 mm [74]. Diederich [76] had five axially-aligned cylindrical transducers with an outer diameter of 10 mm and length 10 mm. Prakash [14] simulated an intraluminal device with two cylindrical transducers with an outer diameter of 3.5 mm, length of 10 mm, and 2 mm of space between each. To keep the transducer and cavity wall cool, chilled water can be circulated either inside the cylindrical transducers, or exterior to it within the catheter walls [71] [74] [75] [76] [14]. An example of a device with external cooling is displayed in Figure 19.

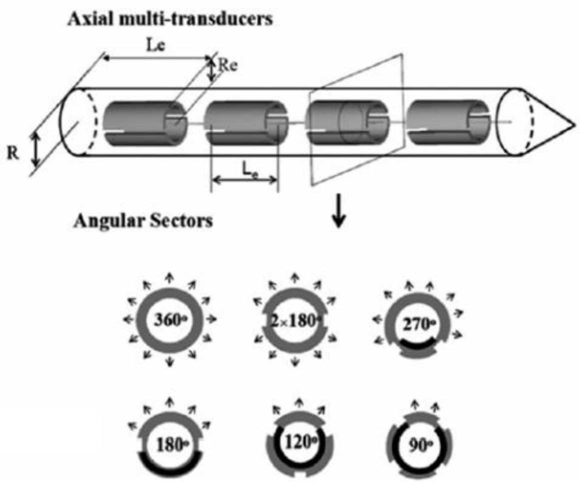

Figure 18 Intraluminal transducer schematic displaying four independently-controlled cylindrical transducers with angular segments that can be blocked so power is only emitted in desired angular direction [71].

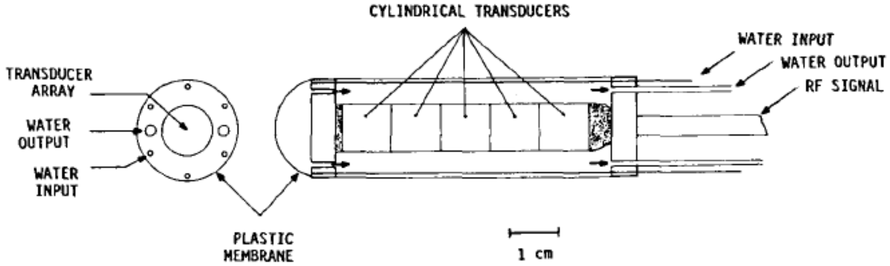

Figure 19 Schematic of Diederich's transducer used in simulations and in vivo experiments on dogs. It also demonstrates the configuration of cooling water in between catheter wall and cylindrical transducer outer diameter [76].

Individual focused transducers of radius 8 and 15 cm, and phased arrays with 16 and 32 elements of the same radii were tested and compared by Fan [73]. A flat phased array was tested by Saleh [6] (64 elements creating a 2 cm x 2 cm square) and Hutchinson [8] (a linear array of 1.5 cm x 9.0 cm x 0.2 cm with an element width that varies depending on the current simulation frequency to be half the wavelength). Liu [79] tested a curved phased array with 400 elements arranged in a 20 x 20 configuration with a radius of curvature of 12 cm. Wan [49] simulated a phased array shaped as a square section of a 10 cm diameter sphere, with 3 mm x 3 mm square elements arranged 35 x 35 (Figure 20). A cylindrical phased array of transducers which surrounds the breast was tested by Ho [15], Ju [29], and Lin [78]. Ho's design had a diameter of 20 cm, height of 2 cm, and included 200 elements. Lin used 384 elements, creating a cylinder of diameter 25 cm. Malinen simulated and optimized necrosis for a hemispherical shell transducer of 530 elements (Figure 21) [18]. Cheng [72] split a part of a 10 cm radius square section of a spherical transducer into four equal transducers, each with a 45^o angle between their face and the central axis of the breast. Huang [77] tested two phased array transducers, which were curved towards the breast and 24 cm apart on opposite ends of the breast. The dimensions of the transducers were 15 cm x 16 cm x 1.5 cm, and they could be translated around the breast and rotated on their own axes parallel to each other and the base of the breast.

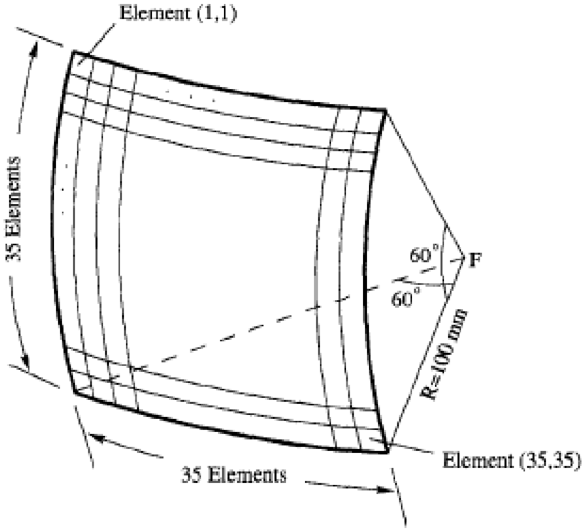

Figure 20 A phased array transducer which is a square section of a 10 cm diameter sphere of 35 elements by 35 elements, as was simulated by Wan [49].

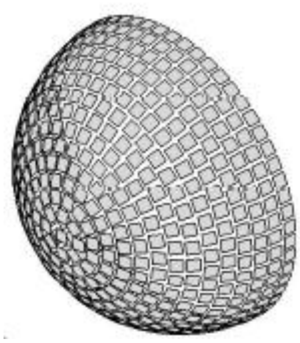

Figure 21 The hemispherical shell phased array transducer with 530 elements, simulated by Malinen [18].

Frequencies of 0.5 MHz [72] [8], 1 MHz [15] [77] [79] [18] [8], 1.5 MHz [8], 2.0 MHz [8], 2.5 MHz [78], and 4.0 – 4.5 MHz [78] were tested. Ho [15], Cheng [72], and Lin [78] tested a physical scanning of the ultrasound transducer, where the focal points did not change location with respect to the transducer, but the transducer translated around the breast to ablate the entire tumor region.

For phased arrays, different focal patterns were tested. The effect of one transducer was tested for both phased arrays and spherical transducers [72]. Ju [29] and Hutchinson [8] scanned a single focal point continuously throughout the ablation region. Some studies tested multiple transducers concurrently ablating the tissue with a common focal point [77] [72] [18]. Other studies used a multifocal pattern which had the transducer split its focus on points in different locations around the volume to widen the necrosed volume tissue per ultrasound dose [15] [6] [79]. Cheng [72] tested the use of multiple transducers around the breast, each with a focal point in a different location (Figure 22).

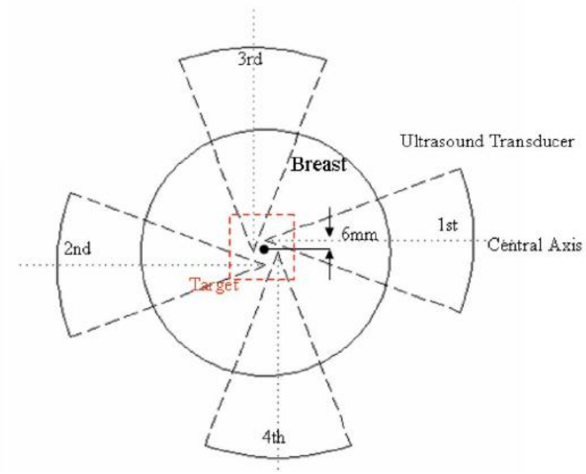

Figure 22 A simulation study where there were four transducers surrounding the breast, each with a different focal point within the current volume to be ablated [72].

Conclusions of Previous Simulation Studies

Cylindrical intraluminal ultrasound transducers were found to be able to effectively heat targeted sections of the prostate with the correct set of transducer parameters [71] [75]. Tyréus [74] compared his data with previous *ex vivo* and *in vivo* experiments and found an agreement between the results, and Diederich [76] proved matching results with his own in vivo experiments: these verified that this model for cylindrical transducers is accurate. Another finding was that the chilled water cooling the transducers not only lowered the temperature at the catheter wall, but also moved the point of highest heat away from the axis of the cavity and transducer [74] [75] [76]. Tyréus [74] and Diederich [76] found that larger diameter devices created larger necrosed tissue lesions, which was also useful because the devices that had cooling external to the transducers needed to be larger and were found to cool the cavity wall more effectively [74]. They also determined that the tissue perfusion was a larger factor in affecting the lesion size than the attenuation, where more perfusion decreased the temperature and lesion size, so it is important to choose an accurate value for it [74] [76]. Prakash [14] concluded that although using a constant value of acoustic attenuation and blood perfusion is less computationally expensive, there are large differences in the results obtained between these constant conditions and those which vary with thermal dose so the results will be less accurate.

For the breast cancer focused simulations, it was found that using one curved transducer with a single focal point allows the heating around the focal point to be easily controlled [72]. The cylindrical design coaxial to the breast was found to effectively reach the desired target locations, and avoids excessive heat at the ribcage because the ultrasound propagates parallel to the ribs [15]. It was proven that using a phased array instead of a single curved array reduces the treatment time [73]. Furthermore, the multifocus design allows for less cooling time between each sonication because the intensity is spread throughout the volume, and therefore led to reduced treatment times [15] [72]. Huang [77] found that with tilted transducers, rib heating could be avoided if the angle between the vertical and the transducer axis was greater than 56.6^o. When phased transducers are electrically steered away from the central transducer axis, they must be designed to avoid grating lobes because they produce unwanted heating in the areas around the focal point [6]; this means that the near-field temperature is higher for larger scan widths [8]. Including more transducers in phased array systems decreases the number of grating lobes, and therefore there is less unwanted heating in the space between the focal point and the transducers [18]. Another conclusion was that electrical scanning is quicker than physically scanning the focal point [6]. Also, since the focal point can be shifted very quickly to different locations that were not experiencing high heats before, then cooling time isn't necessary before the next sonication. In contrast, Wan [49] discovered that non-scanned multifocal patterns decreased treatment time when compared to multiple focus scanning.

It was found that the driving frequency needed to be set low for deep tumors, and high frequencies were appropriate for superficial tumors since their power is absorbed in a shorter space [29] [78]. Therefore, to obtain an even heating of the entire breast, a combination of low and high frequencies can be used [29].

Previously-Developed Device Concepts

Ultrasound thermal therapy has gained interest and popularity throughout the years, so there have already been devices created which are currently being tested, including some which are in use at treatment clinics outside of the United States. Currently, transurethral US probes inside a catheter are still in the developmental stage [16], and concepts which have not yet come to market have been proposed in patents and are being tested. A patent from 1995 describes a transurethral US device for BPH and prostate cancer treatments [83]. It includes cooling external to the transducer, and individually-controlled segments oriented axially from one another, with the transducers segmented angularly for control of angular US propagation (Figure 23). Prakash [80] designed an interstitial device to be used for clinical pilot studies where the transducer slides into a catheter, has segmented transducers, and water flowing between the transducer and the catheter wall (Figure 24, upper and lower left). He has also designed a concept for a flexible transurethral applicator with includes angularly segmented transducers and an inflatable balloon at the top to arrest the device in the bladder (Figure 24, upper and lower right).

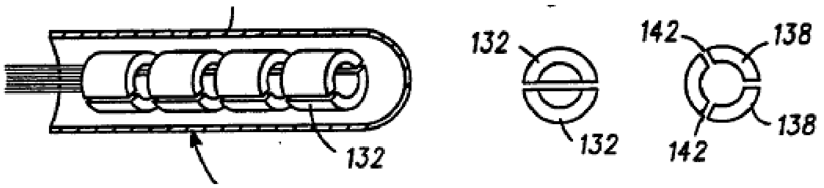

Figure 23 Intraluminal patent idea with multiple cylindrical transducers arranged axially, and the right view shows two possible angular segmentation configurations [83].

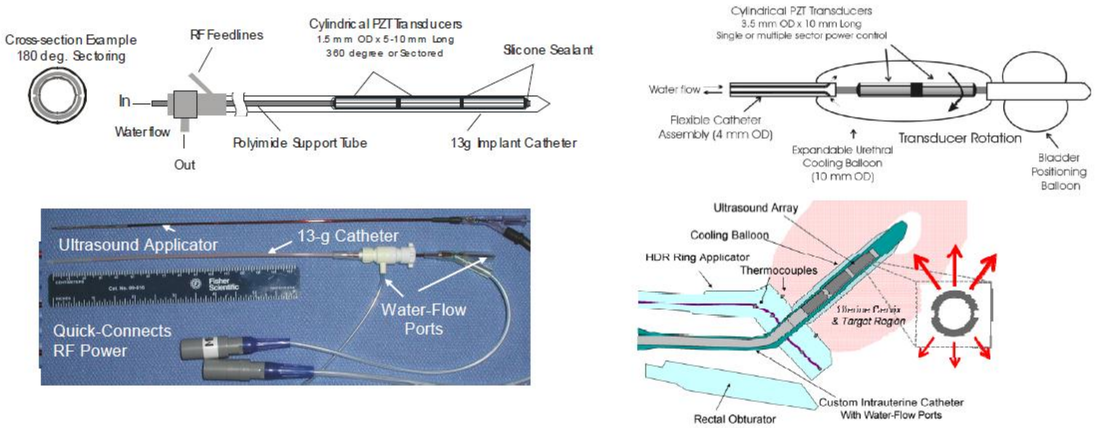

Figure 24 Interstitial device for clinical pilot trials (upper and lower left), and intraluminal concept for simulation purposes (upper and lower right).

Zhou [7] has compared different devices which are currently in-use in Europe or being clinically tested for HIFU ablation, and his table comparing these devices is reproduced (with permission) in Table 4. The transrectal devices with a concave transducer for prostate cancer treatment include the Ablatherm (6-month post-treatment efficacy demonstrated by Thuroff [84]) and the Sonablate-500 (5-year post-treatment efficacy demonstrated by Uchida [85]) [7]. Extracorporeal devices with phased arrays arranged in a spherical bowl include the Exablate 2000 and the FEP-BY02 [7] [13]. Images of the FEP-BY02 and Ablatherm devices are shown in

Table 4 Comparison of different HIFU devices currently in-use, reproduced with permission from [7].

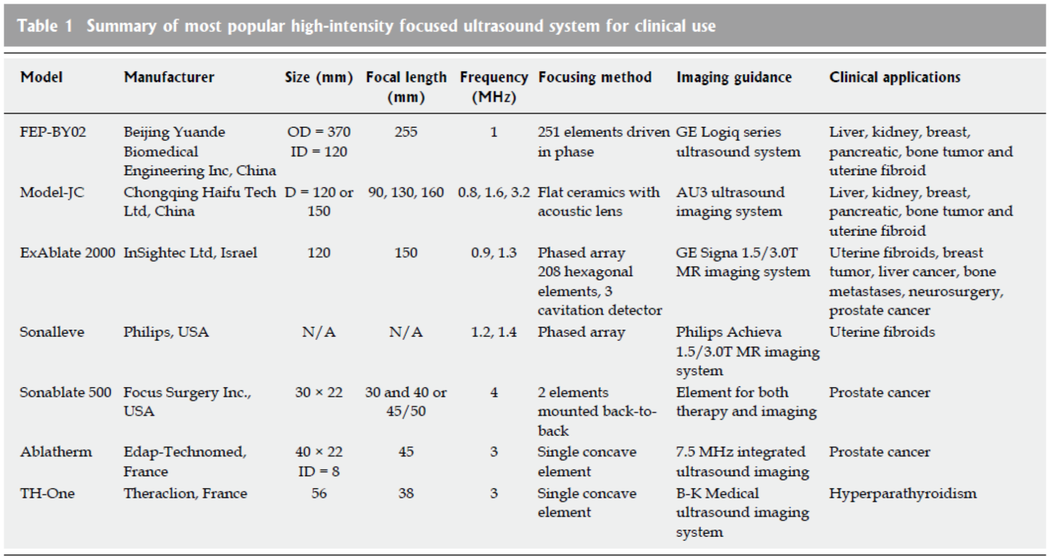

Table 1 Summary of most popular high-intensity focused ultrasound system for clinical use

Model	Manufacturer	Size (mm)	Focal length (mm)	Frequency (MHz)	Focusing method	Imaging guidance	Clinical applications
FEP-BY02	Beijing Yuande Biomedical Engineering Inc, China	OD = 370 ID = 120	255	1	251 elements driven in phase	GE Logiq series ultrasound system	Liver, kidney, breast, pancreatic, bone tumor and uterine fibroid
Model-JC	Chongqing Haifu Tech Ltd, China	D = 120 or 150	90, 130, 160	0.8, 1.6, 3.2	Flat ceramics with acoustic lens	AU3 ultrasound imaging system	Liver, kidney, breast, pancreatic, bone tumor and uterine fibroid
ExAblate 2000	InSightec Ltd, Israel	120	150	0.9, 1.3	Phased array 208 hexagonal elements, 3 cavitation detector	GE Signa 1.5/3.0T MR imaging system	Uterine fibroids, breast tumor, liver cancer, bone metastases, neurosurgery, prostate cancer
Sonalleve	Philips, USA	N/A	N/A	1.2, 1.4	Phased array	Philips Achieva 1.5/3.0T MR imaging system	Uterine fibroids
Sonablate 500	Focus Surgery Inc., USA	30 × 22	30 and 40 or 45/50	4	2 elements mounted back-to-back	Element for both therapy and imaging	Prostate cancer
Ablatherm	Edap-Technomed, France	40 × 22 ID = 8	45	3	Single concave element	7.5 MHz integrated ultrasound imaging	Prostate cancer
TH-One	Theraclion, France	56	38	3	Single concave element	B-K Medical ultrasound imaging system	Hyperparathyroidism

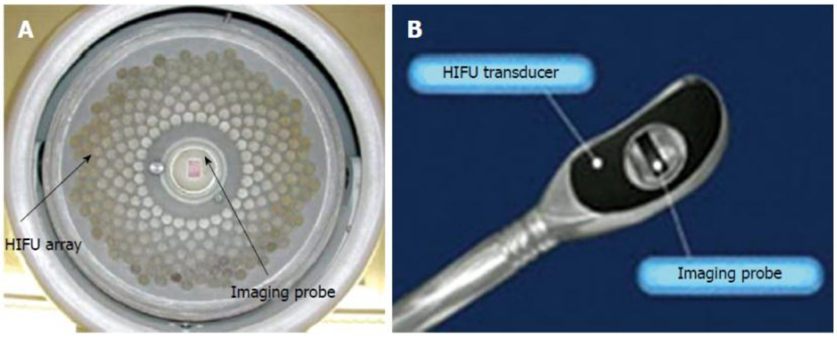

Figure 25 Images of (A) the FEP-BY02 extracorporeal phased array transducer and (B) the Ablatherm transrectal curved transducer [7].

Chapter 3: Summary of Cell Thermal Therapy Studies

To determine the mathematical model to represent thermal damage, thermal therapy studies must be conducted in a controlled experimental setting. *In vitro* experiments are performed to isolate the cancer cells during testing, although the inaccuracies which are associated with this segregation must be kept in mind while reviewing the results of such experiments.

Previous review papers have compared the required thermal doses for hyperthermia in many human and animal cells in vitro. In 1979, Bhuyan [86] reviewed the heat sensitivities for different cell types, finding the time to result in 90% cell destruction for temperatures between 41 – 45^{o}C. He [52] and Wright [64] compiled the Arrhenius parameters needed for the mathematical model which describes their cell death (explain later in this paper) for different types of cells. Some of the data from these three authors has been compiled in Table 5.

Table 5. Compilation of most results from previous reviewon cell death for different human and animal cell lines. Tested temperature ranges and cell survival assays also presented [52, 86, 64].

Review Ref	Cancer Cell Type	Temp Range (^{o}C)	Survivability Assay	Time to 90% Cell Death (min)	Arrhenius Parameters		Reference
					E_a (kJ/mol)	A (s^{-1})	
Bhuyan 1979	Chinese Hampster Ovary (CHO)	43		100			Sapareto 1978
				94			Bhuyan 1977
				83			Gerwerk 1977
		44		30			Westra 1971
				50			Sapareto 1978
				23.3			Gerwerk 1977
		45		13.3			Westra 1971
	V79	43		150			Johnson 1974
				140			Schulman 1974
		44		84			Johnson 1974
	L1210	43		50			Bhuyan 1977
	EMT-6	43		30			Marmor 1977
				102			Leith 1977
	HeLa	43		82			Palzer 1973
				86			Bhuyan 1977
				150			Gerner 1976
He 2003	Human Erythrocyte	37-45	Hemolysis (1%)		121.34	$4.2x10^{13}$	Gershfeld 1988
		44-60	Hemolysis (5%)		193.72	$7.6x10^{27}$	Moussa 1979
		46-54	K+ Leakage		246.02	$3.3x10^{39}$	Prinsze 1991
		60-77	Ghosting		210.87	$1.8x10^{30}$	Lloyd 1973
	Fibroblast	43-46	K+ Leakage		587.43	$9.5x10^{95}$	Prinsze 1991
			Clonogenicity		773.62	$8.8x10^{125}$	Prinsze 1992
		40-70	Calcein Leakage		158.99	not found	Bischof 1995
	HeLa	41-44	Clonogenics		1697.03	$7.37x10^{277}$	Landry 1978
		44-49			705.42	$1.91x10^{113}$	
		49-55			108.37	$1.0x10^{16}$	
		44-68	Membrane Bubbling		248.95	$9.1x10^{36}$	Moussa 1977
		48.2-65	50% eosin Y-stain		388.28	$8.8x10^{59}$	Mixter 1963
	CHO	39-43	Clonogenics		1181.14	$2.4x10^{190}$	Dikomey 1991
		not specified			1266.08	$4.86x10^{207}$	Bauer 1979
					550.61	$7.28x10^{89}$	
		48.2-65	Clonogenicity		616.72	$2.1x10^{100}$	Prinsze 1992
	Skeletal Muscle	40-60	Flourescent Dye Leakage		137.65	$2.27x10^{19}$	Padanilam 1994
		41-60	Mechanical Contraction		121.34	$2.1x10^{19}$	Cravalho 1992
		45-60	Increased Permeability to FADH		241	$1.6x10^{37}$	Gaylor 1989
			CDFA Leakage		176.98	$7.3x10^{21}$	Cravalho 1992
Wright 2003	HeLa	40-48	Chromatin Increase		363	$5.74x10^{58}$	Roti Roti 1979
		44-48	Cell Death		644	$9.61x10^{104}$	
		44-68	**Bubble Formation**		**249**	$\mathbf{9.09x10^{36}}$	**Moussa 1977**
		48-65	**Eosin Y-Staining**		**369**	$\mathbf{1.00x10^{57}}$	**Mixter 1963**
	Erythrocytes	44-60	Lysis, Reversible		250	$4.10x10^{38}$	Moussa 1979
			Lysis, Irreversible		128	$1.70x10^{19}$	
	Hampster Kidney	37-70	1% Survival		498	$1.7x10^{64}$	Borrelli 1990
			10% Survival		498	$1.26x10^{78}$	
			90% Survival		498	$8.40x10^{78}$	
	Rat Muscle	37-70	Calcein-AM Leakage		138	$6.36x10^{19}$	Padanilam 1993

These three authors demonstrate the difference in cell survivability between the different cell types, especially between human and animal cell lines. This is further shown in a review by Dewhirst [53]. He compared results from Chinese hamster ovary cells against hyperthermia tests on human melanoma cells of the same temperature range. It was found that both exhibited a similar shape, but the same temperature tests took longer to result in the same cell death for the human cells than it did for the animal cells. Graphs from the mathematical models (Arrhenius) were also compared for different human and rodent cell lines, and the shallower slopes for the human cells also support the claim that human cells are more resistant. Therefore, to have the appropriate thermal dose, it is important to be experimentally determined for each cancer cell type.

The following chapter will review recent *in vitro* cell studies that have been performed on human cells, and summarize the mathematical models determined by these experiments which describe the cell death rate with respect to the thermal dose. The type of cell, cell survival assay, and heating method are important experimental parameters because they greatly impact the testing results [28, 87], so the different cell types and testing methods of these studies are discussed.

Cell Types and Preparation Protocols

The thermal therapy experiments discussed below have been conducted on cancer cells of the prostate [62, 88], liver [11, 63, 65], bladder [10], kidney [66, 67, 89], and lung [90] (although the lung data is not analyzed further than its experimental setup). He and Walsh cultured cells in 5% fetal bovine serum (FBS) in a 5% CO_2 environment at 37°C [66, 89], while the other authors used 10% FBS and 1% penicillin/streptomycin and incubated in 95% humidity and either 10% CO_2 [65, 67] or 5% CO_2 [10, 11, 62, 63, 88].

Some studies tested only attached cells, while other performed experiments on both attached and suspended cells for comparison. Jen [10] and Huang [11, 67] prepared only attached cells by first washing away the dead cells with phosphate-buffered saline (PBS) and removing the live cells from the flask on which they were cultured with Trypsin. These cells were placed on a 35mm Petri dish and allowed to attach for 24 hours. It was washed twice more with PBS and mixed with 0.6mL of its media. Feng [62] placed the flasks on which the cells were cultured directly into the water bath after removing the medium and replacing it with PBS. Bhowmick [88] trypsinized prostate cancer cells off of the flasks, and plated them on either 12 mm x 12 mm glass coverslips, single-well microslides, or in a 25 cm^2 flask (for the survival assay calcein leakage, propidium iodide, and clonogenic survival assays, respectively, to be discussed in the Assay section) and left them overnight to attach. Afterwards, the cells on the cover glasses were washed with PBS, and the cells on the slides were washed with salt solution and covered with a coverslip and silicone grease. O'Neill [63] seeded the cultured cells into a 96-well plate and allowed them to attach overnight – this was the receptacle used during the heating experiments. Finally, Walsh [89] also only tested attached cells, and prepared the renal carcinoma cells by plating them in either well chamber slides or a 35 mm petri dish, and allowed them to attach for 48 hours.

Shah [65] and He [66] tested both attached and suspended cancer cells. Shah tested suspended liver cancer cells, which were resuspended after trypsinizing them for 5-10 minutes to remove them from the flask on which they were grown, centrifuging for 5 minutes at 1200 rpm, and resuspending the cells in their media. 3 µL of the cell suspension was placed between two 12 mm diameter cover glasses. To test attached cells, Shah left some cover glasses to sit overnight with the cells on top. He used the same procedures, except he only trypsinized the renal cancer cells for 3-5 minutes and specified the centrifuge speed in acceleration, 400g.

Heating Methods

The cell heating method has a noticeable effect on the experimental results. One common method to heat the cells is using a heated water bath. However, water baths heat cells at a slow rate. This is a problem because if an isothermal experiment has a high target temperature (>50°C), then a slow heating rate will cause cell damage during the non-isothermal ramping before the peak temperature has been reached [88]. This is detrimental to the determination of a mathematical model to correlate thermal dose and cell death.

Placing the cells on a heated plate or stage is another heating method used in the reviewed studies. The heat is quickly transferred to the slide or petri dish containing the cells, so there is a significantly shorter time to reach high peak temperatures than with a water bath. However, even with a heating stage the high temperature of thermal ablation still causes some cell death to occur while the sample's temperature is ramping, so there will always be some error when determining the isothermal damage. Also, it is more difficult to ensure an even temperature at all of the cells than with a water bath because a thicker layer of cells is tested, so the temperature of the solution in which they are suspended heats more uniformly.

Some cell viability assays need to be used with a particular method of heating cells. For example, although clonogenic survival is a trusted indicator of cell death, it requires the use of a heated water bath (restricting its use to low temperature studies) [88].

Cell Survival Assay and Heating Protocols

In order to define the success of thermal therapy treatments, there must be a measurable assay to determine the that cell death that has occurred. As previously mentioned, clonogenic survival is one such assay. It counts the number of cells which can still reproduce; when this ability is destroyed, cancer cells can no longer proliferate. This makes it the most reliable indicator for cancer treatment studies [28, 88]. However, for *in vitro* experiments it takes at least a week for this assay to manifest after the treatment dose delivery [28].

All studies which used the clonogenic survival assay heated the cells with a water bath. Bhowmick [88] used an immersion heater and a stirrer in the water bath to maintain the temperature. After heating, the flasks of cells were then set in an incubator at normal body temperature (37°C) for seven days [88]. After Walsh [89] heated cells in the water bath, they were trypsinized and re-plated to be incubated for 10 days. For both studies, the cell colonies are counted after this incubation period.

For Bhowmick, the time it took for the temperature to reach its peak (ramping time) was about 3 minutes for temperatures of 50°C or less and 4 minutes for 55°C, and about 1 minute of ramp down time back to 37°C. The ramping time for Walsh was between 80 and 130 seconds for his hold temperatures that ranged from 55°C to 70°C.

Vital dyes have become a popular method for determining cell viability. The dye is added to the cells and infiltrates the ruptured membrane of dead cells, resulting in a color change. A second dye may also be added which will fluorescently stain the live cells as well. Four common vital dyes are trypan blue dye (used by [10, 11, 67]), propidium iodide (PI) (used by [62, 66, 88]), EthD-1 (used by [65, 89]), and an MTT assay (used by [55, 90]). For the same study, a vital dye assay will result in higher measurement of cell vitality than the clonogenic survival assay [28, 88, 91]. Incubation time needs to be included post-heating because it can also take up to a few hours for the injury to the cell membranes to occur [28].

Most studies that used a vital dye assay heated their cells through use of a heating stage, but a few used a water bath. Jiang [90] heated the cells in a water bath at the hold temperature for 2 hours, and then placed them in a 37°C incubator for the next 24 hours. The cells were then plated and incubated for 2 days, at which point the MTT solution was introduced to them. The solution was incubated at body temperature for another 4 hours. Walsh [89] also used a heated bath with the EthD-1 dye assay. As was done for his clonogenic survival studies, the cells were placed in the heated water bath for the appropriate period of time (with ramping times of 80 to 130 seconds, depending on the peak temperature), and then incubated at 37°C.

However, for the dye it was only incubated for 24 hours post-heating, at which time the cells were washed with phosphate-buffered saline (PBS) and the dye was added. Finally, Feng [62] used a water bath with the vital dye PI uptake assay. The cells were placed in a 25 cm^2 flask with PBS. The flask was placed in the appropriately heated water bath (ranging from 44-60°C, ramp time of about 4 seconds) for the different treatment times (1-30 minutes). The cells were then incubated for 72 hours at 37°C.

The following are the methods used for the cell studies utilizing a heating stage and a vital dye assay. Bhowmick [88] used a copper heating stage for studies using PI uptake. The cells were plated overnight before they were washed and mixed with PI dye. Then they were incubated for 15 minutes, covered with a cover slip, and then heated to the appropriate temperature on the stage (with about 10 seconds of ramping time). Afterwards the cells were incubated for three hours at 37°C. He [66] used PI uptake and Shah [65] used EthD-1 dye, but they had similar procedures (and both tested attached and suspended cells). Their 12 mm cover glasses with the cells were placed on the heating stage (He used a quartz crucible between the cells and the stage). There was only one heating rate for He, 130°C/min (and cooling rate of 65°C/min), but Shah tested the effect of multiple heating rates: 100, 200, and 300°C/min, and performed "isothermal" testing with a heating rate of 525°C/min (the cooling rate for all studies was 100°C/min). Then the cells were placed in their dye solution, which included both the previously-mentioned vital dye and Hoechst dye so that both the live and dead cells could be monitored. Next, they were incubated for 3 hours at 37°C before the stained cells were counted. Jen [10] used trypan blue dye for the cells, which were heated on a customized copper heating block. The cells were heated on the stage (ramp time <50 seconds). Afterwards they were stained with trypan blue to determine the viability. Huang used the same method as Jen for experiments on liver [11] and kidney cells [67], except the liver cells were also stained with calcein AM prior to heating to stain the live cells green, and EthD-1 dye post-heating to stain the dead cells red. Both dyes stained the cells for 30 minutes.

Other methods which are commonly used in cell studies include calcein leakage assay [88], lysis assay [92], flow cytometry [90], and fluorescence [63]. As previously mentioned, the assay choice was also influenced by the desired heating method.

Summary of Experimental Results

Determining the correct thermal dose is an important part of hyperthermic studies. Temperatures below about 43°C are incapable of inducing apoptosis, regardless of treatment times, so there is a large difference between the cell toxicity below this "breakpoint" and above it [27, 55, 60, 70, 86]. The required thermal doses for bladder, prostate, liver, and kidney cells have been compiled from recent studies (Figure 26 – Figure 28). Each data point represents a different isothermal test, and the lines connect experiments of the same cell line. The graphs all have a steep negative slope at the shortest testing times, demonstrating the minor difference in treatment time at very high temperatures. Then the graphs flatten out because there are large differences in the time required for cell death at the lower temperatures.

The time necessary for 10% of the tested cells to die is displayed in Figure 26(a-d), where each graph is a different cell type, and is sub-separated by cell line. Most of the cell lines were able to reach 10% death within 10 minutes at temperatures above 40°C.

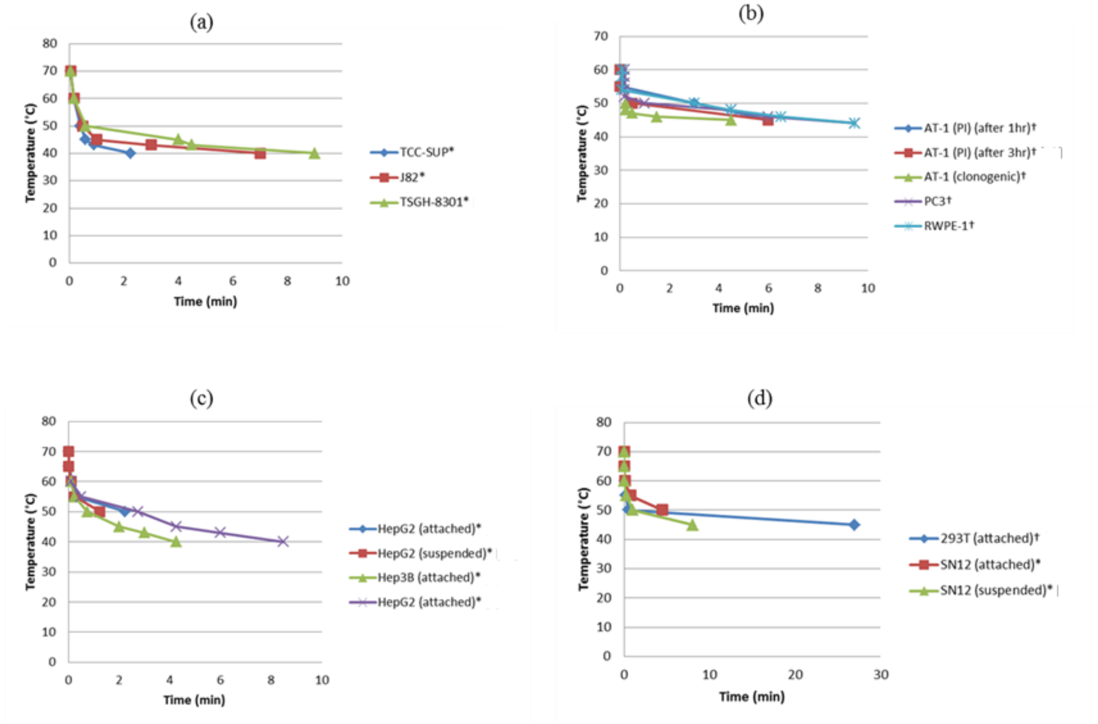

Figure 26. Times needed to achieve 10% cell death when subjected to isothermal heating at temperatures specified for (a) bladder cells [10], (b) prostate cells [62, 88], (c) liver cells [11, 65], and (d) kidney [66, 67].

Figure 27(a-d) displays the time it took for 50% cell destruction to occur in the different types of cancer cells. At 50°C[1], kidney cells required the most time to reduce by half: 7-8 minutes. The bladder cells had the fastest response at this temperature, taking 2-4 minutes.

---

[1] arbitrary temperature chosen for comparison since it is the lowest available in all graphs

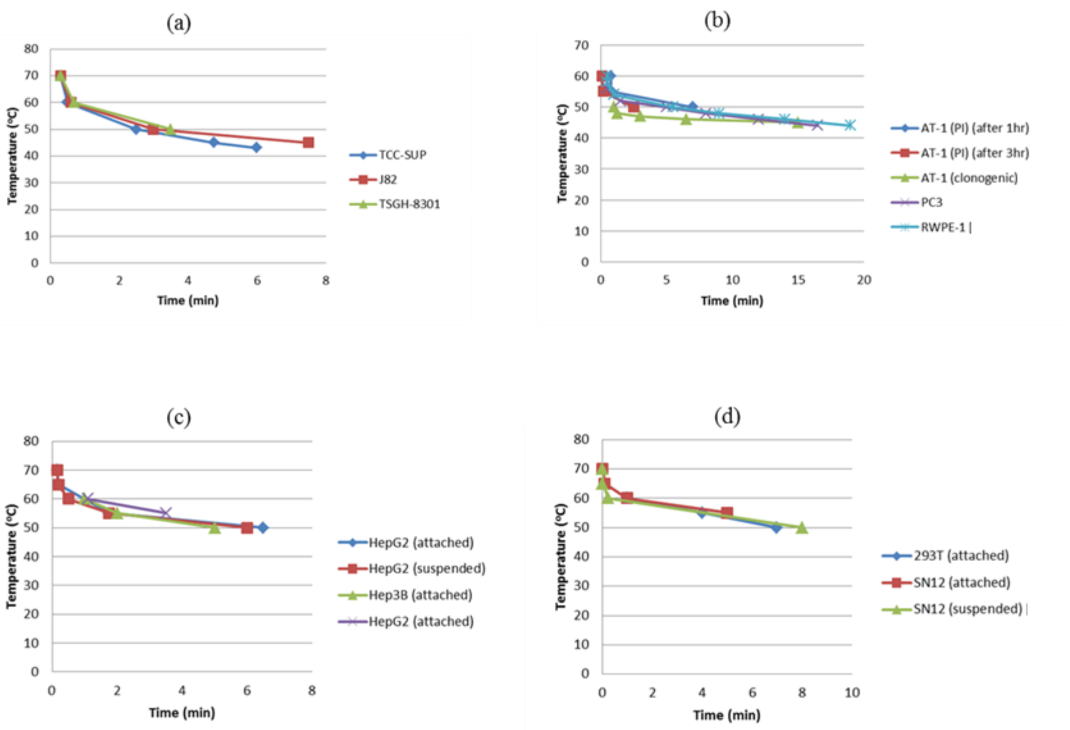

Figure 27. Times needed to achieve 50% cell death when subjected to isothermal heating at temperatures specified for (a) bladder cells [10], (b) prostate cells [62, 88], (c) liver cells [11, 65], and (d) kidney [66, 67].

Figure 28 shows the necessary thermal dose for 90% cell death. There are fewer data points for these graphs than the previous figures because most of the lower temperature experiments were not run until 90% of the cells died (with the exception of Feng's [62] prostate cell experiments, which were run for 30 minutes). The kidney cells required the most time at 55°C[2] to reach 90% cell death: 10 minutes. The other three cell types only needed about 5 or 6 minutes at that same temperature.

---

[2] arbitrary reference temperature

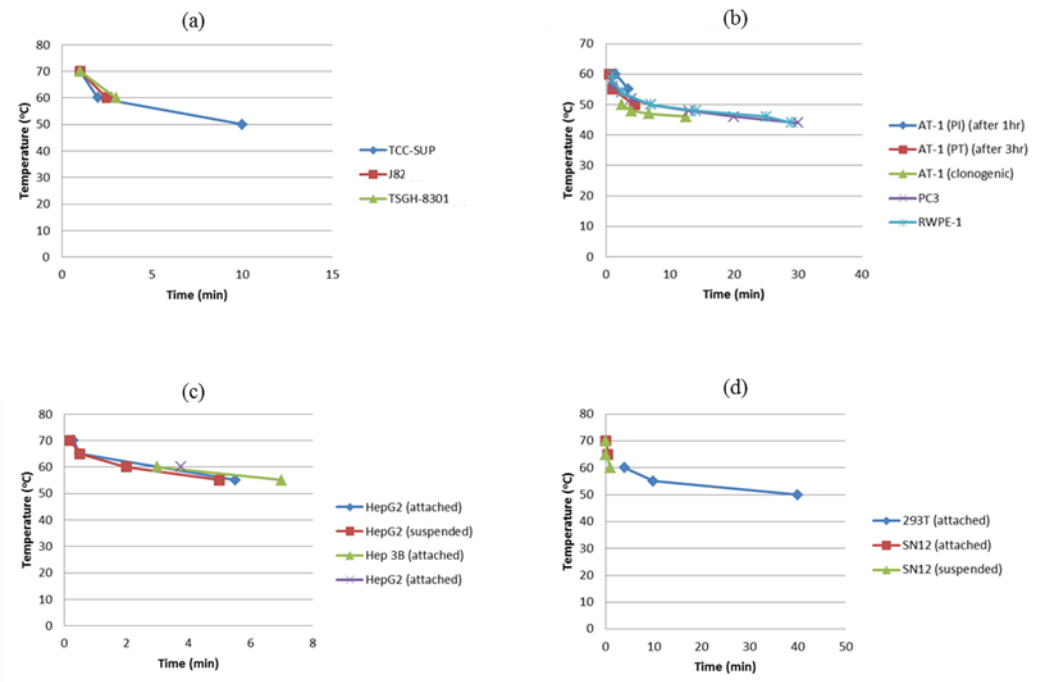

Figure 28. Times needed to achieve 90% cell death when subjected to isothermal heating at temperatures specified for (a) bladder cells [10], (b) prostate cells [62, 88], (c) liver cells [11, 65], and (d) kidney [66, 67].

Discussion of Results

The data displayed in Figure 26 – Figure 28 was derived from the survival curves provided by each source (survival curves display the percentage of cell survival versus time for different hold temperatures). For hyperthermic temperatures, these curves typically have two distinct regions: a shallow slope at the beginning of the heating time (shoulder region), and then a steeper slope develops, showing a fast rate of cell death when a damage threshold is surpassed [53, 60]. In contrast, at high thermal therapy temperatures the cell death rate is very high initially, and then it slows. This occurs because at high temperatures the "damage threshold" is surpassed at the outset of the test. Figure 29 shows the survival curves of PC3 prostate cancer cells from Feng [62] (with permission), and it depicts this phenomenon because shoulder region only exists in the curves for experiments run at 50°C and below.

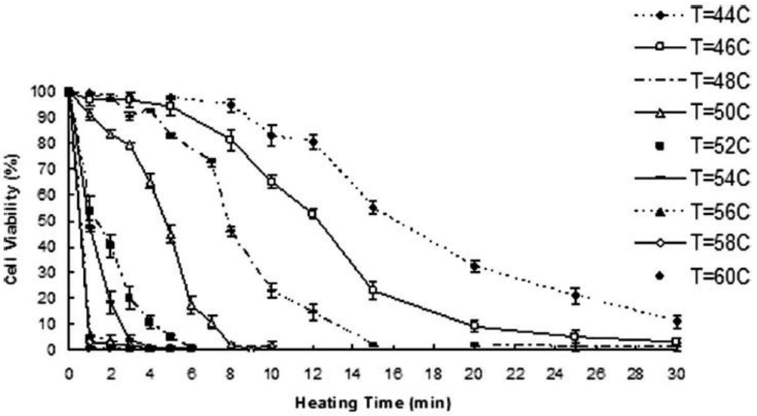

Figure 29. Reproduction of survival curves for PC3 prostate cancer cells (with permission) [62].

The graphs displayed in the results summary section are condensed into Figure 30 for 10% (a), 50% (b), and 90% (c) cell destruction, separated by cell type. A logarithmic trend line has been fitted to the compilation of the data from each general cell type[3]. The graph for kidney cells flattens out the fastest for 50% and 90% cell death, and in all three graphs the bladder trend lines have the steepest slope at the later times and lower temperatures. This means that at lower temperatures, a small decrease in hold temperature had a much larger effect on the treatment time for kidney cells than bladder cells.

---

[3] graphs exclude the prostate data from the clonogenic survival assay, prostate cells counted after only 1 hour post-treatment incubation, and any data past 10 minutes treatment time (all designated by "truncated")

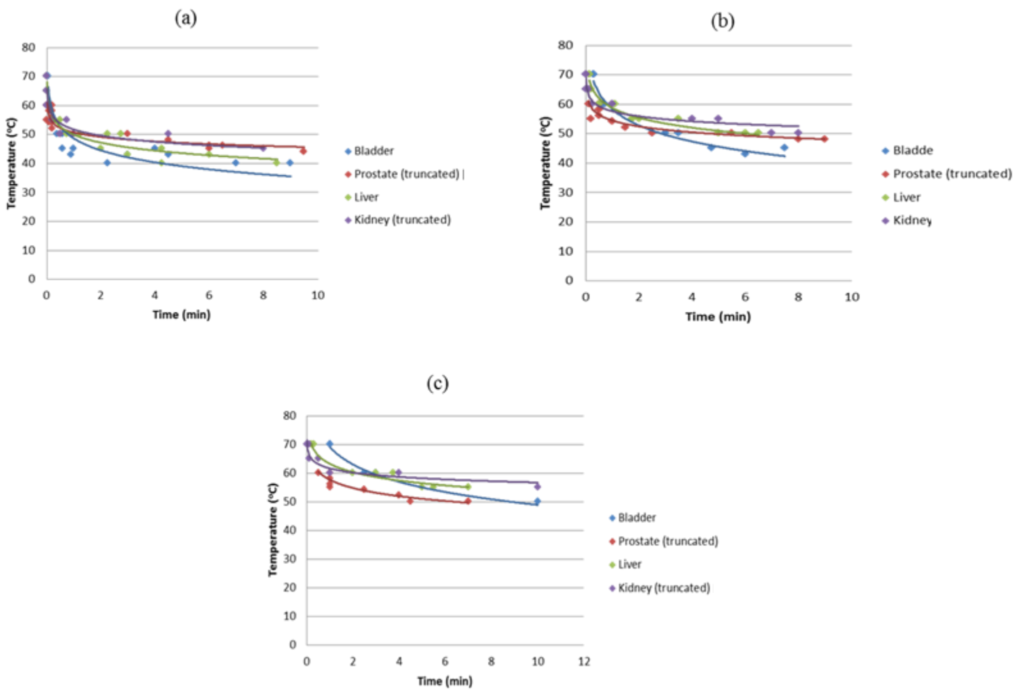

Figure 30. Times needed to achieve (a) 10%, (b) 50%, and (c) 90% cell death for bladder, prostate, liver, and kidney cells, when subjected to isothermal heating at temperatures specified.

Figure 31(a-d) displays those same trend lines[4], but each graph contains one type of cell which has lines for the different survival rates. Bladder cells required a lot of time to go from 10% - 50% and 50% - 90% cell destruction at any given temperature. For example, at 50°C, 10% of the bladder cells died after 30 seconds, half died after about 3 minutes, and it took 10 minutes for 90% of the cells to die. Similarly, kidney cells required very little time to reach 10% cell destruction, but up to 40 minutes for 90% cell death at 50°C. This is in contrast to prostate cells, which have very similar curves for all three cell death percentages, and it is not until below 50°C that there are distinct differences in the treatment times needed to achieve each.

---

[4] now including data collected after 10 minutes

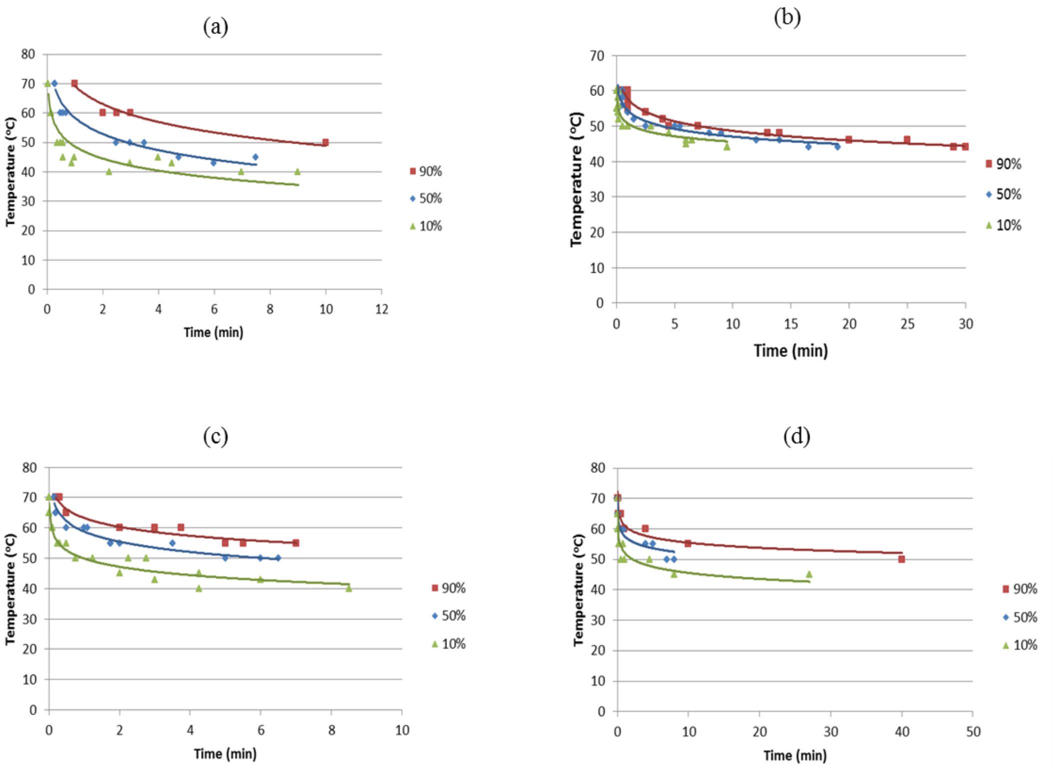

Figure 31. Times needed to achieve 10%, 50%, and 90% cell death for (a) bladder cells, (b) prostate cells, (c) liver cells, and (d) kidney cells when subjected to isothermal heating at temperatures specified.

Decreasing heating time is often a goal of hyperthermic treatment, so to decrease it to less than an hour, following the curves in the figures above, it is necessary to raise the peak temperature above normal hyperthermic conditions. Temperatures below 46°C require a much longer hold time, and possibly multiple treatments, to be used as the sole method for cell death.

Since eradicating cancer cells is the goal of treatment, the 90% curves are of the most interest to analyze. However, most of the cell studies were not performed for sufficiently long time periods to reach 90% cell destruction at moderate hyperthermic temperatures, so the thermal doses can only be determined for thermal ablative temperatures. According to the trend line for bladder cells, it takes 10 minutes at 50°C, 3 minutes at 60°C, and 1 minute at 70°C to cause 90% cell death. For prostate cells (which were tested for longer time periods) to achieve this same level, they require 30 minutes at 44°C, 7 minutes at 50°C, and less than a minute at 60°C. Liver cells needed 7, 2.5, and 0.25 minutes at 55, 60, and 70°C, respectively. The trend line for kidney cells will not cross 50°C until after 40 minutes, but will reach 90% cell death around 2 minutes at 60°C and almost immediately at 70°C.

To estimate the necessary thermal dose at any temperature, this data was fit to an Arrhenius model. The parameters from these recent cell studies are listed in Table 6. The heating method and survival assay are also presented in the table because they have a significant impact on the resulting parameters.

Table 6. Compilation of Arrhenius parameters for different cell studies.[5]

Cancer Cell Type	Heating Method	Survivability Assay	Notes	Arrhenius Parameters		Reference
				E_a (kJ/mol)	A (s^{-1})	
Liver (HepG2)	heating stage	EthD-1	HR = 100°C/min	272.4	7.757×10^{40}	Shah 2006
			HR = 200°C/min	262.02	1.502×10^{39}	
			HR = 300°C/min	257.38	2.576×10^{38}	
			HR = 525°C/min (attached)	248.64	5.396×10^{36}	
			HR = 525°C/min (suspended)	229.46	3.495×10^{31}	
Liver (HepG2)	heating stage	trypan blue dye		170.17	4.11×10^{24}	Huang 2010
Liver (Hep3B)	heating stage	trypan blue dye		152.44	1.07×10^{22}	Huang 2010
Prostate (AT-1)	heating stage	calcein leakage	0.7 threshold	81.33	5.069×10^{10}	Bhowmick 2000
	heating stage	PI uptake	0.7 threshold	244.8	2.99×10^{37}	Bhowmick 2000
	water bath	clonogenic survival	0.7 threshold	526.39	1.04×10^{84}	Bhowmick 2000
Bladder (TSGH-8301, grade 2)	heating stage	trypan blue dye		164.65	7.04×10^{23}	Jen 2009
Bladder (J82, grade 3)	heating stage	trypan blue dye		145.48	8.15×10^{20}	Jen 2009
Bladder (TCC-SUP, grade 4)	heating stage	trypan blue dye		114.4	1.35×10^{16}	Jen 2009
Kidney (SN12)	heating stage	PI uptake	Suspended w/all T(t)	287.49	4.362×10^{43}	He 2005
			Suspended w/T(t) @ 0 hold	338.54	6.375×10^{51}	
			Attached w/all T(t)	314.89	3.153×10^{47}	
			Attached w/T(t) @ 0 hold	358.51	2.291×10^{54}	
Kidney (A498)	water bath	EthD-1	99% destruction	202.80	1.29×10^{29}	Walsh 2007
Kidney - embryonic (293T)	heating stage	trypan blue dye		211.79	5.95×10^{30}	Huang 2008

These cells types all have an activation energy in the range of 100 – 360 kJ/mol, but their frequency factor ranges from the order of $10^{23} – 10^{54}$ s^{-1}. He [52] performed a similar review of both human and animal cells, and found that activation energy tended to be much higher for the clonogenic survival assay than with vital

---

[5] HR = heating rate

dyes, which can be seen in Table 6 from the AT-1 cell studies performed by Bhowmick.

Conclusion of Cell Studies

The graphs of the cell data from this literature review display the significant difference in thermal dose results for different types of cells. It is important to note that none of the studies in this review included breast cancer cells. Literature for *in vitro* experiments was not available for breast cancer cells, so to have an accurate model for cell death of breast cancer, experiments on those cell lines will have to be performed. Chapter 6 of this study will explain the experiments done to obtain this data.

Chapter 4: Numerical Modeling and Device Design for Ultrasound Thermal Therapy of Prostate Cancer

As was proven in Chapter 2, numerical modeling of ultrasound propagation and heat transfer in biological tissues can accurately predict the outcome of a hyperthermic treatment. It is a useful tool for both designing new devices to perform ultrasound thermal therapy and for treatment-planning purposes because it can individualize patient treatments [14]. Therefore, it is important to continually improve the numerical models so that the results will be closer to experimental values.

The following prostate cancer simulations include a few novelties which distinguish them from the previous studies. First, the tissue and blood properties vary throughout the duration of the simulation. The acoustic attenuation and blood perfusion are dependent on the thermal dose and US power, respectively, where most studies just used constant values. Without considering a variable attenuation and perfusion, the results could have a significantly different result from the realistic value [14].

Another important aspect of the prostate cancer simulations is the use of the Arrhenius equation to determine cell death, with parameters specific to prostate cancer cells. Most simulations use an equivalent number of minutes at $43^{o}C$ according to Sapareto and Dewey’s thermal effective dose, which is common to all soft tissue. As was proven in Figure 30 in Chapter 3, there is a significant difference between the rate of cell death by thermal therapy for different cell types, so it is important to use a model which is specific to the type of cell under study.

This chapter will discuss the methods used to develop this numerical simulation, the results of these studies, and concepts designs of the US delivery device and treatment planning protocols. The results will provide a relationship between ultrasound parameters and the final necrosed volume, which is important for treatment planning for physicians.

Methods

MATLAB software was used to compute the final temperature throughout the volume and the resulting necrosed tissue locations. The first step to achieving this is to define the geometry of the computational domain, which is the prostate gland in this case. Next, the tissue, blood, and ultrasound properties are defined. Then, the code runs through the total heating time. At each time step, the acoustic attenuation and heat generation are calculated for every node in the domain. Then the temperature distribution is calculated based on the heat generation value. The necrosed cells are determined by the nodes (and therefore their associated volume elements) which have surpassed the thermal dose for cell death outlined by the Arrhenius relationship for prostate cancer. The methods used to develop this simulation are described in this section, which include the discretization of the governing equation, the geometry used for the simulation, and the constants and variables used for testing.

Finite Difference Method

Using the numerical technique of finite difference (FD) is a common method for solving differential equations, and was used in many numerical studies of ultrasound thermal therapy (see Previous Studies with Ultrasound section). It is only an approximation of the solution the results are discretized into finite volumes and time steps, so its accuracy is directly dependent on the size of those intervals. This simulation uses an explicit scheme, so at each time step the results are calculated once, instead of an implicit scheme where the solution is determined by iterations at each time step until there is a sufficiently small error between the results in that step. The implicit scheme was not needed because the solution converged for this model.

Each differential equation is split into a finite central difference by the Taylor Series approximation, Equation 33.

$$f(x+\Delta x) = f(x) + f'(x+\Delta x)\Delta x + HOT \qquad \text{Equation 33}$$

where x is the current location, Δx is the length step in the x-direction, and HOT are higher order terms, which can be neglected because they are negligibly small compared to the preceding terms. Rearranging this equation results in an approximation of a first-order derivative, shown in Equation 34.

$$f'(x+\Delta x) = \frac{f(x+\Delta x) - f(x)}{\Delta x} \qquad \text{Equation 34}$$

Equation 34 is an example of a forward difference, to compute a central difference the derivative at x spans two nodes, and is calculated by Equation 35.

$$f'(x) = \frac{f(x+\Delta x) - f(x-\Delta x)}{2\Delta x} \qquad \text{Equation 35}$$

A second derivative is derived by plugging the forward (and backwards) difference of the derivative shown in Equation 34 in for f'(x), resulting in Equation 36

$$f'(f'(x)) = \frac{f'(x+\Delta x) - f'(x)}{\Delta x}$$

$$= \frac{\frac{f(x+\Delta x) - f(x)}{\Delta x} - \frac{f(x) - f(x-\Delta x)}{\Delta x}}{\Delta x}$$

$$f''(x) = \frac{f(x+\Delta x) + f(x-\Delta x) - 2f(x)}{\Delta x^2} \qquad \text{Equation 36}$$

Discretizing the Bioheat Transfer Equation

Equation 35 and Equation 36 will be used to discretize the bioheat transfer equation (BHTE), defined in Chapter 2 and rewritten below.

$$\rho c_p \frac{\partial T}{\partial t} = k\nabla^2 T + c_{pb}\mathrm{w}(T_b - T) + q''' \qquad \text{Equation 21}$$

The ultrasound propagation does not have to be modeled with a central differencing scheme because the heat generation at each point is solely a function of its location and the temperature distribution at the previous time step.

The first term on the left and right sides of Equation 21 will be discretized with the Taylor series approximation because they include differential equations; they describe the storage of heat and conduction of heat, respectively. The derivative of temperature with respect to time is written with the backwards difference method, and results in Equation 37.

$$\frac{\partial T(t)}{\partial t} = \frac{T(t) - T(t - \Delta t)}{\Delta t} \qquad \text{Equation 37}$$

The spatial derivatives are all determined based on the temperatures calculated at the previous time step at each point. The Laplacian of temperature only includes second derivatives in a Cartesian coordinate system, but changes when the coordinates are no longer expressed in terms of (x,y,z). For geometric simplicity, a cylindrical coordinate system (Figure 32) is used for prostate studies.

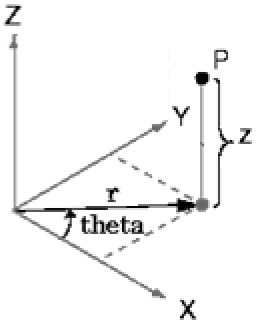

Figure 32 3D cylindrical coordinate system used for prostate simulations (adapted from [93]).

The cylindrical system transforms the perpendicular linear (x,y,z) coordinates into the orthogonal radial, angular, and linear coordinates (r,θ,z), depicted by Figure 32. The Laplacian in cylindrical coordinates is described by Equation 38.

$$\nabla^2 T = \frac{\partial^2 T}{\partial r^2} + \frac{1}{r}\frac{\partial T}{\partial r} + \frac{1}{r^2}\frac{\partial^2 T}{\partial \theta^2} + \frac{\partial^2 T}{\partial z^2} \qquad \text{Equation 38}$$

The discretization of each of these terms is determined by either Equation 35 or Equation 36, and is displayed in Equation 39 – Equation 42. All coordinates not specified in the equation are held constant.

$$\frac{\partial^2 T(t,x)}{\partial r^2} = \frac{T(t - \Delta t, x + \Delta x) + T(t - \Delta t, x - \Delta x) - 2T(t - \Delta t, x)}{\Delta x^2} \qquad \text{Equation 39}$$

$$\frac{\partial T(t,x)}{\partial x} = \frac{T(t - \Delta t, x + \Delta x) - T(t - \Delta t, x - \Delta x)}{2\Delta \mathrm{x}} \qquad \text{Equation 40}$$

$$\frac{\partial^2 T(t,\theta)}{\partial \theta^2} = \frac{T(t-\Delta t,\theta+\Delta\theta) + T(t-\Delta t,\theta-\Delta\theta) - 2T(t-\Delta t,\theta)}{\Delta\theta^2} \quad \text{Equation 41}$$

$$\frac{\partial^2 T(t,z)}{\partial z^2} = \frac{T(t-\Delta t,z+\Delta z) + T(t-\Delta t,z-\Delta z) - 2T(t-\Delta t,z)}{\Delta z^2} \quad \text{Equation 42}$$

Geometry of Domains/ Testing Parameters for Prostate Studies

The geometry of the prostate is simplified to a cylindrical shape commonly-used in the former simulation studies detailed in Chapter 2. The prostate is modeled as a hollow cylinder with thick walls, whose dimensions are displayed in Figure 33.

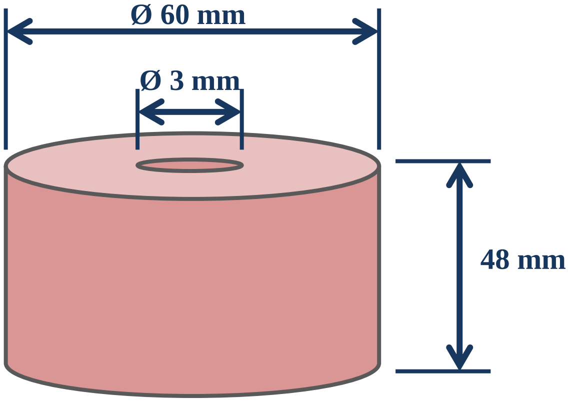

Figure 33 Dimensions of cylindrical prostate geometry.

The US device simulated includes three cylindrical transducers which are independently powered and can emit power in a discrete set of angles between 90° and 360°. Chilled water runs between the transducers and the prostate wall, providing a convective boundary condition at the inner wall of the prostate. This setup is depicted in Figure 34, where the coordinate system is also displayed.

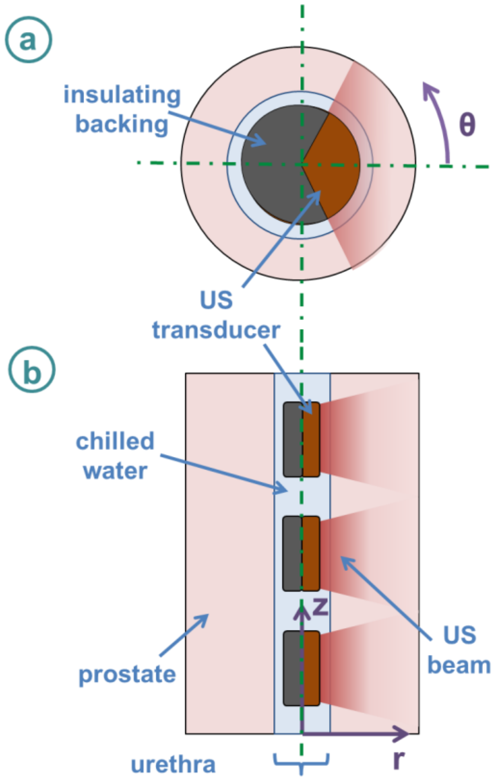

Figure 34 Schematic of prostate simulation model, showing the prostate, transducers, chilled water, and r-θ-z coordinate system in the a) top view, and b) front cross-sectional view.

Each transducer is 8 mm tall with a radius of 1.1 mm. There is a 4 mm gap between each transducer in the z-direction. The prostate tissue is initially set to body temperature, 37°C, and the external boundary condition is also held to that temperature.

Testing Parameters

Table 7 displays the values of the parameters tested for the independent variables for the prostate simulations. Throughout the results and discussion, the transducer powers will be written as $Q = [Q_1\ Q_2\ Q_3]$, where Q_1 is the power for the bottom transducer, Q_2 is for the middle transducer, and Q_3 represents the top transducer power. The dependent variables for the prostate simulations were the maximum temperature and the final volume of necrosed tissue.

Table 7 Prostate simulation testing parameters and their values used in simulations.

Independent Variables	Tested Values
Transducer Powers, Q_i (W)	**0, 30, 45, 60**
Heating Time, t_h (sec)	**30-300**
Transducer Angle, Θ (degrees)	**90, 120, 150, 180, 210, 270**

The temperature in the tissue should not get too high because a patient's pain threshold is generally exceeded after about 45^oC, so minimizing temperatures above this value is important [94] [36]. For that reason and because cavitation effects were not taken into account for this simulation, a constraint on these studies was that the maximum temperature could not exceed 100^oC anywhere in the computational domain. The prostate code was run until either a set heating time was reached, or the necrosis reached a prescribed radial location.

Determination of Cell Necrosis

To determine cell necrosis, as was explained in the Background section, it is important to first determine the heat generation at each point in the volume. For the prostate study a cylindrical transducer is used, so it is governed by previously-defined Equation 30, re-written below.

$$q''' = 2\eta\alpha I_o r_o e^{-2\alpha^{r-r_o}/r} \qquad \text{Equation 30}$$

Therefore, it is only a function of the transducer efficiency η, acoustic attenuation α, the initial intensity I_o, the outer radius of the transducer r_o, and the radial location of the current cell. A transducer efficiency of 50% (η = 0.5) was used for all studies. The acoustic attenuation was defined in Chapter 2 (Equation 5), rewritten below

$$\begin{aligned} &for\ thermal\ dose < 100, \quad && \alpha = 5 \\ &for\ thermal\ dose \geq 100, \quad && \alpha = 5 + log\big((thermal\ dose) - 2\big) \end{aligned} \qquad \text{Equation 5}$$

The intensity is calculated from the input transducer powers by Equation 43 [34]

$$\mathrm{I}_o = \frac{\eta Q}{S} \qquad \text{Equation 43}$$

where the values for Q are defined in Table 7 and S is the surface area of the transducer. The radius of the transducer is the same as the inner radius of the prostate, defined in Figure 33.

After the heat generation is known, the temperature at each point is calculated using the discretized bioheat transfer equation. The blood properties used in the bioheat equation can be referenced in Table 3 of Chapter 2.

The final step is to determine if the thermal dose administered to each node in the volume is sufficient to conclude if the cells have been killed. In this study, the Arrhenius relationship is defined in Equation 22 of Chapter 2, rewritten below

$$k(T) = Ae^{-E_a/RT} \qquad \text{Equation 22}$$

The Arrhenius parameters used in this study were found through a literature study for prostate cancer cell death [88]. A two-step equation was used[6], where there are different parameters for temperatures below 50°C than above it. Their values are listed in Table 8, and their accuracy was validated with canine prostate studies [47].

Table 8 Arrhenius parameters for prostate cancer studies.

	Ea (kJ)	A (s^{-1})
Below 50°C	**526.39**	**1.04×10^{84}**
Above 50°C	**244.8**	**2.99×10^{37}**

Grid Validation

To ensure that the grid of nodes within the volume was sufficiently dense to account for the thermal gradients, a grid refinement study was performed. The number of nodes in the three dimensions started with nominal values and were evenly multiplied by higher factors for different levels of grid fineness, and the maximum temperature and necrosed volume for two different sets of ultrasound parameters (parameters listed in Table 9) were recorded at each level.

Table 9 Transducer parameters of two different cases tested for grid refinement study.

Case #	Center Transducer Power	Transducer Angle	Heating Time
1	**45 W**	**90°**	**55 sec**
2	**60 W**	**90°**	**30 sec**

---

[6] The Arrhenius parameters for the prostate were derived from Bhowmick's study comparing different survival assays for prostate cancer cell death [67]. He recommended using the PI uptake numbers for temperatures above 50°C and the clonogenic survival parameters for temperatures below 50oC, which is what is presented in Table 8.

The multiplication factor was increased until the two most-fine grids have a negligible error between their values of maximum temperature and necrosed volume. Table 10 also includes the multiplication factor for the final node and its percent error, and Figure 35 displays the temperature and necrosed volume of each grid. The final differential elements were $\Delta r = 0.6750$ mm, $\Delta\theta = 11.25^{o}$, and $\Delta z = 1.000$ mm. Separately, an accurate time step was calculated to be $\Delta t = 0.3052$ sec.

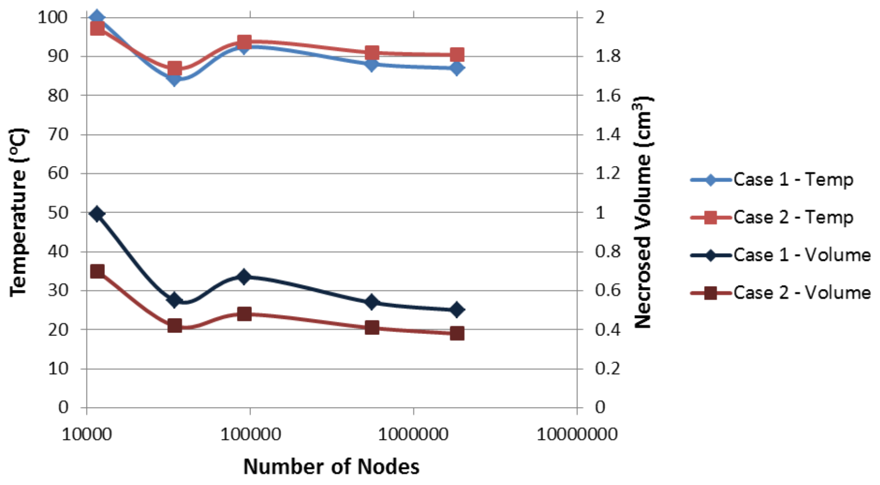

Figure 35 Temperature and necrosed volume for the different grids for $\Theta = 90^{o}$ for case 1 ($Q = [0\ 45\ 0]$ W and $t_h = 55$ s) and case 2 ($Q = [0\ 60\ 0]$ W and $t_h = 30$ s).

Table 10 The percent errors of the temperature and necrosed volume of each case when compared with the finest grid.

		Case 1		Case 2	
# of nodes		T_{error}	V_{error}	T_{error}	V_{error}
nominal	11500	**14.79 %**	**98.00 %**	**7.60 %**	**84.21 %**
1.5x	34600	**3.00 %**	**10.00 %**	**3.83 %**	**10.53 %**
2x	92200	**6.25 %**	**34.00 %**	**3.64 %**	**26.32 %**
3x	553000	**1.30 %**	**8.00 %**	**0.70 %**	**7.89 %**
4x	1840000	**0**	**0**	**0**	**0**

Results from Prostate Studies

Multiple combinations of the parameters displayed in Table 7 were tested in multiple combinations, and the results were studied if the thermal dose was sufficient to result in necrosed tissue and the maximum temperature was less than 100^{o}C. The complete results are listed in Table 30 – Table 39 in Appendix A. Each test produced different temperature fields, and therefore different tissue necrosis contours. The results will first display the effect of different parameters on the temperature fields, and then will demonstrate the resulting necrosed volumes.

Temperature Fields

An example of a temperature distribution created by the cylindrical transducer is displayed in the 2D cross-sections at $\theta = 0^o$ (Figure 36a) and at z = 0 mm (Figure 36b), created by 3 transducers at Q = [45 45 45] W, propagating at $\Theta = 90^o$ for t_h = 100 s. The white region between r = 0 and 3 mm in Figure 36a (rectangular region) and Figure 36b (circular region) represent the urethra, where the transducers are located.

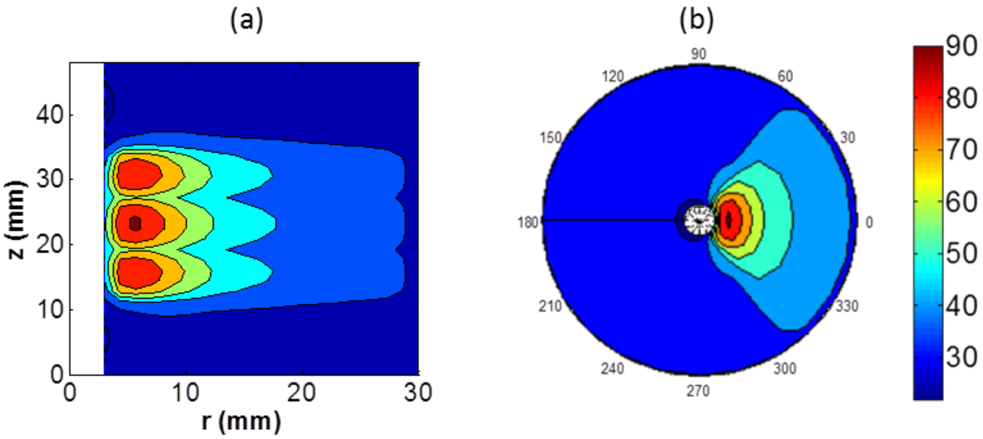

Figure 36 Temperature contours for Q = [45 45 45] W, Θ = 90°, and t_h = 100 s at (a) θ = 0° and (b) z = 0 mm.

Another example is shown in Figure 37 for Q = [0 60 0] W, propagating at Θ = 270° for t_h = 600 s.

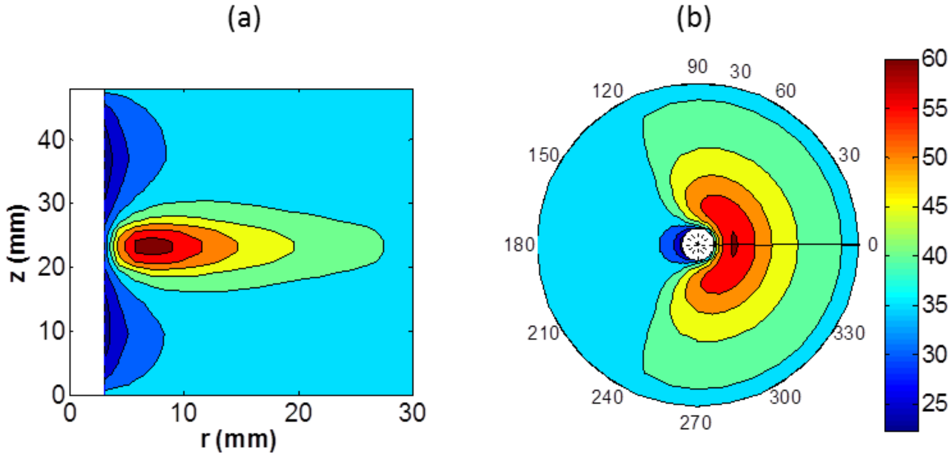

Figure 37 Temperature contours for Q = [0 60 0] W, Θ = 270°, and t_h = 600 s at (a) θ = 0° and (b) z = 0 mm.

The effect of one transducer on the maximum temperature versus the treatment time are displayed in Figure 38 and Figure 39, where Figure 38 compares graphs of different transducer powers Q for each transducer angle Θ, and Figure 39 compares graphs of the same data but with different transducer angles for each power.

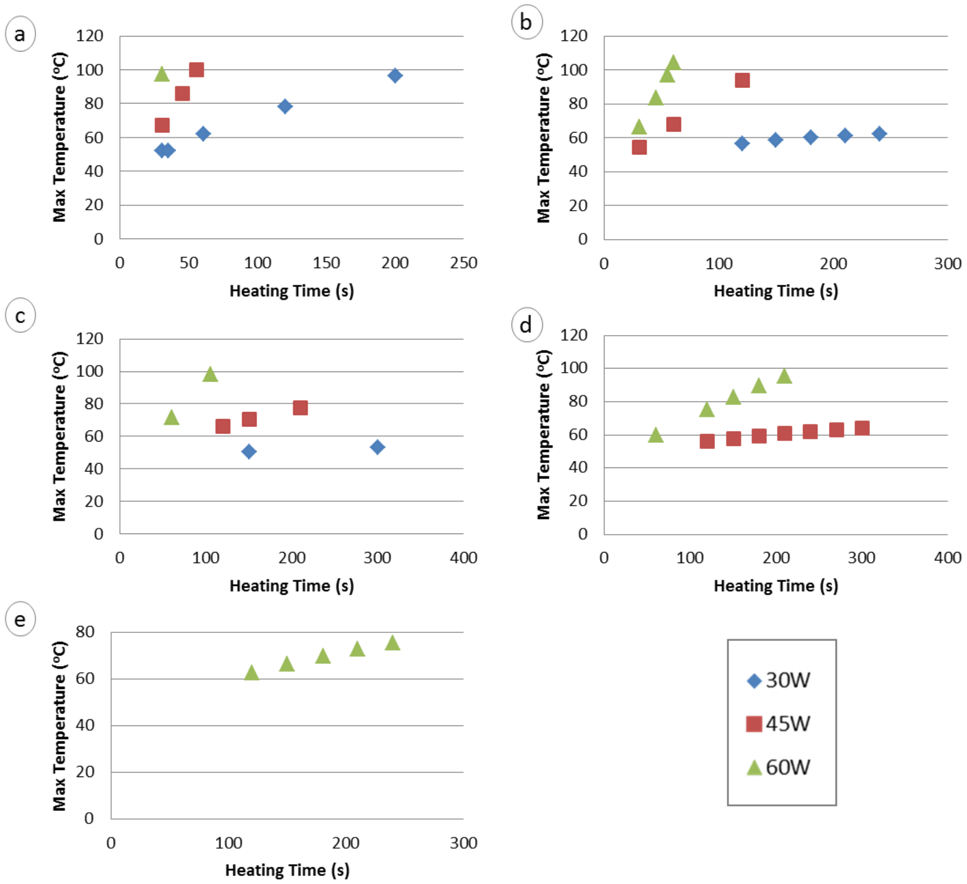

Figure 38 For single transducer simulation, the maximum temperature versus the heating time for 30 W (blue diamonds), 45 W (red squares), and 60 W (green triangles). Graphed for (a) Θ = 90°, (b) Θ = 120°, (c) Θ = 150°, (d) Θ = 180°, (e) Θ = 210°.

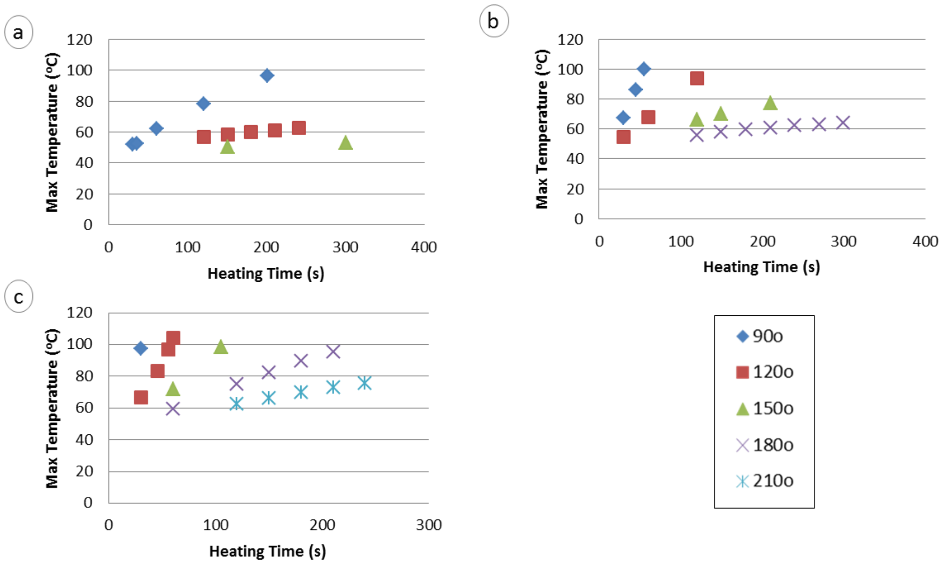

Figure 39 For single transducer simulation, the maximum temperature versus the heating time for Θ = 90° (blue diamonds), Θ = 120° (red squares), Θ = 150° (green triangles), Θ = 180° (purple x's), and Θ = 210° (teal stars). Graphed for (a) 30 W, (b) 45 W, (c) 60 W.

Next, the effect of varying the powers of two transducers was studied. An example of the temperature contours created by transducers at two different powers is displayed in Figure 40 for Q = [45 60 0] W, propagating at Θ = 180° for t_h = 200 s.

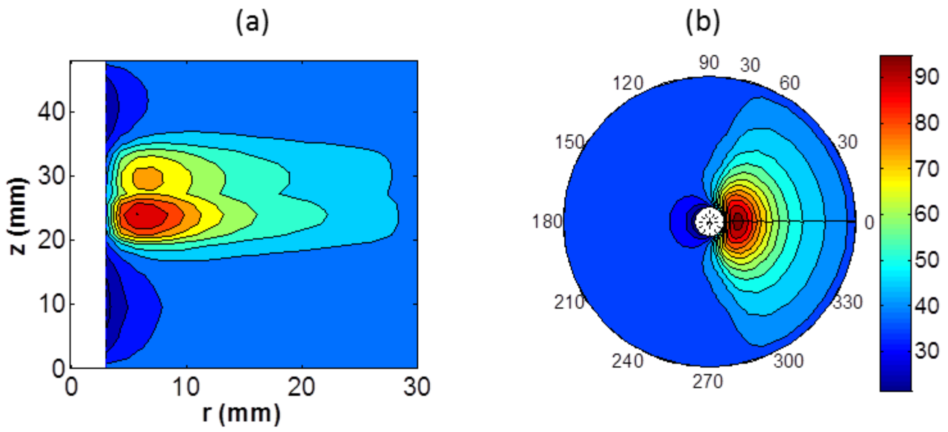

Figure 40 Temperature contours for Q = [45 60 0] W, Θ = 180°, and t_h = 200 s at (a) θ = 0° and (b) z = 0 mm.

A sample of the data for selected angles is graphed to compare the effect of the power from a second transducer for a constant value of the middle transducer. The angles were chosen to result in the largest population of data points within the constraints of $T_{max} \leq 100^oC$ and $V_{necr} > 0$ mm^3. Figure 41a displays the resulting T_{max} versus heating time for $\Theta = 90^o$ the middle transducer set to 30 W, the top transducer varying from 0 – 60 W, and the bottom transducer is set to 0 W. Figure 41b and Figure 41c display similar graphs as Figure 41a, except for $\Theta = 150^o$ and 210^o, and the middle transducer power set equal to 45 W and 60 W, respectively.

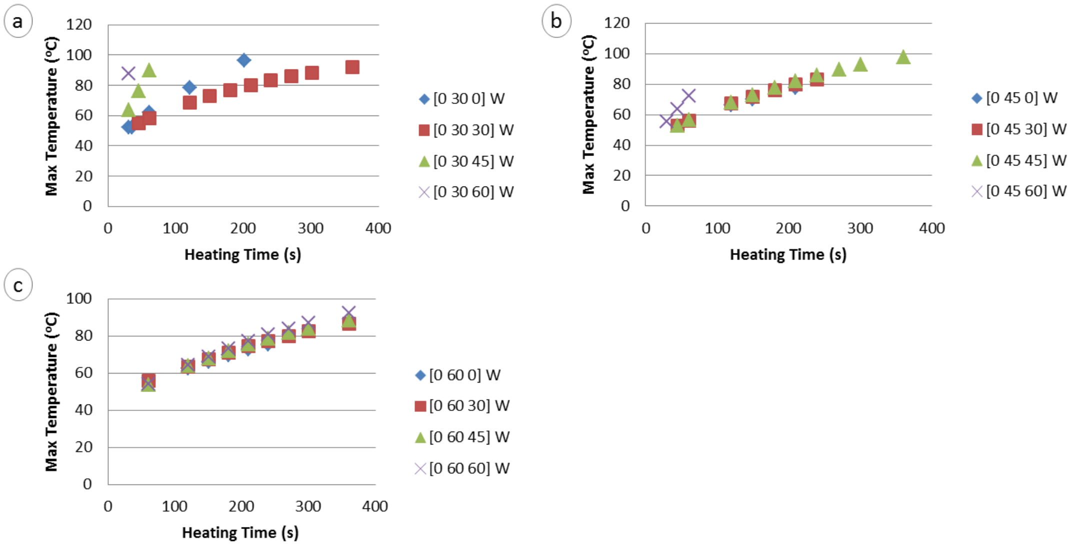

Figure 41 Maximum temperature versus heating time for a constant heating power for the center transducer compared to different transducer power on the third transducer for (a) Q2 = 30 W at $\Theta = 90^o$, (b) Q2 = 45 W at $\Theta = 150^o$, and (c) Q2 = 60 W at $\Theta = 210^o$.

Similar graphs were produced to compare the effect of activating multiple transducers at the same power level. Figure 42a displays T_{max} versus time for either one, two, or three transducers on at 30 W for $\Theta = 90^o$, Figure 42b is for 45 W and $\Theta = 150^o$, and Figure 42c displays the data for 60 W and $\Theta = 210^o$.

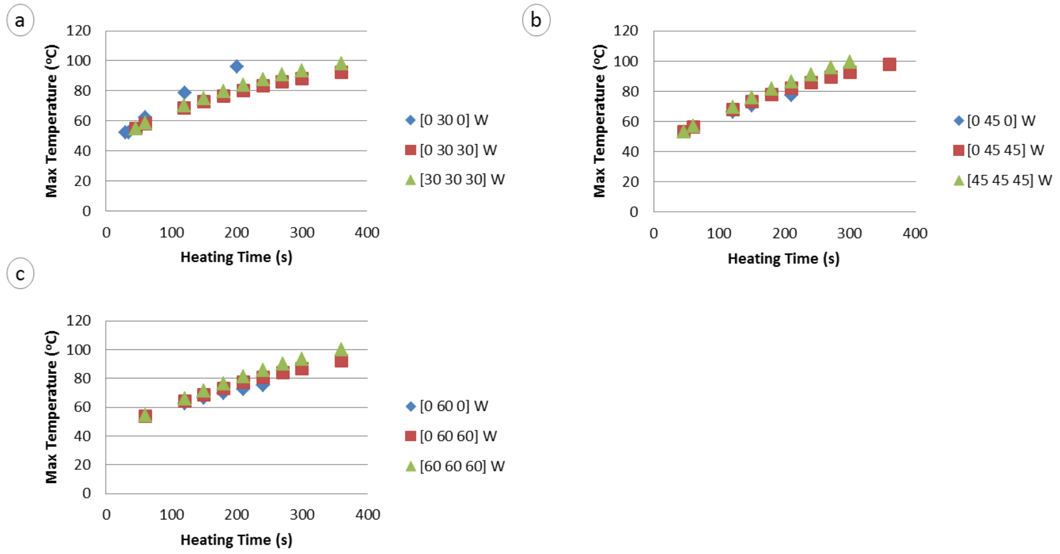

Figure 42 Maximum temperature versus heating time for a specific heating power for different numbers of active transducers for (a) Q = 30 W at $\Theta = 90^{\circ}$, (b) Q = 45 W at $\Theta = 150^{\circ}$, and (c) Q = 60 W at $\Theta = 210^{\circ}$.

Necrosed Tissue Contours

When the thermal dose for prostate cancer cell death has been surpassed in a volume element of the computational domain, that element will be marked as dead cells. To pictorially present the necrosed tissue from the simulations, two different types of graphs are employed and shown in Figure 43: the first is similar to Figure 36a except instead of the temperature contour it is the necrosis contour displayed; and the second is a three-dimensional isometric view of both the urethra and necrosed tissue. The frontal cross-section (Figure 43a) is split into areas where the highest temperature which caused the coagulation is displayed, and non-necrosed tissue is uncolored. In the isometric view (Figure 43b), the blue cylinder represents the urethra, within which the transducer is located, and the red volumes are the areas of necrosed tissue inside of the prostate. The prostate gland, but it can be imagined to be a thick-walled cylinder surrounding the urethra. The graphs are of the same set of US parameters as in Figure 36 (Q = [45 45 45] W, Θ = 90°, t_h = 100 s).

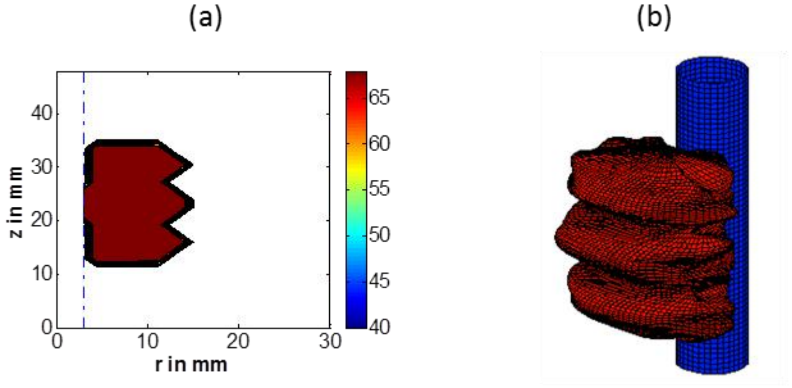

Figure 43 Necrosis contours for Q = [0 60 0] W, Θ = 90°, and t_h = 100 s at (a) θ = 0° and (b) 3D view.

Another example of these graphs is shown in Figure 44 for the same transducer parameters as Figure 37 (Q = [0 60 0] W, Θ = 270°, t_h = 600 s).

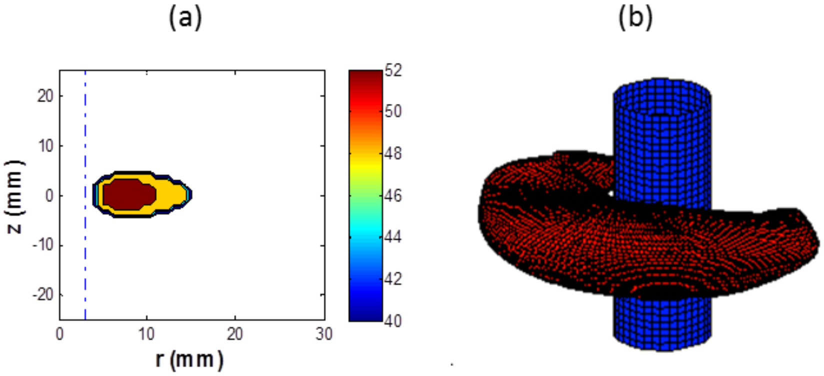

Figure 44 Necrosis contours for Q = [0 60 0] W, Θ = 270°, and t_h = 600 s at (a) θ = 0° and (b) 3D view.

The results for the effect of one transducer on the necrosed volume versus the treatment time are displayed in Figure 45 and Figure 46, where Figure 45 compares graphs of different transducer powers Q for each transducer angle Θ, and Figure 46 compares graphs of different transducer angles for each power.

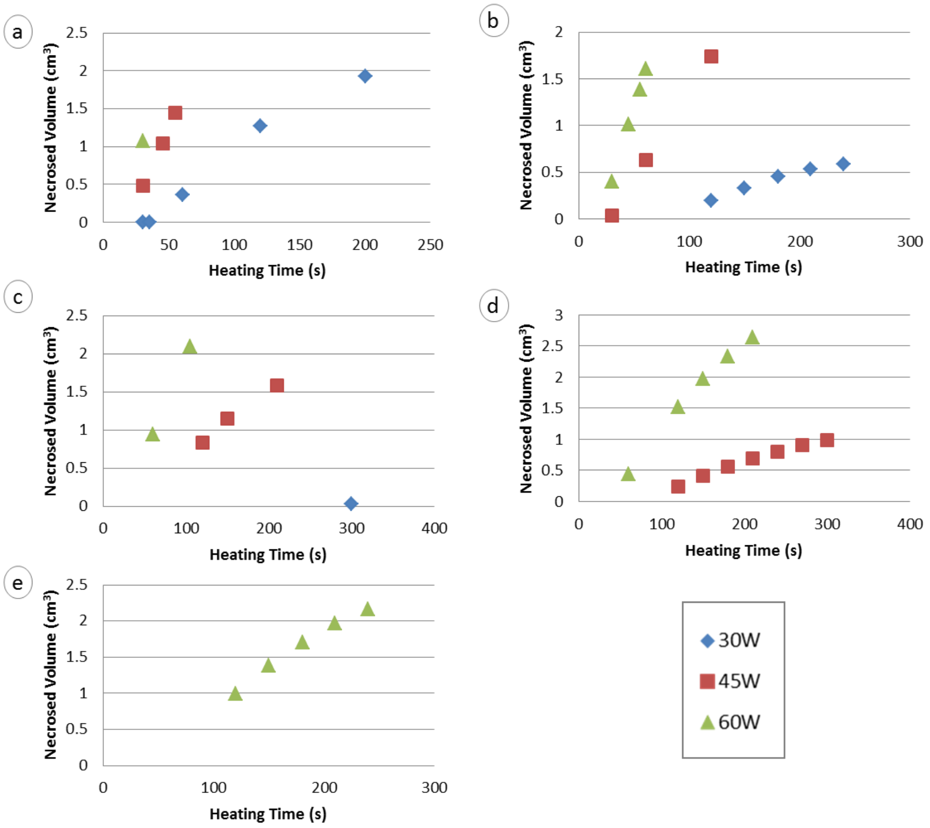

Figure 45 For single transducer simulation, the necrosed volume versus the heating time for 30 W (blue diamonds), 45 W (red squares), and 60 W (green triangles). Graphed for (a) $\Theta = 90^{\circ}$, (b) $\Theta = 120^{\circ}$, (c) $\Theta = 150^{\circ}$, (d) $\Theta = 180^{\circ}$, (e) $\Theta = 210^{\circ}$.

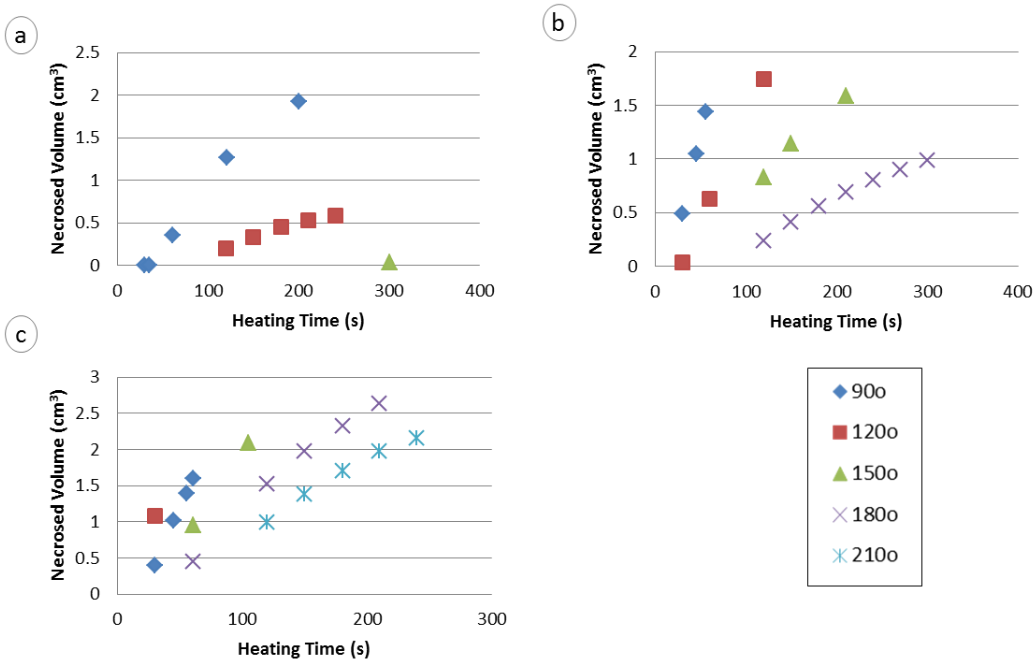

Figure 46 For single transducer simulation, the necrosed volume versus the heating time for Θ = 90o (blue diamonds), Θ = 120o (red squares), Θ = 150o (green triangles), Θ = 180o (purple x's), and Θ = 210o (teal stars). Graphed for (a) 30 W, (b) 45 W, (c) 60 W.

Another important result of these studies is the location of the necrosis. Predicting the location of necrosed tissue in the angular and axial directions is relatively accurate when considering the bounds defined by the transducer heights and angles of propagation. However, the resulting radial distance that the cell necrosis reaches is important to measure because it takes longer heating times and higher powers to reach further towards the edge of the prostate gland with a cylindrical transducer. Therefore, the depth of radial necrosis is limited by the necessity to remain under 100^{o}C.

Figure 47 – Figure 51 have graphs showing the maximum radial distance reached by the necrosis (open markers) and the radial centroid of the necrosed volume (filled markers). They are compared for one transducer at (a) 30 W, (b) 45 W, and (c) 60 W, at $\Theta = 90^{o}$ (Figure 47), $\Theta = 120^{o}$ (Figure 48), $\Theta = 150^{o}$ (Figure 49), $\Theta = 180^{o}$ (Figure 50), and $\Theta = 210^{o}$ (Figure 51).

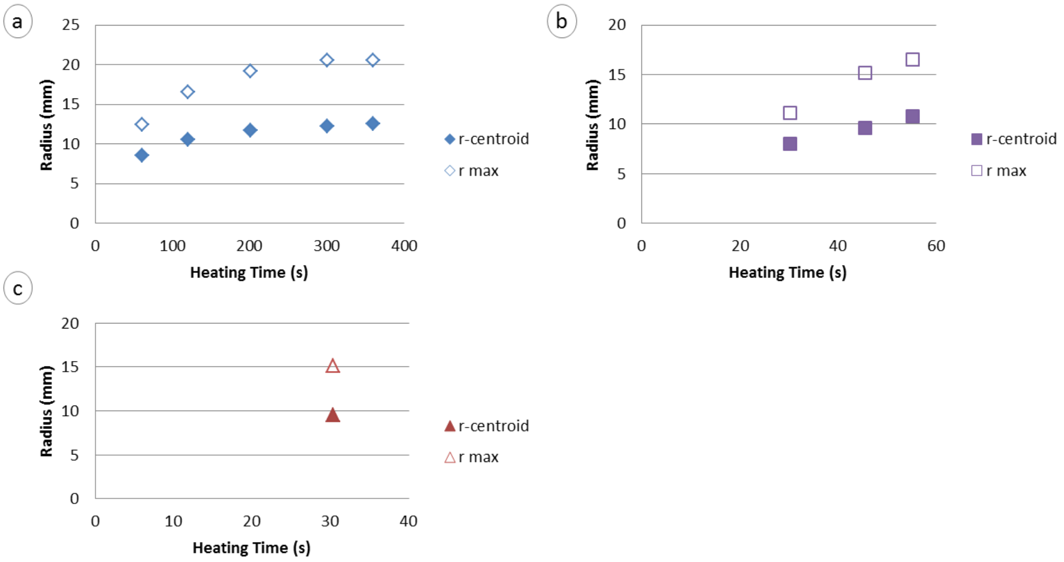

Figure 47 The centroidal and maximum radial coordinates for the necrosed lesion at Θ = 90° for one transducer set to (a) 30 W, (b) 45 W, and (c) 60 W.

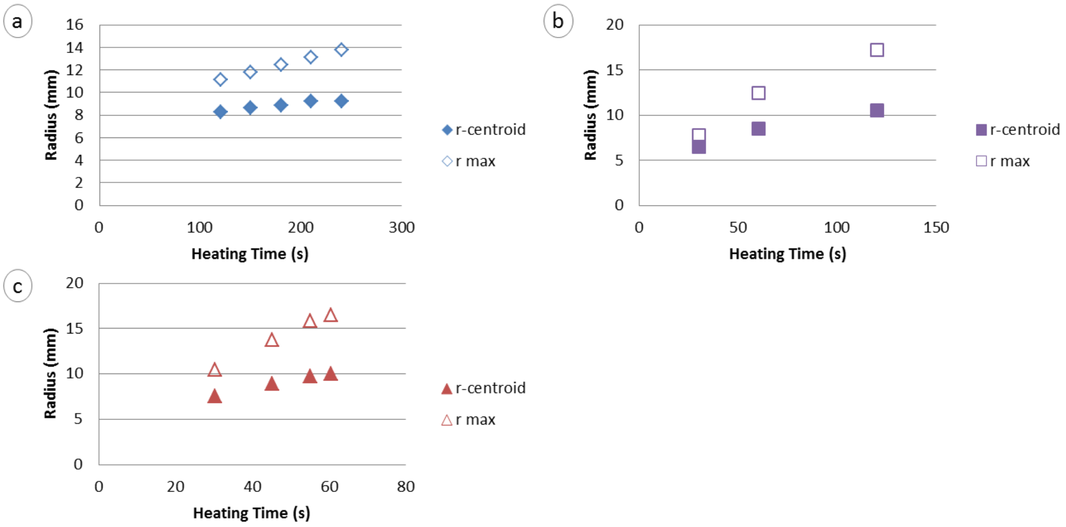

Figure 48 The centroidal and maximum radial coordinates for the necrosed lesion at Θ = 120° for one transducer set to (a) 30 W, (b) 45 W, and (c) 60 W.

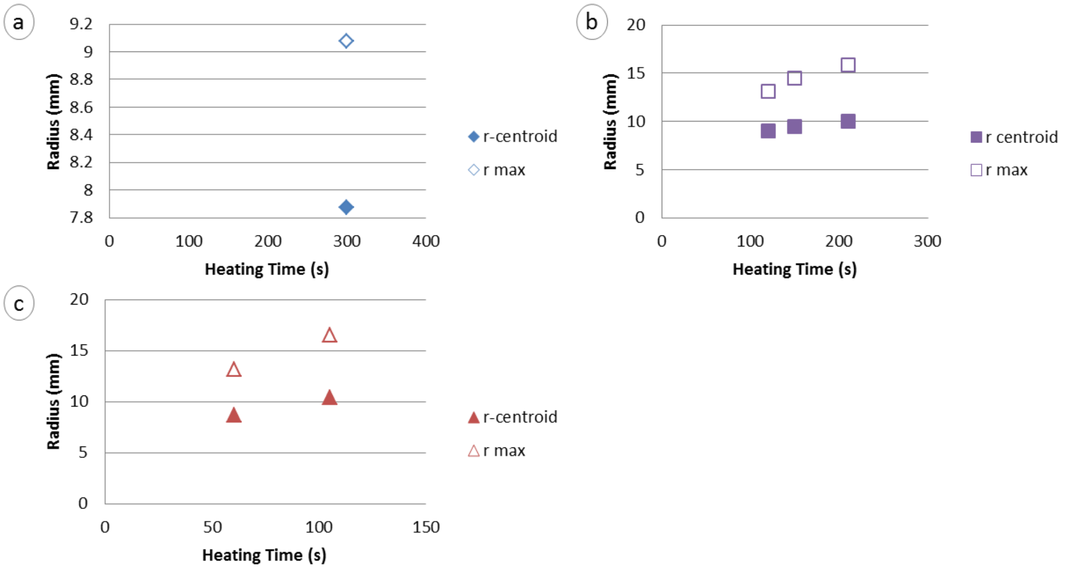

Figure 49 The centroidal and maximum radial coordinates for the necrosed lesion at Θ = 150° for one transducer set to (a) 30 W, (b) 45 W, and (c) 60 W.

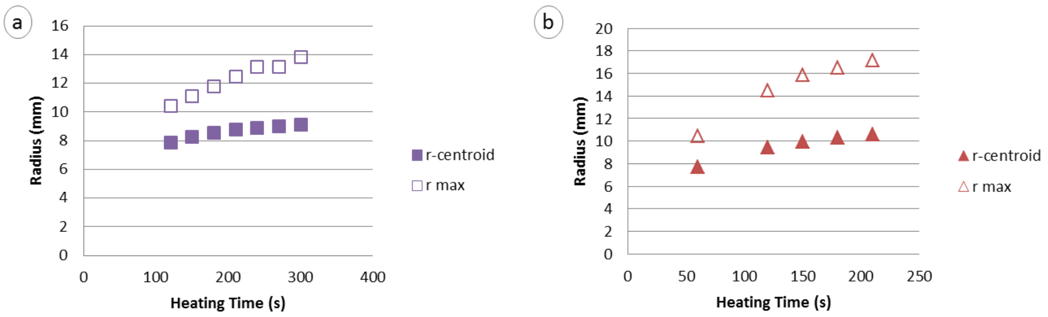

Figure 50 The centroidal and maximum radial coordinates for the necrosed lesion at Θ = 180° for one transducer set to (a) 45 W and (b) 60 W.

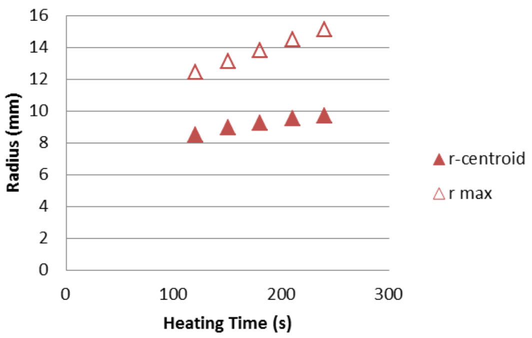

Figure 51 The centroidal and maximum radial coordinates for the necrosed lesion at Θ = 210° for one transducer set to 60 W.

Figure 52 graphs the maximum radial necrosed point versus the heating time for each power at different propagation angles. Figure 52a shows the maximum radius location necrosed for 30 W at different angles of propagation, Figure 52b displays this for 45 W, and Figure 52c is for 60 W.

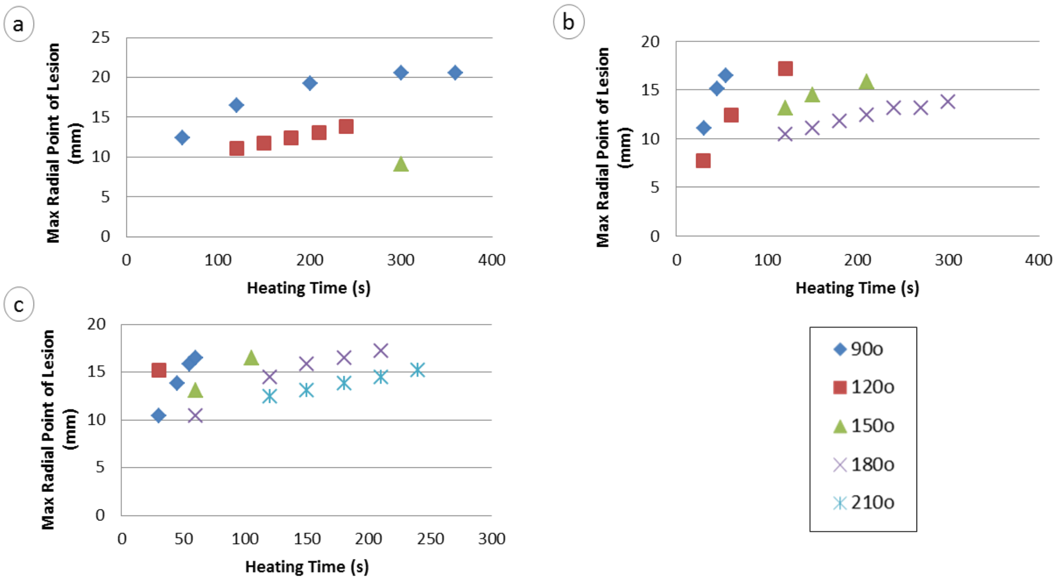

Figure 52 The maximum radial location of the necrosed legion for $\Theta = 90^o$ (blue diamonds), $\Theta = 120^o$ (red squares), $\Theta = 150^o$ (green triangles), $\Theta = 180^o$ (purple x's), and $\Theta = 210^o$ (teal stars). Graphed for (a) 30 W, (b) 45 W, (c) 60 W.

For multiple transducers, in Figure 53 graphs similar to Figure 41 show the necrosed volume with two active transducers: the top transducer set to varying powers and the middle transducer at a constant power (30 W at $\Theta = 90^o$ for Figure 53a, 45 W at $\Theta = 150^o$ for Figure 53b, and 60 W at $\Theta = 210^o$ for Figure 53c).

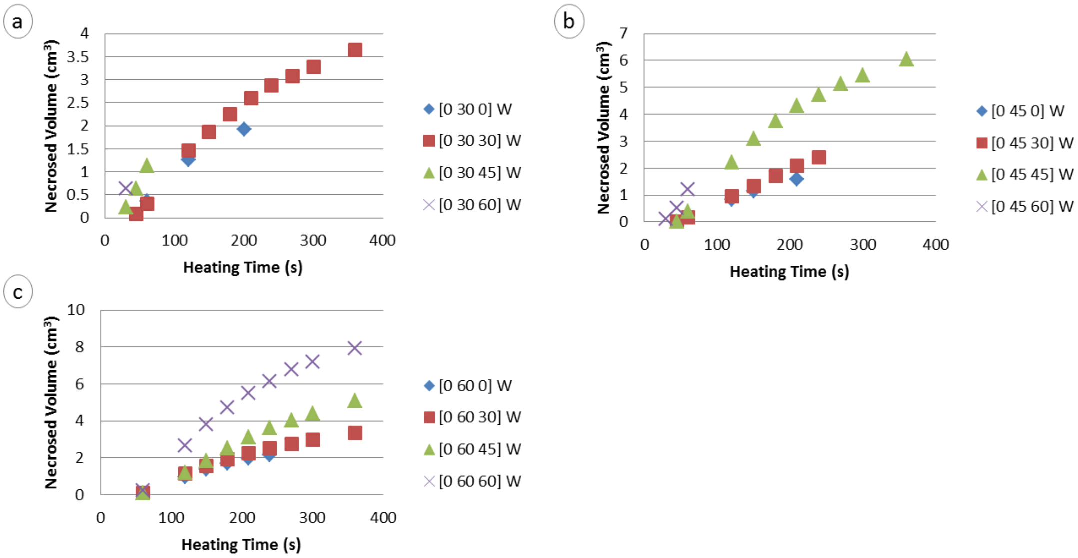

Figure 53 Necrosed volume versus heating time for a constant heating power for the center transducer compared to different transducer power on the third transducer for (a) Q2 = 30 W at Θ = 90°, (b) Q2 = 45 W at Θ = 150°, and (c) Q2 = 60 W at Θ = 210°.

The necrosed volume versus heating time graphs for multiple transducers at the same power level are displayed in Figure 54. Transducers emitting 30 W at Θ = 90° are compared in Figure 54a, 45 W at Θ = 150° in Figure 54b, and 60 W at Θ = 210° in Figure 54c.

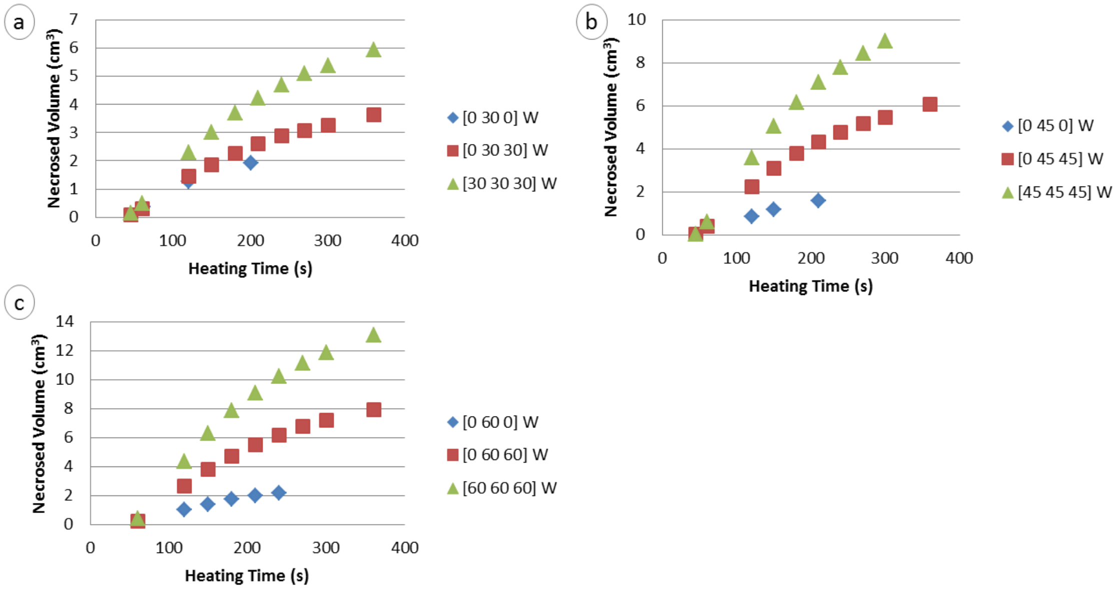

Figure 54 Necrosed volume versus heating time for a specific heating power for different numbers of active transducers for (a) Q = 30 W at $\Theta = 90^{o}$, (b) Q = 45 W at $\Theta = 150^{o}$, and (c) Q = 60 W at $\Theta = 210^{o}$.

Discussion

The r-θ temperature contours (such as those seen in Figure 36b and Figure 37) show a clear distinction between the temperatures within and outside of the angle of US propagation (Θ). This is important for treatment-planning because the healthy tissue outside of the chosen propagation angle will not experience high treatment temperatures (only reaches around 30^{o}C).

These figures also display the highest temperatures occurring closest to the transducers. However, the location of the maximum temperature is slightly shifted away from the surface of the transducer, which is a result of the cooling water flowing between the transducer and the catheter wall. To investigate this further, different coolant properties were tested. The temperature contours are shown for Q = [45 60 0] W, $\Theta = 180^{o}$, and $t_h = 200$ s at $T_c = 10^{o}$C and $t_c = 0$ s in Figure 55a (reproduction of Figure 40a), and $T_c = 5^oC$ and $t_c = 150$ s in Figure 55b. There is a drastic difference in their maximum temperatures, and the areas of highest heat have moved away from the urethra with the cooler water temperature and precooling time. Also, the temperature of the tissue is colder at the urethral wall.

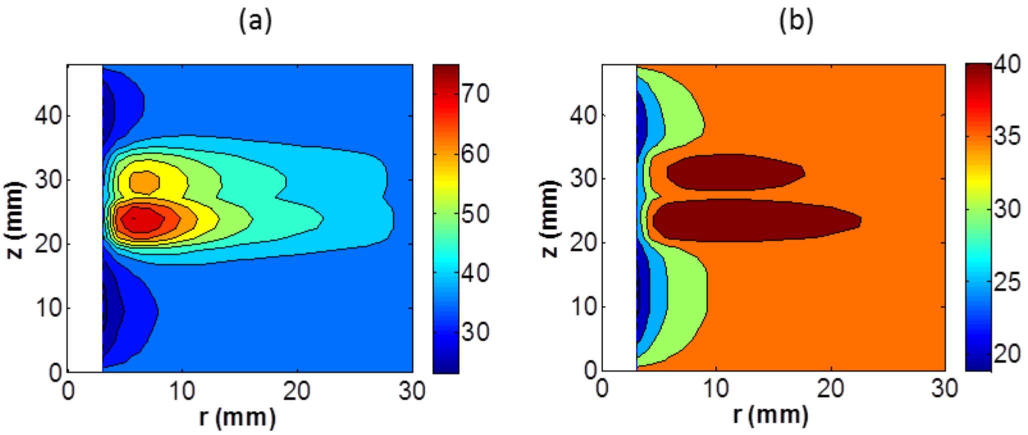

Figure 55 Temperature contours for Q = [45 60 0] W, $\Theta = 180^o$, and $t_h = 200$ s at $\theta = 0^o$ for (a) $T_c = 10^oC$ and $t_c = 0$ s and (b) $T_c = 5^oC$ and $t_c = 150$ s.

As would be expected, the maximum temperature increases more quickly with for the higher power settings. In Figure 38a, for 30 W to reach about 95^oC it took almost seven times as long as with the transducer set to 60 W. This difference becomes more exaggerated as the propagation angle increases.

Figure 39 shows the importance of the angle of propagation of the transducer to the final maximum temperature. At 30 W there are no graphs for $\Theta > 150^o$ (and only two data points at 150^o) because the temperature never reached a value sufficient to cause tissue necrosis. Therefore, if a tumor stretches around a large angle, then a higher power setting will be necessary. Conversely, at 60 W there is only one data point for $\Theta = 90^o$ because after a short time the maximum temperature will exceed 100^oC, and the surrounding healthy tissue will quickly become too hot. Therefore, with tumors that only require tight propagation angles, it may be necessary to use a lower power setting to have more control over the necrosed region.

When a second transducer was activated, the maximum temperature was only dependent on the power of the transducer with the highest setting. Figure 41a has a slight difference between one and two transducers activated to 30 W, and then the temperature increases quicker for the increasing power of that first transducer. In Figure 41b, the data almost exactly overlaps if the top transducer is powered less than or equal to the center 45 W transducer. The fourth data series in that graph is much steeper because the top transducer is set to a higher power (60 W). All of the data overlaps in Figure 41c because the center transducer is set to the maximum power of 60 W, so the top transducer is always less than or equal to this setting. This is further proven in Figure 42, where the effect of increasing the number of transducers with the same power on the maximum temperature yields little difference in any of the graphs.

When Figure 43a and Figure 44a are compared with Figure 36a and Figure 37a, respectively, it becomes apparent that the shape of the necrosis contour closely follows the temperature contours with the highest magnitudes. This is a reasonable result because higher heats take less time to cause tissue ablation, so they would necrose first. Also, the isometric views of the dead cells (Figure 43b and Figure 44b) display the wide variety of necrosis shapes which can be created by different sets of treatment parameters. When three transducers are activated at a low angle of propagation, the dead tissue is in a long, thin rectangular shape spanning most of the height of the prostate (Figure 43b). Conversely, one transducer activated at a large angle will create a volume that wraps around the urethra, but at a short vertical height

(Figure 44b). This depicts the extremes of the wide variety of tumor shapes which can be accommodated with the cylindrical US transducers.

The graphs of the necrosed volume versus heating time shown in Figure 45 were always steeper for the higher powers regardless of the propagation angle, showing the expected conclusion that higher powers cause tissue death more quickly. However, it is interesting to note that for $\Theta = 90^o$ (Figure 45a), when one transducer is set to 30 W it is able to achieve a higher volume of necrosed tissue than 45 W and 60 W because it is able to propagate the necrosis further before 100^oC was reached. Similarly, 45 W reaches a higher volume of necrosed tissue than 60 W at the same angle. However, at the highest angle, 210^o, 60 W is the only one that was able to cause tissue necrosis.

For 45 W and 60 W, almost the same volume of necrosis is able to be attained for differing angles of propagation (as seen in Figure 46b and c), it just takes longer with the larger angles. This is helpful because different tumor shapes, whether oriented longer in the radial or angular direction, can be targeted with the correct combination of transducer properties. For 30 W (Figure 46a), angles above $\Theta = 90^o$ do not create a sufficient region of ablated tissue.

Based on the volume of tissue necrosed, the resulting radial necrosis locations are predictable: the maximum and centroid location of the necrosis are greater for lower transducer powers at $\Theta = 90^o$ (Figure 47). At that angle with a power of 30 W, the necrosis reaches its furthest distance of all single transducer trials, about 20 mm from the central axis. This is a third of the distance to the edge of the prostate. If tumors fall much past that location, a different transducer design may be necessary, such as a transrectal, interstitial, or external device.

At the higher angles of propagation, a higher power is necessary to reach further radially through the prostate. For example, at $\Theta = 180^o$ (Figure 50d), in 100 less seconds 60 W is able to ablate tissue about 3.5 mm further than 45 W. This shows that tumors which are large in both the radial and angular directions will need a high power setting, as would be expected.

As shown in Figure 52, as the angle of propagation increases, the maximum radial location of necrosis decreases. This occurs because the acoustic energy is spread around the larger angle instead of focusing on one section as it does at the higher angle.

Figure 53 shows the greatest necrosed volume occurring for two transducers set to the same power setting. However, this is misleading because propagation angles were chosen where the middle transducer was able to have the most data points within the constraints of temperatures under 100^oC and non-zero necrosis volumes. Therefore, it is not the fact that the powers are the same which causes the greatest tissue ablation, but that they are both values which were optimized at the specified angle. So it is most important to realize that there is a specific power which needs to be chosen for large tumors which are situated at each angle.

As would be predicted, the necrosed volume increases with increasing number of transducers activated, as seen in Figure 54. This is attributed to the increase of ultrasound energy distributed in the axial direction. Since the maximum temperature was not affected by turning on more transducers at the same power, a tumor with a large distance in the axial direction can be necrosed by using the power and angle setting appropriate for the r-θ area of the tumor in those directions, and then the transducers at the appropriate axial distance along the transducer can be activated.

To succinctly examine the results, an energy parameter was created which combines each of the transducer settings based on their influence on the final necrosed volume, where the goal is to result in a linearly positive relationship between this parameter and the necrosed volume. This energy parameter, ξ, is displayed in Equation 44

$$\xi = \frac{{t_h}^k \left(Q_2 + \frac{1}{3}(Q_1 + Q_3)\right)}{\Theta} \qquad \text{Equation 44}$$

where k is an exponential constant less than one. The heating time and transducer powers are both on the top of the fraction because an increase in either causes an increase in the necrosed volume, and the propagation angle is in the denominator because an increase in the angle causes a decrease in volume with other parameters held constant. t_h has an exponent between zero and one because it is less influential than the power. The power is not simply a summation of all three powers because as was shown previously, the highest power transducer has the greatest effect on the resulting temperature and necrosis curves. Q_2, the center transducer, is assumed to be the highest power. One third of the average of the top and bottom transducers is therefore the importance of their contribution to the total input power for ξ.

For all of the data, k is determined to create the best fit when equal to 0.5. The resulting plot of V_{necr} v. ξ is shown for all data collected in Figure 56, along with its line of best fit (including the equation and R^2 value). The resulting volume of ablated tissue is most predictable for small values of ξ (and therefore smaller tumors).

This can be a helpful initial resource for physicians to find a good combination of transducer parameters for a tumor of a certain volume. However, with only an R^2 value of 0.72, further analysis is needed.

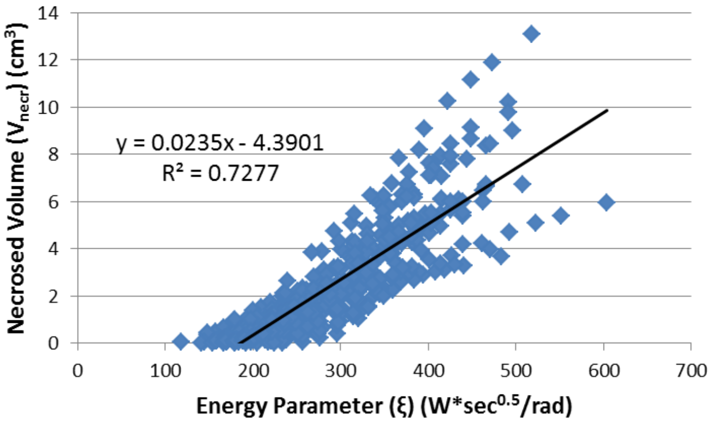

Figure 56 Graph of the necrosed volume Vnecr versus the energy parameter ξ. The line of best fit, its equation, and its corresponding R2 value are also shown.

This energy parameter is considered for single transducer trials, and separated by power level. The value of k is altered for each power level, and its resulting value which achieved the best linear fit of each data series is displayed in Table 11. The graph showing the individual fits of each transducer power is shown in Figure 57, and they all have a very accurate linear fit, with R^2 values ranging from 0.88 to 0.98.

Table 11 The exponential constant of the heating time for different individual transducer powers.

Q_2 (W)	k
30	**0.30**
45	**0.35**
60	**0.50**

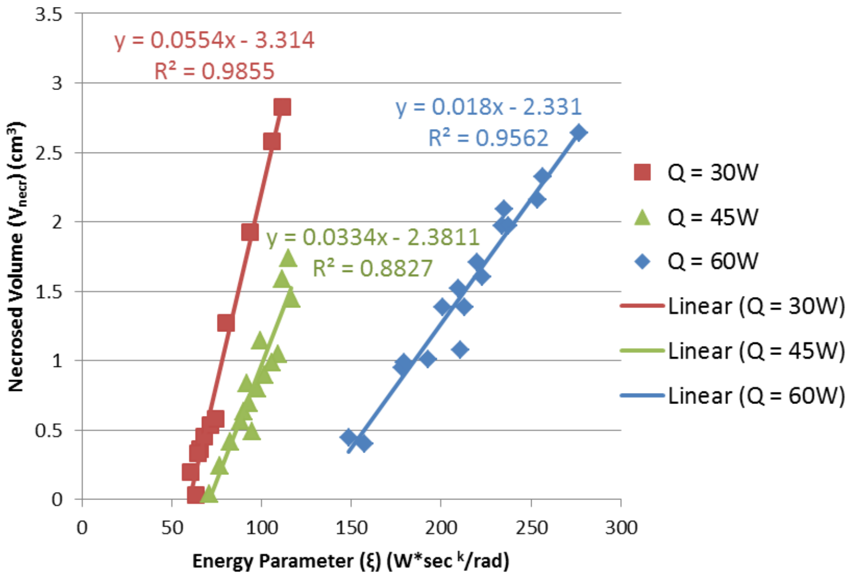

Figure 57 Graph of V_{necr} v. ξ for one active transducer at different powers. Also includes their linear fits, their equations, and R^2 values.

Device Design and Protocol Development for Prostate Cancer

The prostate cancer studies are focused on finding the appropriate set of transducer parameters for different size and location tumors. This section will outline a concept of the device which can be used for this treatment, along with important considerations for determining the treatment planning for physicians.

Device Concept

For designing the US transducer for prostate cancer ablation, it was important to first determine the important functional requirements and design parameters of the device. The functional requirements are the requirements which satisfy the customer needs, and design parameters are the features which fulfill the functional requirements [95]. The functional requirements for the transducer are listed in Table 12.

Table 12 Functional requirements for US device to ablate prostate cancer.

Functional Requirements
1) Necrosed tissue must reach tumor area.
2) Minimal ablation of healthy tissue (only a margin should remain).
3) Easy to use correctly.

The design parameters which satisfy these functional requirements are shown in Table 13. The second column of this table also provides the functional requirements (FRs) which are satisfied by each design parameter.

Table 13 Design parameters for US device to ablate prostate cancer, including the functional requirements they each satisfy.

Design Parameters	FR satisfied
Situated near prostate gland.	**(1)**
Targets tumorous tissue.	**(2)**
Harmful rays blocked from healthy prostate.	**(2)**
Easily arrests in correct location.	**(3)**

Designs which fulfilled many of the parameters were presented in Figure 18 and Figure 19 in Chapter 2 and are reprinted below. Figure 18 shows a schematic of the intraluminal transducer which was simulated for an optimization study [71]. This device has multiple transducers inserted into a catheter, arranged axially, and independently controlled. Its angle of propagation can be partially blocked to allow for a control of the ultrasound intensity distribution. Figure 19 shows a drawing of the transrectal device used by Diederich for *in vivo* experiments on dog prostates [16].

This also has multiple axially-arranged transducers inside of a catheter, and includes an integrated coolant external to the transducers. The coolant was input through the base of the device, flowed through tubes to the tip of the catheter, and then flowed across the transducer surface back towards the base of the catheter. The coolant exited the device through tubes at the base.

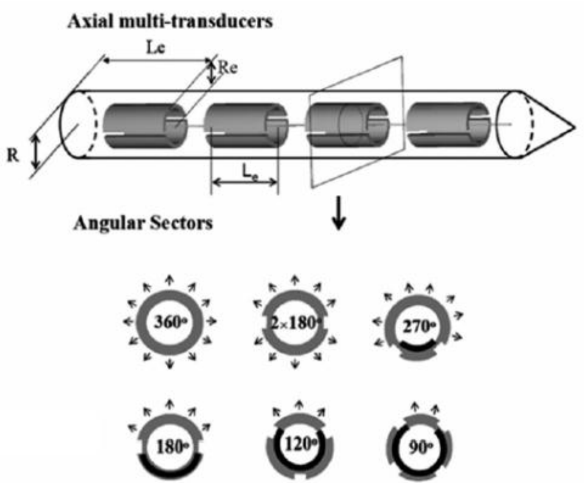

Figure 18 reprinted, displaying the intraluminal transducer schematic displaying four independently-controlled cylindrical transducers with angular segments that can be blocked so power is only emitted in desired angular direction [71].

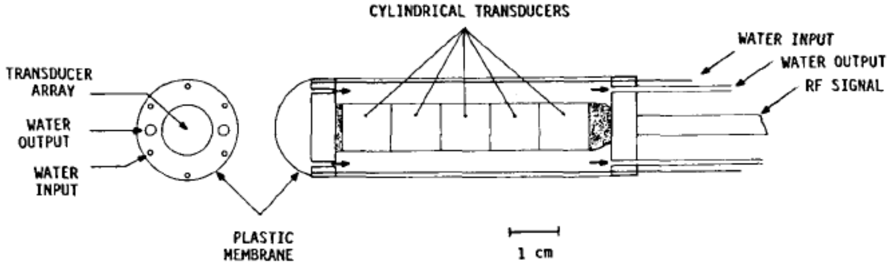

Figure 19 reprinted, which is a schematic of Diederich's transducer used in simulations and in vivo experiments on dogs [76].

These ideas were integrated into the concept sketch of the transducer, which was designed to fulfill all design parameters. This concept is shown in a CAD three-dimensional view in Figure 58. The diameter of the catheter was designed to be sufficiently small to fit inside of the urethra to gain access to the center of the prostate, so a large range of tumor locations can be treated. Three cylindrical transducers are inserted into the catheter and arranged axially, with inert material separating the transducers. The multiple transducers will allow the device to easily target tumors which are in any axial location without having to perfectly position the device and tumors which are longer in the axial direction.

Physicians will have multiple of these devices, each with a different set angle of propagation because the transducer will only be a fraction of a circular cylinder, with the remainder of the circle completed with non-transmitting backing material. The location and size of the tumor will dictate which of those catheters will be used for the duration of the treatment. Also, coolant fluid flows past the transducer surface to prevent the urethral tissue from burning (and to move the necrosed region further into the prostate if desired, as discussed in the previous section). The fluid enters and exits the device through tubes at the base of the catheter, and channels are built to create different paths for the inlet and outlet flows. There is a locating balloon situated at the tip of the catheter, which will inflate in the patient's bladder to arrest the device in the correct location.

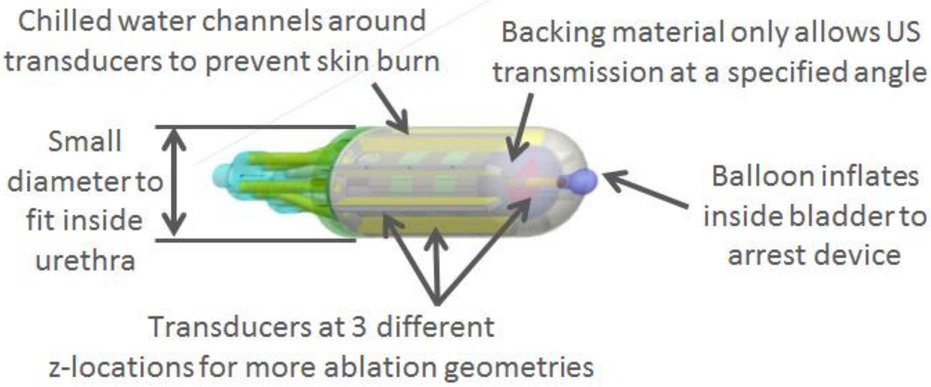

Figure 58 Concept drawing of intraluminal prostate design.

Physician Protocol

An important aspect of creating patient-specific treatment planning protocols is to design an easy method for physicians to determine the best treatment option for each case. The studies performed in this chapter resulted in a database of input US parameters and output temperatures and necrosed volumes. This information can be used to create a guide for physicians, where the physician would input the tumor positioning, and the output will be the ultrasound parameters. An example of this is shown in the flowchart in Figure 59. In the Treatment Outcome section of the chart, a necrosed tissue margin is mentioned. Not only does the tumor need to be completely engulfed by the necrosed region, but there should be at least a margin of 1 mm which is ablated around all sides to ensure that all cancerous cells are destroyed, so this needs to be taken into consideration for treatment planning.

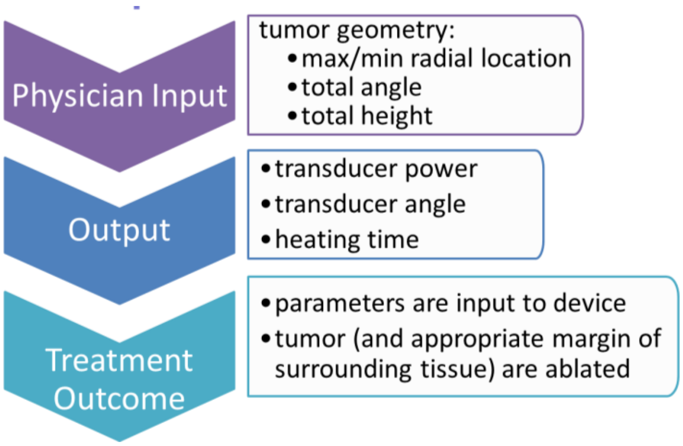

Figure 59 Flowchart showing the patient-specific protocol for physicians to use for prostate cancer treatment planning.

To show an example of this, a separate code was written which determines the largest spherical tumor which can be treated with different sets of ultrasound parameters for one active transducer. An example result is shown in Figure 60 for transducer settings Q = [0 45 0] W, Θ = 120°, and t_h = 60 s, showing the frontal cross-section at θ = 0°. The largest spherical tumor which this set of parameters could ablate had a diameter of Ø6 mm (depicted as a black circle). An orange target zone surrounds this tumor with the appropriate margin of healthy tissue ablation, and as can be seen the necrosed tissue (red area) mostly fills this area. This will kill the tumor with a minimal amount of healthy tissue destroyed, although a slightly larger region of necrosis may be chosen to fully ablate the margin as well. The complete results of this study are shown in Table 40 – Table 42 in Appendix B.

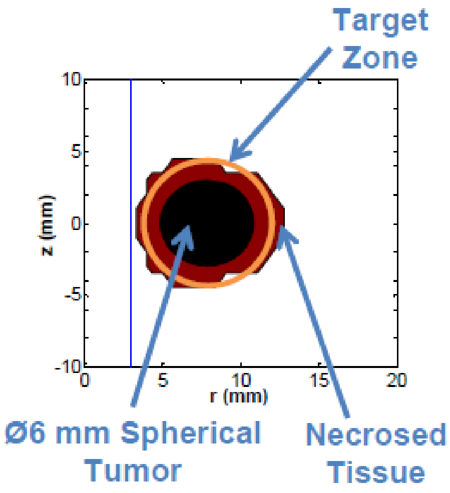

Figure 60 Tumor (black circle) of diameter Ø6 mm is the largest spherical tumor which can be fully ablated (necrosed tissue is red volume) with the appropriate 1 mm margin from US parameters Q = [0 45 0] W, Θ = 120°, and t_h = 60 s. The target zone (orange open circle) displays the 1 mm margin which needs to be ablated outside of the tumor.

The physician should have an easy-to-use configuration for both the device and the treatment planning tools. Figure 61 displays an example of a possible user interface, where the physician just has to provide the patient's tumor specifics into a "black box" (left column of the interface), and after clicking the "Calculate" button the resulting transducer parameters will be given (right column of the interface). The device will be created to connect to this software and automatically input these parameters.

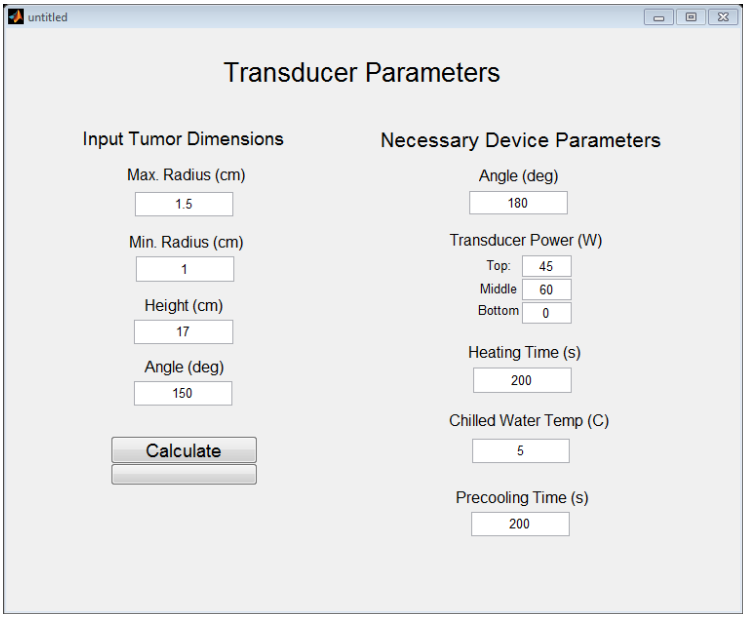

Transducer Parameters

Input Tumor Dimensions

Max. Radius (cm): 1.5
Min. Radius (cm): 1
Height (cm): 17
Angle (deg): 150

Necessary Device Parameters

Angle (deg): 180
Transducer Power (W)
Top: 45
Middle: 60
Bottom: 0
Heating Time (s): 200
Chilled Water Temp (C): 5
Precooling Time (s): 200

Figure 61 Physician user interface to easily receive device parameters. They input the tumor information on the left, and receive the information on the right when "Calculate" is clicked.

Chapter 5: Numerical Modeling and Device Design for Ultrasound Thermal Therapy of Breast Cancer

Simulating breast cancer ablation has a lot of similarities as the prostate studies, but the different geometry and the use of HIFU instead of planar ultrasound creates important differences. As in the prostate studies, these simulations use variable properties for the acoustic attenuation and tissue perfusion to obtain realistic results. However, a thermal damage model specifically for breast cancer cells is not used because the Arrhenius parameters for these cells are not available. Instead, the general tissue model with the thermal isoeffective dose is used, which decreases the accuracy of these simulations.

A phased array with electrical focusing for HIFU is simulated for tissue ablation. The following study tests different transducer geometries, including the overall shape of the transducer and the height of the individual elements of the transducer. The results determine the shape and volume of the necrosed tissue created by each combination of the transducer geometry and parameters. The concepts of the device design and physician protocols which can be used with the results of these simulations will be presented.

Ideally, one sonication would be sufficient to completely ablate the breast tumor with little cell death of the healthy tissue. However, this is generally not possible with the small necrosed volumes typically created by HIFU, so finding a set of parameters which results in the maximum necrosed volume is important, while still resulting in a predictable shape of that volume. These considerations are accounted for during the testing and reviewing the results of the breast cancer thermal therapy simulations. This chapter will first describe the methods used to simulate the HIFU treatments, and then present the results from these simulations, discuss their implications, and provide the considerations for device design and patient-specific protocol development.

Methods

MATLAB software is again used for the breast cancer simulations. The order of the computation is the same for the breast cancer studies as it was for the prostate simulations: define the computational domain and tissue and ultrasound properties, calculate the heat generation and temperature at every node in the domain at every time step, and finally determine the nodes which represent dead breast cells from the temperature history.

As was done before, the FD method discretizes the bioheat transfer equation (BHTE). However, this time a spherical coordinate system is used for geometric simplicity (so the spatial derivatives in the BHTE are defined differently). This system is defined by a radial coordinate and two angular coordinates (r,θ,φ), depicted in Figure 62. Note that the angle φ is not defined in the traditional manner of descending from the z-axis, but instead MATLAB defines it ascending from the x-y plane.

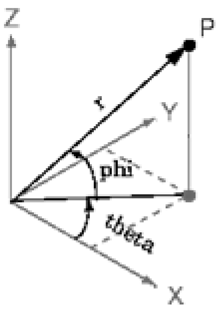

Figure 62 3D spherical coordinate system used for breast simulations [96].

The Laplacian in spherical coordinates is defined by Equation 45

$$\nabla^2 T = \frac{\partial^2 T}{\partial r^2} + \frac{2}{r}\frac{\partial T}{\partial r} + \frac{1}{r^2 \sin^2(90^o - \phi)}\frac{\partial^2 T}{\partial \theta^2} + \frac{1}{r^2}\frac{\partial^2 T}{\partial \phi^2} + \frac{\cos(90^o - \phi)}{r^2 \sin(90^o - \phi)}\frac{\partial T}{\partial \phi} \qquad \text{Equation 45}$$

The partial derivatives of T with respect to r and θ are the same as were derived in Equation 39 – Equation 41, and the derivatives with respect to φ are similarly derived, and displayed in Equation 46 and Equation 47, where the r and θ coordinates are held constant.

$$\frac{\partial^2 T(t,\phi)}{\partial \phi^2} = \frac{T(t-\Delta t, \phi + \Delta\phi) + T(t-\Delta t, \phi - \Delta\phi) - 2T(t-\Delta t, \phi)}{\Delta\phi^2} \qquad \text{Equation 46}$$

$$\frac{\partial T(t,\phi)}{\partial \phi} = \frac{T(t-\Delta t, \phi + \Delta\phi) - T(t-\Delta t, \phi - \Delta\phi)}{2\Delta\phi} \qquad \text{Equation 47}$$

The preceding discretized differential functions are inserted into the BHTE, which is rearranged to be solved in terms of T(t,**r**) (where **r** is the spatial vector), and the temperature at each point is calculated at each time step.

Geometry of Domains/ Testing Parameters for Breast Studies

A simple hemispherical geometry is used to represent the breast in the simulations, which was also often used in the previous studies which simulated HIFU to the breast (described in Chapter 2). The radial dimension of this hemisphere is displayed in Figure 63.

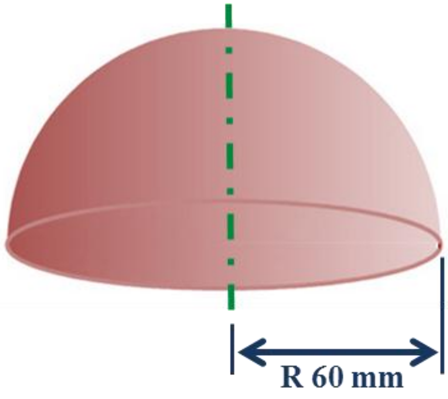

Figure 63 Dimensions of the hemispherical breast geometry.

The coordinate system is displayed in Figure 64, and the bounds of the region are r = [0, 60] mm, $\theta = [0, 360]^{o}$, and $\varphi = [0, 90]^{o}$. Figure 64 also depicts the coupling water which is used for a smooth transmission of the US waves to the breast, and cools the surface of the breast to prevent burning. There are two main transducer configurations: flat and curved. With each configuration, the transducers are arranged around the breast in four segments, and elements span perpendicular to the chest from the base of the breast to the top (60 mm height). The transducer variables are the number of transducers in each row parallel to the base of the chest, the number of rows of these elements from the bottom to the top of the breast (which in turn determines the transducer height since the total height is fixed at 60 mm), the number of active transducers, and the shape. Half of the rows of transducers are always activated, where the middle row of active elements is centered on the tumorous region. The transducer configurations are shown in Figure 64 (curved transducer) and Figure 65 (flat transducer) with a sample number of elements (5 elements per angular segment (n_e) and 5 rows of elements in the height (n_r)).

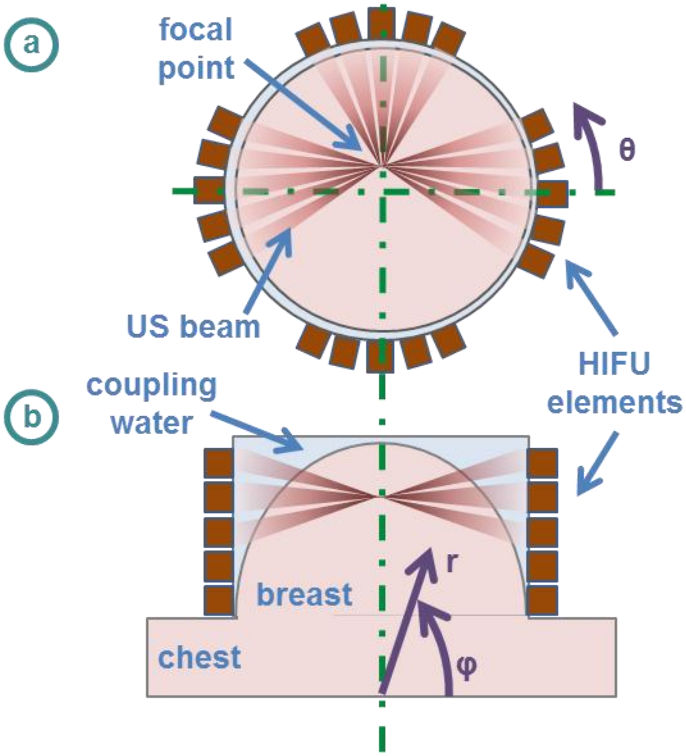

Figure 64 Schematic of breast simulation model for a curved transducer, showing the breast, chest (not part of simulation domain), transducer elements, coupling water, and r-θ-ϕ coordinate system in the a) top view, and b) front cross-sectional view. This is showing a sample where there are 5 elements per transducer segment, and 5 rows of segments tall. The US beams are focused on a point in the upper half of the breast and off-center in the plane perpendicular to the chest, the bottom two rows of elements and the segment across from the focal point quadrant are not on.

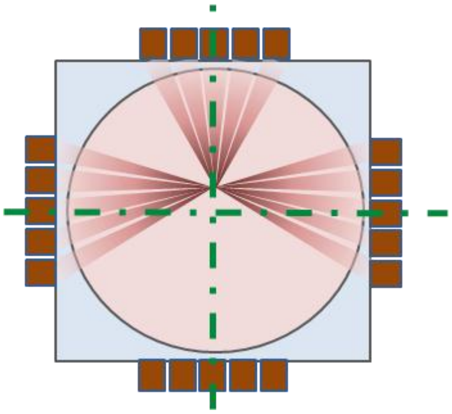

Figure 65 Schematic of breast simulation for flat transducer.

Each element width (l_e) is 1.5 mm (which determines the resulting US frequency to be f = 0.5 MHz because $f = \frac{c}{2l_e}$ where c is the speed of sound, 1500 m/s [8]). There is no gap between the elements within each segment or between the rows up the height of the breast; it is displayed this way in the schematics for clarity. The breast tissue is initially set to body temperature, 37°C, the interface between the base of the breast and the chest is held to a constant 37°C, and the exterior of the breast is subject to a convection condition from the coupling water (T_c = 10°C).

Testing Parameters

Studies are run to first test the affect the transducer parameters have on the location and magnitude of the heat generation (q'''). Then, separate studies are performed which examine the temperature gradients and necrosis contours resulting from the transducer settings.

Parameters for Heat Generation Studies

Before simulating the heat transfer through the tissue, different transducer configurations were tested to determine optimal parameters to achieve a focal point of the heat generation in the desired location. The shape of the transducer, the number of segments activated (n_s), the number of elements per segment (n_e), and the number of rows (n_r) were varied. The values tested are shown in Table 14. If $n_s = 1$, then the first transducer is activated, and if $n_s = 3$, then the two transducers which are on either side of the first transducer (the second and fourth transducer segments) are activated as well. The shape and number of rows of elements are fixed values for a given device, but the number of transducers activated and the number of elements per transducer can be adjusted on a patient-specific basis (as long as the total number on the device are initially at the maximum).

Table 14 Values tested for the different transducer configurations. If this value needs to be fixed before transducer fabrication or not is also noted.

Transducer Configuration	Values Tested	Fixed per Device?
shape	**curved, flat**	**yes**
n_s	**1, 2, 3**	**no**
n_e	**41, 51, 61**	**no**
n_r	**20, 30, 40**	**yes**

Also, there were 9 different focal locations tested, each in the plane in front of the first transducer ($\theta = 0^o$). The foci are in three evenly-spaced heights (the total height is the breast radius, R, so the distance between heights is R/4), and three evenly-spaced locations from the center of the breast to its side at that height (the line segment length from the center to side of the breast is called l_s), which changes at each height, so the distance between the points tested on this line were $l_s/4$. These focal locations are depicted in Figure 66.

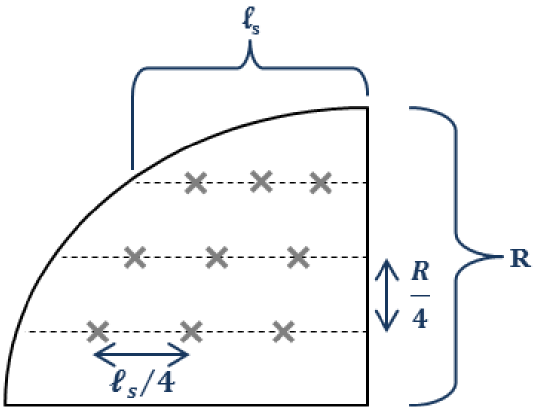

Figure 66 Locations of tested focal point in the plane of θ = 0° (in front of 1st transducer).

The location of the maximum q''' is determined for each set of transducer parameters for a set transducer power of Q = 100W. This location is compared to the location of the desired focal point, so the studies which minimize the difference in their distances are the optimal settings. The desired focal point locations which were defined in Figure 66 are labeled in Figure 67, where each point is given the ordered pair (xn, zn) to represent its location in the x and z directions (not the actual value of the x-z coordinates). This is the notation which will be used for the remainder of this report.

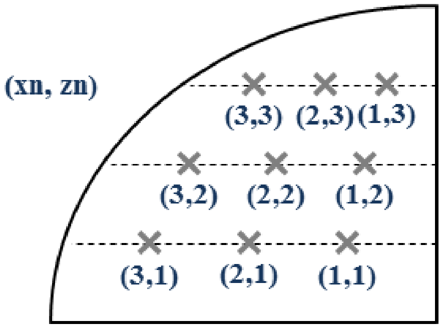

Figure 67 Labels of the desired focal points, where the ordered pair (xn, zn) defines the point as the x-location (xn) and z-location (zn) but is not giving the actual coordinate values

Parameters for Necrosis Studies

Table 15 displays the testing parameters for the breast cancer studies which examined the tissue ablation caused by different sets of transducer parameters. The majority of the tests were performed with just one transducer to determine the effect of the other transducer parameters. If multiple transducers are used, the transducer powers will be listed as [Q_1 Q_2 Q_3 Q_4], where Q_1 is the power for the transducer centered on the desired focal point, and moving clockwise around breast for transducers $Q_2 – Q_4$. Each study heated the tissue until 100°C was reached anywhere in the volume. The dependent variables for the breast cancer thermal therapy simulations were the heating time and the final necrosed volume.

Table 15 Breast simulation testing parameters and their values used in simulations.

Independent Variables	Tested Values
Transducer Powers, Q_i (W)	**0, 50, 75, 100**
Transducer Fixed Geometry:	
Shape	**flat, curved**
Number of Heights	**20, 30, 40**
Number of Horizontal Active Elements	**41, 51, 61**
Number of Active Transducers	**1, 2, 3, 4**
Location of Necrosis	
xn-value	**1, 2, 3**
zn-value	**1, 2, 3**

As with the prostate studies, the breast cancer studies did not surpass 100°C because the temperature in the surrounding healthy tissue needs to be kept below the pain threshold, and because the effects of water at its boiling point temperature are not accounted for in this study. These simulations were stopped when the maximum temperature in the tissue reached 100°C.

Determination of Cell Necrosis

A similar procedure is followed as with the prostate studies, where first the heat generation is determined, then the temperature fields within the computation volume, and finally the resulting cell necrosis is found. However, the heat generation in the breast cancer studies first needs the pressure at each point defined because it uses a phased array transducer. This was defined in Equation 9 in Chapter 2, and is rewritten below

$$p_i(x,y,z) = \sqrt{\frac{2W\rho}{cA}}\left(\frac{fS}{d}\right)e^{\left(\phi-\frac{2\pi d}{\lambda}\right)i-d\alpha} \qquad \text{Equation 9}$$

Then the heat generation at each point was determined in Chapter 2 to be defined according to Equation 11, rewritten here

$$q'''(x,y,z) = \frac{\alpha P^2(x,y,z)}{\rho c} \qquad \text{Equation 11}$$

where α is the same as that for the prostate studies (Equation 5), P is the sum of all individual element pressures, tissue density ρ is defined in Table 3, and c is the speed of sound, which is 1500 m/s in tissue [8].

As would be expected, the same blood properties (Table 3) are used for the BHTE for the breast studies as was used for the prostate simulations. That equation uses the heat generation to determine the final temperature at each node in the domain.

To determine the thermal dose for the cell necrosis, a general tissue model using the thermal isoeffective dose (TID) of CEM43^{o}C = 240 minutes was used (as was shown to be used by multiple studies in Chapter 2 [15] [73] [79] [8] [80] [14]). The equation of this model was given in Equation 28 in Chapter 2, and is rewritten below.

$$CEM43℃ = tR^{43-T} = 240\ min \qquad \text{Equation 28}$$

240 minutes was the most-common value used for simulations in the previous literature reviewed. An Arrhenius model was not used here as it was for the prostate cancer studies because there is little information available on the Arrhenius parameters specific to breast cancer, and this equation changes drastically with different cell lines.

Grid Validation

A similar grid refinement study was performed for the breast ultrasound simulations as was conducted for the prostate studies. The nodes in the r (r_n) are tested from 41 to 81, in the theta (θ_n) 65 – 125 nodes are tested, and in phi the nodes (φ_n) are varied from 17 – 67. There are fewer nodes in phi than in theta because phi only varies from 0 – 90^{o}, while theta varies from 0 – 270^{o}. A test case with a flat shape, $n_s = 1$, $n_e = 61$, and $n_r = 6$ was used for the study.

For the breast cancer grid study, the individual numbers of nodes in each coordinate direction must be chosen separately because the shape of the volume element changes a lot based on the number of nodes in each coordinate (as opposed to the prostate cancer study which increased all nodes simultaneously). Therefore, graphs holding two of the directions constant were created for every combination of grid. The maximum temperature was compared for each grid, and the percent error compared to the finest grid was calculated. Two sample graphs are displayed in Figure 68 and Figure 69. Figure 68 shows the graphs of percent error compared to the maximum temperature of the finest grid size v. θ_n for a set value of $r_n = 41$ and for different series of φ_n. For this value of r_n, $\theta_n = 85$ gives very similar results to the finest size in that coordinate, $\theta_n = 125$, and also minimizes the error when coupled with $\varphi_n = 27$.

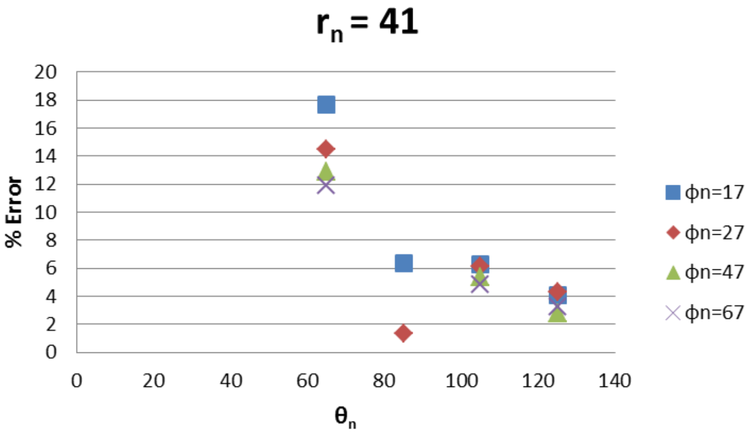

Figure 68 The % Error of Tmax compared to the most fine grid versus the number of nodes in the θ axis (θ_n) for r_n=41 and different values of ϕ_n.

Figure 69 displays the graph of the percent error v. r_n for a set $\varphi_n = 27$ for different values of θ_n. Error for this grid size is minimized with the smallest node size of $r_n = 41$. Therefore, the final grid size chosen for the experiments to be used was $\Delta r = 1.500$ mm, $\Delta\theta = 4.286^o$, and $\Delta\varphi = 3.462^o$. Also, it was tested that the code will converge at a time step of $\Delta t = 3.802 \times 10^{-5}$ sec.

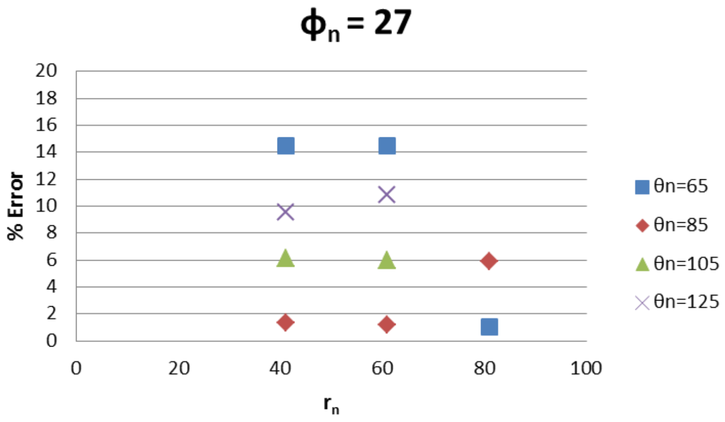

Figure 69 The % Error of Tmax compared to the most fine grid versus the number of nodes in the r axis (r_n) for ϕ_n=27 and different values of θ_n.

Calculating Acoustic Attenuation

As explained in the introduction to this section, the acoustic attenuation is again varied for these simulations as a function of the thermal dose. The thermal dose will change at every iteration, so to calculate the exact attenuation throughout the simulation it also needs to be determined at each time step. For the prostate studies, the time step was sufficiently large that this could be easily performed; however with the breast cancer studies this is very computationally expensive since the time step is much smaller. To reduce its expense, the attenuation was only calculated at certain time intervals instead of every time step. The number of iterations between calculations was determined by testing different numbers to ensure it would retain the accuracy of the results. The maximum temperature after 0.4 seconds of heating with one transducer activated at 100W was determined for simulations with a different number of iterations between calculations of the attenuation coefficient (α), and the results of these tests are shown in Figure 70. Figure 70a shows the maximum temperature versus the number of iterations and the percent error between the maximum temperature of the current point and the case where α is calculated every iteration. At 1000 iterations there is less than a 0.5% error, so this is the value which will be used during the simulations. This will be greatly beneficial for computation time, as shown in Figure 70b, where α calculated at each iteration takes about 570 minutes to complete the heating loop, while if it is calculated only every 1000 iterations it takes less than 5 minutes.

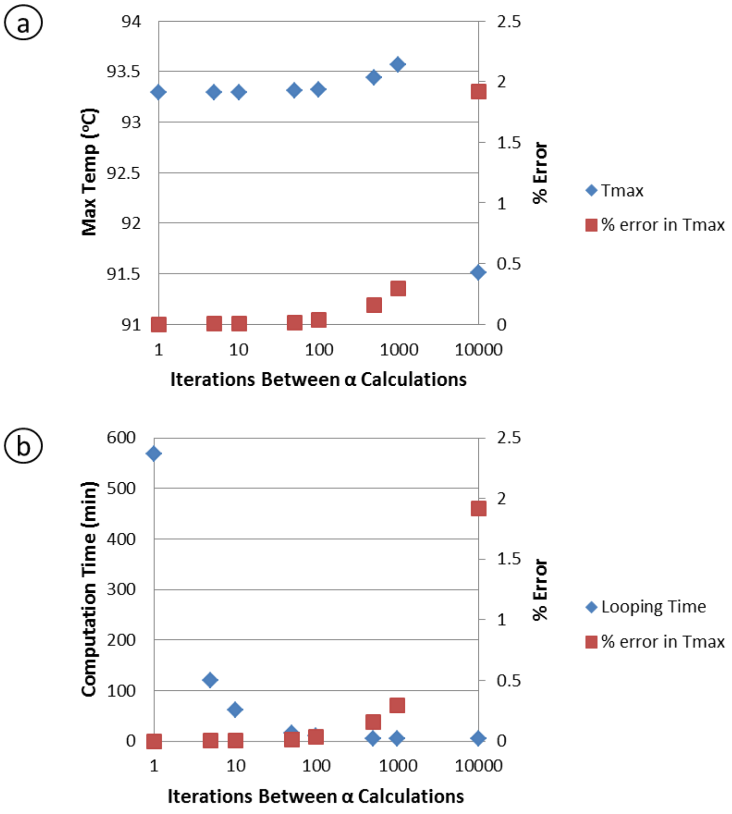

Figure 70 Graphs showing (a) the maximum temperature and % error, and (b) the computation time and % error versus the number of iterations between each α calculation. The % error in Tmax series in each graph is the same, just reproduced for comparison purposes.

Results from Breast Studies

For the breast cancer simulations, first the results of the focal point studies will be presented. Next, the temperature and necrosis contours will be provided concurrently for comparison purposes.

Focal Location Studies

The data from all focal location studies are listed in in Table 43 – Table 54 Appendix C. The heat generation created by the different transducer parameters and focal locations varies from 2.05 x 10^8 W/m^3 to 7.37 x 10^9 W/m^3. The values are spread evenly through this range, as is depicted by Figure 71, which displays the natural log of the heat generation for each trial.

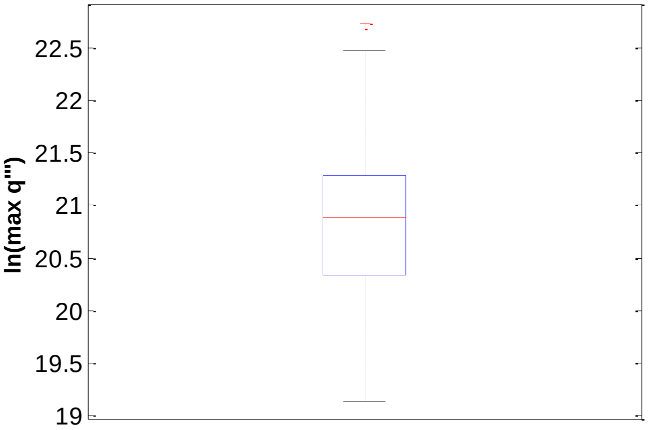

Figure 71 Boxplot of the natural log of the heat generation for the focal location studies. The red line in the center is the mean, the blue box spans the upper (75%) and lower (25%) quartiles, the black horizontal lines span the data range without outliers, and the red plus is an outlier.

An example of the resulting contour plot of the heat generation is shown in Figure 72 (transducer parameters: flat, 41 elements/row, 40 rows, focused at (3,1)). The top image is a sliced isometric plot displaying the contours on the three x-y-z orthogonal planes coinciding with the desired focal point: x = xn, y = 0, and z = zn (the patient’s chest is located at the z = 0 plane). There is a very sharp difference in heat generation between the focal point and the rest of the breast.

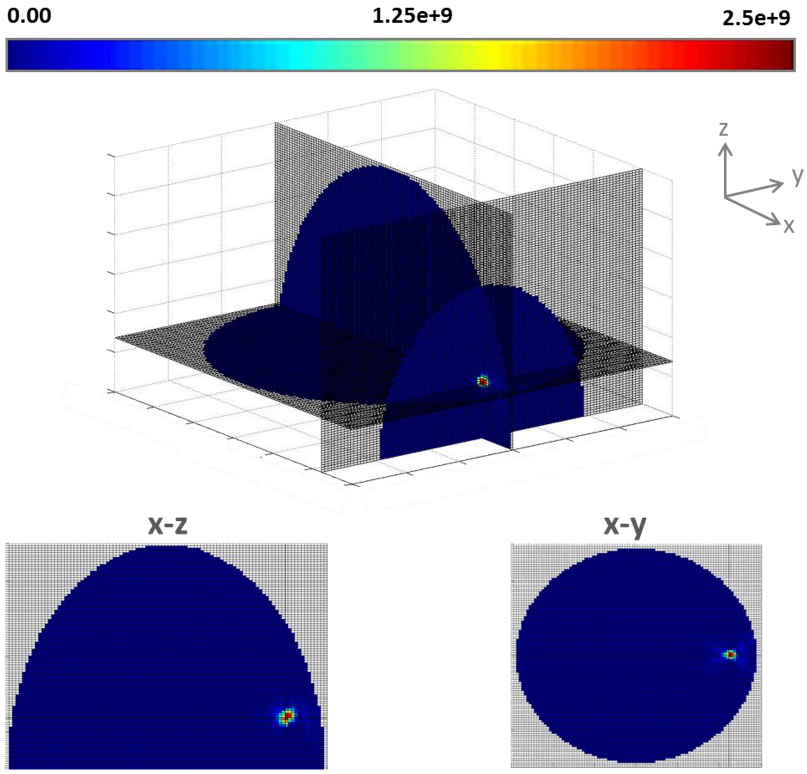

Figure 72 Contour plot of the heat generation (W/m^3) in the sliced isometric view (top), x-z plane (bottom left), and x-y plane (bottom right). (Transducer parameters: flat, 41 elements/row, 40 rows, focused at (3,1)).

The shape of this focal point varies drastically depending on its location. When the location of the focus is shifted to the coordinate (1,1) (with all of the same transducer parameters), a much larger focus is created, as demonstrated by Figure 72. It should also be noted that this larger focal point has a maximum heat generation which is almost a full order of magnitude smaller than the heat generation created at (3,1).

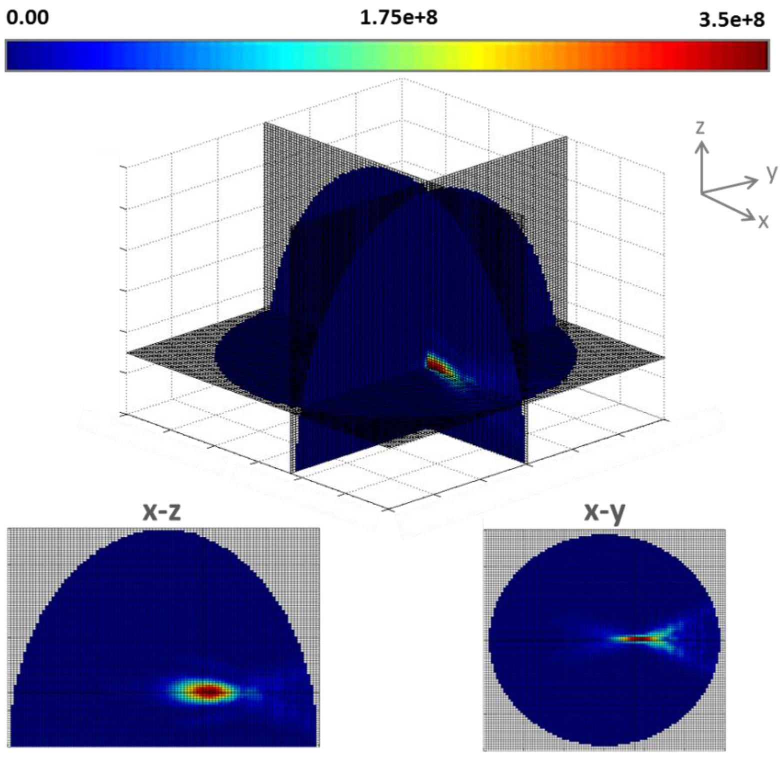

Figure 73 Contour plot of the heat generation (W/m^3) in the sliced isometric view (top), x-z plane (bottom left), and x-y plane (bottom right). (Transducer parameters: flat, 41 elements/row, 40 rows, focused at (1,1)).

Effect of Transducer Parameters on Heat Generation

The goal of the focal location studies was to find the optimal transducer parameters, both for qualities which need to be decided before fabrication (the shape and number of rows of elements) and ones which should be adjusted based on the tumor location (the number of active elements and transducers). The final focal point of the simulations was defined by the location of the maximum heat generation. The accuracy of each transducer configuration is shown in the pie chart in Figure 74, where difference between the final focal point and the desired location are examined for each trial performed. The majority of the different transducer configurations resulted in the focal point exactly on the node which was input as the desired focal location. The trials which resulted in a distance of 1 to 2 mm away from this point were one node away in any direction. The trials which were more than 2 mm away were one node away in two coordinate directions. There were no trials which resulted in maximum heat generation points more than two nodes away.

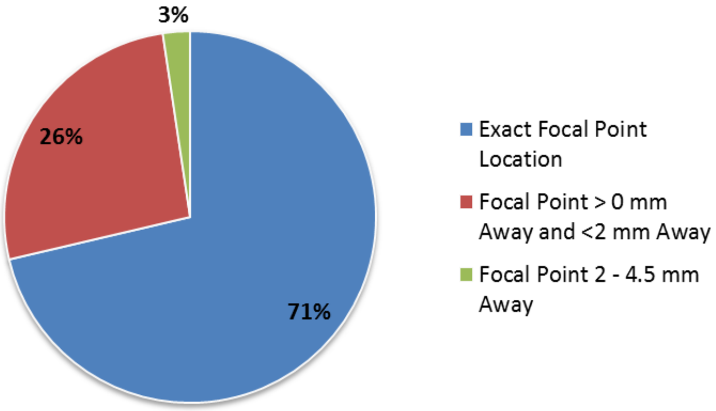

Figure 74 The percentage of total trails which resulted within different ranges for the distance of the location of the maximum heat generation from the desired focal point. Tests between 1 and 2 mm away were one node off in any direction, and above 2 mm away the tests were one node away in two different coordinate directions.

To determine which parameters created an accurate focal point, a bar graph was created which gives the number of tests that resulted in exact matches between the focal point and the desired location for each parameter (Figure 75). Each color groups the different types of parameters together, so the blue graphs represent the different shapes, red is for the different number of elements in one transducer row, the green bars are the different numbers of possible rows, and purple represents the number of active transducers. The teal color for the desired location of the focal point is further delineated by its shade, where the light shade represents the focal points at the bottom height level (zn = 1), the medium shade is for the second height level halfway up the breast (zn = 2), and the dark shade is for the third height level (zn = 3). The gray bars on top of each value represent the number of studies with each parameter that did not result in exact focal point matches.

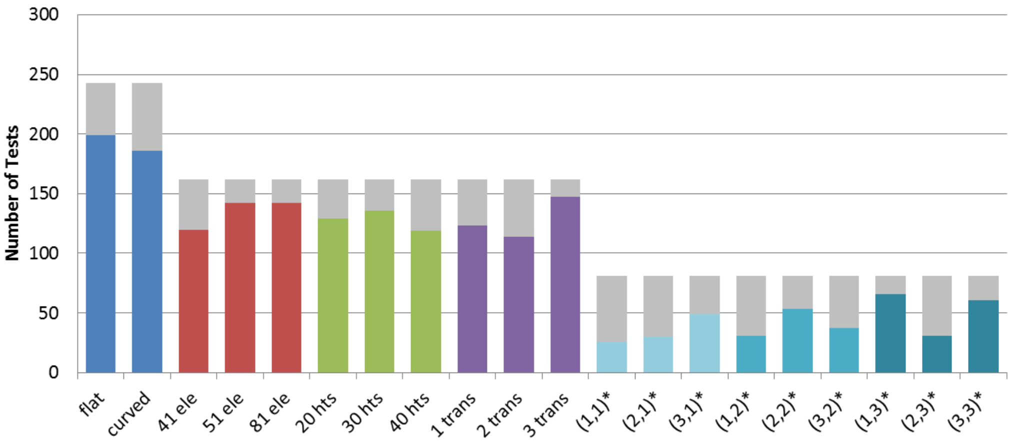

Figure 75 Number of trials which resulted in the focal point exactly coinciding with the desired location. Blue graphs are for the transducer shape, red graphs are for the number of elements in each transducer row, green graphs are for the number of transducer rows, purple graphs are for the number of active transducers, and teal graphs are for the location of the desired focal point. The gray bars on top of each value represent the number of studies with each parameter that did not result in exact focal point matches. *(xn,zn)

Most of the parameters achieved similar success in resulting in an accurate focal point. The transducer parameters which had the most successful trials were flat, 51 elements per row, 30 rows, and 3 transducers. The most accurate focal points were at the focal point location (1,3) which is in the top third of the breast and closest to the center, while (1,1) at the bottom third and closest to the center of the breast had the least successful trials. From this graph it is apparent that each transducer parameter individually has the potential to be acceptable for HIFU treatments, so later the combinations of parameters need to be examined for patient-specific treatments

Next, the heat generations created by each combination of these parameters are compared. Graphs of the maximum heat generation versus the number of active transducers are shown in Figure 76 – Figure 81. In all cases, an increase in the number of rows of elements resulted in an increase in the maximum heat generation. While examining these graphs, it is important to keep in mind that the y-scales are different for each plot so that the overall trend was easily apparent.

Figure 76 displays the curves for the flat transducer at the height level at the bottom third of the breast (zn = 1) for each of the xn-values. At xn = 1, where the focal point is closest to the center of the breast, the heat generation increases as the number of transducers increases for all combinations of number of elements and rows. However, for xn = 2, when there was 41 and 51 elements per row, three transducers caused a decrease in the maximum generation. Similarly for xn = 3, with 41 elements greater than two elements decreased the final heat generation.

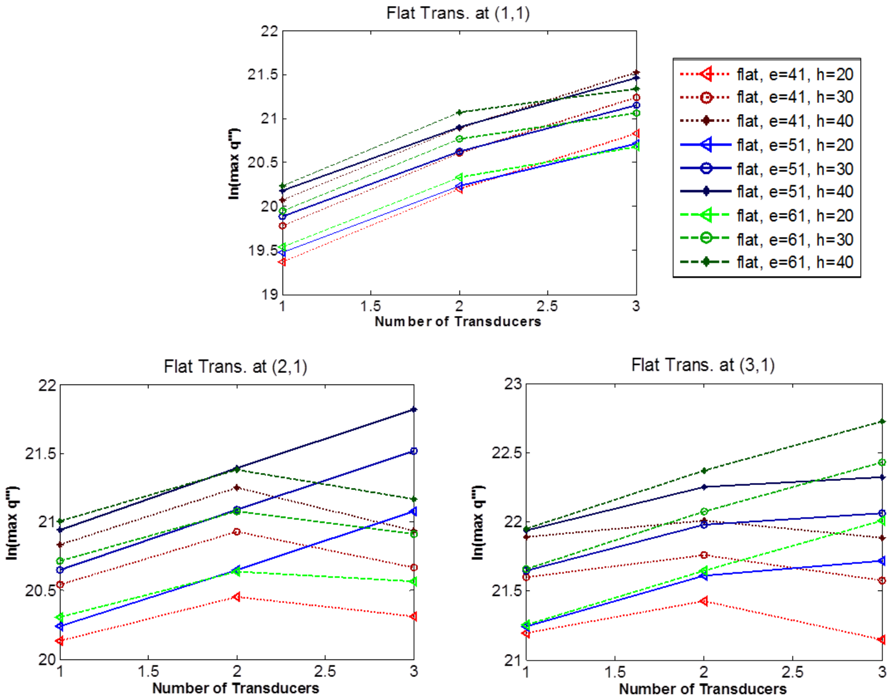

Figure 76 For the flat transducers focusing on the height zn = 1 (top: xn = 1; bottom left: xn = 2; bottom right: xn = 3). Plots of the natural log of the maximum heat generation versus the number of active transducers, for different numbers of elements and rows of elements.

Figure 77 displays the plots for a curved transducer at zn = 1. With the curved geometry, increasing the number of transducers never decreased the heat generation, but with xn = 2 and 3, with 61 elements per row there was only a slight increase between one and two transducers.

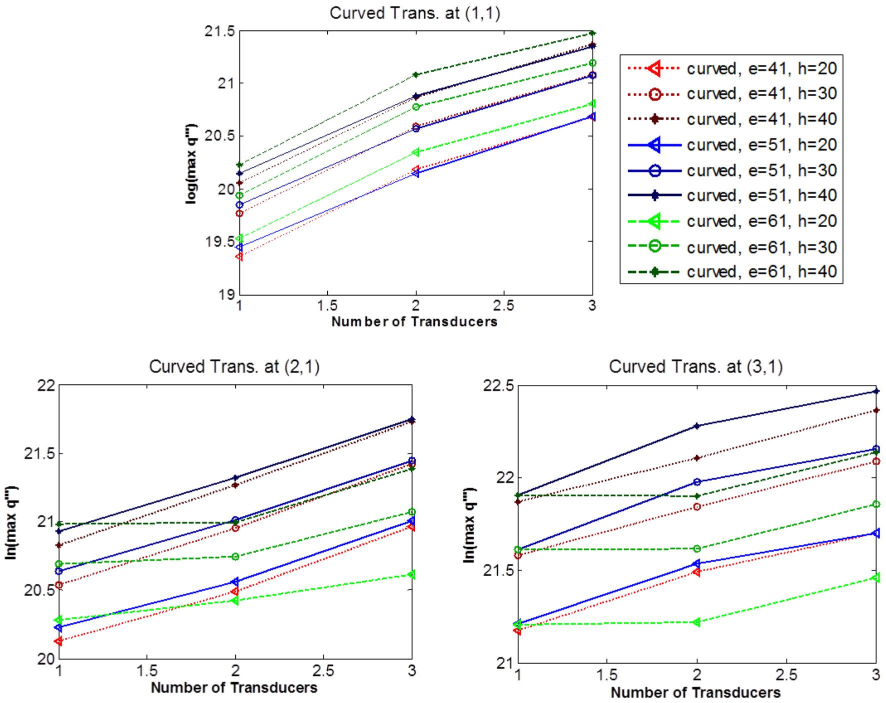

Figure 77 For the curved transducers focusing on the height zn = 1 (top: xn = 1; bottom left: xn = 2; bottom right: xn = 3). Plots of the natural log of the maximum heat generation versus the number of active transducers, for different numbers of elements and rows of elements.

Figure 78 shows these same graphs for the flat transducer at zn = 2. At xn = 2, 61 elements causes a decrease in the max q''' with more than two transducers activated, and at xn = 3 this is also true for 41 elements with 30 rows.

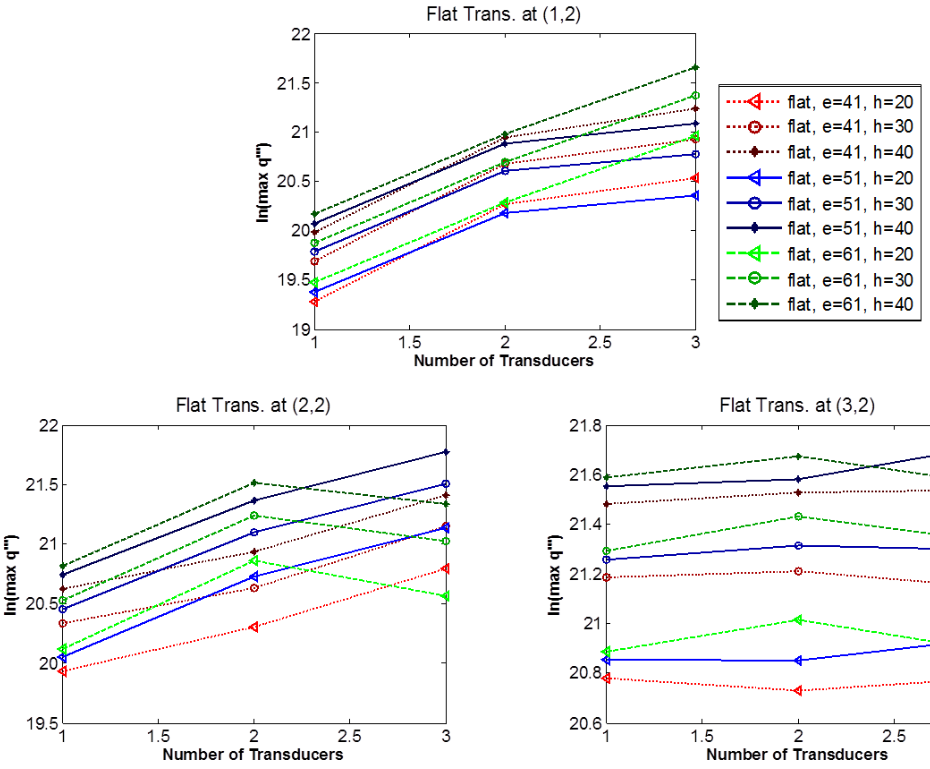

Figure 78 For the flat transducers focusing on the height zn = 2 (top: xn = 1; bottom left: xn = 2; bottom right: xn = 3). Plots of the natural log of the maximum heat generation versus the number of active transducers, for different numbers of elements and rows of elements.

Figure 79 shows the trends of maximum heat generation versus the number of active transducers for curved transducers focusing at zn = 2. The maximum heat generated increases with increasing numbers of transducers except when the focal point is at xn = 2 and 3 with 61 elements per row, where a third transducer decreases this value.

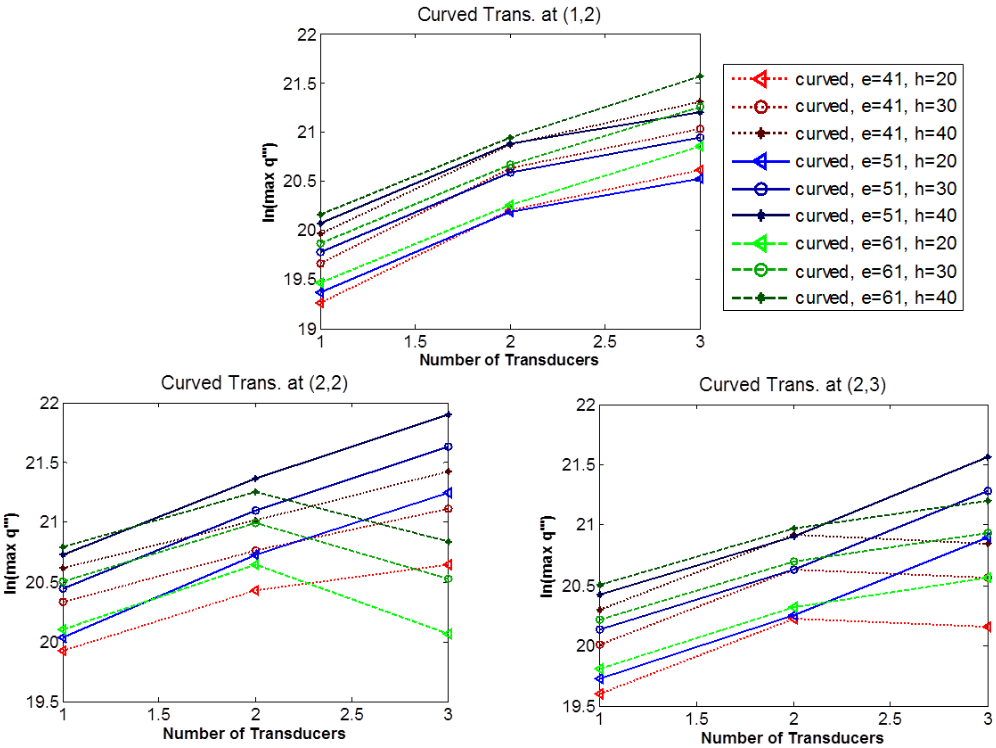

Figure 79 For the curved transducers focusing on the height zn = 2 (top: xn = 1; bottom left: xn = 2; bottom right: xn = 3). Plots of the natural log of the maximum heat generation versus the number of active transducers, for different numbers of elements and rows of elements.

Figure 80 depicts the graphs for flat transducers at zn = 3, in the top third of the breast. For this case, it is 51 elements which causes a decrease in the heat generated with three transducers at xn = 2 and 3.

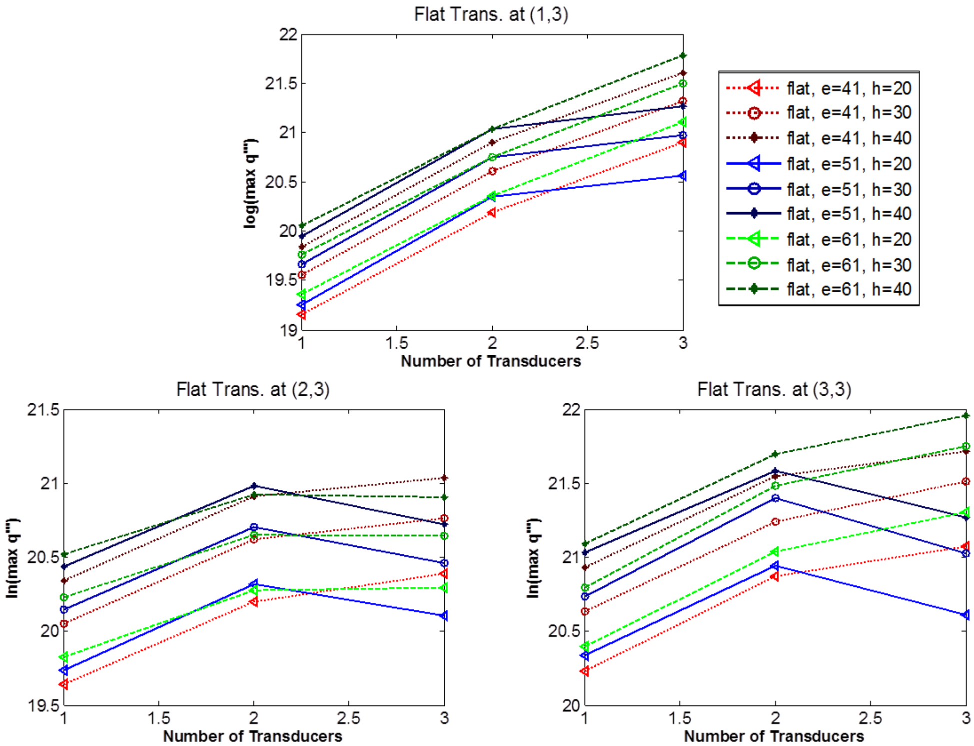

Figure 80 For the flat transducers focusing on the height zn = 3 (top: xn = 1; bottom left: xn = 2; bottom right: xn = 3). Plots of the natural log of the maximum heat generation versus the number of active transducers, for different numbers of elements and rows of elements.

Figure 81 depicts the same graphs but for a curved transducer at zn = 3. The heat generation decreases when the number of active transducers is increased from 2 to 3 for xn = 2 with 41 elements per row, and xn = 3 just for the case with 20 rows of 30 elements.

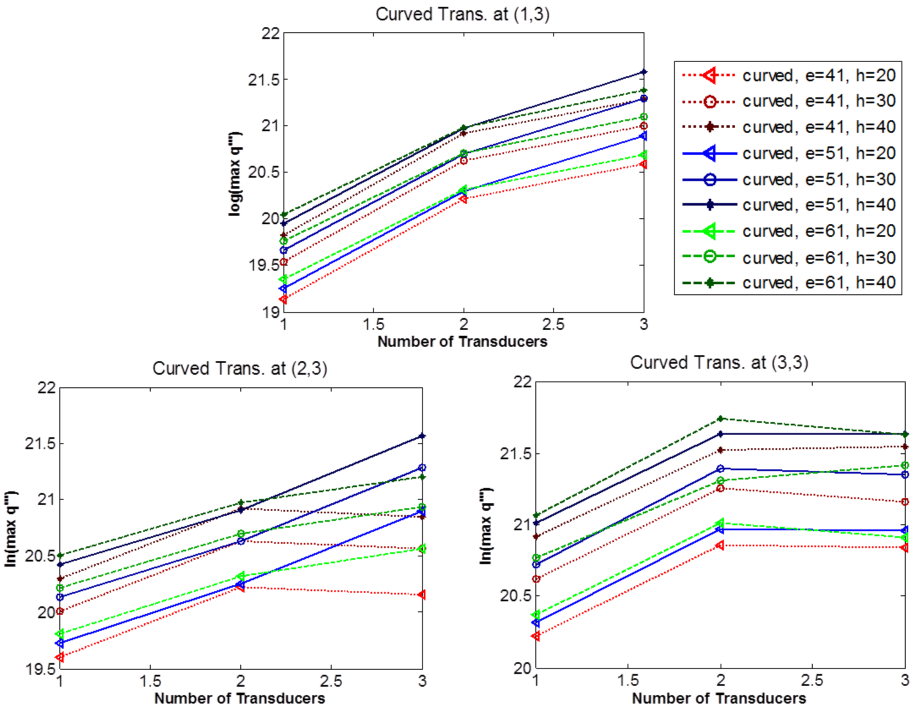

Figure 81 For the curved transducers focusing on the height zn = 3 (top: xn = 1; bottom left: xn = 2; bottom right: xn = 3). Plots of the natural log of the maximum heat generation versus the number of active transducers, for different numbers of elements and rows of elements.

The outcome of these parameter studies shows that increasing the number of transducers is most beneficial for increasing the maximum heat generation when the desired focal point is close to the center of the breast (xn = 1). This is reasonable because the tumor is further from the transducer when it is closer to the breast's center, so more transducers are needed to reach the same heat generation. For locations towards the edge of the breast, the number of elements in the row needs to be determined individually based on the exact location of the tumor. Also, with just one transducer the heat generation generally increased as the focal point moved closer to the edge of the breast.

The results are very similar for all cases close to the breast's center (xn = 1). Also, the magnitudes of the heats generated were usually very similar for the flat and curved transducers, but for zn = 1 and 3, the flat transducer was more effected by the decrease in heat generation with the inclusion of the third transducer. Also, as was noted at the beginning of this section, the maximum heat generation always increases with increasing number of rows of elements. The contour graphs of these studies show that the focal point has the exact same shape between graphs of two different numbers of rows, just with a change in magnitude.

Effect of Change in Acoustic Attenuation

The preceding heat generation results were generated prior to heating the tissue (at the first time step). The heat generation will change throughout the simulation because of the changes in the tissue's acoustic attenuation. To determine the importance of including the variability of this parameter, the heat generation contours are compared for two example cases. Figure 82 shows the first example case (transducer parameters: curved, 51 elements, 40 rows, at (1,1)), where Figure 82a is the heat generation contour prior to heating, and Figure 82b contains the same contours after the heating completes (when temperature reaches 100^{o}C, in 0.53 seconds). There is a degeneration of the focal point, so the highest magnitude is moving towards the transducer and there is a larger fringe area of high heat generation. In the x-y plane the elliptical shape of the focus has become a Y-shape. Also, the magnitude of the maximum q''' has decreased by almost 50%.

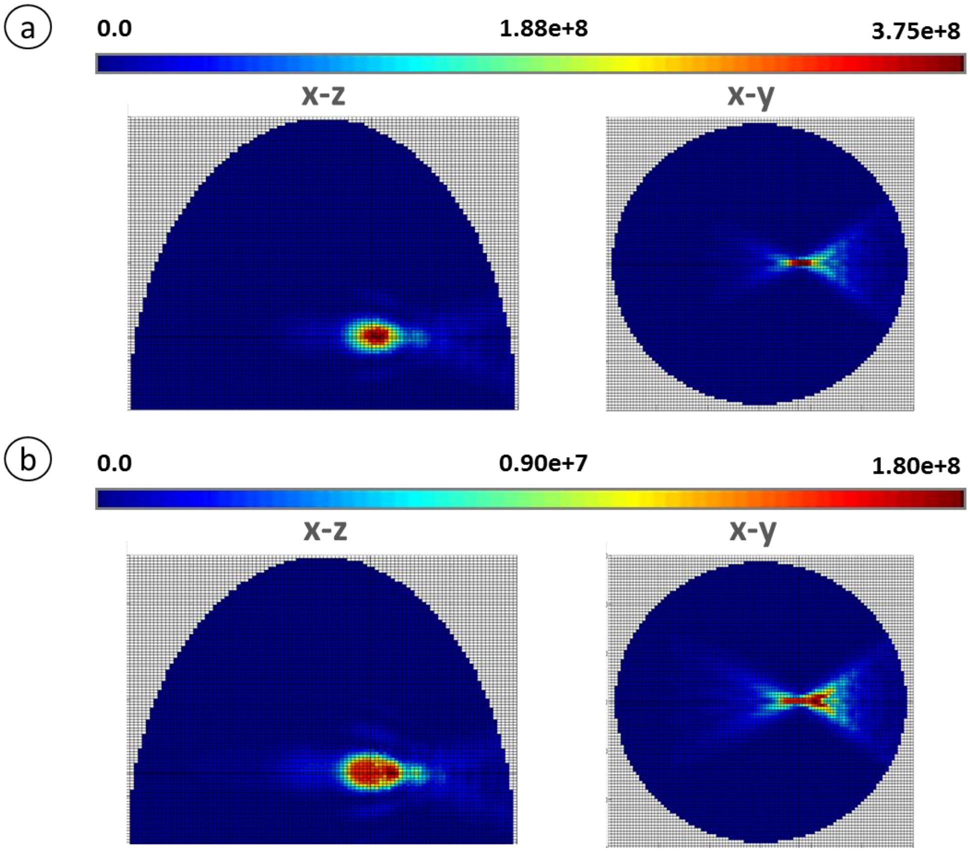

Figure 82 The maximum heat generation (W/m^3) contours in the x-z and x-y planes (a) prior to tissue heating, and (b) upon completion of heating when temperature has reached 100°C. (Transducer parameters: curved, 51 elements, 40 rows, at (1,1)).

In Figure 83, this same comparison is made for the same transducer parameter, except moving the focal point to the edge of the breast (transducer parameters: curved, 51 elements, 40 rows, at (3,1)). In contrast with the first case, the beginning and end of the heating cycle showed little change in the heat generation contours. This can be attributed to the higher initial heat generation (about one order of magnitude increase), so the temperature reached 100°C much quicker (only 0.06 seconds), therefore the changing acoustic attenuation of the tissue was not as significant. As was noted in the Focal Location Studies section, the heat generation increases as the focal point moves closer to the edge of the breast (and therefore closer to the transducer), so the heat generation will be more predictable throughout heating for those locations.

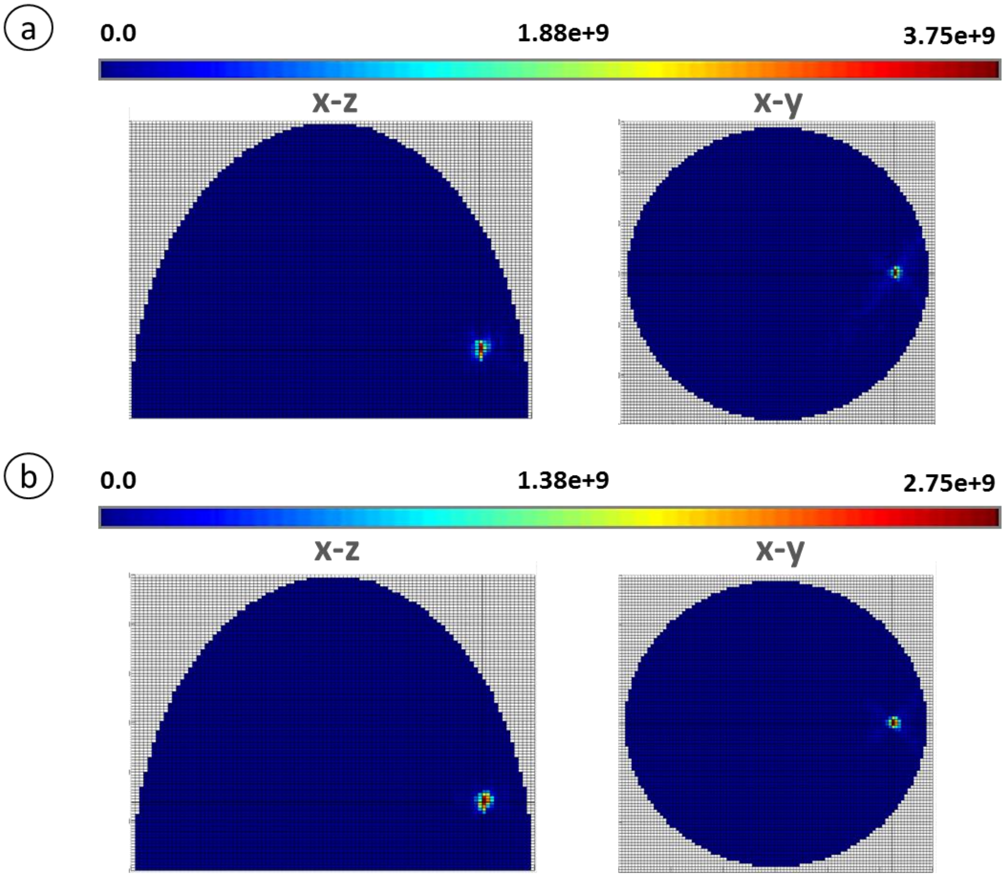

Figure 83 The maximum heat generation (W/m^3) contours in the x-z and x-y planes (a) prior to tissue heating, and (b) upon completion of heating when temperature has reached 100°C. (Transducer parameters: curved, 51 elements, 40 rows, at (3,1)).

Temperature and Necrosis Contours

This section examines how the temperature throughout the breast and the resulting necrosed tissue change from the different transducer parameters. The data from all necrosis studies are listed in Table 55 – Table 64 in Appendix D. The two representative cases used in the heat generation study (transducer parameters: flat, Q = 100 W, 41 elements/row, 40 rows, focused at (3,1) and (1,1)) are used to show an example of the resulting temperature and necrosis contours. The first case, focused at (3,1) is shown in Figure 84 (temperature) and Figure 85 (necrosis). As would be expected, the location of the highest temperature coincides with the location of the necrosis. Also, both coincide with the location of the maximum heat generation (as seen in Figure 72 and Figure 83). This agrees with the literature on the expected outcome of a HIFU treatment, where a small volume of tissue is necrosed at the focal point (71.3 mm^3, which has an equivalent radius of 2.58 mm). The temperature in the majority of the breast was kept to around 40^{o}C, which is below the pain threshold of 45^{o}C [94] [36].

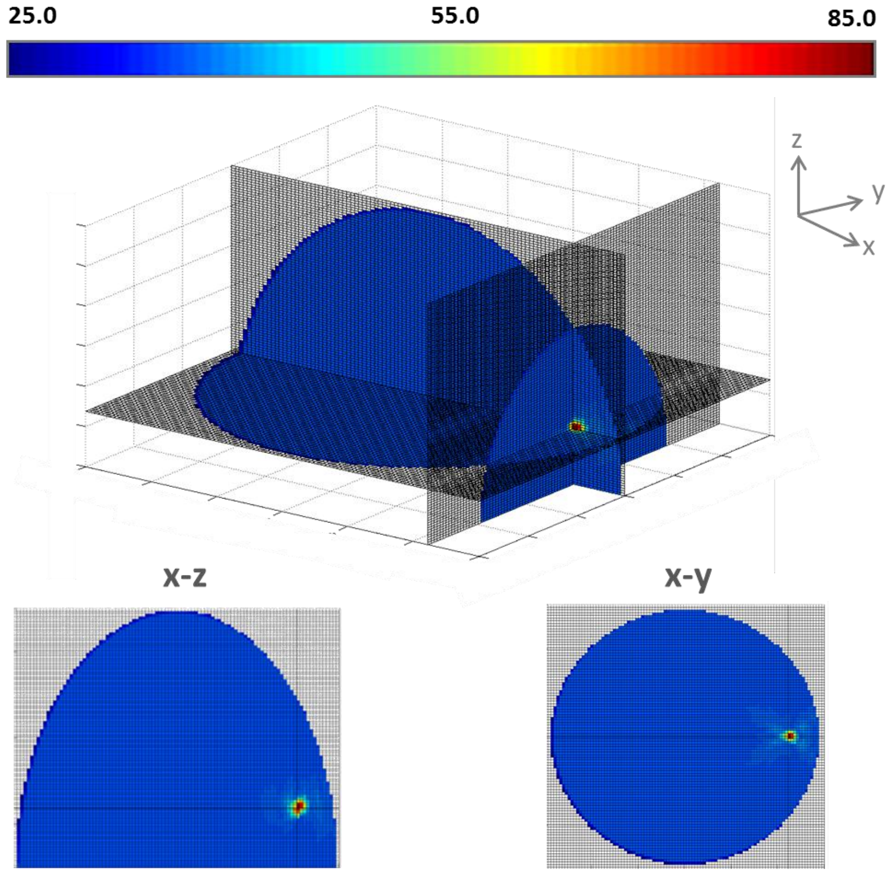

Figure 84 Contour plot of the temperature (^{o}C) in the sliced isometric view (top), x-z plane (bottom left), and x-y plane (bottom right). (Transducer parameters: flat, Q = 100 W, 41 elements/row, 40 rows, focused at (3,1)).

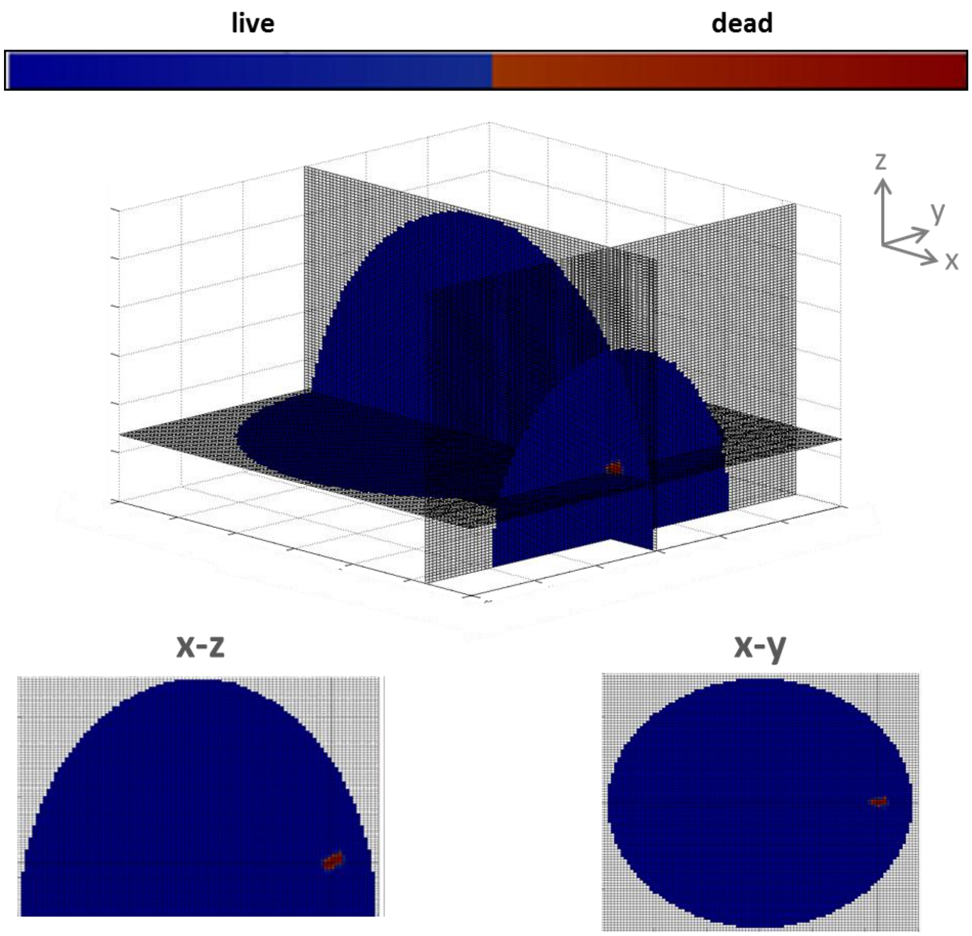

Figure 85 Contour plot of the necrosed cells in the sliced isometric view (top), x-z plane (bottom left), and x-y plane (bottom right). (Transducer parameters: flat, Q = 100 W, 41 elements/row, 40 rows, focused at (3,1)).

However, the second representative case in Figure 86 for temperature and Figure 87 for necrosis shows a less expected result of the treatment. When the focal point moves towards the center of the breast at (1,1), the highest temperatures are spread from the focal point, creating a larger lesion with a less-predictable shape. When it is compared with the heat generation prior to heating (Figure 73 and Figure 82a) the necrosed tissue falls outside of just the highest heat generation locations, but the heat generation contour at the end of heating (Figure 82b) matches more closely. This shows that the normal shapes of necrosis for HIFU treatments are less valid when acoustic attenuation has changed significantly from its initial value.

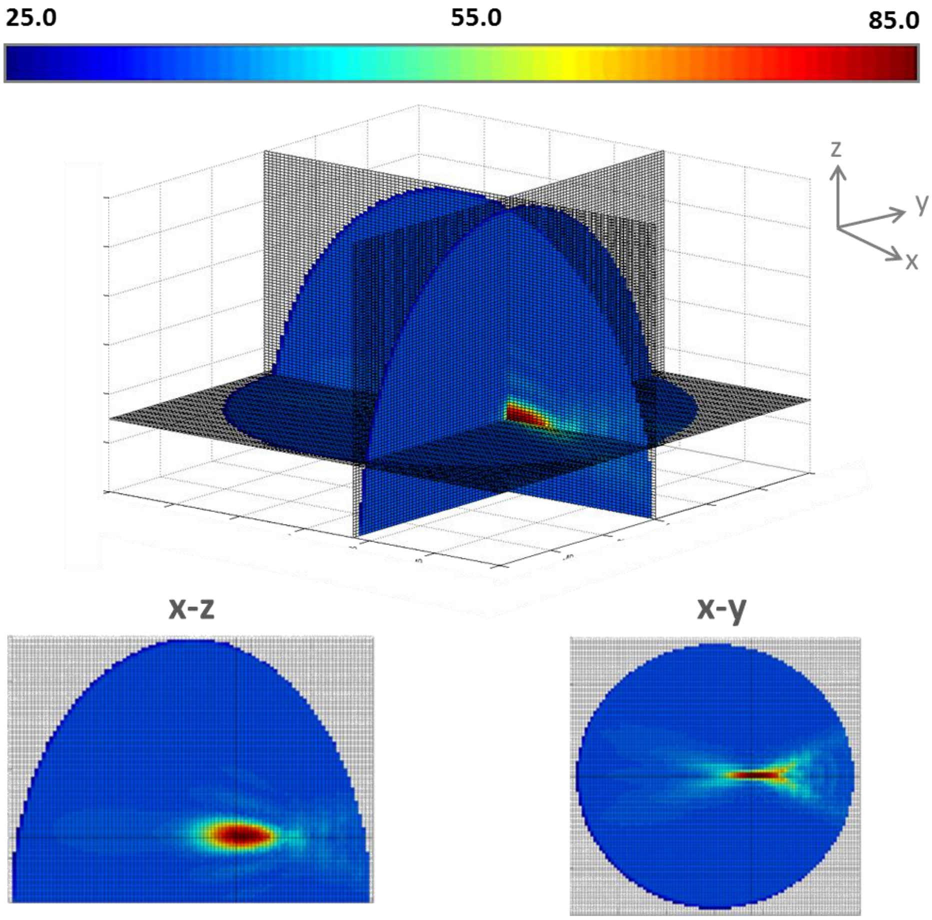

Figure 86 Contour plot of the temperature (°C) in the sliced isometric view (top), x-z plane (bottom left), and x-y plane (bottom right). (Transducer parameters: flat, Q = 100 W, 41 elements/row, 40 rows, focused at (1,1)).

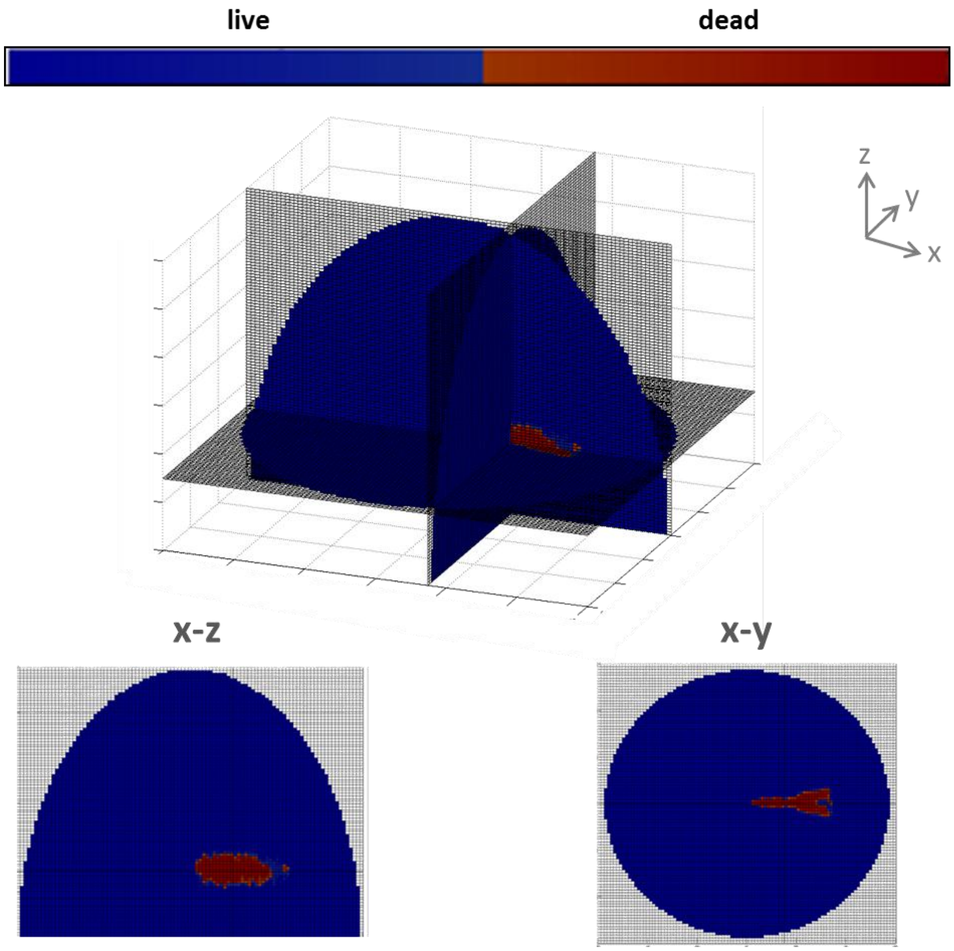

Figure 87 Contour plot of the necrosed cells in the sliced isometric view (top), x-z plane (bottom left), and x-y plane (bottom right). (Transducer parameters: flat, Q = 100 W, 41 elements/row, 40 rows, focused at (1,1)).

This section first examines the effect of the parameters of an individual transducer. Then, how the necrosed region changes by introducing more active transducers is shown.

Effect of Transducer Parameters on Necrosis

The volume of the necrosed region is an important outcome of the HIFU simulations. An equivalent radius is also used to describe the volumes in this section, defined by Equation 48

$$r_{eq} = \left(\frac{3V_{necr}}{4\pi}\right)^{1/3} \qquad \text{Equation 48}$$

where r_{eq} is the equivalent radius and V_{necr} is the necrosed volume. The resulting equivalent radius from different combinations of transducer parameters is explored. Figure 88 and Figure 89 display graphs of the necrosed equivalent radius versus the transducer power for one active transducer. For most graphs, the radius increases with decreasing number of elements. Also, for all graphs, as the focal point moves closer to the edge of the breast (from xn = 1 to 3), the necrosed volume decreases.

Figure 88 displays these plots for flat transducers at zn = 1 (a), zn = 2 (b), and zn = 3 (c) for different values of xn. For xn = 1, as the power increases, the radius decreases. This relationship is weaker for xn = 2, at the edge of the breast (xn = 3) there is no change in the equivalent necrosed radius when the power increases except at zn = 3. These relationships are similarly true for curved transducers, shown with the same graphs in Figure 89, except the negative slopes are flatter.

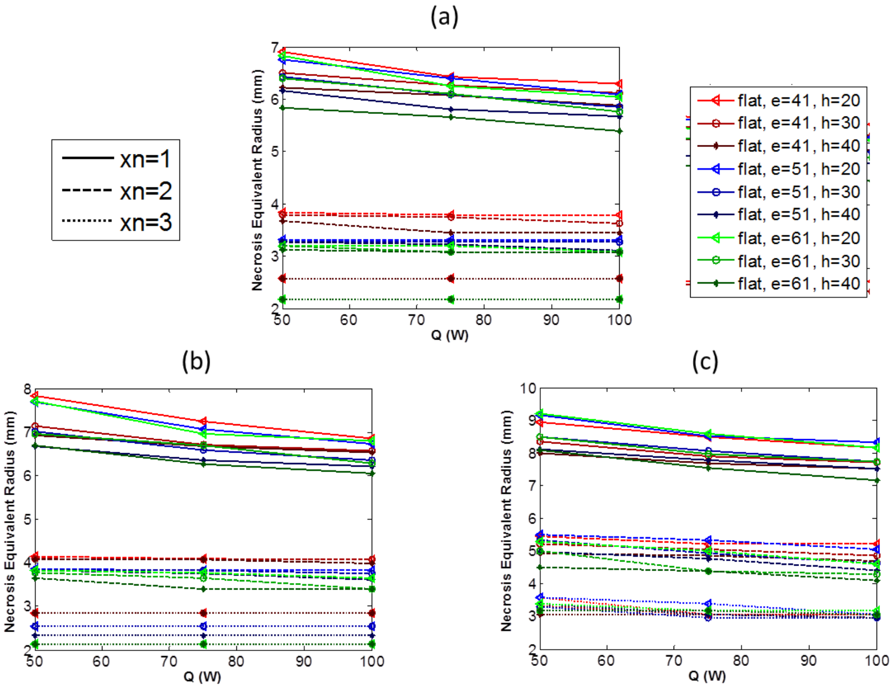

Figure 88 Necrosed equivalent radius versus transducer power for flat transducers focused at (a) zn=1, (b) zn=2, (c) zn=3 for different values of xn (distinguished by line type) and transducer parameters (distinguished by color).

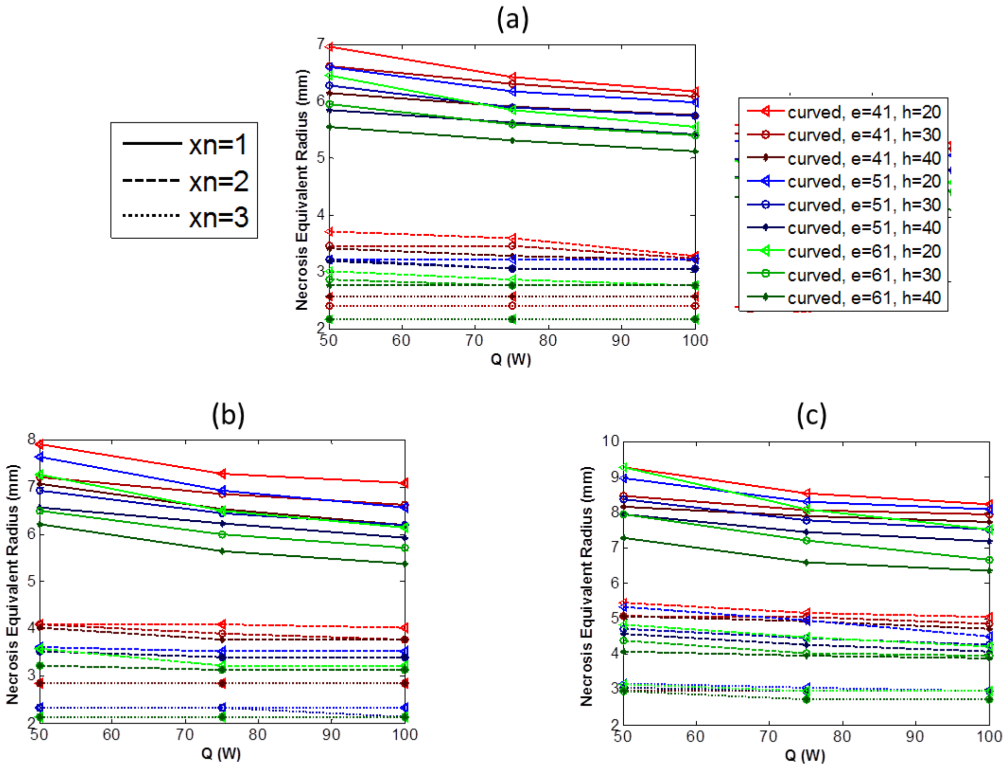

Figure 89 Necrosed equivalent radius versus transducer power for curved transducers focused at (a) zn=1, (b) zn=2, (c) zn=3 for different values of xn (distinguished by line type) and transducer parameters (distinguished by color).

As mentioned previously, the equivalent radius of the necrosed volume decreases towards the edge of the breast (and therefore closer to the transducer, towards xn = 3), which is in agreement with the example necrosed contours shown in Figure 85 and Figure 87. Also, in all cases, as the focus gets closer to the edge of the breast, the transducer power has less of an effect on the final necrosed volume.

Effect of the Number of Active Transduces on Necrosis

The necrosis contours when more than one transducer was activated was also tested. The same transducer parameters were tested with 1, 2, 3, and 4 active transducers all set to Q = 100 W. Also, the transducers were tested when the total power summed to 100 W, so there may be the powers [50 50 0 0] W, [33 33 0 33] W, or [25 25 25 25] W. These transducer tests were performed for the extreme cases for the focal point closest to the transducers (xn = 3, zn = 1) and furthest from the transducers (xn = 1, zn = 3).

Figure 90 shows the case of (3,1) for increasing numbers of transducers activated at 100 W (transducer parameters: flat, 41 elements, 40 rows). The shape of the focal point changes minimally with increasing numbers of transducers at the same power. The exact volume of the necrosed region and the heating times are displayed in Table 16. The necrosed volume is the most and the same for one and three active transducers (71.30 mm^3), and all four cases had the same heating time, just 0.06 seconds.

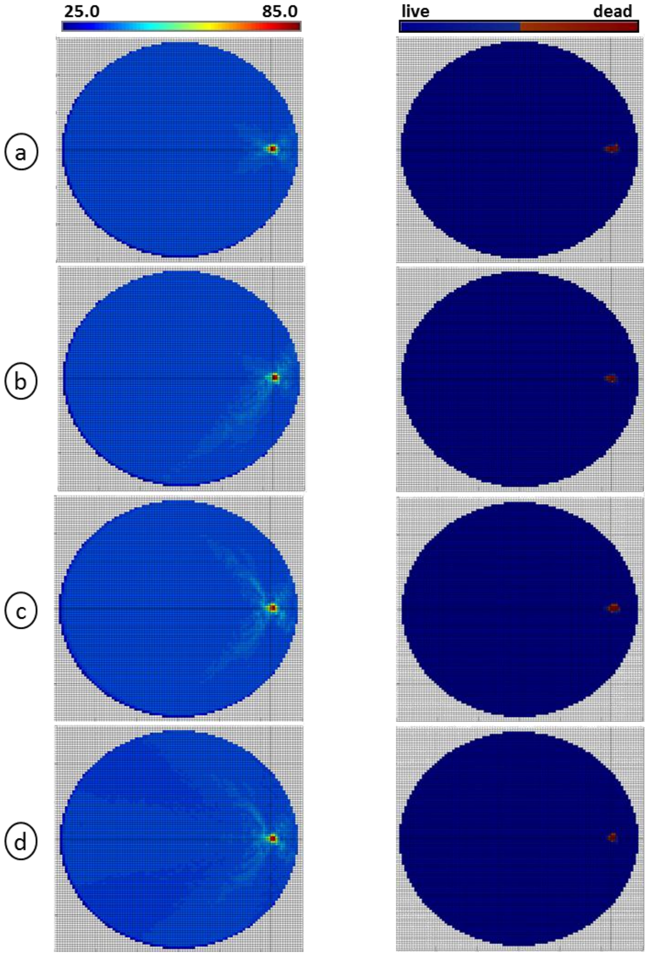

Figure 90 Temperature (left, °C) and necrosis (right) contours in the x-y plane for (a) one, (b) two, (c) three, and (d) four transducers activated to 100 W. (Transducer parameters: flat, 41 elements, 40 rows, (3,1)).

Table 16 The necrosed volume and heating time for different numbers of active transducers at (3,1).

Location	# of Trans	Q (W)	V_{necr} (mm^3)	Heat Time (s)
(3,1)	1	[100 0 0 0]	**71.30**	**0.06**
	2	[100 100 0 0]	**55.17**	**0.06**
	3	[100 100 0 100]	**71.30**	**0.06**
	4	[100 100 100 100]	**42.72**	**0.06**

Figure 91 shows the temperature and necrosis contours for increasing numbers of transducers which sum to 100 W (Figure 91a is the same as Figure 90a). There is a slight difference in the temperature contours between this decreased transducer power and having all transducers set to 100W, but the necrosis contours look the same. The volume of the necrosis and the heating time are displayed in Table 17. The necrosed volumes are the same for each number of active transducers as in Table 16, but as the individual transducer power decreases, the heating time increases.

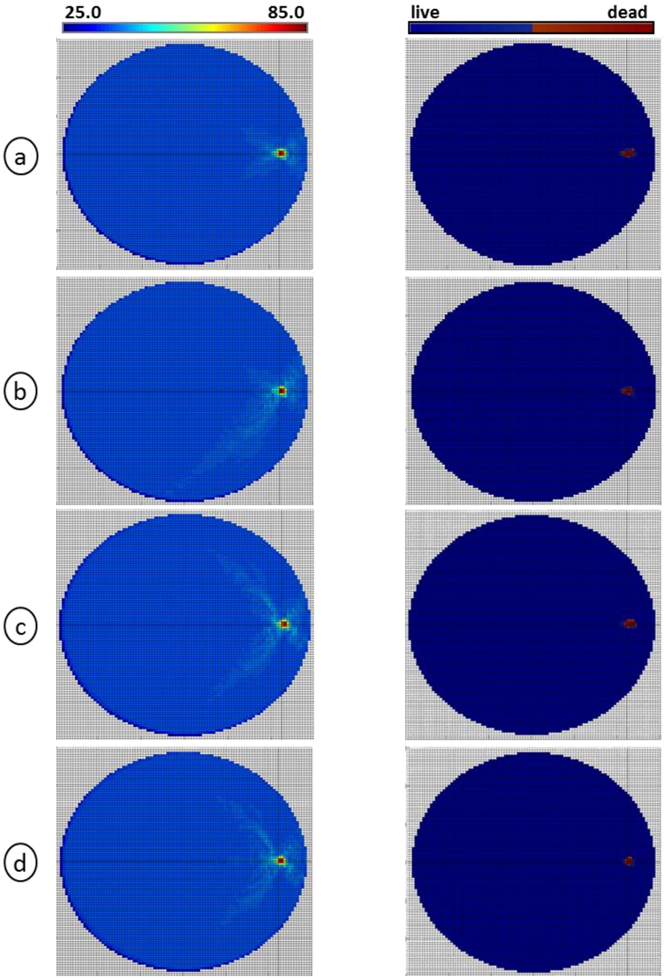

Figure 91 Temperature (left, °C) and necrosis (right) contours in the x-y plane for (a) one, (b) two, (c) three, and (d) four transducers activated, powers summing to 100 W. (Transducer parameters: flat, 41 elements, 40 rows, (3,1)).

Table 17 The necrosed volume and heating time for different numbers of active transducers at (3,1).

Location	# of Trans	Q (W)	V_{necr} (mm^3)	Heat Time (s)
(3,1)	1	[100 0 0 0]	**71.30**	**0.06**
	2	[50 50 0 0]	**55.17**	**0.11**
	3	[33 33 0 33]	**71.30**	**0.19**
	4	[25 25 25 25]	**42.72**	**0.22**

The case with the same transducer parameters, but at xn = 1 and zn = 3, there is a much larger initial volume. Figure 92 shows the temperature and necrosis contours with increasing numbers of transducers all activated to 100 W. Contrasting to the previous case, there is now a very big difference in the necrosis contours. The necrosed volume decreases when more than one transducer is activated, but the necrosis is more focused towards the center of the focal point. Table 18 displays the necrosed volumes and heating times of these simulations. Three transducers takes the least time to heat but also results in the least volume necrosed.

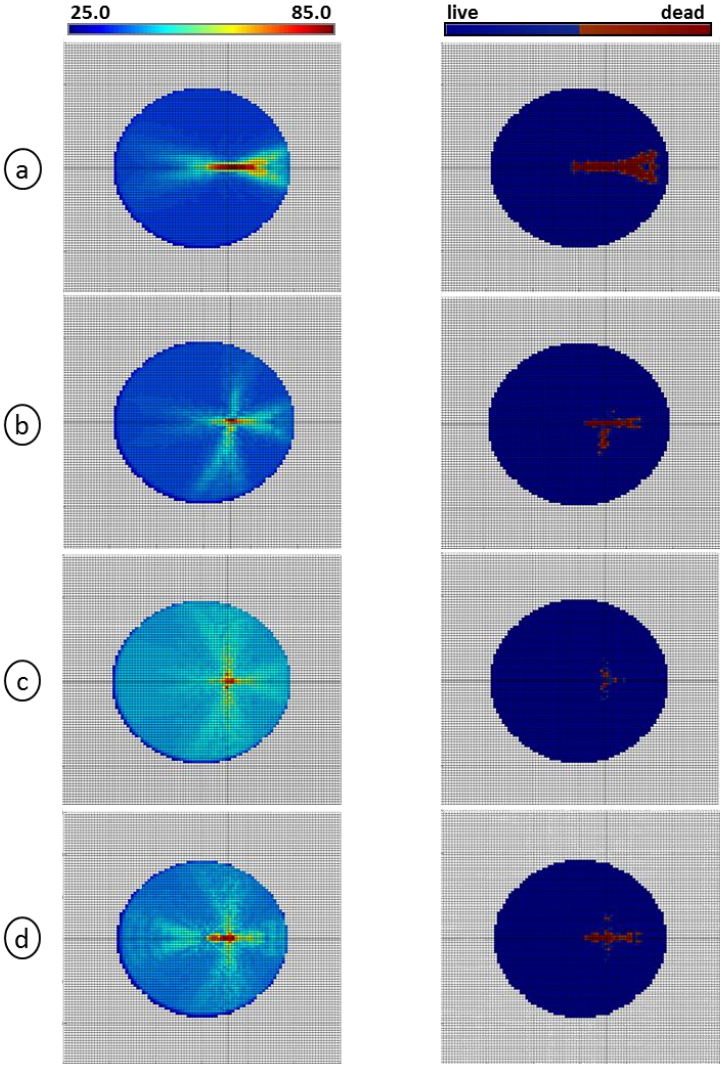

Figure 92 Temperature (left, °C) and necrosis (right) contours in the x-y plane for (a) one, (b) two, (c) three, and (d) four transducers activated to 100 W. (Transducer parameters: flat, 41 elements, 40 rows, (1,3)).

Table 18 The necrosed volume and heating time for different numbers of active transducers at (1,3).

Location	# of Trans	Q (W)	V_{necr} (mm^3)	Heat Time (s)
(1,3)	1	[100 0 0 0]	**1779**	**0.71**
	2	[100 100 0 0]	**561.8**	**0.29**
	3	[100 100 0 100]	**135.0**	**0.11**
	4	[100 100 100 100]	**652.6**	**0.15**

Figure 93 shows the temperature and necrosis contours for multiple transducers summing to 100 W. The necrosed volumes are larger than when all transducer were activated to 100 W, but one focused region of necrosis is not created. Table 19 displays the necrosed volumes and heating times of these simulations. The case with four transducers activated to 25 W each takes 1 second to reach 100^{o}C, but also results in the largest necrosed volume.

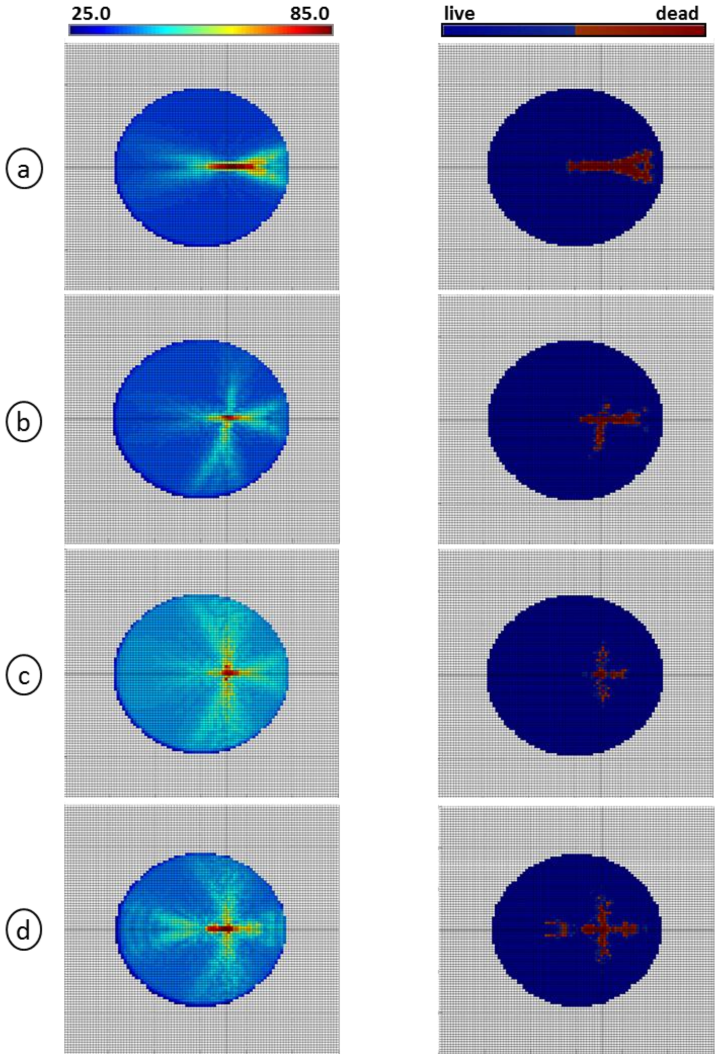

Figure 93 Temperature (left, °C) and necrosis (right) contours in the x-y plane for (a) one, (b) two, (c) three, and (d) four transducers activated, powers summing to 100 W. (Transducer parameters: flat, 41 elements, 40 rows, (1,3)).

Table 19 The necrosed volume and heating time for different numbers of active transducers at (1,3).

Location	# of Trans	Q (W)	V_{necr} (mm^3)	Heat Time (s)
(1,3)	1	[100 0 0 0]	**1779**	**0.71**
	2	[50 50 0 0]	**930.2**	**0.69**
	3	[33 33 0 33]	**498.5**	**0.53**
	4	[25 25 25 25]	**1781**	**1.00**

Discussion of Breast Studies Results

As was previously-established, there is a clear connection between the heat generation created, the resulting temperature contours, and finally the necrosed tissue in the breast. Figure 85 showed a small lesion with the predictable ellipsoidal shape known for HIFU. A larger lesion would be desirable to decrease the high treatment times of the multiple HIFU sonications which are needed for the smaller ablated volumes. Figure 87 showed how having the focal location at a distance further from the transducer achieves this larger volume with the tested transducer parameters, but it must also be noted that the necrosis contour was not a predictable shape. This is mainly attributed to the change in the heat generations as is dictated by the dependence of the acoustic attenuation on the thermal dose experienced by the tissue.

The first case described (at (3,1)) had a maximum heat generation which was almost a full order of magnitude greater than the maximum heat generation in the second case (at (1,1)), which resulted in a larger lesion. The negative relationship between the necrosed volume and the maximum heat generation is shown in Figure 94.

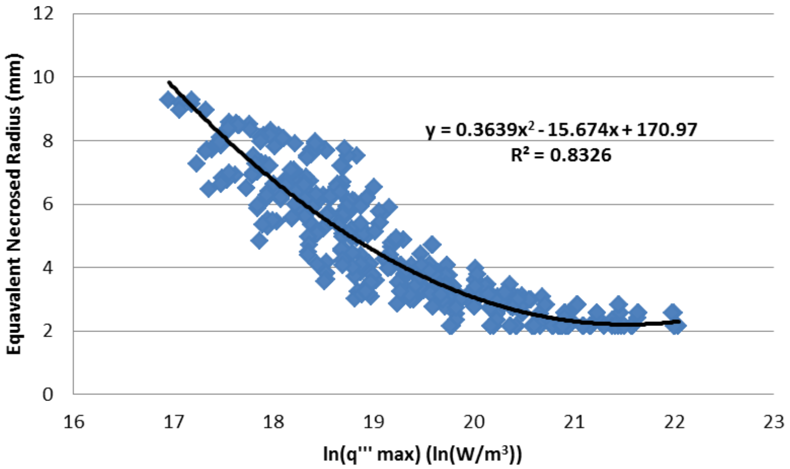

Figure 94 Graph of the equivalent necrosed radius versus the natural log of the maximum heat generation for single transducer cases. The equation of the line of best fit and its R^2 value are given.

A lower heat generation will result in a greater heating time before 100°C is reached. This is an important factor in creating the larger necrosed volumes with the lower heat generations, however it must also be minimized to decrease treatment time.

The difference between the heat generation before and after the heating cycle was proven through Figure 82, which showed degeneration of the focal point. Figure 87 shows the effect of this on the shape of the necrosis, where there is no longer a well-defined volume of dead cells. This proves that it is very important to include the dynamic definition of acoustic attenuation in a HIFU simulation so that accurate treatment planning can occur. Shorter heating times were shown to minimalize this effect, so manipulating the transducer parameters to allow for shorter heating times for the larger lesions will be necessary for patient treatments.

The effect of the individual transducer parameters on the final necrosed volume was also examined. The input transducer power had a much greater effect on the amount of tissue ablated if the desired focal point was closer to the center of the breast – for most cases it had no effect when the focus was at the points closest to the transducer, xn = 3. The relationship between the necrosed volume and the x-coordinate (in mm with the origin at the breast center, not xn) is shown in Figure 95. As was earlier described, the necrosed volume generally decreases as the focal point moves towards the edge of the breast and the transducer (breast radius x = 60 mm and transducer edge at x = 65mm).

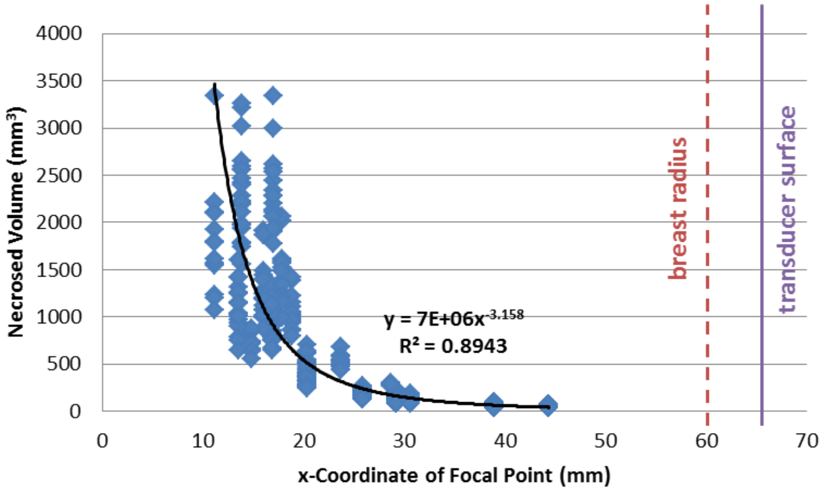

Figure 95 Graph of the necrosed volume versus the x-coordinate of the focal point. The equation of the line of best fit and its R^2 value are given. The breast radius is shown at x = 65 mm, and the transducer surface is shown at x = 65 mm.

The cases closer to the breast's center had a higher necrosed volume with 50 W when compared with an input power of 100 W. However, this will also increase the treatment time. The relationship between the transducer power and the heating time for different combinations of transducer parameters is shown in Figure 96. In all cases, the heating time decreased with increasing transducer power. Also, each set of transducer parameters decreased proportionally to each other because none of the lines were intersecting.[7]

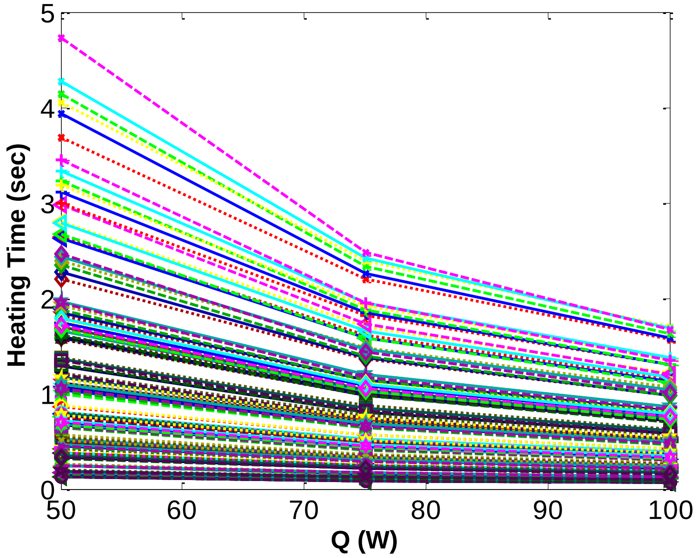

Figure 96 Heating time versus transducer power for different series of transducer shape, number of elements per row, and the number of rows. Graphs showing individual parameters displayed in Figure 128 and Figure 129 of Appendix E.

The inclusion of more active transducers shortened the long geometry in the x-y plane of the necrosed tissue for focal points close to the breast center (Figure 92 and Figure 93). The temperature contours showed a more focused area of the maximum temperature, especially with three active transducers, but the final necrosis shape was still a cross-like geometry. This is showing that the tissue remained at the lower temperature for a sufficient period of time to cause cell death, so it may be beneficial to halt the ultrasound heating prior to the 100^{o}C maximum has been achieved.

Another method which was discussed in previous literature to increase the necrosed volume is with multiple focal points used for each trial. This was tested

---

[7] The legend is not provided because the focus of this graph is the overall trend. For the effect of the transducer power on the equivalent necrosed radius on individual transducer parameters, see graphs in Figure 128 and Figure 129 of Appendix E.

with three or four transducers activated, each focusing on a different point. The three geometries tested are shown in Figure 97, where a focal point configuration with three transducers (a), and two different configurations with four active transducers (b and c) are tested. Transducer 1 focuses on the given (xn,zn) focal point.

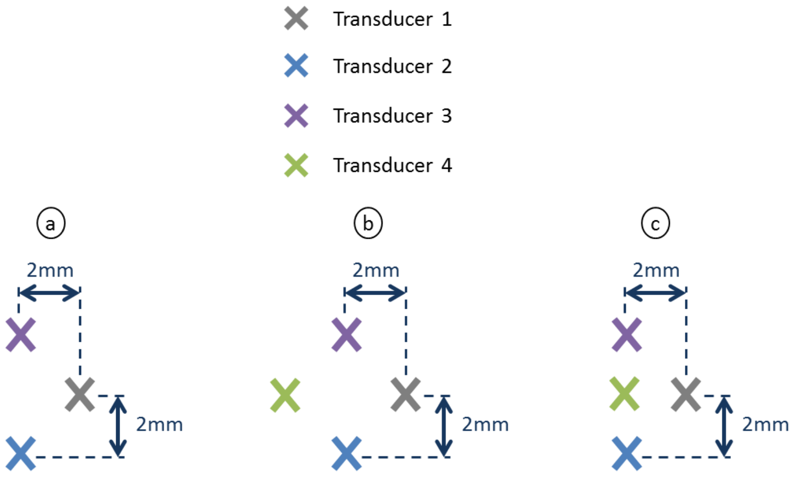

Figure 97 Focal point configurations for tests with multiple focal points for (a) three transducers, (b) four transducers spaced evenly, or (c) four transducers in t-shape. Transducer 1 is focusing on the given (xn,zn) value.

These configurations were tested for the focal points (1,1) and (3,1) to determine effect for a large and small necrosed volume with one transducer, respectively. The transducer power was set to either every transducer at 100 W, or all transducers sum to 100 W. For a curved transducer with 51 elements and 40 rows, the final necrosed volumes and heating times are computed for each configuration. Table 20 compares these values for the different focal point configurations and each power. The largest necrosed volume was created by configuration (c) for the initial focal point (1,1), but for the smaller focal point at (3,1) the different configurations made no difference in the necrosed volume other than when compared to the coinciding focal points. This occurs because the only transducer which changes between the three configurations is transducer 4, which is too far away from the focal point at (3,1) to cause tissue ablation. Mainly, the different focal point locations increased the necrosed volume, except for location (1,1) when all transducers were set to 100 W. This decrease in necrosed volume could be attributed to the ultrasound waves of one transducer causing destructive interference at the focal point of another transducer.

Table 20 The final necrosed volume and heating time for different configurations of multiple focal points. (Transducer parameters: curved, 51 elements, 40 rows).

Location	Q (W)	Focal Point Configuration	V_{necr} (mm^3)	Heat Time (s)
(1,1)	[100 100 0 100]	coinciding	**244.92**	**0.16**
	[100 100 0 100]	(a)	**563.45**	**0.23**
	[33 33 0 33]	coinciding	**630.12**	**0.74**
	[33 33 0 33]	(a)	**1203.59**	**1.01**
	[100 100 100 100]	coinciding	**425.67**	**0.16**
	[100 100 100 100]	(b)	**301.27**	**0.13**
	[100 100 100 100]	(c)	**371.59**	**0.16**
	[25 25 25 25]	coinciding	**1884.33**	**1.41**
	[25 25 25 25]	(b)	**2176.23**	**1.46**
	[25 25 25 25]	(c)	**2187.85**	**1.48**
(3,1)	[100 100 0 100]	coinciding	**27.56**	**0.04**
	[100 100 0 100]	(a)	**42.72**	**0.06**
	[33 33 0 33]	coinciding	**27.56**	**0.11**
	[33 33 0 33]	(a)	**42.72**	**0.18**
	[100 100 100 100]	coinciding	**27.56**	**0.03**
	[100 100 100 100]	(b)	**42.72**	**0.05**
	[100 100 100 100]	(c)	**42.72**	**0.05**
	[25 25 25 25]	coinciding	**27.56**	**0.13**
	[25 25 25 25]	(b)	**42.72**	**0.21**
	[25 25 25 25]	(c)	**42.72**	**0.21**

Another consideration for the physician along with the necrosed volume and the treatment time is the input energy. The relationship between the input energy (power*time) and the necrosed volume is displayed in Figure 98. The graph is split up by number of rows of elements, and a quadratic equation fits well to the data (all

R^2 values around 0.96). Increasing the input energy also increases the necrosed volume, so this creates the tradeoff for the physician.

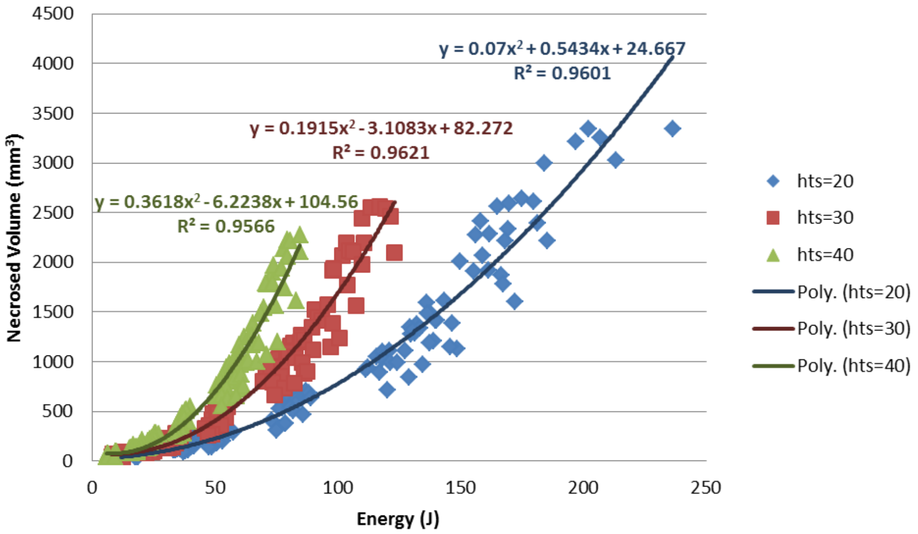

Figure 98 Graph of the necrosed volume versus the input energy, split by the number of transducer heights. The equation of the line of best fit for each number of rows of elements is displayed, along with its R^2 value.

The quadratic relationship between the necrosed volume and energy still holds true for multiple active transducers. A graph of the necrosed volume versus the input energy is shown in Figure 99 for the simulations for multiple transducers focusing at different points (results shown in Table 20). The R^2 value is almost 1, showing the very close fit between the energy and volume of these studies.

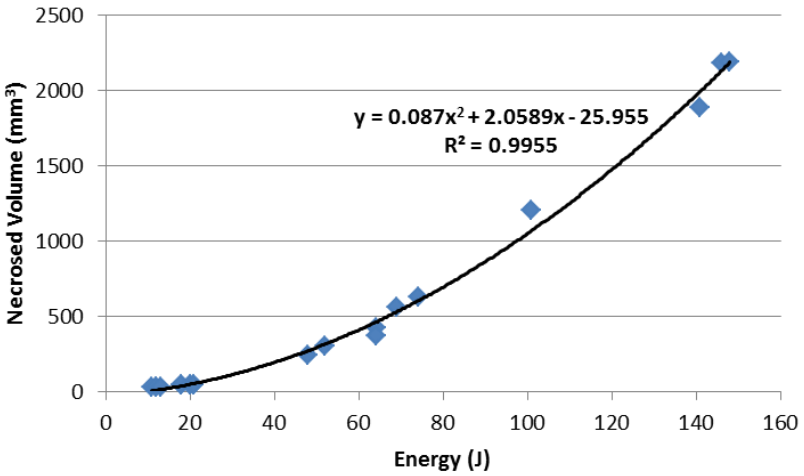

Figure 99 Graph of the necrosed volume versus the input energy for multiple active transducers, with the parameters described in Table 20. The equation of the line of best fit for each number of rows of elements is displayed, along with its R^2 value.

Device Design and Protocol Development for Breast Cancer

The final outcome of the simulations of ultrasound ablation for breast cancer is to determine the best device to perform this treatment, along with the accompanying patient-specific treatment planning protocols for the physician. This section will give the concept designed for the device, and then will detail how the physician can use this device.

Device Concept

The functional requirements for the breast cancer study are similar to the prostate study's requirements; however the different anatomy and nature of HIFU instead of planar ultrasound waves does change the needs of the delivery device. Table 21 displays the functional requirements for the breast cancer HIFU device.

Table 21 Functional requirements for US device to ablate breast cancer.

Functional Requirements
1) Necrosed tissue must reach tumor area.
2) Predictable necrosis geometry.
3) Can be used for most/ all patients.
4) Easy to use correctly.

The design parameters which are needed to satisfy these functional requirements are shown in Table 22. The second column specifies which FR is satisfied by each design parameter.

Table 22 Design parameters for US device to ablate breast cancer, including the functional requirements they each satisfy.

Design Parameters	FR satisfied
Creates distant focal point with minimal near-field heating.	**(1)**
Creates ellipsoidal lesion.	**(2)**
Creates lesion at desired focal point.	**(2)**
Adjustable for different patient sizes.	**(3)**
Can reach tumor at any point in the breast.	**(3)**
Includes symmetry.	**(4)**

The simulations showed that the first three and the fifth design parameters can be satisfied by many different combinations of transducer parameters. The physical embodiment of the device needs to include the fourth and sixth design parameters, along with a consideration for patient-comfort. An example of a design concept which includes the symmetry parameter was designed by Payne [97] and is shown in Figure 100. The breast lies inside of the hole, a cylindrical phased array surrounds it, and the patient's face is situated in the cushion at the right. The cylinder is submerged in a tank of water, and there is a cushion not shown which sits on top of the platform matching the contours of the patient's body. Problems with this design are that it does not accommodate for all patient sizes and it requires the patient lie in an uncomfortable position for a considerable period of time.

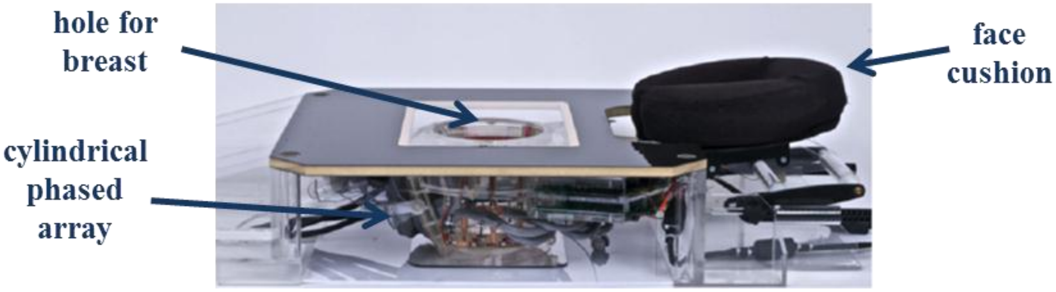

Figure 100 Device concept for breast cancer HIFU ablation [97].

The cylindrical array shown in Figure 100 is integrated into one embodiment of the device concept determined by this study. Segmented cylindrical transducer sections were tested in the simulations, but those results can similarly be used for a complete cylindrical array (multiple active transducers can be represented with more active elements in the angular direction). A concept sketch including this feature is shown in Figure 101. The transducer will be concentric to the breast axis, and there is a cuff between the transducer and the breast which fills with fluid to minimize the ultrasonic energy lost between the transducer to the tissue, cooling the breast exterior, and arresting the breast in place (it works similar to a blood pressure cuff). The transducer is secured to the patient with a chest strap, so they are able to be situated in their choice of a comfortable position during treatment. Shoulder straps may also be included for increased stability. This design is symmetrical for ease of physician use. However, although the chest strap can be adjusted, this design is limiting because the patient's breast must be smaller than the phased array.

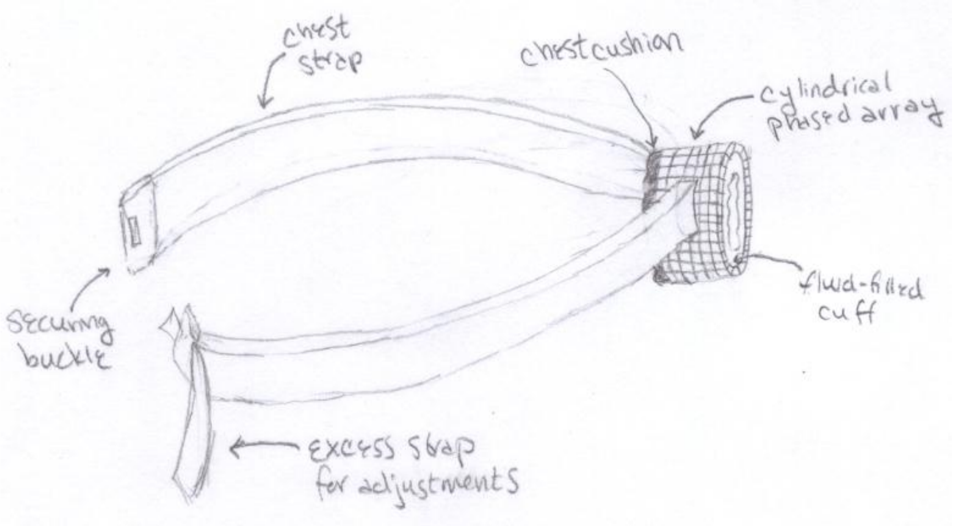

Figure 101 Device design concept for cylindrical phased array HIFU transducer for breast cancer.

The flat transducer design that was tested gave similar results to the curved transducer, and increases the flexibility for use with more patients. Figure 102 depicts this concept, showing four planar transducers which fit into a holder, attached to a chest strap similar to the one in the previous design. There are multiple chest straps with different-sized transducer holders, to accommodate any patient size without needing different transducers. There is also a fluid-filled cuff (not pictured) which can attach to the different transducer holders.

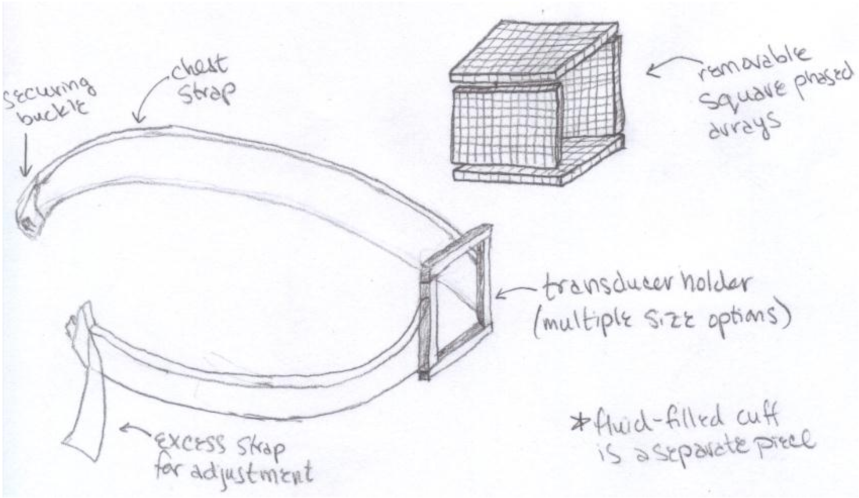

Figure 102 Device concept for flat phased array HIFU transducers for breast cancer. The four planar arrays are individually removable from the chest strap, and there are multiple transducer holder size options. The separate fluid-filled cuff is not pictured.

Physician Protocol

The goal of this research was to ablate breast tumors using ultrasound thermal therapy without the combination of chemotherapy or radiation treatments. At a minimum, the simulations need to demonstrate that these devices can ablate common sizes of breast cancer tumors. Data from the National Cancer Institute [98] is graphed in Figure 103. Three standard deviations away from the mean in both directions place the majority of the known tumor diameters between 10 and 29 mm (not shown in graph).

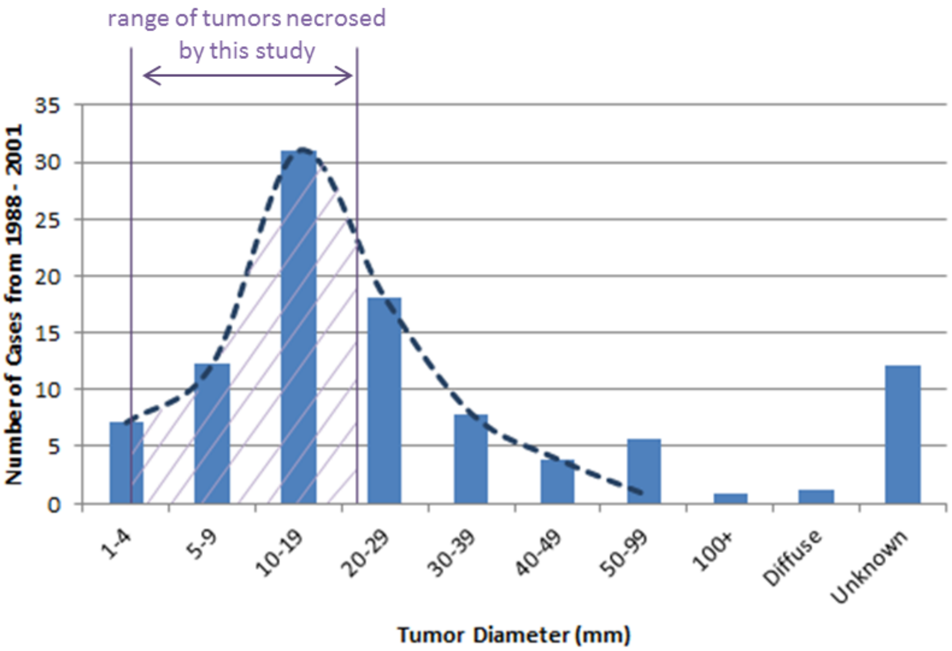

Figure 103 Prevalence of different tumor sizes from 1988 - 2001 [98]. Includes curve connecting data points, with the range of tumors which were proven to be able to be necrosed with this study filled in.

From the simulations performed, the equivalent radii calculated from the different sets of transducer parameters for one active transducer ranged between 2 – 9.5 mm with a mean of 4.5 mm (equivalent to 4 – 19 mm diameter, with a mean of 9 mm). This encompasses a large portion of the tumor sizes within the six standard deviation range of Figure 103 with just the one sonication (filled-in under the curve created by history data); however, the larger tumors generally had an unpredictable shape. The average ablated volume from the simulations is about 10% of the estimated mean tumor volume from Figure 103. This shows that if the larger radius lesions could be developed in a more predictable shape, the number of ultrasound sonications (and therefore the total treatment time) can be reduced. As was shown from the studies with multiple active transducers, the shape of this lesion can be manipulated to keep the focus closer to the desired point when the ultrasound is originated from multiple locations (multiple active transducers).

The treatment planning for HIFU is simpler than it is for the prostate studies because if the lesion diameter is known, then the focal point can be shifted to sufficiently overlap the previous region ablated until the total tumor is ablated. The transducers described in the previous section use electronic scanning to move the focal point, so after the physician secures the device onto the patient, it will not need to be moved until the treatment is complete. After further studies are performed, the correct set of transducer parameters will be determined which create an ellipsoidal lesion at any location. Once this is known, the physician only needs to input the tumor geometry into the device's software. This protocol is shown in a flowchart similar to the one which was given for the prostate treatment planning in Figure 104. The sonications' outputs will include multiple simultaneous focal points and any cooling time needed between sonications to avoid healthy tissue damage.

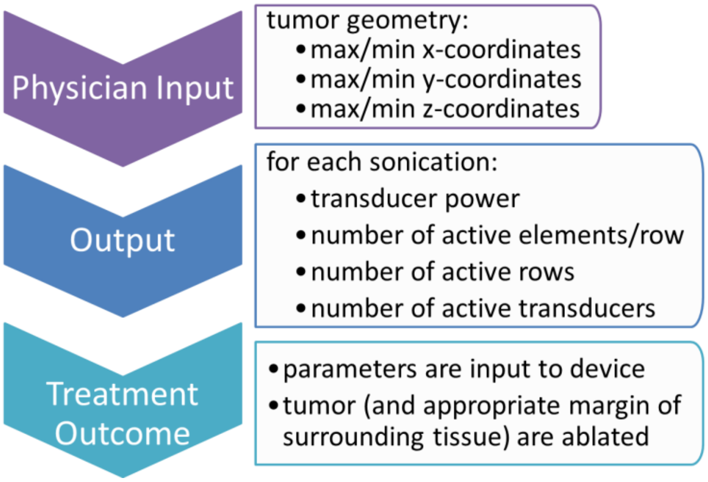

Figure 104 Flowchart showing the patient-specific protocol for physicians to use for prostate cancer treatment planning.

The change in acoustic attenuation caused high temperatures in locations outside of the focal point, which is hard to predict before treatments. Using these simulations will assist with realizing the impact of this changing tissue property, but implementing real-time temperature monitoring with ultrasound or MRI imaging will further better the clinical results.

Accuracy of Results from Breast Simulations with TID

Studies have shown that above 50^{o}C, the TID tissue model is no longer accurate [28] [99]. HIFU causes cell necrosis solely with temperatures above this value because the time of each sonication is too short for the lower temperatures to be effective. The Arrhenius model can be used for these higher temperatures, but the parameters specific to the type of cells studied must be known because there is a significant difference between the parameters of different cell types [14].

As previously-stated, there are few studies which have performed experiments on thermal therapy for breast cancer cells, and the Arrhenius parameters for these results were not present. To accurately model the HIFU simulations for breast cancer in the future, the next step of this study was to determine the Arrhenius parameters for the thermal damage of breast cancer cells. Those results can then be input back into the simulations performed here, which will improve treatment planning for thermal therapy.

Chapter 6: Developing Thermal Damage Models for Breast Cancer Ablation

To determine the necrosed regions in future breast US thermal therapy simulation studies, the thermal damage correlations must be experimentally determined. As was shown in Chapter 3, this dosage can be determined through *in vitro* experimentation with thermal therapy.

This study experiments with MCF-7 and T-47D breast cancer cell lines, which are two of the most commons cell lines used to accurately model breast cancer [100] [101]. They are hormone-dependent invasive ductal carcinomas, and originate from a metastic pleural effusion of tissue [100] [101]. Also, they are estrogen receptive cell lines, and estrogen can cause cancer (although the reason it does is not known) [100] [101].

These cells lines were tested to determine the Arrhenius parameters associated describing the thermal dose for their cell death. To ensure an even, quick heating of the cells, a monolayer of cells was plated on a slide, which was placed on top of a custom-designed heater. Different time and temperature combinations were tested ranging from 50^{o}C – 60^{o}C to calculate the parameters. The methods and results of this study are presented in this chapter.

Methods

The methods used to develop the thermal damage model include creating a custom heater setup, validating its ability to heat cells evenly and consistently, and following the specific protocols for these thermal therapy cell studies. First, the heater design considerations are explained, then the thermal therapy testing procedures are detailed, an explanation of the tests which were performed is given, the test setup validation is discussed, and finally the methods used for data analysis are provided.

Heater Setup

The complete heater setup comprised of an original heater assembly, three treatment slides within the heater assembly, a temperature controller, and a data acquisition (DAQ) instrument which connects to a computer to record the temperature measurements (Figure 105). The heater's power cord is connected to the controller. There are nine thermocouples assessing the system temperature at different locations: one connects to the controller and the other eight are in various positions on the heater assembly. The exact location of each thermocouple is explained in further detail later in this section. This section also describes each of these components.

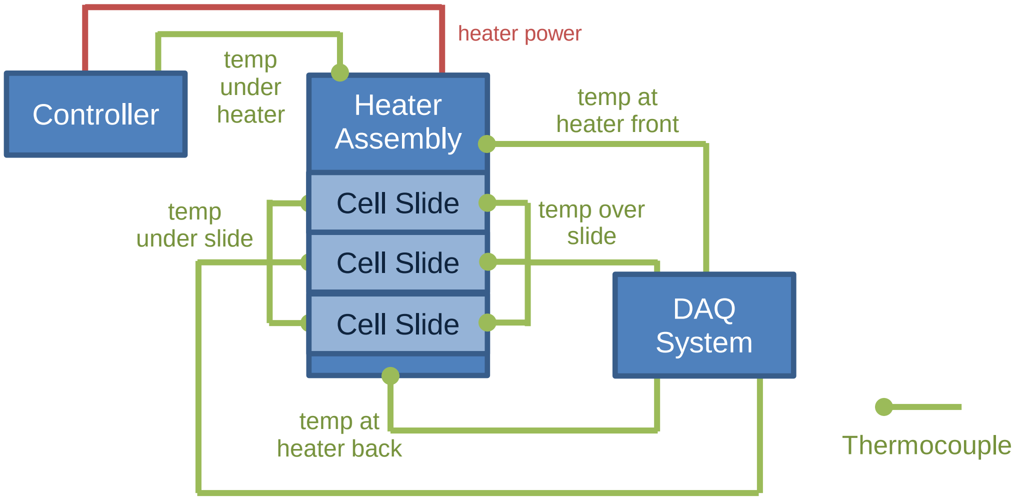

Figure 105 Diagram of cell heating setup. The green lines are thermocouples, where the ends with the dot represent the junction and flat ends are the connectors to the electronics.

Heater Assembly

The cell heater consisted of a wooden base, temperature-insulating foam, silicone heater, aluminum adapter, plastic slide holder, U-aligner, plexiglas top, and top aluminum piece (Figure 106, technical drawings provided in Appendix F). The design choices for each component of this heater are explained in this section.

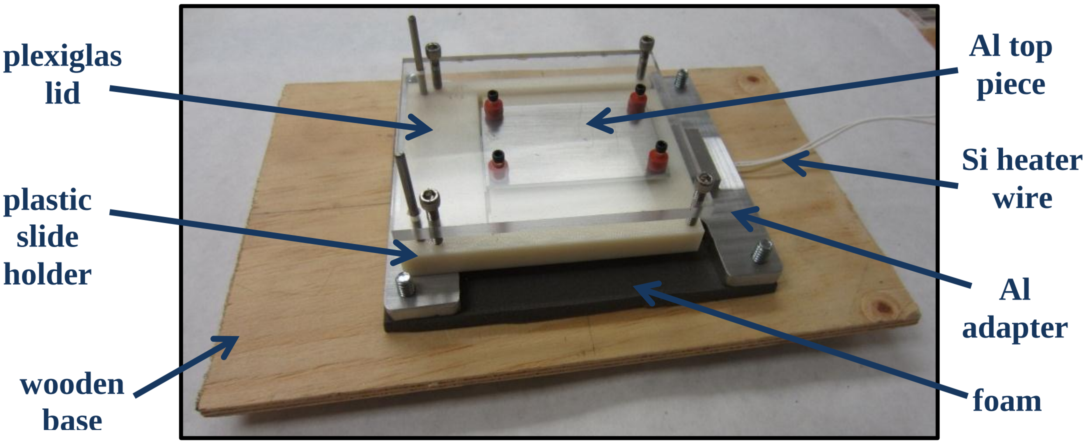

Figure 106 Cell heater, silicone strip heater sits between foam and aluminum adapter (not pictured except for white wire).

To heat the cells, a 120V W3"x L6" silicone strip heater was purchased (TEMPCO Electric Heater Corporation, Model #80408), displayed in Figure 107. The maximum temperature of the heater is 232°C, so it was an appropriate choice for the setup since the temperature of the cells would not exceed 100°C.

Figure 107 TEMPCO 120V, 3" x 6" silicone strip heater [102].

The aluminum adapter, shown in Figure 108, was created to have a flat surface on which the slides could sit, which spread the heat for an even temperature distribution. A W5" x L6" x t1/8" aluminum plate was machined to a ¼" thickness everywhere except a 1.300" x 5.000" rectangle in the center of the piece. The cell slides (standard W1" x L3" x t0.039" glass slides) sit flat on the raised platform with their length perpendicular to its length, so only the center of the slides are heated and the ends of the slides are exposed so they can be easily placed and removed during experimentation.

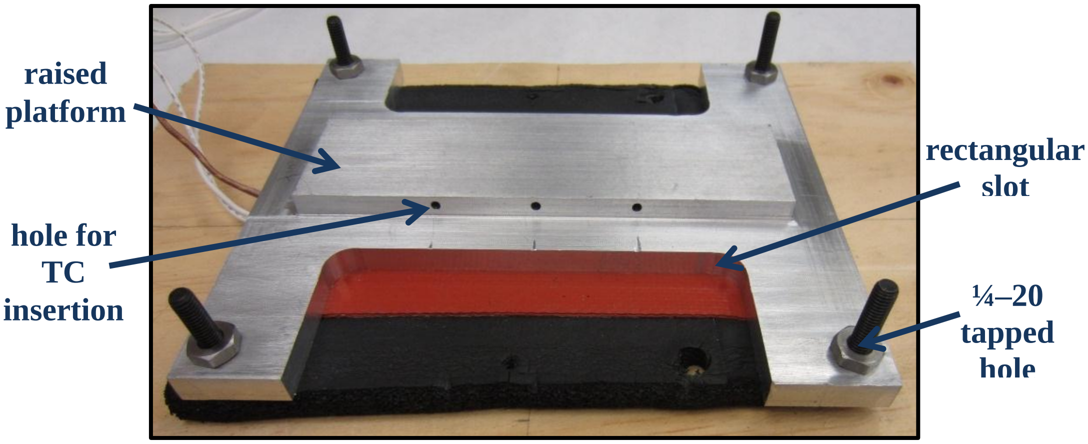

Figure 108 Aluminum adapter sitting on the silicone heater (orange), foam (black), and wooden base, with 1/4-20 screws securing it to the base.

Four ¼-20 tapped holes were drilled through the thickness at the corners of the plate for securing it to the base. The screws used have a rubber foot on one end which sits under the wooden base, so as they are screwed into the aluminum plate a compression force is created between the aluminum adapter and the base, which flattens the silicone heater and ensures an even heat distribution through the aluminum.

Three blind holes Ø0.0930" x 0.6500" depth are drilled parallel to the base into the middle of the raised platform. They are located at the center of the width of each of the three treatment slides, so a thermocouple (TC) can be inserted into each hole to measure the temperature directly below the center point of the slide (more details on thermocouple placement discussed in Thermocouples section).

Finally, a 1.3500” x 4.000” rounded rectangular slot was removed from the base of the aluminum, centered lengthwise on the adapter. Its purpose was to allow for the manufacture of the three previously-mentioned holes without interference between the drill chuck and the aluminum base. A second slot was added on the other half of the base to ensure thermal symmetry. The final part was polished to create a smooth surface for heat transfer.

The foam and wooden base provide thermal insulation for the heater and aluminum adapter. This allows most of the heat to propagate upwards towards the slides, and provides a cool surface for user safety and work-surface preservation.

The ABS plastic slide holder was created by an automatic prototyping machine. Its purpose is to quickly get the slides on and off the heater, which is especially important during high-temperature testing. Figure 109 shows the holder with the three treatment slides sitting in their designated positions. It is open in the center to allow for the raised platform of the heater to touch the slides, and slightly lift them off of the holder to ensure full contact.

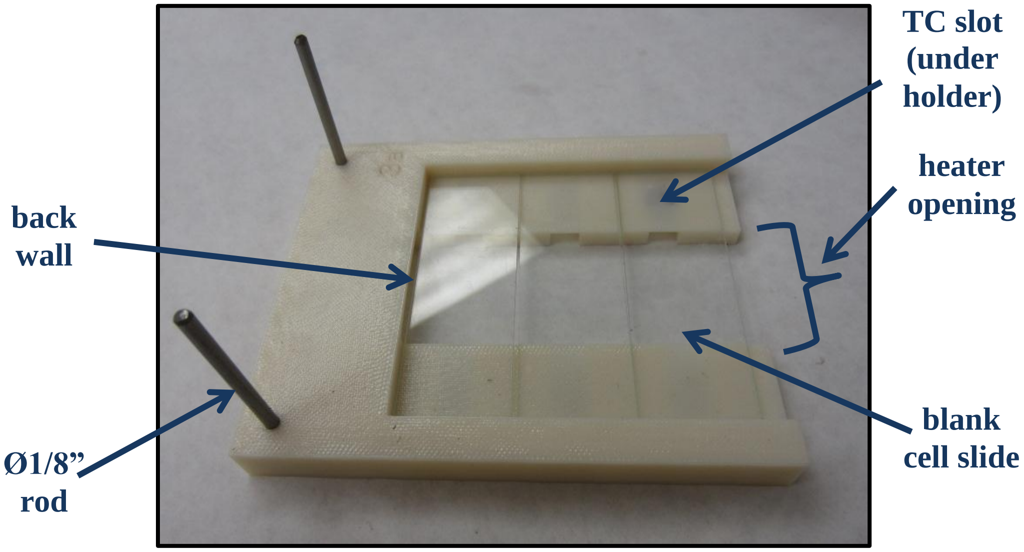

Figure 109 Plastic slide holder, with 3 blank slides in their designated positions.

The walls of the holder keep the slides in position during placement and removal of the holder from the heater, and there are only three walls for ease of getting the slides into and out of the holder. There is a slot at the beneath each slide on the bottom of the holder and parallel to the length of the slides to give an opening for the thermocouples which are inserted in the aluminum adapter. Without these, the holder and therefore the slides would not sit flatly on the adapter.

Two Ø1/8" steel rods were inserted into blind holes perpendicular to the base at the closed end of the holder. Holes in the plexiglas lid (Figure 112) will slide into these rods, centering and securing the lid on the plastic holder, but allowing for a quick removal of the lid after the experiment. Two identical plastic heating holders were built so one could hold empty cells while the heater reached steady state (see Testing Procedure section).

The rapid-prototyped ABS plastic U-aligner holds the coverslips, which sit on top of the cells on the slide, in place during heating. Sliding of these coverslips creates a shear stress on the cells, which can cause cell death not related to the thermal dose, so it is important to keep them still. Figure 110a shows the top view of the aligner, and Figure 110b is the bottom view. Figure 111 displays the U-aligner on top of the treatment slides on the plastic holder. The two long walls on the bottom sit flat along the two short sides of the three slides. The slot is slightly wider than the width of the coverslips, so the inner walls of the slot are just outside of the sides of the coverslips.

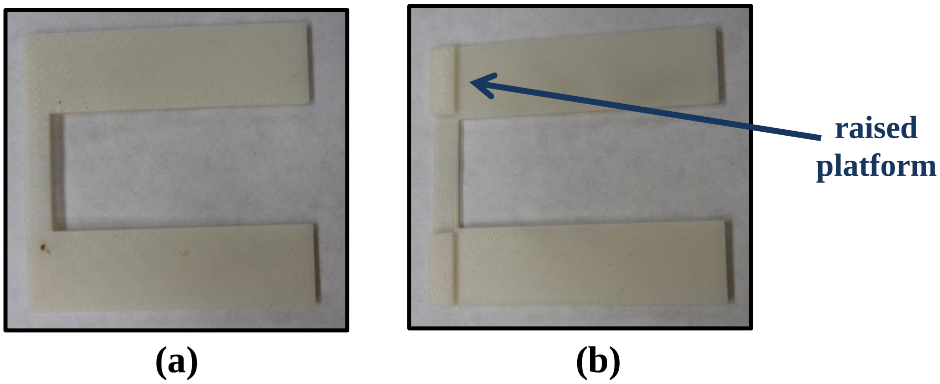

Figure 110 The top (a) and bottom (b) views of the U-aligner.

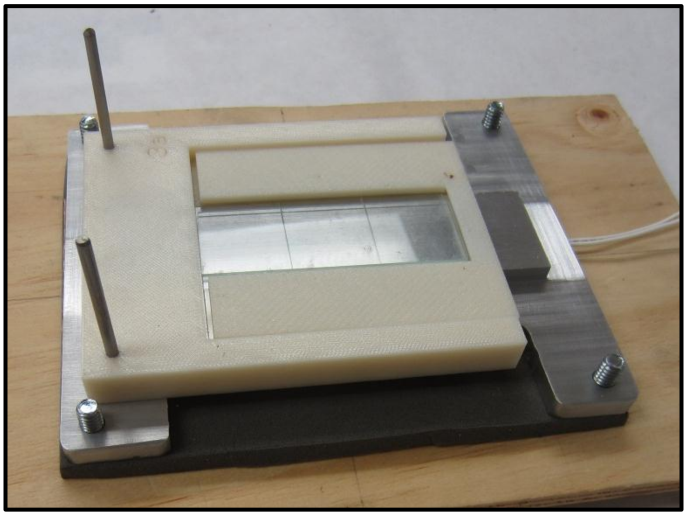

Figure 111 The U-aligner is situated on top of the slides on the plastic holder, and its sides are outside of where the coverslips are situated (not shown).

The two raised platforms on the bottom of the U-aligner sit on top of the plastic holder's base, just to the side of the slides. This takes some of the pressure off of the slides, so that the extra weight in the back will not tip the slides off of the surface of the heater. Between them the connection of the two walls of the U has a very thin thickness, so it does not touch the aluminum raised platform but solely connects and supports the sides of the U.

The machined plexiglas lid and aluminum top piece are rigidly attached to each other (bottom view shown in Figure 112). The purpose of the aluminum top piece is to provide a means of measuring the temperature at the top of the coverslip. The temperature below the slides is not sufficient to accurately determine the temperature of the cells, even if the temperature gradient is known, because the temperature read by the thermocouples in the aluminum adapter does not show the transient temperature of the cells when first placed upon the heater. However, a thermocouple could not be attached to the top of the coverslip because it would create a shear stress on the coverslip and the adhesive would mar the optical clarity needed to look at the cells under the microscope.

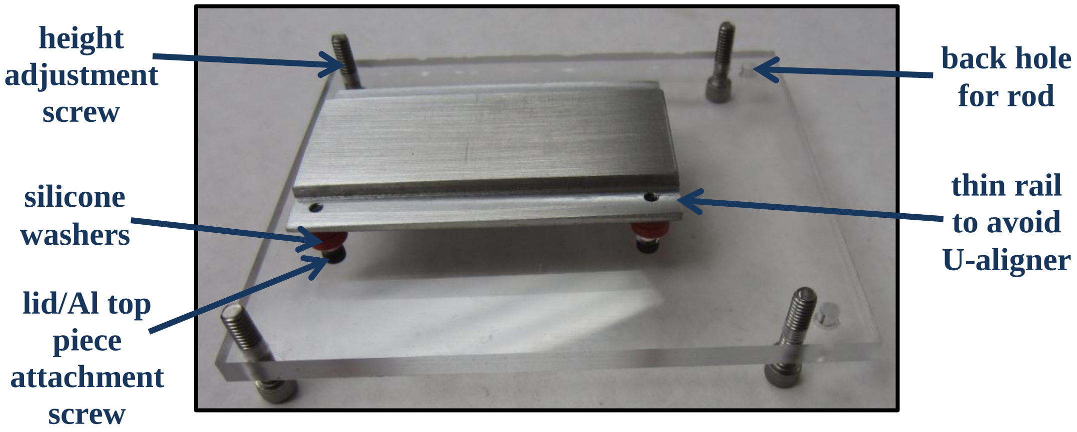

Figure 112 Bottom view of plexiglas lid and aluminum top piece.

The aluminum top piece sits just above the coverslips, but does not apply pressure to them (which also causes cell damage) because it is supported by the lid. It was manufactured from a W1.8000” x L2.7000” x t1/8” aluminum plate, and 1/8” of the thickness was symmetrically removed on the long sides 0.3250” into the piece. This ensures the aluminum top piece will not touch the U-aligner (shown in Figure 113). Four 4-40 tapped through holes are perpendicular to the thickness at the corners of the piece, to allow attachment to the lid. Four screws each fit through a clearance hole in the plexiglas lid, through two silicone washers, and screw into the designated tapped hole.

The W3.7700” x L4.500” x t¼” plexiglas lid contained ten through holes drilled perpendicular to its thickness. The two in the back are Ø0.1360” to allow clearance for the rods in the plastic slide holder. The four in the middle are Ø0.1285” clearance holes for the screws which attach to the aluminum top piece. And finally, the four holes at the corners of the lid are tapped for an 8-32 screw. The four screws which are screwed through those holes are the only parts of this lid assembly which touch the plastic holder. They can be adjusted so that the distance from the lid to the holder keeps the aluminum top piece just above the top of the coverslip (shown in Figure 113). The screws provide the tight tolerance needed for this height (which is derived because of the thinness of the coverlip); this tolerance was smaller than the accuracy of the manual milling machine.

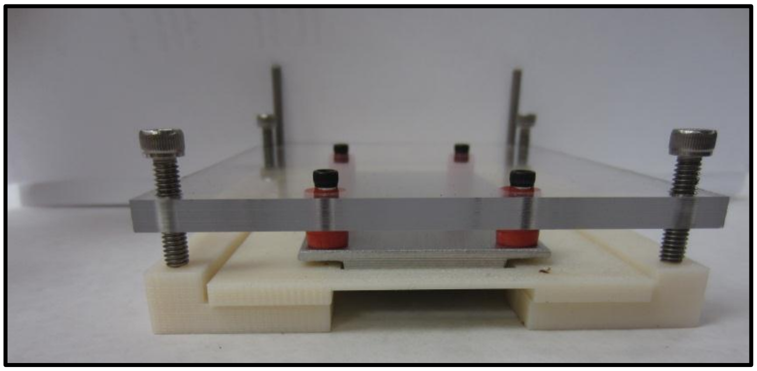

Figure 113 Plastic holder with lid on top and U-aligner between them. The screws in the lid position the aluminum top piece above the coverslips (not shown), and the aluminum top has rails machined out so it does not touch the U-aligner.

Controller

The controller in this system was used to maintain a constant experimental temperature from the heater (Digi-Sense Advanced Temperature Controller, 115V, Model #EW-89000-10). This controller contained a Proportional Integral Derivative

(PID) controller, and its parameters could be auto-tuned before each test period to ensure accuracy in different ambient environments. After tuning, the controller could be set to any desired temperature and maintain the set temperature ±0.2^{o}C.

The power cord from the silicone heater plugged into the controller, which controlled the temperature by turning the power on and off as was necessary (when the desired temperature was reached, there was a high frequency of the power turning on and off). A thermocouple was also plugged into the controller, and its junction was placed between the silicone heater and the foam insulation to provide the controller the temperature of the heater.

Data Acquisition System

The DAQ system consisted of a 31-channel port for the thermocouple input (National Instruments TC-2095) connected to an isolation amplifier module (National Instuments SCXI-1121), which connected to the computer for data collection and storage. Eight thermocouples connect to the DAQ, with their junction in various locations on the setup: one on the front surface of the aluminum adapter’s raised platform, one on the back surface of the raised platform, three in the holes in the aluminum adapter raised platform under the slides, and three on top of the aluminum top piece (above the centers of the treatment slides).

The final system with all of the setup components is shown in Figure 114.

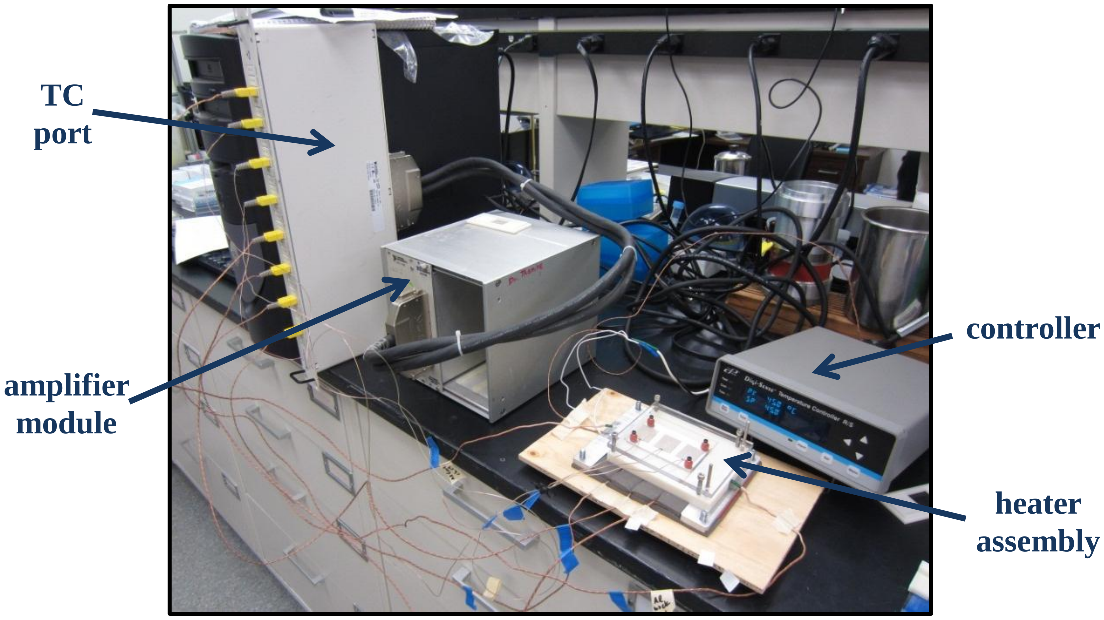

Figure 114 Full heater setup.

Thermocouples

K-type thermocouples were used to measure the temperature because their temperature boundaries are well outside of the necessary range, and their sensitivity is sufficient at the operating temperatures of this experiment. Two different series of thermocouples were used: for measurements under the silicone heater and in the holes in the aluminum adapter, an insulated thermocouple with an exposed junction was used (Omega Engineering, Inc. Model # 5SRTC-GG-K-30-36). Thermocouples with surface mount adhesives (Omega Engineering, Inc. Model # SA1-K-SRTC) were used for thermocouples which were attached to the aluminum top piece and the raised platform of the aluminum adapter.

As mentioned at the beginning of this section, there are nine thermocouples total: one which provides feedback to the controller (TC under the silicone heater) and the remaining eight read measurements for the DAQ system. The physical locations of each thermocouple during testing are shown in Figure 115.

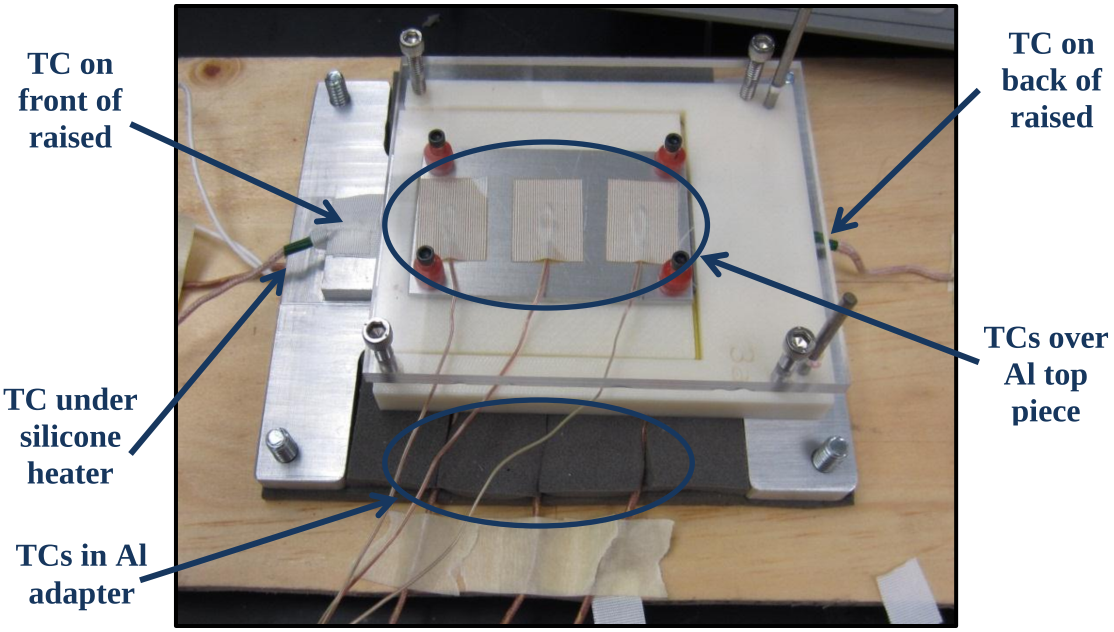

Figure 115 Thermocouple positions during testing.

Thermocouple Calibration

To ensure the thermocouples have the correct reference temperature values, they are calibrated before testing begins. The controller only uses one temperature point to calibrate the thermocouples, so the temperature was set while the junction was submerged in boiling water (assumed to be 100^{o}C). The thermocouples inserted into the DAQ could use multiple temperature points, so the thermocouples were calibrated at three temperatures: ambient room temperature, an ice water bath (assumed to be 0^{o}C), and the boiling water.

Cell Culture

MCF-7 and T-47D breast cancer cell lines were grown to confluency and resuspended in their appropriate mediums. The concentration of the cells were noted, which varied between 250 x 10^6 cells/mL and 450 x 10^6 cells/mL. During the experimentation, the cell solution was kept in an ice bath.

Testing Procedure

Before testing began, the temperature and humidity of the room were recorded. A plastic heating holder with 3 blank slides was placed on the heater, and the controller was set to the first testing temperature. The test could begin once the entire heating setup reached a constant temperature.

150µL of the current cell solution was mixed with 150µL of Trypan Blue viability staining dye. Five slides were set out on a slide-centering mat, each within one of five the rectangles (Figure 116). They were labeled with the cell line, heating temperature, and heating time of the current test, and each one was given a slide identification of C-37, C-var, 1, 2, or 3. A coverslip with side rails (W0.868" x L1.182" x t0.010", Thermo Scientific Lifterslip P# 22x301-2-4734) was placed on top of each slide within the smaller rectangle drawn on the centering mat, with its rail-side on the slide with the rails parallel to the long sides of the slide. The rails created a short gap between the top of the slide and the bottom of the coverslip so that there was no compression force on the cells from the coverslip, and an even distribution of solution was ensured. 50µL of the cell solution/ Trypan Blue mixture was pipetted slowly at one non-railed end each coverslip; capillary action drew the mixture through the coverslip in an even layer (Figure 117).

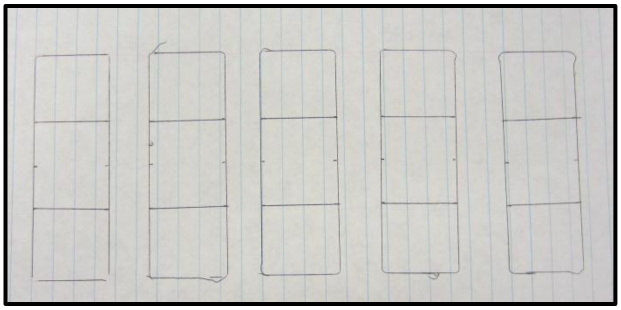

Figure 116 Slide centering mat. Each slide is placed within a large rectangle and the coverslip is put on top of it within the smaller rectangle.

Figure 117 Labeled slide with cell solution/ Trypan Blue inserted under the coverslip.

Each slide was placed under an upright microscope fitted with a camera (OPELCO), and 3 photographs were taken at 100x magnification in varying locations across the coverslip area. This recorded the initial viability of the cells.

The slide identified as "C-37" was placed in an incubator set to 37^{o}C at 5% CO_2. The "C-var" slide was placed on the counter next to the heater setup. These are the two controls for the experiment: the former is to compare the treatment slides to cells that remain at body temperature for the duration of testing (compared with respect to body cells), and the latter compares the treatment slides to cells which experience the testing environments without heating (compared with respect to experimental control). Slide "3" was placed in the plastic heating holder, and was pushed all of the way to the back. Next, slide “2” was placed in the holder, so its side was touching the side of slide “3”. Finally, slide “1” was inserted into the plastic slide holder in the same manner, touching slide “2” (Figure 118). The U-aligner was placed on top of the slides, with the closed end of the “U” facing the open end of the slide holder. The lid was slid on top of the plastic slide holder.

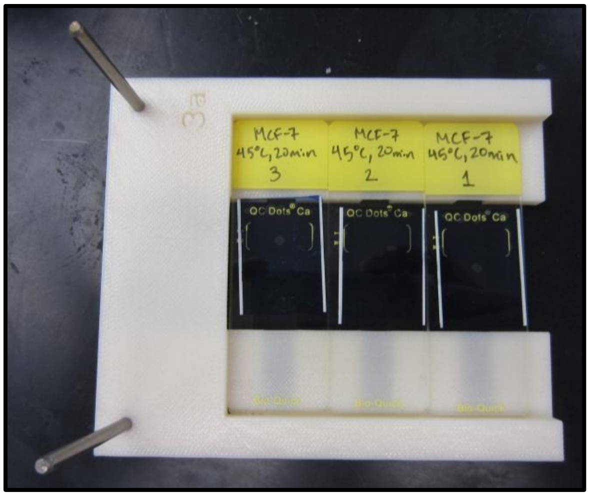

Figure 118 Slides with cells inserted into plastic slide holder; slide "3" was placed first, then slide "2", and slide "1" was at the front of the holder.

The DAQ began recording and the slide holder with the treatment slides and the lid replaced the empty slide holder on the heater. After the desired heating time passed, the slide heating holder assembly was removed from the heater, the lid and U-aligner were removed, and the C-var slide and the holder with the treatment slides were placed in a fridge at 4^{o}C for five minutes to prevent the cells from heating further.

The five slides were again placed under the upright microscope and photographed in three locations for each slide (an example of one of these photos is displayed in Figure 119).

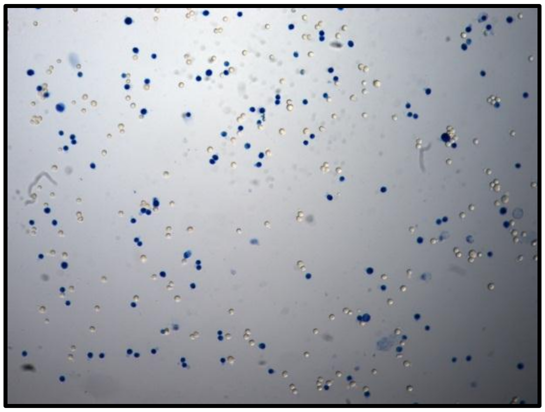

Figure 119 A photo taken at 100x of T-47D cells after heating for 4.5 mins at 50°C. The white dots are the live cells and the blue dots are the dead cells.

Tests Performed

To obtain an accurate mathematical model to describe the thermal damage correlations of these breast cancer cell lines, a sufficient number of time and temperature combinations must be tested. Table 23 displays the tests performed.

Table 23 The time and temperature combinations of the trials performed for each cell line.

Trial #	Cell Temperature (^oC)	Cell Line	Heating Time (min)
1	**50**	MCF-7	**14**
2			**16**
3			**18**
4			**20**
5			**22**
6		T-47D	**20**
7			**24**
8			**28**
9			**32**
10			**34**
11	**52/53**	MCF-7 (53)	**8**
12			**11**
13			**14**
14			**16.5**
15			**18**
16		T-47D (52)	**12**
17			**14**
18			**16**
19			**18**
20			**20**
21	**54/55.5**	MCF-7 (55.5)	**2**
22			**4**
23			**5**
24			**6**
25			**7**
26		T-47D (54)	**4**
27			**6**
28			**8**
29			**10**
30			**12**

31	**57**	MCF-7 (57)	**0.5**
32			**1**
33			**2**
34			**3**
35			**5**
36		T-47D (57)	**2**
37			**3**
38			**4.5**
39			**6**
40			**8**

Setup Validation and Thermal Gradient Determination

The holes which were drilled into the aluminum adapter's raised platform for the temperature measurements beneath the slides could possibly create an uneven temperature distribution under the slides. Thermal uniformity cannot be compromised at the expense of the temperature measurement, so it was important to validate that no cool spots were created from these drilled holes.

First, the heater was tested prior to the drilling of these holes. Using a thermally-conductive compound (Arctic Silver, Céramique) and thermally-insulating tape, thermocouples were secured to the top of the aluminum adapter where the centers of the slides would. Two more thermocouples were attached to the front and back of this raised platform, in the locations the thermocouples would sit during testing (Figure 120). The adhesive thermocouples were not used for these tests to avoid any residual adhesive remaining on the aluminum adapter after they were removed, which would result in an uneven heat transfer to the slides.

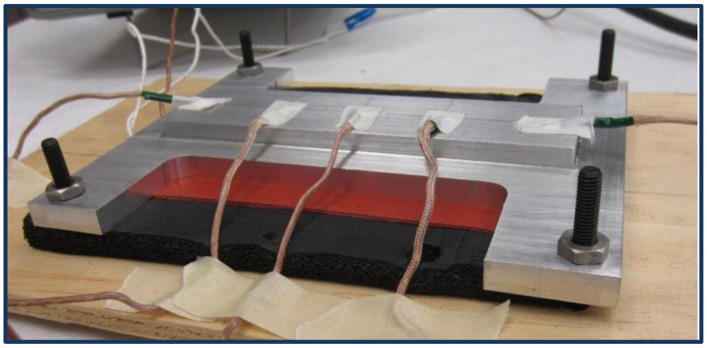

Figure 120 Setup to test of the temperatures at the top of the aluminum adapter prior to drilling holes for TCs.

This setup was tested with the silicone heater set to 48°C and 65°C, which outside of the testing extremes. Then, the holes were drilled in the aluminum adapter, and the test was repeated, but now with measurements being taken within the aluminum as well (setup shown in Figure 121).

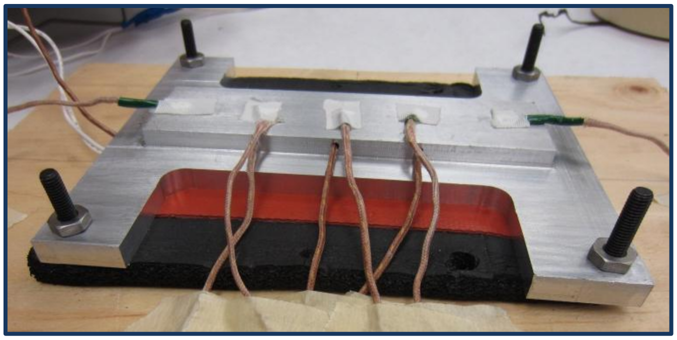

Figure 121 Setup to test of the temperatures at the top of the aluminum adapter after drilling holes for TCs, also measuring the temperature in the drilled holes.

The results of this testing are summarized in Table 24. There is only about a 3% change in the temperatures measured before and after the holes are drilled, which is sufficiently small to give valid testing results.

Table 24 The average of the temperatures measured on the top of the aluminum adapter before and after drilling the holes for the thermocouples in the side of its raised platform.

	Without holes		With holes		Percent Error	
Silicone Heater Temp (°C)	48	65	48	65	48	65
Average Temp Over Slide Locations (°C)	**46.98**	**64.50**	**45.54**	**62.56**	**3.15**	**3.10**

Next, it was important to determine the thermal gradient between the temperature read by the thermocouples beneath the slides and the actual temperature of the cells. The temperature observed by the cells cannot be obtained during testing, so it was estimated according to this pre-determined gradient. Since the exact thermal contact resistances are not known, this thermal gradient is determined experimentally.

To experimentally determine the thermal gradient, three thermocouples were attached to the top and center of three blank slides. The slides were placed in the plastic holder and onto the heater. Thermocouples were also inserted into the holes under the slides, so the temperature was being measured both below the slides (as would occur during testing) and in the location where the cells would be located. This experiment was conducted again outside of the extreme settings used for the silicone heater, 45°C and 65°C. The average temperatures resulting from these experiments are displayed in Table 25, and the differences between the temperature at the cells and below them are calculated in the last row of the table.

Table 25 Temperature at cell location and directly below the slides in the aluminum adapter at the temperature extremes of the silicone heater. The resulting thermal gradients are calculated for each silicone heater temperature.

Silicone Heater Temp (°C)	45	65
Average Temp at cells (°C)	**45.02**	**64.02**
Average Temp under cells (°C)	**47.90**	**69.03**
Gradient (°C)	**2.88**	**5.01**

This discrepancy between thermal gradients at the two silicone temperatures can be attributed to the contact resistance increasing between the aluminum and the slide as the temperature increases. A linear relationship was assumed between the gradient and the temperature measured within the aluminum adapter, so the slope of that relationship is

$$\frac{\Delta gradient}{\Delta T_{TC}} = \frac{5.01 - 2.88}{69.03 - 47.90} = 0.10$$

where T_{TC} is the temperature under the slide as measured by the thermocouple inside of the aluminum adapter. Therefore, the equation for the thermal gradient is

$$gradient = 0.10(T_{TC} - 47.90) + 2.88 \qquad \text{Equation 49}$$

which leads to the equation for the cell temperature based on the temperature under the thermocouple as

$$T_{cell} = T_{TC} - gradient = 0.90T_{TC} + 1.91 \qquad \text{Equation 50}$$

To validate this experimental calculation of the gradient, a theoretical determination of the cell temperature was performed. A schematic of the thermal resistances for the final test setup is shown in Figure 122. The purple dots labeled T_{Al} and T_{top} represent the temperatures measured by the thermocouples in the aluminum base and on top of the top aluminum plate, respectively. The heat flows up through the aluminum base into the slide (losing some energy to the contact resistance between them), then through the cell solution (labeled in blue since it is the desired measurement) and cover slip. At this point there is a thin layer of air between the top of the coverslip and the bottom of the aluminum top piece, so there are both conduction and convection effects (combination represented by dashed resistor). Finally, the heat flows through the aluminum top plate to reach the thermocouples at its top surface.

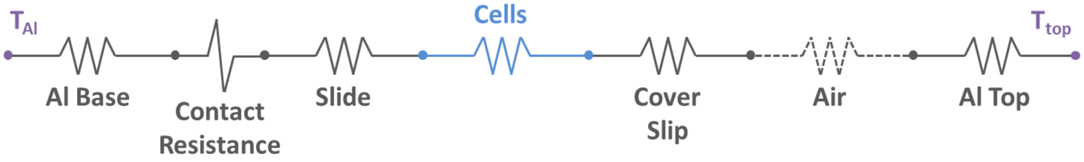

Figure 122 Schematic of thermal resistances in final test setup. The blue cell temperature is the value sought from this calculation.

Through the above process, the heat flux is constant, so if this flux is determined then the temperature at any point can be calculated. As heat flows through a medium, its energy is transferred through convection calculated using Equation 51 [103]

$$q'' = k\frac{\partial T}{\partial x} \qquad \text{Equation 51}$$

where q" is the heat flux, k is the thermal conductivity of the material and x is the direction of interest. Through a medium the temperature at the second wall (T_2) can be calculated if the temperature at the first wall (T_1) is known by discretizing the above equation, shown in Equation 52.

$$T_2 = T_1 - \frac{q''\Delta x}{k} \qquad \text{Equation 52}$$

The heat flux due to thermal contact resistance between two surfaces is calculated by Equation 53 [103]

$$q" = \frac{T_2 - T_1}{R"_{t,c}} \qquad \text{Equation 53}$$

where $R''_{t,c}$ is the thermal contact resistance, which is different for each type of interface. This formula can be similarly discretized as Equation 51 to solve for the temperature at the second material in the interface.

Finally, the layer of air has both conductive and convective effects, which occur because the air is not stagnant during testing so its flow against the surfaces removes heat. The heat flux due to convection is described by Equation 54 [103]

$$q" = h(T_S - T_\infty) \quad \text{Equation 54}$$

where h is the convection heat transfer coefficient of the fluid, T_S is the surface temperature, and T_∞ is the ambient air temperature.

Combining the thermal gradients for each resistance layer results in Equation 55.

$$T_{top} = T_{Al} - q"\left[\left(\frac{\Delta x}{k}\right)_{Al\ Base} + R"_{t,c} + \left(\frac{\Delta x}{k}\right)_{slide} + \left(\frac{\Delta x}{k}\right)_{cells} + \left(\frac{\Delta x}{k}\right)_{coverslip} + \left(\frac{\Delta x}{k}\right)_{air} + \frac{1}{h_{air}} + \left(\frac{\Delta x}{k}\right)_{Al\ Top}\right] \quad \text{Equation 55}$$

This equation can be solved for q”, which is assumed to be constant during all tests. The values for the material thicknesses (Δx_i) are shown in Table 26, and Table 27 displays the material constants k, R”, and h used in this calculation.

Table 26 Thicknesses of different material layers.

Layer	Δx (in)
Al	**0.0625**
Slide	**0.0393**
Cells	**0.00297**
Coverslip	**0.009**
Air (estimated)	**0.001**
Al Top	**0.1875**

Table 27 Material constants for theoretical thermal gradient calculation [103].

k @300K (W/mK)	
Al	**237**
Glass	**1.4**
Air	**0.0263**
Water	**0.613**
h (W/m^{2}K)	
gas, forced	**250**
R"$_{t,c}$ (m^{2}K/W)	
Stainless Steel @ 100 kN/m^2	**0.0025**

A sample test was performed with a layer of water under the coverslip (instead of cell solution) to determine the heat flux. The heater was set to 50^{o}C, and when steady state was reached the temperatures in the aluminum base and above the aluminum top were collected and averaged. Plugging these values into Equation 55 resulted in a heat flux of q" = 0.531 W/m^2.

Finally, to relate the theoretical calculation back to the experimentally determined thermal gradient, the cell temperature was calculated for both the experimental and theoretical method with the test case presented in the previous paragraph. With an average aluminum temperature of 53.0^{o}C, the theoretical calculation yielded a cell temperature of 50.5^{o}C, and the experimental gradient calculation (Equation 50) resulted in an average of 49.6^{o}C. This is less than a 2% error, which is an acceptable margin because the thermal contact resistance value in the theoretical calulation was estimated and does not include the increase in thermal losses at higher temperatures. Also, the thickness of the airgap was an estimate as well. Therefore, the experimentally-determined thermal gradient calculation is acceptable to use to determine the cell temperatures during testing.

Final Consideration: Temperature Ramping

The goal of this testing is to find the cellular responses to isothermal heating because the Arrhenius equation is most-accurate when determined for constant temperatures. However, there is an inherent ramping time where the temperature of the cells is changing rapidly when the treatment slides are first placed on the heater because there cannot be an instantaneous temperature increase. For long testing times, the ramping period will be a negligibly small percentage of the total treatment time. Ramping has the greatest impact on high temperature tests because cell death occurs quickly, therefore many cells will die before the steady state temperature is reached. This is an error that must be considered while reviewing results from this or any thermal therapy cell study.

Equation 50 is used to determine the temperature of the cells from the experiments conducted. The temperatures read from the thermocouples on the aluminum top piece are used to determine when a steady state temperature has been reached during testing. The temperatures measured in the aluminum adapter will not change much when the slides are placed on the heater, so the calculation from Equation 50 (where that temperature is labeled T_{TC}) will not reflect the true temperature of the cells until steady state has been reached. Therefore, cell temperatures were only calculated after the aluminum top piece reached about 90% of its final temperature.

Data Analysis Methods

To analyze the data, first any obvious outliers were removed and the viability of each slide before testing began was calculated by Equation 56

$$\%d_i = \frac{N_d}{N_T} \qquad \text{Equation 56}$$

where $\%d_i$ is the initial percent of dead cells, N_d is the number of dead cells, and N_T is the total number of cells on the slide.

Then, the results from each slide post-heating were normalized by their initial viability, so the number of dead cells becomes the value it would have been if 100 live cells were initially present. This calculation is shown in Equation 57

$$\%d_{n,j} = \frac{\%d_{p-h} - \%d_i}{\%V_i} \qquad \text{Equation 57}$$

where $\%d_{n,j}$ is the percent of dead cells normalized to the initial viability (and j represents the slide being considered, which can be C37 for the controls at 37^{o}C labeled C-37 , CV for the controls at the variable ambient temperatures labeled C-Var, or t for the test slides), $\%d_{p\text{-}h}$ is the percent dead post-heating, and $\%V_i$ is the percentage of viable cells before heating.

The normalized viabilities of the control slides post-heating are then averaged for each control (an average of three photos for the C-37 and separately three photos are averaged for C-Var). Finally, each of the nine treatment viabilities (three photos post-heating for three slides) was normalized a second time to account for the control cells which have died, separately for each type of control cell, according to Equation 58 for C-37 cells,

$$\%d_{nC,C37} = \frac{\%d_{n,t}}{\%d_{n,C37}} \qquad \text{Equation 58}$$

where $\%d_{nC,C37}$ is the percent dead normalized to the C-37 control cells, and Equation 59 for C-Var cells,

$$\%d_{nC,CV} = \frac{\%d_{n,t}}{\%d_{n,CV}} \qquad \text{Equation 59}$$

where $\%d_{nC,CV}$ is the percent dead normalized to the C-Var control cells. The percent viable cells were then determined by Equation 60 – Equation 62

$$\%V_{n,t} = 1 - \%d_{n,t} \qquad \text{Equation 60}$$

$$\%V_{nC,C37} = 1 - \%d_{nC,C37} \qquad \text{Equation 61}$$

$$\%V_{nC,CV} = 1 - \%d_{nC,CV} \qquad \text{Equation 62}$$

where $\%V_{n,t}$ is the viability percentage post-heating without normalizing to the controls, $\%V_{nC,C37}$ is the viability percentage normalized to the C-37 slide, and $\%V_{nC,CV}$ is the viability percentage dead normalized to the C-Var slide. The following calculations are performed three times, once for $\%V_{n,t}$, $\%V_{nC,C37}$, and $\%V_{nC,CV}$.

Each of those viability percentages are comprised of nine points, and the final viability was determined by averaging each point. Since less than 30 samples were tested, a t-test statistic was performed to determine the 95% confidence intervals of the data. The calculation of these confidence intervals is based on Equation 63 [104]

$$t = \frac{\bar{X} - \mu}{S/\sqrt{n}} \qquad \text{Equation 63}$$

where $\bar{X}$ is the sample mean, μ is the population mean, S is the standard deviation, and n is the number of samples (9 in this case). The calculation to determine the standard deviation is shown in Equation 64

$$S = \sum_{i=1}^{n} \frac{(X_i - \bar{X})^2}{n - 1} \qquad \text{Equation 64}$$

Therefore, the confidence interval for the population mean is shown in Equation 65 [104]

$$\bar{X} - t_{a/2,v} S \leq \mu \leq \bar{X} + t_{a/2,v} S \qquad \text{Equation 65}$$

where α is the probability that the mean falls outside of this interval, ν is the number of degrees of freedom (ν = n-1), and t is a value determined by the t-Distribution table.

Results and Data Analysis for Cell Studies

First, an example of the resulting temperature curves obtained by the thermocouples during testing is shown. Then, the resulting cell viabilities are presented in in graphical form. The raw data of the cell viabilities can be found in Appendix G.

Temperature Curves

An example of the temperature curves (temperature versus time) measured by the thermocouples during a trial is shown in Figure 123 for T-47D cells at 50°C for 20 minutes. The three thermocouples on the top aluminum piece (red squares, green triangles, and purple X's) clearly delineate the phases of testing: first, there is a short constant temperature portion at the beginning of testing where the DAQ was collecting data but the slides had not yet been placed on the heater. Then, there is a ramping portion of the graph, indicating the time when the cells are heating up but not yet at their steady-state temperature. When the graph flattens indicates the steady-state portion of the test (the start of this period was the time when the temperature reached about 90% of its final value). Finally, the end of the graph shows a steep decrease in temperature, which indicates the end of the test because the slides (and therefore the thermocouples on the top) were removed from the heater.

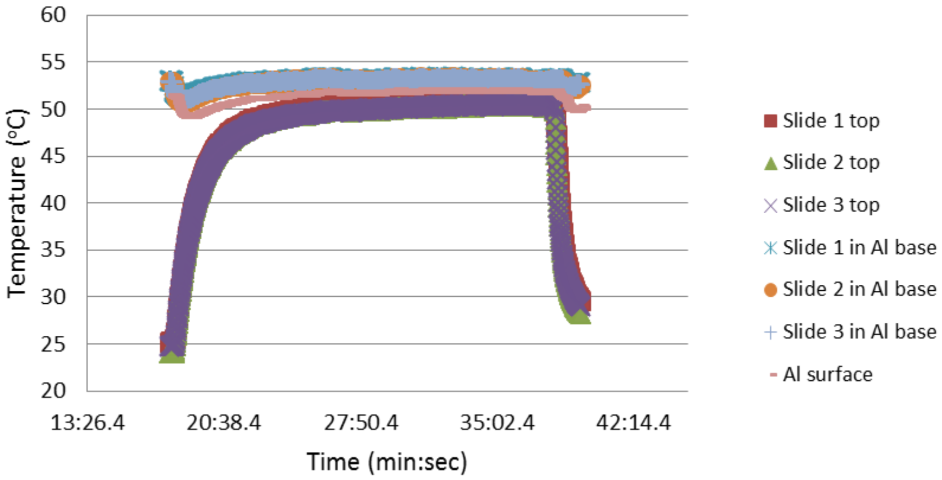

Figure 123 Graph of the thermocouple temperature readings during the trial for T-47D cells at 50°C for 20 minutes.

The data collected during the pre-testing and post-testing time periods were discarded. The temperatures on the tops were used for the purpose of determining the previously-mentioned time periods, but were also not used in any of the data analysis. The graph of the thermocouple attached to the aluminum base's top surface (pink dashes) was also just a reference value (there is only one temperature measurement of the aluminum surface instead of the two described in the procedures because early on in testing this thermocouple stopped giving reliable data, so its results are not shown). The thermocouples in the aluminum base under the slides (blue stars, orange circles, and purple plusses) initially decreased in temperature when the slides were placed on the heater, but then quickly returned to their stead-state value. Only the data taken during the calculated steady-state period was used for the result in the following sections.

MCF-7 Results

The resulting survival curves for the MCF-7 cell lines are displayed in Figure 124. The x-axis shows the heating time, the y-axis is the cell viability, and each data series is for a different temperature. The results are shown for the treatment slides without normalization, and then separate graphs are displayed to show it normalized with respect to the C-37 and C-Var results. The vertical lines represent the confidence intervals at each data point.

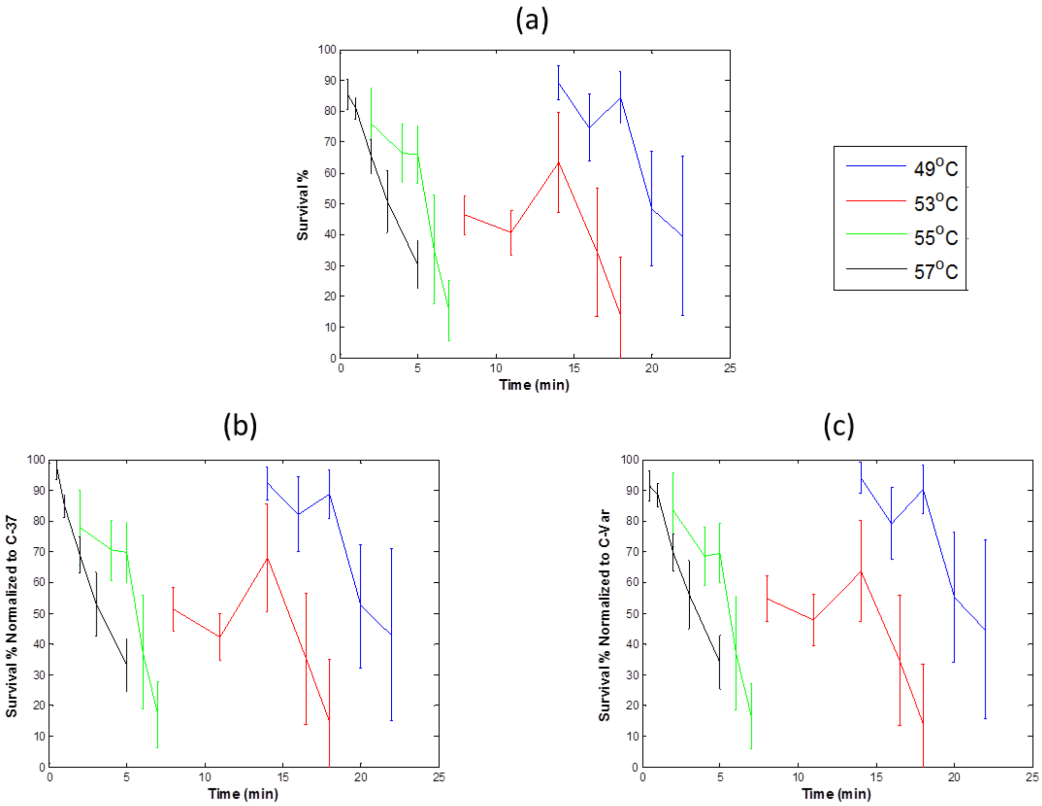

Figure 124 Survival curves of the MCF-7 cell line at different temperatures for (a) the treatment slides, (b) the treatment slides normalized to C-37, and (c) the treatment slides normalized to C-Var.

These graphs show that the higher the heating temperature, the less time required for a decrease in cell viability. With the exception of certain data points, an increase in heating time at a set temperature results in a decrease in cell viability. The means and confidence intervals for each data point are displayed in Appendix H.

T-47D Results

The resulting survival curves for the MCF-7 cell lines are displayed in Figure 125. The means and confidence intervals for each data point are in Appendix H.

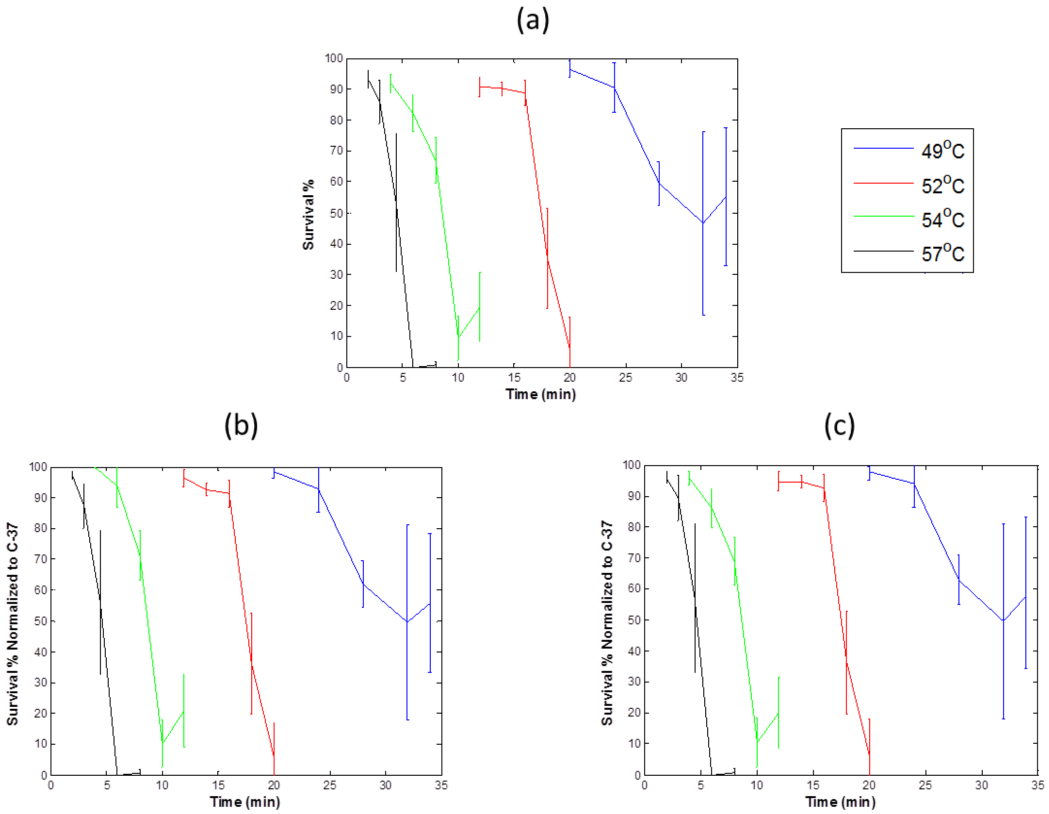

Figure 125 Survival curves of the T47-D cell line at different temperatures for (a) the treatment slides, (b) the treatment slides normalized to C-37, and (c) the treatment slides normalized to C-Var.

The T-47D cell line requires more time for cell death to occur than the MCF-7 cells. For example, at 49°C it took 27 min for the T-47D cells to decline to 50% viability, whereas it was only 19 min for MCF-7 cells to reach that same viability.

Discussion

During testing, there was a problem where the cell viability declined before testing began. After the cells were trypsinized, there was anywhere from 4 – 7 hours that tests were conducted. Even though the cell solutions are kept in an ice bath, the cell viability would decrease. After enough time had passed, the lower viability had an effect on the results, even accounting for the normalization of the cells.

All of the graphs of the results shown in the previous section do not give the same shape of the survival curve that was seen in Figure 29 because some trials were performed with cells that were already dying. For example, for the MCF-7 cells at 52.8°C, the trials heated for 8 and 11 minutes were the last tests performed one day, while the tests heated for 14, 16.5, and 18 minutes were conducted at the beginning of a different day. This has caused the mismatch in viabilities between these two sets of data points.

Determination of Arrhenius Parameters

As was discussed in Chapter 2, one method to determine the mathematical model of the cell death is using the Arrhenius Equation (Equation 22), reproduced below,

$$k(T) = \frac{d\Omega}{dt} = Ae^{-E_a/RT} \qquad \text{Equation 22}$$

where Ω is the percentage of dead cells. Equation 22 can be rearranged into the integral in Equation 66

$$\int_0^{0.50} \Omega = \int_0^{\tau_{50}} Ae^{-E_a/RT} dt \qquad \text{Equation 66}$$

where τ_{50} is the time where 50% of the cells have died. 50% viability was chosen for determination of the parameters because this is the half-life of the cells. Since the tests were assumed to be isothermal, the integral can be evaluated as Equation 67

$$0.50 = Ae^{-E_a/RT} * \tau_{50} \qquad \text{Equation 67}$$

The parameters which need to be determined are the frequency factor A and the activation energy E_a, so evaluating the natural log of Equation 67 will separate these factors, shown in Equation 68

$$ln(0.50) = ln(A) + \frac{-E_a}{R}\left(\frac{1}{T}\right) + ln(\tau_{50}) \qquad \text{Equation 68}$$

This becomes a linear equation of $\ln(\tau_{50})$ v. (1/T) when rearranged as shown in Equation 69

$$\begin{aligned} ln(\tau_{50}) &= \frac{E_a}{R}\left(\frac{1}{T}\right) - ln(A) - ln(0.50) \\ \approx ln(\tau_{50}) &= \frac{E_a}{R}\left(\frac{1}{T}\right) - ln(A) \end{aligned} \qquad \text{Equation 69}$$

The ln(0.50) can be neglected because it is negligible compared to ln(A).

The graphs shown in Figure 124b and Figure 125b are used to determine the mathematical model of each cell line because it is most accurate to normalize the cells to the control which represents non-treated cells in the body (since it is at 37°C). The point where the cell viability is 50% is estimated for each temperature, whose values are listed in Table 28. The natural logarithms of these values are calculated, and they are plotted against the inverse of the temperature in Kelvin in Figure 126.

Table 28 Times when the cell viability declines to 50% for each cell line at each tested temperature.

Cell Line	Temp	Time for 50% Viability
MCF-7	49	**19**
	53	**8**
	55	**4.5**
	57	**2**
T-47D	49	**27**
	52	**14.5**
	54	**8**
	57	**4**

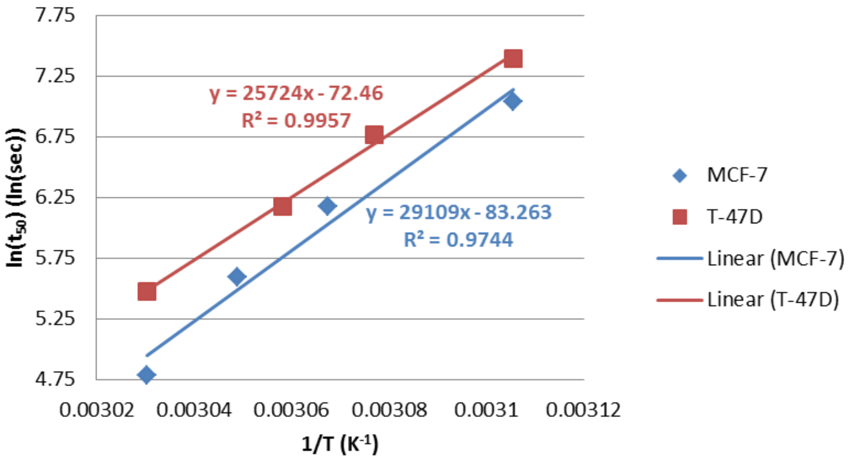

Figure 126 Graph of the natural log of the time when the viability declines to 50% versus the inverse of the temperature for MCF-7 cells (blue) and T-47D cells (red). The equations and R^2 values are included for the line of best fit of each line, and the Arrhenius parameters are determined by these functions.

The slope of the line indicated E_a/R ($R = 8.314$J/molK), and the y-intercept represents ln(A) [62]. Therefore, the final Arrhenius parameters are shown in Table 29 for each cell line.

Table 29 Arrhenius parameters determined by the cell experiments.

	Ea (J)	A (1/s)
MCF-7	**201.2×10^3**	**3.445×10^{29}**
T-47D	**210.2×10^3**	**1.743×10^{31}**

Recommendations for Future Testing

For future testing, the cell viability prior to heating should be ensured to be close to 100% for accurate results. To do this, the time spent testing cells in a particular vial should be shortened. To avoid wasting cells, smaller flasks of cells should be grown; after trypsinization no more than three hours should pass until the end of the testing session.

There were also some inaccuracies with the heating setup. The error bars on the graphs are very large because there was a lot of variability in the results between the different photographs taken of each trial. Although an even heating was ensured down the length of the heater before experimentation began, the thermal gradient along with width of the heater was not tested – one side of the slides usually had a higher viability than the other side, indicating that this was a problem. This variability could also be a function of the low concentration in some of the studies, so not enough cells were present to get an accurate measurement. The controller system also had times of temperature fluctuations, so a more accurate controller is necessary.

The calculations of the Arrhenius parameters were assuming a constant temperature, but as was discussed in the Temperature Ramping section, this causes inaccuracies in the mathematical model. In Figure 123 there is a distinct non-isothermal ramping portion of the trial. In this case, with 20 total minutes of heating, the nonisothermal portion was only a small percentage of the total testing time, but for shorter tests at higher temperatures this ramping period makes up a large portion of the trial. An example of this is shown in Figure 127 for T-47D cells at 57^{o}C for 2 minutes – the thermocouples on the top aluminum piece do not reach their steady-state temperature before the test was completed. For consistency, the temperatures used for determining the Arrhenius parameters are calculated the same for these tests as with the previous tests (once 90% of the final temperature is reached), but it obviously introduces inaccuracies. Future calculations of the mathematical models for breast cancer cells will consider the non-isothermal heating time.

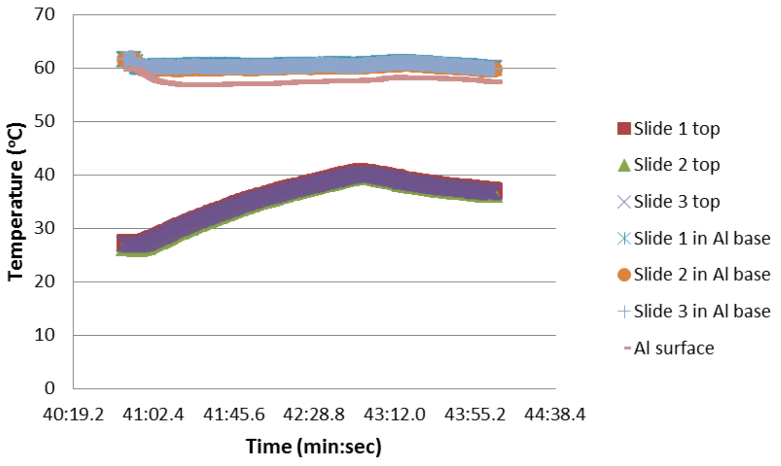

Figure 127 Graph of the thermocouple temperature readings during the trial for T-47D cells at 57°C for 2 minutes.

A different viability assay may also increase the accuracy of these experiments. It was suggested that since Trypan Blue is harmful to the cells, it would be more accurate to re-plate the cells after heating and put them back in a 37°C incubator for about two days. If more cells are present after incubation than before, then it is proven that that thermal dose was not sufficient to cause complete cell death. Also, a higher volume of cell solution on each slide should improve the temperature consistency along the slide. However, it must be kept in mind that this will increase the temperature ramping error of these "isothermal" tests.

Finally, it has been proven that cell viability continues to decrease after the heating trial has completed; Shah [65] tested different incubation times and found that cell death ceased after three hours at 37°C. This study mainly focused on the immediate impact of the hyperthermic treatment (so there will be more certainty of tumor destruction using this data), but a sample of trials with the three-hour post-heating incubation period were also attempted. However, there was an appreciable amount of evaporation occurring during this incubation period, so very little cell solution remained and all cells were always dead (including controls). To prevent this evaporation in future testing, silicone grease should be applied at the exposed edges of the coverslip.

Chapter 7: Conclusion

This study was split into three main sections: the simulations of and device design for prostate cancer US ablation, the simulations of and device design for breast cancer HIFU ablation, and the determination of the thermal damage model for breast cancer cell. The results of these studies are important for the future of treating cancer with ultrasound thermal therapy, which are summarized in this chapter. Then, future work will be detailed.

Summary of Prostate Simulation Results

The goal of the prostate studies was to determine sets of ultrasound parameters that are needed to necrose different size tumors within the prostate. As would be expected, the necrosed region coincided with the regions which experienced the highest temperatures in the prostate. The necrosed volume was a function of the heating time, transducer power, and transducer angle used for the treatment, so an appropriate combination of those parameters needs to be used depending on the patient. The graphs of necrosed volume versus the energy parameter (Figure 56 and Figure 57) can be used as a preliminary resource to determine the appropriate transducer parameters, but more thorough treatment-planning is needed than just knowing the necrosed volume. To account for the location and shape of the necrosed region, a sample code was written to demonstrate how the US parameters can be linked to the specific size and location of the tumors which they can ablate.

The practical use of these results was shown by the device design and treatment planning section. A device was created which satisfies the design parameters and can transmit the same US that was simulated in the studies. However, the device will not be useful if the physician cannot operate it correctly. Creating a database with the code mentioned in the previous paragraph will allow the physician to solely need to determine the tumor location and geometry, and then the device parameters will be provided to him/her and automatically input into the device.

Summary of Breast Simulation Results

HIFU treatments are usually not designed to fully ablate the tumorous tissue with one sonication because the necrosed regions are so small. However, it was the attempt of this study to increase that necrosis volume so the number of sonications can be minimized, therefore minimizing the treatment time. Larger volumes were able to be created in the simulations (up to 3340 mm^3), but studies will need to be run to develop an ellipsoidal shape with the larger necrosed volumes as is created with the smaller volumes.

There was a good agreement between the location of the maximum heat generation, maximum temperature, and the necrosed tissue in the breast. The variable acoustic attenuation was incorporated into this model, which affected the heat generation during the simulation and caused a degeneration of the focal point. This will need to be taken into account for treatment-planning, and it showed that shorter sonication times were important for avoiding this variable having a significant effect.

Flat and curved transducers were tested, and it was found that both work well with certain combinations of their number of elements and the number of rows of elements. Concepts of the devices which incorporate these transducers were created which will increase patient comfort, while still being easy-to-use for physicians and working for multiple patients. The simulations from this section will need to be updated because a general tissue model was used to model the thermal damage since breast cancer data was not available, which decreased the accuracy of the results.

Summary of in vitro *Cell Experimentation Results*

These studies have established the procedures which will be used for finding the breast cancer thermal dose model. The results from the *in vitro* cell experiments are similar to those shown in the literature review of previous experiments, and the activation energy and frequency factor which were calculated from these studies fall well within the range of values from the past studies (seen in Table 6). However, there was a lot of variability in the results, so more studies will need to be performed to validate the means determined for each trial. These results will be very useful in receiving better results from the breast cancer simulations.

Future Work

The next step is to improve all three of the studies performed during this research. The prostate and breast cancer simulations do not account for porous media or cavitational effects. More *in vitro* experiments need to be performed to validate the results from those studies. After improving the experiments (as was recommended by the “Recommendations for Future Testing” section in Chapter 5), the new Arrhenius parameters should be input into the breast simulations and those results will be recalculated.

Ultrasound thermal therapy has the potential to be very effective for the treating tumors, and since the entirety of the treatment involves a vibration of the body's tissue, it is much better for patient health. Both the intraluminal and external devices were proven to be effective in targeting tumors in the prostate and breast, respectively. Improving the devices available and the treatment planning protocols associated with those devices will allow this treatment to be more-quickly implemented in cancer treatment programs in the U.S, and will result in an increase in the quality of life for patients suffering from this all-too-common disease.

Appendix A: Prostate Simulations Results

Results from the simulations of US thermal therapy ablation for prostate cancer are displayed in Table 30 – Table 39.

Table 30 Prostate simulations parameters and results for Tests 1-50.

Test #	Q1 (W)	Q2 (W)	Q3 (W)	Angle (deg)	Heat Time (s)	Tmax (^{o}C)	Vnecr (cm^3)	Surf Area (cm^2)	r centroid (mm)	z centroid (mm)	r min (mm)	r max (mm)	z min (mm)	z max (mm)	theta min (deg)	theta max (deg)
1	0	30	0	90	60.77	62.01	0.36	9.69	8.60	0.00	5.70	12.45	-4.00	4.00	-30.00	30.00
2	0	30	0	90	120.46	78.37	1.27	20.96	10.60	0.00	4.35	16.50	-4.00	4.00	-30.00	30.00
3	0	30	0	90	200.76	96.17	1.92	30.52	11.71	0.00	3.00	19.20	-6.00	6.00	-45.00	45.00
4	0	30	0	120	120.25	56.60	0.20	9.39	8.24	0.00	5.03	11.10	-3.00	3.00	-33.75	33.75
5	0	30	0	120	150.16	58.45	0.33	13.36	8.63	0.00	5.03	11.78	-3.00	3.00	-33.75	33.75
6	0	30	0	120	180.38	60.00	0.45	16.93	8.85	0.00	5.03	12.45	-3.00	3.00	-33.75	33.75
7	0	30	0	120	210.29	61.30	0.53	18.63	9.19	0.00	4.35	13.13	-3.00	3.00	-33.75	33.75
8	0	30	0	120	240.20	62.42	0.58	20.54	9.18	0.00	4.35	13.80	-4.00	4.00	-33.75	33.75
9	0	30	0	150	300.33	52.90	0.03	2.65	7.88	0.00	6.38	9.08	-1.00	1.00	-11.25	11.25
10	0	45	0	90	30.39	67.38	0.49	10.08	8.01	0.00	4.35	11.10	-4.00	4.00	-30.00	30.00
11	0	45	0	90	45.58	85.90	1.04	17.56	9.62	0.00	4.35	15.15	-4.00	4.00	-30.00	30.00
12	0	45	0	90	55.35	99.84	1.44	23.04	10.82	0.00	3.00	16.50	-4.00	4.00	-30.00	30.00
13	0	45	0	120	30.22	54.62	0.04	3.27	6.50	0.00	5.03	7.73	-2.00	2.00	-22.50	22.50
14	0	45	0	120	60.43	67.89	0.63	21.94	8.52	0.00	3.68	12.45	-4.00	4.00	-45.00	45.00
15	0	45	0	120	120.25	93.97	1.74	48.90	10.53	0.00	3.00	17.18	-5.00	5.00	-56.25	56.25
16	0	45	0	150	120.25	66.11	0.83	27.50	8.98	0.00	4.35	13.13	-4.00	4.00	-45.00	45.00
17	0	45	0	150	150.16	70.30	1.15	35.12	9.47	0.00	3.68	14.48	-4.00	4.00	-56.25	56.25
18	0	45	0	150	210.29	77.40	1.58	45.61	10.05	0.00	3.68	15.83	-5.00	5.00	-56.25	56.25
19	0	45	0	180	120.25	55.91	0.24	11.85	7.84	0.00	5.03	10.43	-2.00	2.00	-45.00	45.00
20	0	45	0	180	150.16	57.85	0.41	17.53	8.29	0.00	5.03	11.10	-3.00	3.00	-45.00	45.00
21	0	45	0	180	180.38	59.48	0.56	21.94	8.54	0.00	5.03	11.78	-3.00	3.00	-56.25	56.25
22	0	45	0	180	210.29	60.85	0.69	24.96	8.77	0.00	4.35	12.45	-3.00	3.00	-56.25	56.25
23	0	45	0	180	240.20	62.04	0.80	27.86	8.90	0.00	4.35	13.13	-4.00	4.00	-56.25	56.25
24	0	45	0	180	270.42	63.09	0.90	31.02	9.00	0.00	4.35	13.13	-4.00	4.00	-56.25	56.25
25	0	45	0	180	300.33	64.00	0.98	32.47	9.13	0.00	4.35	13.80	-4.00	4.00	-56.25	56.25
26	0	60	0	90	30.39	97.29	1.08	18.14	9.50	0.00	3.00	15.15	-4.00	4.00	-30.00	30.00
27	0	60	0	120	30.22	66.52	0.40	14.66	7.50	0.00	3.68	10.43	-3.00	3.00	-45.00	45.00
28	0	60	0	120	45.17	83.55	1.01	29.58	8.92	0.00	3.00	13.80	-4.00	4.00	-45.00	45.00
29	0	60	0	120	55.24	96.76	1.39	40.70	9.69	0.00	3.00	15.83	-5.00	5.00	-45.00	45.00
30	0	60	0	120	60.43	104.17	1.60	46.15	10.02	0.00	3.00	16.50	-5.00	5.00	-56.25	56.25
31	0	60	0	150	60.43	71.73	0.95	30.25	8.67	0.00	3.68	13.13	-4.00	4.00	-56.25	56.25
32	0	60	0	150	105.30	98.35	2.09	58.21	10.36	0.00	3.00	16.50	-5.00	5.00	-56.25	56.25
33	0	60	0	180	60.43	59.64	0.44	17.84	7.68	0.00	4.35	10.43	-3.00	3.00	-56.25	56.25
34	0	60	0	180	120.25	75.26	1.52	44.17	9.46	0.00	3.68	14.48	-4.00	4.00	-67.50	67.50
35	0	60	0	180	150.16	82.46	1.97	55.83	9.95	0.00	3.00	15.83	-5.00	5.00	-67.50	67.50
36	0	60	0	180	180.38	89.36	2.32	63.95	10.30	0.00	3.00	16.50	-5.00	5.00	-67.50	67.50
37	0	60	0	180	210.29	95.54	2.64	71.92	10.61	0.00	3.00	17.18	-5.00	5.00	-67.50	67.50
38	0	60	0	210	120.25	62.55	0.99	34.01	8.50	0.00	4.35	12.45	-3.00	3.00	-78.75	78.75
39	0	60	0	210	150.16	66.30	1.38	43.88	8.94	0.00	4.35	13.13	-4.00	4.00	-78.75	78.75
40	0	60	0	210	180.38	69.70	1.71	50.76	9.26	0.00	3.68	13.80	-4.00	4.00	-78.75	78.75
41	0	60	0	210	210.29	72.71	1.97	57.17	9.52	0.00	3.68	14.48	-4.00	4.00	-90.00	90.00
42	0	60	0	210	240.20	75.39	2.16	61.72	9.71	0.00	3.68	15.15	-4.00	4.00	-90.00	90.00
43	0	30	30	90	45.17	54.66	0.09	5.71	7.39	6.00	5.70	9.08	-2.00	14.00	-11.25	11.25
44	0	30	30	90	60.43	57.95	0.31	13.54	8.43	6.00	5.03	11.78	-3.00	15.00	-11.25	11.25
45	0	30	30	90	120.25	68.44	1.46	46.98	10.30	6.02	4.35	15.83	-4.00	16.00	-22.50	22.50
46	0	30	30	90	150.16	72.77	1.87	54.80	10.89	6.01	3.68	17.18	-4.00	16.00	-22.50	22.50
47	0	30	30	90	180.38	76.66	2.25	64.25	11.32	6.01	3.68	18.53	-4.00	16.00	-22.50	22.50
48	0	30	30	90	210.29	80.08	2.60	73.50	11.62	6.01	3.68	19.20	-5.00	17.00	-33.75	33.75
49	0	30	30	90	240.20	83.11	2.88	80.09	11.77	6.02	3.68	19.20	-5.00	17.00	-33.75	33.75
50	0	30	30	90	270.42	85.82	3.08	83.45	11.89	6.03	3.68	19.88	-5.00	17.00	-33.75	33.75

Table 31 Prostate simulations parameters and results for Tests 51-100.

Test #	Q1 (W)	Q2 (W)	Q3 (W)	Angle (deg)	Heat Time (s)	Tmax (^{o}C)	Vnecr (cm^3)	Surf Area (cm^2)	r centroid (mm)	z centroid (mm)	r min (mm)	r max (mm)	z min (mm)	z max (mm)	theta min (deg)	theta max (deg)
51	0	30	30	90	300.33	88.17	3.27	87.49	12.01	6.02	3.68	19.88	-5.00	17.00	-33.75	33.75
52	0	30	30	90	360.46	92.13	3.64	97.23	12.38	6.01	3.00	21.23	-5.00	17.00	-33.75	33.75
53	0	30	30	120	120.25	57.61	0.61	27.07	8.48	6.00	5.03	11.78	-3.00	15.00	-33.75	33.75
54	0	30	30	120	150.16	59.87	1.01	38.47	8.90	6.00	5.03	12.45	-3.00	15.00	-33.75	33.75
55	0	30	30	120	180.38	61.85	1.30	44.54	9.34	6.01	4.35	13.80	-3.00	15.00	-33.75	33.75
56	0	30	30	120	210.29	63.55	1.57	52.20	9.55	6.02	4.35	14.48	-4.00	16.00	-33.75	33.75
57	0	30	30	120	240.20	65.04	1.87	62.08	9.69	6.05	4.35	14.48	-4.00	16.00	-45.00	45.00
58	0	30	30	150	180.38	52.22	0.00	1.02	7.73	6.00	7.73	7.73	0.00	12.00	-45.00	45.00
59	0	30	30	150	210.29	52.95	0.07	6.10	8.06	6.17	6.38	9.08	-1.00	13.00	-11.25	11.25
60	0	30	30	150	240.20	53.57	0.17	11.32	8.15	6.00	6.38	9.75	-1.00	13.00	-22.50	22.50
61	0	30	45	90	30.22	63.77	0.22	8.95	7.70	11.93	4.35	11.10	9.00	15.00	-22.50	22.50
62	0	30	45	90	45.17	76.05	0.63	21.27	9.13	11.05	3.68	14.48	-2.00	16.00	-22.50	22.50
63	0	30	45	90	60.43	89.63	1.14	35.93	10.14	10.09	3.00	17.18	-3.00	17.00	-33.75	33.75
64	0	30	45	120	30.22	54.65	0.04	3.64	6.53	11.89	5.03	7.73	10.00	14.00	-22.50	22.50
65	0	30	45	120	45.17	61.43	0.34	12.77	7.64	11.94	4.35	10.43	9.00	15.00	-33.75	33.75
66	0	30	45	120	60.43	68.27	0.68	23.00	8.57	11.81	3.68	13.13	8.00	16.00	-45.00	45.00
67	0	30	45	120	120.25	96.04	2.44	73.03	10.33	9.68	3.00	17.18	-3.00	17.00	-56.25	56.25
68	0	30	45	150	45.17	52.86	0.01	0.63	6.73	12.00	6.38	7.05	12.00	12.00	-11.25	11.25
69	0	30	45	150	60.43	56.17	0.17	8.79	7.40	11.90	5.03	9.75	9.00	14.00	-33.75	33.75
70	0	30	45	150	120.25	67.18	0.97	31.11	9.18	11.72	4.35	13.80	8.00	16.00	-56.25	56.25
71	0	30	45	150	150.16	71.86	1.34	40.70	9.62	11.68	3.68	15.15	1.00	16.00	-56.25	56.25
72	0	30	45	150	180.38	76.12	1.71	53.57	9.92	11.14	3.68	15.83	-1.00	16.00	-56.25	56.25
73	0	30	45	150	210.29	79.87	2.07	63.86	10.14	10.75	3.68	16.50	-1.00	17.00	-56.25	56.25
74	0	30	45	150	240.20	83.21	2.41	73.28	10.25	10.36	3.68	16.50	-2.00	17.00	-56.25	56.25
75	0	30	45	180	120.25	56.59	0.31	14.31	7.99	11.67	5.03	10.43	9.00	14.00	-45.00	45.00
76	0	30	45	180	150.16	58.79	0.52	20.19	8.47	11.74	5.03	11.78	8.00	15.00	-56.25	56.25
77	0	30	45	180	180.38	60.66	0.73	26.44	8.76	11.66	4.35	12.45	8.00	15.00	-56.25	56.25
78	0	30	45	180	210.29	62.25	0.89	30.32	8.99	11.61	4.35	13.13	8.00	15.00	-56.25	56.25
79	0	30	45	180	240.20	63.63	1.03	34.52	9.16	11.64	4.35	13.80	8.00	16.00	-56.25	56.25
80	0	30	45	210	150.16	52.74	0.04	3.94	7.56	11.65	6.38	8.40	11.00	13.00	-33.75	33.75
81	0	30	45	210	180.38	53.85	0.15	9.30	7.70	11.61	5.70	9.08	10.00	13.00	-45.00	45.00
82	0	30	45	210	210.29	54.79	0.26	14.32	7.92	11.74	5.70	9.75	9.00	14.00	-56.25	56.25
83	0	30	45	210	240.20	55.59	0.37	17.82	8.08	11.65	5.70	10.43	9.00	14.00	-56.25	56.25
84	0	30	60	90	30.22	87.54	0.63	19.16	9.18	11.96	3.00	14.48	8.00	16.00	-22.50	22.50
85	0	30	60	210	60.43	53.79	0.09	6.54	6.99	11.96	5.70	8.40	11.00	13.00	-56.25	56.25
86	0	30	60	210	120.25	63.30	1.15	38.22	8.66	11.74	4.35	12.45	8.00	15.00	-78.75	78.75
87	0	30	60	210	150.16	67.39	1.56	48.11	9.10	11.80	3.68	13.80	8.00	16.00	-78.75	78.75
88	0	30	60	210	180.38	71.12	1.92	56.45	9.47	11.78	3.68	14.48	7.00	16.00	-90.00	90.00
89	0	30	60	210	210.29	74.43	2.24	64.71	9.72	11.74	3.68	15.15	7.00	16.00	-90.00	90.00
90	0	30	60	210	240.20	77.37	2.52	70.77	9.94	11.72	3.68	15.15	7.00	17.00	-90.00	90.00
91	0	30	60	210	270.42	80.00	2.74	76.34	10.08	11.76	3.68	15.83	6.00	17.00	-90.00	90.00
92	0	30	60	210	300.33	82.30	2.96	81.83	10.21	11.72	3.00	15.83	6.00	17.00	-90.00	90.00
93	0	30	60	210	360.46	86.35	3.33	91.01	10.47	11.70	3.00	16.50	6.00	17.00	-90.00	90.00
94	0	45	45	90	30.22	63.79	0.45	18.39	7.70	6.00	4.35	11.10	-3.00	15.00	-22.50	22.50
95	0	45	45	90	45.17	76.17	1.20	37.51	9.26	6.00	3.68	14.48	-4.00	16.00	-22.50	22.50
96	0	45	45	90	60.43	89.95	2.05	60.07	10.47	6.00	3.00	17.18	-5.00	17.00	-33.75	33.75
97	0	45	45	120	30.22	54.67	0.08	7.29	6.52	6.00	5.03	7.73	-2.00	14.00	-22.50	22.50
98	0	45	45	120	45.17	61.51	0.69	26.12	7.67	6.00	4.35	10.43	-3.00	15.00	-33.75	33.75
99	0	45	45	120	60.43	68.46	1.42	47.75	8.62	6.00	3.68	13.13	-4.00	16.00	-45.00	45.00
100	0	45	45	120	120.25	97.58	4.31	115.15	10.89	6.01	3.00	17.85	-5.00	17.00	-56.25	56.25

Table 32 Prostate simulations parameters and results for Tests 101-150.

Test #	Q1 (W)	Q2 (W)	Q3 (W)	Angle (deg)	Heat Time (s)	Tmax (^oC)	Vnecr (cm^3)	Surf Area (cm^2)	r centroid (mm)	z centroid (mm)	r min (mm)	r max (mm)	z min (mm)	z max (mm)	theta min (deg)	theta max (deg)
101	0	45	45	150	45.17	52.91	0.01	1.62	6.68	6.00	6.38	7.05	0.00	12.00	-11.25	11.25
102	0	45	45	150	60.43	56.28	0.38	18.85	7.44	6.00	5.03	9.75	-2.00	14.00	-33.75	33.75
103	0	45	45	150	120.25	67.84	2.21	70.28	9.31	6.01	3.68	13.80	-4.00	16.00	-56.25	56.25
104	0	45	45	150	150.16	72.94	3.08	89.36	9.82	6.00	3.68	15.15	-4.00	16.00	-56.25	56.25
105	0	45	45	150	180.38	77.72	3.76	103.40	10.24	6.00	3.68	15.83	-4.00	16.00	-56.25	56.25
106	0	45	45	150	210.29	82.04	4.32	115.38	10.56	6.02	3.68	16.50	-5.00	17.00	-56.25	56.25
107	0	45	45	150	240.20	85.93	4.74	124.76	10.81	6.02	3.00	17.18	-5.00	17.00	-56.25	56.25
108	0	45	45	150	270.42	89.44	5.15	133.52	11.00	6.02	3.00	17.85	-5.00	17.00	-56.25	56.25
109	0	45	45	150	300.33	92.52	5.45	141.33	11.16	6.02	3.00	17.85	-5.00	17.00	-67.50	67.50
110	0	45	45	150	360.46	97.83	6.05	156.24	11.42	6.02	3.00	18.53	-5.00	17.00	-67.50	67.50
111	0	45	45	180	120.25	56.97	0.76	31.58	8.15	6.02	5.03	11.10	-2.00	14.00	-45.00	45.00
112	0	45	45	180	150.16	59.38	1.27	48.81	8.59	6.00	5.03	11.78	-3.00	15.00	-56.25	56.25
113	0	45	45	180	180.38	61.49	1.71	60.03	8.92	6.01	4.35	13.13	-3.00	15.00	-56.25	56.25
114	0	45	45	180	210.29	63.32	2.13	70.79	9.17	6.01	4.35	13.13	-3.00	16.00	-56.25	56.25
115	0	45	45	180	240.20	64.92	2.50	79.36	9.37	6.01	4.35	13.80	-4.00	16.00	-56.25	56.25
116	0	45	45	210	150.16	53.14	0.16	13.67	7.64	6.00	6.38	9.08	-1.00	13.00	-45.00	45.00
117	0	45	45	210	180.38	54.41	0.47	27.00	7.93	6.08	5.70	9.75	-2.00	14.00	-56.25	56.25
118	0	45	45	210	210.29	55.48	0.77	36.10	8.11	6.00	5.70	10.43	-2.00	14.00	-56.25	56.25
119	0	45	45	210	240.20	56.41	1.02	46.01	8.34	6.02	5.03	11.10	-2.00	14.00	-67.50	67.50
120	0	45	60	90	30.22	87.57	0.87	28.67	8.77	8.77	3.00	14.48	-3.00	16.00	-22.50	22.50
121	0	45	60	120	30.22	66.58	0.46	19.03	7.42	10.79	3.68	11.10	-2.00	15.00	-45.00	45.00
122	0	45	60	120	45.17	83.89	1.43	45.51	8.62	8.87	3.00	13.80	-3.00	16.00	-45.00	45.00
123	0	45	60	150	30.22	55.69	0.10	6.07	6.48	12.00	5.03	7.73	10.00	14.00	-33.75	33.75
124	0	45	60	150	45.17	63.62	0.53	19.54	7.84	11.72	4.35	11.10	0.00	15.00	-45.00	45.00
125	0	45	60	150	60.43	72.23	1.21	41.49	8.50	9.88	3.68	13.13	-2.00	16.00	-56.25	56.25
126	0	45	60	180	45.17	55.41	0.15	8.61	6.91	11.86	5.03	8.40	10.00	14.00	-45.00	45.00
127	0	45	60	180	60.43	59.96	0.47	18.71	7.73	11.87	4.35	10.43	9.00	15.00	-56.25	56.25
128	0	45	60	180	120.25	76.96	2.26	71.60	9.38	9.37	3.68	15.15	-2.00	16.00	-67.50	67.50
129	0	45	60	180	150.16	85.10	3.18	94.86	9.82	8.79	3.00	15.83	-3.00	17.00	-67.50	67.50
130	0	45	60	180	180.38	92.91	3.96	111.16	10.22	8.55	3.00	17.18	-3.00	17.00	-67.50	67.50
131	0	45	60	180	210.29	99.93	4.55	124.63	10.53	8.38	3.00	17.85	-4.00	17.00	-78.75	78.75
132	0	45	60	210	60.43	53.87	0.10	7.45	6.94	11.82	5.70	8.40	10.00	13.00	-56.25	56.25
133	0	45	60	210	120.25	63.69	1.21	39.52	8.71	11.63	4.35	12.45	8.00	15.00	-78.75	78.75
134	0	45	60	210	150.16	67.99	1.85	62.49	9.05	10.67	3.68	13.80	-1.00	16.00	-78.75	78.75
135	0	45	60	210	180.38	71.94	2.51	81.49	9.36	9.90	3.68	14.48	-2.00	16.00	-90.00	90.00
136	0	45	60	210	210.29	75.47	3.11	97.65	9.54	9.41	3.68	15.15	-2.00	16.00	-90.00	90.00
137	0	45	60	210	240.20	78.63	3.62	109.02	9.71	9.13	3.68	15.83	-2.00	17.00	-90.00	90.00
138	0	45	60	210	270.42	81.46	4.05	118.85	9.85	8.95	3.68	15.83	-3.00	17.00	-90.00	90.00
139	0	45	60	210	300.33	83.98	4.41	126.00	9.99	8.85	3.00	16.50	-3.00	17.00	-90.00	90.00
140	0	45	60	210	360.46	88.36	5.10	142.57	10.23	8.61	3.00	16.50	-3.00	17.00	-90.00	90.00
141	0	60	60	90	30.22	87.61	1.30	39.95	9.16	6.00	3.00	14.48	-4.00	16.00	-22.50	22.50
142	0	60	60	120	30.22	66.60	0.85	31.56	7.50	6.00	3.68	11.10	-3.00	15.00	-45.00	45.00
143	0	60	60	120	45.17	84.01	2.19	64.49	8.96	6.00	3.00	13.80	-4.00	16.00	-45.00	45.00
144	0	60	60	150	30.22	55.71	0.21	12.14	6.48	6.00	5.03	7.73	-2.00	14.00	-33.75	33.75
145	0	60	60	150	45.17	63.68	1.08	38.40	7.84	6.00	4.35	11.10	-3.00	15.00	-45.00	45.00
146	0	60	60	150	60.43	72.42	2.09	66.30	8.73	6.00	3.68	13.13	-4.00	16.00	-56.25	56.25
147	0	60	60	180	45.17	55.45	0.29	17.23	6.91	6.00	5.03	8.40	-2.00	14.00	-45.00	45.00
148	0	60	60	180	60.43	60.07	0.98	38.98	7.74	6.00	4.35	10.43	-3.00	15.00	-56.25	56.25
149	0	60	60	180	120.25	77.72	3.86	106.64	9.75	6.00	3.68	15.15	-4.00	16.00	-67.50	67.50
150	0	60	60	180	150.16	86.47	5.07	134.39	10.37	6.01	3.00	16.50	-5.00	17.00	-67.50	67.50

Table 33 Prostate simulations parameters and results for Tests 151-200.

Test #	Q1 (W)	Q2 (W)	Q3 (W)	Angle (deg)	Heat Time (s)	Tmax (^{o}C)	Vnecr (cm^{3})	Surf Area (cm^{2})	r centroid (mm)	z centroid (mm)	r min (mm)	r max (mm)	z min (mm)	z max (mm)	theta min (deg)	theta max (deg)
151	0	60	60	180	180.38	95.02	6.00	155.95	10.86	6.02	3.00	17.18	-5.00	17.00	-67.50	67.50
152	0	60	60	210	60.43	53.95	0.22	16.00	7.00	6.00	5.70	8.40	-1.00	13.00	-56.25	56.25
153	0	60	60	210	120.25	64.16	2.64	87.02	8.78	6.00	4.35	12.45	-3.00	16.00	-78.75	78.75
154	0	60	60	210	150.16	68.79	3.81	113.70	9.31	6.01	3.68	13.80	-4.00	16.00	-78.75	78.75
155	0	60	60	210	180.38	73.18	4.73	133.92	9.66	6.01	3.68	14.48	-4.00	16.00	-90.00	90.00
156	0	60	60	210	210.29	77.16	5.48	147.89	10.01	6.00	3.68	15.15	-4.00	16.00	-90.00	90.00
157	0	60	60	210	240.20	80.76	6.14	162.18	10.25	6.02	3.68	15.83	-5.00	17.00	-90.00	90.00
158	0	60	60	210	270.42	84.03	6.76	176.35	10.47	6.02	3.00	16.50	-5.00	17.00	-90.00	90.00
159	0	60	60	210	300.33	87.01	7.21	186.36	10.63	6.01	3.00	16.50	-5.00	17.00	-90.00	90.00
160	0	60	60	210	360.46	92.12	7.93	202.06	10.90	6.03	3.00	17.18	-5.00	17.00	-90.00	90.00
161	30	30	30	90	45.17	54.80	0.14	8.73	7.43	0.00	5.70	9.08	-14.00	14.00	-11.25	11.25
162	30	30	30	90	60.43	58.27	0.49	21.18	8.48	0.00	5.03	11.78	-15.00	15.00	-11.25	11.25
163	30	30	30	90	120.25	69.92	2.31	73.81	10.36	0.00	4.35	16.50	-16.00	16.00	-22.50	22.50
164	30	30	30	90	150.16	74.95	3.02	87.12	11.01	0.00	3.68	17.85	-16.00	16.00	-22.50	22.50
165	30	30	30	90	180.38	79.57	3.71	104.13	11.48	0.00	3.68	19.20	-16.00	16.00	-33.75	33.75
166	30	30	30	90	210.29	83.67	4.23	117.69	11.72	0.00	3.68	19.88	-17.00	17.00	-33.75	33.75
167	30	30	30	90	240.20	87.32	4.69	127.37	11.90	0.00	3.68	19.88	-17.00	17.00	-33.75	33.75
168	30	30	30	90	270.42	90.56	5.09	135.25	12.07	0.00	3.00	20.55	-17.00	17.00	-33.75	33.75
169	30	30	30	90	300.33	93.41	5.36	140.07	12.20	0.00	3.00	20.55	-17.00	17.00	-33.75	33.75
170	30	30	30	90	360.46	98.25	5.94	155.00	12.50	0.00	3.00	21.23	-17.00	17.00	-33.75	33.75
171	30	30	30	120	120.25	58.63	1.02	44.56	8.55	0.00	5.03	11.78	-15.00	15.00	-33.75	33.75
172	30	30	30	120	150.16	61.31	1.66	61.74	9.00	0.00	4.35	13.13	-15.00	15.00	-33.75	33.75
173	30	30	30	120	180.38	63.66	2.17	74.30	9.45	0.00	4.35	14.48	-15.00	15.00	-33.75	33.75
174	30	30	30	120	210.29	65.71	2.70	90.45	9.71	0.00	4.35	15.15	-16.00	16.00	-45.00	45.00
175	30	30	30	120	240.20	67.52	3.19	102.41	9.84	0.00	4.35	15.15	-16.00	16.00	-45.00	45.00
176	30	30	30	150	150.16	52.17	0.00	0.26	7.73	0.00	7.73	15.15	0.00	16.00	-45.00	45.00
177	30	30	30	150	180.38	53.23	0.05	4.95	8.01	0.00	6.38	9.08	-12.00	12.00	-22.50	22.50
178	30	30	30	150	210.29	54.10	0.20	13.86	8.14	0.00	6.38	10.43	-13.00	13.00	-22.50	22.50
179	30	30	30	150	240.20	54.85	0.38	23.15	8.27	0.00	5.70	11.10	-13.00	13.00	-33.75	33.75
180	30	30	45	90	30.22	63.77	0.22	8.95	7.70	11.93	4.35	11.10	9.00	15.00	-22.50	22.50
181	30	30	45	90	45.17	76.05	0.67	24.21	9.02	9.51	3.68	14.48	-14.00	16.00	-22.50	22.50
182	30	30	45	90	60.43	89.63	1.31	43.43	9.93	7.34	3.00	17.18	-15.00	17.00	-33.75	33.75
183	30	30	45	120	30.22	54.65	0.04	3.64	6.53	11.89	5.03	7.73	10.00	14.00	-22.50	22.50
184	30	30	45	120	45.17	61.43	0.34	12.77	7.64	11.94	4.35	10.43	9.00	15.00	-33.75	33.75
185	30	30	45	120	60.43	68.27	0.68	23.00	8.57	11.81	3.68	13.13	8.00	16.00	-45.00	45.00
186	30	30	45	120	120.25	96.05	2.87	90.33	10.11	6.94	3.00	17.18	-15.00	17.00	-56.25	56.25
187	30	30	45	150	45.17	52.86	0.01	0.63	6.73	12.00	6.38	7.05	12.00	12.00	-11.25	11.25
188	30	30	45	150	60.43	56.17	0.17	8.79	7.40	11.90	5.03	9.75	9.00	14.00	-33.75	33.75
189	30	30	45	150	120.25	67.18	0.97	31.11	9.18	11.72	4.35	13.80	8.00	16.00	-56.25	56.25
190	30	30	45	150	150.16	71.87	1.37	43.91	9.60	11.41	3.68	15.15	-1.00	16.00	-56.25	56.25
191	30	30	45	150	180.38	76.13	1.81	58.25	9.86	10.58	3.68	15.83	-12.00	16.00	-56.25	56.25
192	30	30	45	150	210.29	79.90	2.26	72.83	10.02	9.74	3.68	16.50	-13.00	17.00	-56.25	56.25
193	30	30	45	150	240.20	83.24	2.66	83.81	10.12	9.02	3.68	16.50	-13.00	17.00	-56.25	56.25
194	30	30	45	150	270.42	86.23	3.00	91.75	10.24	8.56	3.00	17.18	-13.00	17.00	-56.25	56.25
195	30	30	45	150	300.33	88.84	3.29	100.59	10.35	8.25	3.00	17.18	-14.00	17.00	-56.25	56.25
196	30	30	45	150	360.46	93.24	3.94	117.38	10.53	7.16	3.00	17.85	-14.00	17.00	-67.50	67.50
197	30	30	45	180	120.25	56.59	0.31	14.31	7.99	11.67	5.03	10.43	9.00	14.00	-45.00	45.00
198	30	30	45	180	150.16	58.79	0.52	20.19	8.47	11.74	5.03	11.78	8.00	15.00	-56.25	56.25
199	30	30	45	180	180.38	60.67	0.73	26.51	8.76	11.64	4.35	12.45	8.00	15.00	-56.25	56.25
200	30	30	45	180	210.29	62.26	0.89	30.37	8.99	11.62	4.35	13.13	8.00	15.00	-56.25	56.25

Table 34 Prostate simulations parameters and results for Tests 201-250.

Test #	Q1 (W)	Q2 (W)	Q3 (W)	Angle (deg)	Heat Time (s)	Tmax (^{o}C)	Vnecr (cm^3)	Surf Area (cm^2)	r centroid (mm)	z centroid (mm)	r min (mm)	r max (mm)	z min (mm)	z max (mm)	theta min (deg)	theta max (deg)
201	30	30	45	180	240.20	63.65	1.03	34.54	9.16	11.62	4.35	13.80	8.00	16.00	-56.25	56.25
202	30	30	45	210	150.16	52.74	0.04	3.94	7.56	11.65	6.38	8.40	11.00	13.00	-33.75	33.75
203	30	30	45	210	180.38	53.86	0.15	9.35	7.72	11.61	5.70	9.75	10.00	13.00	-45.00	45.00
204	30	30	45	210	210.29	54.80	0.26	14.31	7.91	11.74	5.70	9.75	9.00	14.00	-56.25	56.25
205	30	30	45	210	240.20	55.60	0.37	17.92	8.09	11.61	5.70	10.43	9.00	14.00	-56.25	56.25
206	30	30	60	90	30.22	87.54	0.63	19.16	9.18	11.96	3.00	14.48	8.00	16.00	-22.50	22.50
207	30	30	60	120	30.22	66.56	0.42	15.34	7.51	11.89	3.68	11.10	8.00	15.00	-45.00	45.00
208	30	30	60	120	45.17	83.78	1.03	30.67	8.94	11.93	3.00	13.80	7.00	16.00	-45.00	45.00
209	30	30	60	150	30.22	55.68	0.10	6.07	6.48	12.00	5.03	7.73	10.00	14.00	-33.75	33.75
210	30	30	60	150	45.17	63.55	0.50	17.61	7.80	11.95	4.35	11.10	8.00	15.00	-45.00	45.00
211	30	30	60	150	60.43	72.06	0.98	30.73	8.70	11.91	3.68	13.13	8.00	16.00	-56.25	56.25
212	30	30	60	180	45.17	55.36	0.14	8.55	6.90	11.86	5.03	8.40	10.00	14.00	-45.00	45.00
213	30	30	60	180	60.43	59.85	0.46	18.29	7.74	11.94	4.35	10.43	9.00	15.00	-56.25	56.25
214	30	30	60	180	120.25	76.36	1.67	48.52	9.58	11.77	3.68	14.48	7.00	16.00	-67.50	67.50
215	30	30	60	180	150.16	84.13	2.16	60.53	10.11	11.76	3.00	15.83	6.00	17.00	-67.50	67.50
216	30	30	60	180	180.38	91.56	2.64	72.86	10.50	11.70	3.00	16.50	6.00	17.00	-67.50	67.50
217	30	30	60	180	210.29	98.20	3.01	83.26	10.80	11.60	3.00	17.18	4.00	17.00	-67.50	67.50
218	30	30	60	210	60.43	53.79	0.09	6.54	6.99	11.96	5.70	8.40	11.00	13.00	-56.25	56.25
219	30	30	60	210	120.25	63.30	1.15	38.22	8.66	11.74	4.35	12.45	8.00	15.00	-78.75	78.75
220	30	30	60	210	150.16	67.40	1.56	48.07	9.10	11.79	3.68	13.80	8.00	16.00	-78.75	78.75
221	30	30	60	210	180.38	71.13	1.92	56.45	9.47	11.78	3.68	14.48	7.00	16.00	-90.00	90.00
222	30	30	60	210	210.29	74.44	2.24	64.81	9.72	11.73	3.68	15.15	7.00	16.00	-90.00	90.00
223	30	30	60	210	240.20	77.39	2.52	70.77	9.94	11.72	3.68	15.15	7.00	17.00	-90.00	90.00
224	30	30	60	210	270.42	80.03	2.75	76.92	10.07	11.74	3.68	15.83	6.00	17.00	-90.00	90.00
225	30	30	60	210	300.33	82.34	2.97	82.43	10.21	11.70	3.00	15.83	6.00	17.00	-90.00	90.00
226	30	30	60	210	360.46	86.40	3.34	91.18	10.47	11.68	3.00	16.50	6.00	17.00	-90.00	90.00
227	30	45	45	90	30.22	63.84	0.46	18.57	7.72	5.83	4.35	11.10	-3.00	15.00	-22.50	22.50
228	30	45	45	90	45.17	76.38	1.26	41.30	9.25	5.21	3.68	15.15	-14.00	16.00	-22.50	22.50
229	30	45	45	90	60.43	90.52	2.28	69.35	10.36	4.42	3.00	17.18	-15.00	17.00	-33.75	33.75
230	30	45	45	120	30.22	54.70	0.08	7.65	6.53	5.76	5.03	7.73	-2.00	14.00	-22.50	22.50
231	30	45	45	120	45.17	61.66	0.70	26.33	7.68	5.88	4.35	11.10	-3.00	15.00	-33.75	33.75
232	30	45	45	120	60.43	68.84	1.48	48.99	8.66	5.69	3.68	13.13	-4.00	16.00	-45.00	45.00
233	30	45	45	120	120.25	99.64	5.01	139.01	10.75	4.03	3.00	17.85	-15.00	17.00	-56.25	56.25
234	30	45	45	150	45.17	53.00	0.01	1.78	6.66	5.55	6.38	7.05	-1.00	12.00	-11.25	11.25
235	30	45	45	150	60.43	56.51	0.40	19.78	7.48	5.57	5.03	9.75	-3.00	14.00	-33.75	33.75
236	30	45	45	150	120.25	68.91	2.35	73.72	9.38	5.56	3.68	14.48	-4.00	16.00	-56.25	56.25
237	30	45	45	150	150.16	74.50	3.27	94.58	9.89	5.52	3.68	15.15	-11.00	16.00	-56.25	56.25
238	30	45	45	150	180.38	79.69	4.11	116.29	10.27	5.11	3.68	16.50	-13.00	16.00	-56.25	56.25
239	30	45	45	150	210.29	84.37	4.82	133.80	10.57	4.82	3.00	17.18	-13.00	17.00	-56.25	56.25
240	30	45	45	150	240.20	88.57	5.46	149.24	10.77	4.49	3.00	17.85	-14.00	17.00	-56.25	56.25
241	30	45	45	150	270.42	92.34	5.97	160.30	10.97	4.28	3.00	17.85	-14.00	17.00	-56.25	56.25
242	30	45	45	150	300.33	95.67	6.44	171.82	11.12	4.12	3.00	18.53	-14.00	17.00	-67.50	67.50
243	30	45	45	180	120.25	57.65	0.84	34.61	8.22	5.34	5.03	11.10	-3.00	14.00	-45.00	45.00
244	30	45	45	180	150.16	60.29	1.39	52.88	8.68	5.37	4.35	12.45	-4.00	15.00	-56.25	56.25
245	30	45	45	180	180.38	62.60	1.90	65.76	9.03	5.30	4.35	13.13	-4.00	15.00	-56.25	56.25
246	30	45	45	180	210.29	64.60	2.34	76.37	9.27	5.36	4.35	13.80	-4.00	16.00	-56.25	56.25
247	30	45	45	180	240.20	66.36	2.72	84.34	9.51	5.43	4.35	14.48	-4.00	16.00	-56.25	56.25
248	30	45	45	210	150.16	53.80	0.24	17.29	7.71	4.10	5.70	9.08	-2.00	13.00	-45.00	45.00
249	30	45	45	210	180.38	55.19	0.60	31.51	8.01	4.74	5.70	10.43	-2.00	14.00	-56.25	56.25
250	30	45	45	210	210.29	56.37	0.91	41.62	8.24	5.00	5.03	11.10	-3.00	14.00	-67.50	67.50

Table 35 Prostate simulations parameters and results for Tests 251-300.

Test #	Q1 (W)	Q2 (W)	Q3 (W)	Angle (deg)	Heat Time (s)	Tmax (^{o}C)	Vnecr (cm^3)	Surf Area (cm^2)	r centroid (mm)	z centroid (mm)	r min (mm)	r max (mm)	z min (mm)	z max (mm)	theta min (deg)	theta max (deg)
251	30	45	45	210	240.20	57.39	1.21	51.65	8.40	4.98	5.03	11.78	-3.00	14.00	-67.50	67.50
252	30	45	60	90	30.22	87.57	0.88	28.87	8.78	8.66	3.00	14.48	-3.00	16.00	-22.50	22.50
253	30	45	60	120	30.22	66.58	0.46	19.36	7.42	10.75	3.68	11.10	-2.00	15.00	-45.00	45.00
254	30	45	60	120	45.17	83.89	1.44	45.66	8.62	8.80	3.00	13.80	-3.00	16.00	-45.00	45.00
255	30	45	60	150	30.22	55.69	0.10	6.07	6.48	12.00	5.03	7.73	10.00	14.00	-33.75	33.75
256	30	45	60	150	45.17	63.62	0.53	20.05	7.83	11.66	4.35	11.10	-1.00	15.00	-45.00	45.00
257	30	45	60	150	60.43	72.23	1.23	42.43	8.50	9.68	3.68	13.13	-3.00	16.00	-56.25	56.25
258	30	45	60	180	45.17	55.41	0.15	8.61	6.91	11.86	5.03	8.40	10.00	14.00	-45.00	45.00
259	30	45	60	180	60.43	59.96	0.47	18.71	7.73	11.87	4.35	10.43	9.00	15.00	-56.25	56.25
260	30	45	60	180	120.25	76.96	2.35	74.75	9.36	8.98	3.68	15.15	-3.00	16.00	-67.50	67.50
261	30	45	60	180	150.16	85.10	3.32	98.44	9.82	8.39	3.00	15.83	-4.00	17.00	-67.50	67.50
262	30	45	60	180	180.38	92.93	4.15	115.92	10.22	8.09	3.00	17.18	-4.00	17.00	-67.50	67.50
263	30	45	60	180	210.29	99.96	4.76	129.61	10.55	7.96	3.00	17.85	-4.00	17.00	-78.75	78.75
264	30	45	60	210	60.43	53.87	0.10	7.45	6.94	11.82	5.70	8.40	10.00	13.00	-56.25	56.25
265	30	45	60	210	120.25	63.69	1.23	41.97	8.69	11.46	4.35	12.45	0.00	15.00	-78.75	78.75
266	30	45	60	210	150.16	67.99	1.95	66.37	9.02	10.17	3.68	13.80	-2.00	16.00	-78.75	78.75
267	30	45	60	210	180.38	71.96	2.64	84.79	9.33	9.44	3.68	14.48	-2.00	16.00	-90.00	90.00
268	30	45	60	210	210.29	75.49	3.30	102.87	9.51	8.88	3.68	15.15	-3.00	16.00	-90.00	90.00
269	30	45	60	210	240.20	78.66	3.81	114.23	9.69	8.64	3.68	15.83	-3.00	17.00	-90.00	90.00
270	30	45	60	210	270.42	81.50	4.25	123.44	9.86	8.50	3.68	15.83	-3.00	17.00	-90.00	90.00
271	30	45	60	210	300.33	84.04	4.65	133.33	9.99	8.36	3.00	16.50	-4.00	17.00	-90.00	90.00
272	30	45	60	210	360.46	88.44	5.36	149.00	10.22	8.14	3.00	16.50	-4.00	17.00	-90.00	90.00
273	30	60	60	90	30.22	87.67	1.30	40.06	9.17	5.95	3.00	14.48	-4.00	16.00	-22.50	22.50
274	30	60	60	120	30.22	66.65	0.87	32.28	7.51	5.83	3.68	11.10	-4.00	15.00	-45.00	45.00
275	30	60	60	120	45.17	84.24	2.21	65.48	8.97	5.92	3.00	13.80	-5.00	16.00	-45.00	45.00
276	30	60	60	150	30.22	55.73	0.21	12.14	6.48	6.00	5.03	7.73	-2.00	14.00	-33.75	33.75
277	30	60	60	150	45.17	63.81	1.09	39.06	7.84	5.92	4.35	11.10	-4.00	15.00	-45.00	45.00
278	30	60	60	150	60.43	72.75	2.12	66.67	8.74	5.88	3.68	13.13	-4.00	16.00	-56.25	56.25
279	30	60	60	180	45.17	55.54	0.30	17.68	6.92	5.68	5.03	8.40	-2.00	14.00	-45.00	45.00
280	30	60	60	180	60.43	60.28	1.00	39.53	7.75	5.86	4.35	10.43	-3.00	15.00	-56.25	56.25
281	30	60	60	180	120.25	78.82	4.03	111.73	9.81	5.63	3.68	15.15	-5.00	16.00	-67.50	67.50
282	30	60	60	180	150.16	88.11	5.29	139.78	10.45	5.65	3.00	16.50	-6.00	17.00	-67.50	67.50
283	30	60	60	180	180.38	97.11	6.27	162.99	10.91	5.63	3.00	17.18	-6.00	17.00	-67.50	67.50
284	30	60	60	210	60.43	54.10	0.24	16.48	7.00	5.65	5.70	8.40	-1.00	13.00	-56.25	56.25
285	30	60	60	210	120.25	64.91	2.79	91.61	8.82	5.59	4.35	13.13	-4.00	16.00	-78.75	78.75
286	30	60	60	210	150.16	69.85	3.97	116.60	9.36	5.70	3.68	13.80	-4.00	16.00	-78.75	78.75
287	30	60	60	210	180.38	74.49	4.97	139.26	9.75	5.66	3.68	15.15	-5.00	16.00	-90.00	90.00
288	30	60	60	210	210.29	78.67	5.78	155.23	10.09	5.60	3.68	15.83	-5.00	16.00	-90.00	90.00
289	30	60	60	210	240.20	82.46	6.46	169.79	10.34	5.65	3.68	16.50	-5.00	17.00	-90.00	90.00
290	30	60	60	210	270.42	85.92	7.10	185.64	10.55	5.62	3.00	16.50	-6.00	17.00	-90.00	90.00
291	30	60	60	210	300.33	89.07	7.59	196.40	10.72	5.61	3.00	17.18	-6.00	17.00	-90.00	90.00
292	30	60	60	210	360.46	94.35	8.36	214.02	10.98	5.60	3.00	17.18	-7.00	17.00	-90.00	90.00
293	45	30	45	90	30.22	63.77	0.45	17.90	7.70	0.00	4.35	11.10	-15.00	15.00	-22.50	22.50
294	45	30	45	90	45.17	76.05	1.21	39.69	9.20	0.00	3.68	14.48	-16.00	16.00	-22.50	22.50
295	45	30	45	90	60.43	89.63	2.13	65.68	10.25	0.00	3.00	17.18	-17.00	17.00	-33.75	33.75
296	45	30	45	120	30.22	54.65	0.08	7.28	6.53	0.00	5.03	7.73	-14.00	14.00	-22.50	22.50
297	45	30	45	120	45.17	61.43	0.68	25.53	7.64	0.00	4.35	10.43	-15.00	15.00	-33.75	33.75
298	45	30	45	120	60.43	68.27	1.36	45.99	8.57	0.00	3.68	13.13	-16.00	16.00	-45.00	45.00
299	45	30	45	120	120.25	96.05	4.70	134.95	10.44	0.00	3.00	17.18	-17.00	17.00	-56.25	56.25
300	45	30	45	150	45.17	52.86	0.01	1.27	6.73	0.00	6.38	7.05	-12.00	12.00	-11.25	11.25

Table 36 Prostate simulations parameters and results for Tests 301-350.

Test #	Q1 (W)	Q2 (W)	Q3 (W)	Angle (deg)	Heat Time (s)	Tmax (^{o}C)	Vnecr (cm^3)	Surf Area (cm^2)	r centroid (mm)	z centroid (mm)	r min (mm)	r max (mm)	z min (mm)	z max (mm)	theta min (deg)	theta max (deg)
301	45	30	45	150	60.43	56.17	0.34	17.57	7.40	0.00	5.03	9.75	-14.00	14.00	-33.75	33.75
302	45	30	45	150	120.25	67.18	1.93	62.23	9.18	0.00	4.35	13.80	-16.00	16.00	-56.25	56.25
303	45	30	45	150	150.16	71.87	2.77	87.44	9.60	0.00	3.68	15.15	-16.00	16.00	-56.25	56.25
304	45	30	45	150	180.38	76.14	3.58	110.91	9.89	0.00	3.68	15.83	-16.00	16.00	-56.25	56.25
305	45	30	45	150	210.29	79.91	4.34	130.12	10.12	0.00	3.68	16.50	-17.00	17.00	-56.25	56.25
306	45	30	45	150	240.20	83.27	4.97	144.66	10.30	0.00	3.68	16.50	-17.00	17.00	-56.25	56.25
307	45	30	45	150	270.42	86.27	5.51	157.85	10.45	0.00	3.00	17.18	-17.00	17.00	-56.25	56.25
308	45	30	45	150	300.33	88.89	5.96	166.86	10.57	0.00	3.00	17.18	-17.00	17.00	-56.25	56.25
309	45	30	45	150	360.46	93.32	6.72	183.61	10.83	0.00	3.00	17.85	-17.00	17.00	-67.50	67.50
310	45	30	45	180	120.25	56.59	0.62	28.61	7.99	0.00	5.03	10.43	-14.00	14.00	-45.00	45.00
311	45	30	45	180	150.16	58.79	1.04	40.39	8.47	0.00	5.03	11.78	-15.00	15.00	-56.25	56.25
312	45	30	45	180	180.38	60.67	1.46	53.01	8.76	0.00	4.35	12.45	-15.00	15.00	-56.25	56.25
313	45	30	45	180	210.29	62.27	1.78	60.74	8.99	0.00	4.35	13.13	-15.00	15.00	-56.25	56.25
314	45	30	45	180	240.20	63.66	2.06	69.08	9.16	0.00	4.35	13.80	-16.00	16.00	-56.25	56.25
315	45	30	45	210	150.16	52.74	0.08	7.88	7.56	0.00	6.38	8.40	-13.00	13.00	-33.75	33.75
316	45	30	45	210	180.38	53.86	0.30	18.69	7.72	0.00	5.70	9.75	-13.00	13.00	-45.00	45.00
317	45	30	45	210	210.29	54.80	0.53	28.58	7.91	0.00	5.70	9.75	-14.00	14.00	-56.25	56.25
318	45	30	45	210	240.20	55.61	0.75	35.94	8.09	0.00	5.70	10.43	-14.00	14.00	-56.25	56.25
319	45	30	60	90	30.22	87.54	0.85	28.11	8.79	5.71	3.00	14.48	-15.00	16.00	-22.50	22.50
320	45	30	60	120	30.22	66.56	0.45	18.98	7.43	9.83	3.68	11.10	-14.00	15.00	-45.00	45.00
321	45	30	60	120	45.17	83.78	1.37	43.44	8.62	6.05	3.00	13.80	-15.00	16.00	-45.00	45.00
322	45	30	60	150	30.22	55.68	0.10	6.07	6.48	12.00	5.03	7.73	10.00	14.00	-33.75	33.75
323	45	30	60	150	45.17	63.55	0.51	18.24	7.79	11.70	4.35	11.10	-12.00	15.00	-45.00	45.00
324	45	30	60	150	60.43	72.06	1.15	39.51	8.50	8.38	3.68	13.13	-14.00	16.00	-56.25	56.25
325	45	30	60	180	45.17	55.36	0.14	8.55	6.90	11.86	5.03	8.40	10.00	14.00	-45.00	45.00
326	45	30	60	180	60.43	59.85	0.46	18.29	7.74	11.94	4.35	10.43	9.00	15.00	-56.25	56.25
327	45	30	60	180	120.25	76.36	1.98	62.83	9.33	8.10	3.68	14.48	-14.00	16.00	-67.50	67.50
328	45	30	60	180	150.16	84.13	2.69	81.68	9.79	7.20	3.00	15.83	-15.00	17.00	-67.50	67.50
329	45	30	60	180	180.38	91.56	3.38	99.56	10.13	6.63	3.00	16.50	-15.00	17.00	-67.50	67.50
330	45	30	60	180	210.29	98.21	3.92	113.95	10.39	6.29	3.00	17.18	-15.00	17.00	-67.50	67.50
331	45	30	60	210	60.43	53.79	0.09	6.54	6.99	11.96	5.70	8.40	11.00	13.00	-56.25	56.25
332	45	30	60	210	120.25	63.30	1.15	38.22	8.66	11.74	4.35	12.45	8.00	15.00	-78.75	78.75
333	45	30	60	210	150.16	67.40	1.60	52.01	9.06	11.21	3.68	13.80	-13.00	16.00	-78.75	78.75
334	45	30	60	210	180.38	71.14	2.07	65.80	9.34	10.07	3.68	14.48	-13.00	16.00	-90.00	90.00
335	45	30	60	210	210.29	74.45	2.51	79.09	9.53	9.26	3.68	15.15	-14.00	16.00	-90.00	90.00
336	45	30	60	210	240.20	77.40	2.90	88.83	9.70	8.67	3.68	15.15	-14.00	17.00	-90.00	90.00
337	45	30	60	210	270.42	80.04	3.22	97.81	9.81	8.31	3.68	15.83	-14.00	17.00	-90.00	90.00
338	45	30	60	210	300.33	82.36	3.52	105.48	9.92	8.04	3.00	15.83	-15.00	17.00	-90.00	90.00
339	45	30	60	210	360.46	86.43	4.19	124.03	10.16	6.96	3.00	16.50	-15.00	17.00	-90.00	90.00
340	45	45	45	90	30.22	63.86	0.69	27.95	7.71	0.00	4.35	11.10	-15.00	15.00	-22.50	22.50
341	45	45	45	90	45.17	76.50	1.83	57.62	9.31	0.00	3.68	15.15	-16.00	16.00	-22.50	22.50
342	45	45	45	90	60.43	90.85	3.19	93.52	10.50	0.00	3.00	17.85	-17.00	17.00	-33.75	33.75
343	45	45	45	120	30.22	54.72	0.13	11.30	6.53	0.00	5.03	7.73	-14.00	14.00	-22.50	22.50
344	45	45	45	120	45.17	61.73	1.05	39.75	7.69	0.00	4.35	11.10	-15.00	15.00	-33.75	33.75
345	45	45	45	120	60.43	69.04	2.21	73.63	8.66	0.00	3.68	13.13	-16.00	16.00	-45.00	45.00
346	45	45	45	150	45.17	53.05	0.02	2.65	6.70	0.00	6.38	7.05	-12.00	12.00	-11.25	11.25
347	45	45	45	150	60.43	56.63	0.60	29.61	7.46	0.00	5.03	9.75	-14.00	14.00	-33.75	33.75
348	45	45	45	150	120.25	69.58	3.59	113.07	9.39	0.00	3.68	14.48	-16.00	16.00	-56.25	56.25
349	45	45	45	150	150.16	75.59	5.03	142.84	9.93	0.00	3.68	15.83	-16.00	16.00	-56.25	56.25
350	45	45	45	150	180.38	81.28	6.13	165.74	10.37	0.00	3.68	16.50	-16.00	16.00	-56.25	56.25

Table 37 Prostate simulations parameters and results for Tests 351-400.

Test #	Q1 (W)	Q2 (W)	Q3 (W)	Angle (deg)	Heat Time (s)	Tmax (^{o}C)	Vnecr (cm^3)	Surf Area (cm^2)	r centroid (mm)	z centroid (mm)	r min (mm)	r max (mm)	z min (mm)	z max (mm)	theta min (deg)	theta max (deg)
351	45	45	45	150	210.29	86.47	7.07	184.88	10.72	0.00	3.00	17.18	-17.00	17.00	-56.25	56.25
352	45	45	45	150	240.20	91.17	7.79	200.11	10.98	0.00	3.00	17.85	-17.00	17.00	-56.25	56.25
353	45	45	45	150	270.42	95.43	8.44	215.31	11.21	0.00	3.00	18.53	-17.00	17.00	-67.50	67.50
354	45	45	45	150	300.33	99.29	9.01	229.36	11.38	0.00	3.00	18.53	-17.00	17.00	-67.50	67.50
355	45	45	45	180	120.25	58.03	1.26	51.34	8.22	0.00	5.03	11.10	-14.00	14.00	-45.00	45.00
356	45	45	45	180	150.16	60.87	2.14	79.90	8.68	0.00	4.35	12.45	-15.00	15.00	-56.25	56.25
357	45	45	45	180	180.38	63.39	2.91	99.88	9.07	0.00	4.35	13.80	-15.00	15.00	-56.25	56.25
358	45	45	45	180	210.29	65.60	3.65	118.84	9.33	0.00	4.35	14.48	-16.00	16.00	-56.25	56.25
359	45	45	45	180	240.20	67.57	4.23	131.37	9.54	0.00	4.35	14.48	-16.00	16.00	-56.25	56.25
360	45	45	45	210	120.25	52.44	0.01	1.23	7.40	0.00	7.05	7.73	0.00	0.00	-22.50	22.50
361	45	45	45	210	150.16	54.18	0.38	25.80	7.76	0.00	5.70	9.75	-13.00	13.00	-56.25	56.25
362	45	45	45	210	180.38	55.70	0.92	48.28	8.04	0.00	5.70	10.43	-14.00	14.00	-56.25	56.25
363	45	45	45	210	210.29	57.00	1.42	62.08	8.26	0.00	5.03	11.10	-14.00	14.00	-67.50	67.50
364	45	45	45	210	240.20	58.12	1.90	80.08	8.46	0.00	5.03	11.78	-14.00	14.00	-67.50	67.50
365	45	45	60	90	30.22	87.57	1.11	38.24	8.55	4.42	3.00	14.48	-15.00	16.00	-22.50	22.50
366	45	45	60	120	30.22	66.58	0.51	23.01	7.34	8.87	3.68	11.10	-14.00	15.00	-45.00	45.00
367	45	45	60	120	45.17	83.89	1.79	59.15	8.44	4.76	3.00	13.80	-15.00	16.00	-45.00	45.00
368	45	45	60	150	30.22	55.69	0.10	6.07	6.48	12.00	5.03	7.73	10.00	14.00	-33.75	33.75
369	45	45	60	150	45.17	63.62	0.54	20.88	7.82	11.37	4.35	11.10	-12.00	15.00	-45.00	45.00
370	45	45	60	150	60.43	72.23	1.44	52.33	8.35	6.76	3.68	13.13	-14.00	16.00	-56.25	56.25
371	45	45	60	180	45.17	55.41	0.15	8.61	6.91	11.86	5.03	8.40	10.00	14.00	-45.00	45.00
372	45	45	60	180	60.43	59.96	0.47	18.71	7.73	11.87	4.35	10.43	9.00	15.00	-56.25	56.25
373	45	45	60	180	120.25	76.96	2.78	91.57	9.19	5.97	3.68	15.15	-14.00	16.00	-67.50	67.50
374	45	45	60	180	150.16	85.11	4.08	125.90	9.62	4.99	3.00	15.83	-15.00	17.00	-67.50	67.50
375	45	45	60	180	180.38	92.94	5.15	150.03	10.01	4.56	3.00	17.18	-15.00	17.00	-67.50	67.50
376	45	45	60	180	210.29	99.98	6.06	171.22	10.31	4.13	3.00	17.85	-16.00	17.00	-78.75	78.75
377	45	45	60	210	60.43	53.87	0.10	7.45	6.94	11.82	5.70	8.40	10.00	13.00	-56.25	56.25
378	45	45	60	210	120.25	63.69	1.26	43.49	8.68	11.26	4.35	12.45	-1.00	15.00	-78.75	78.75
379	45	45	60	210	150.16	68.00	2.08	74.84	8.94	9.04	3.68	13.80	-13.00	16.00	-78.75	78.75
380	45	45	60	210	180.38	71.96	2.99	104.02	9.20	7.40	3.68	14.48	-14.00	16.00	-90.00	90.00
381	45	45	60	210	210.29	75.50	3.80	124.14	9.36	6.51	3.68	15.15	-14.00	16.00	-90.00	90.00
382	45	45	60	210	240.20	78.68	4.51	142.38	9.54	5.96	3.68	15.83	-14.00	17.00	-90.00	90.00
383	45	45	60	210	270.42	81.53	5.10	156.33	9.68	5.63	3.68	15.83	-15.00	17.00	-90.00	90.00
384	45	45	60	210	300.33	84.07	5.63	168.81	9.80	5.32	3.00	16.50	-15.00	17.00	-90.00	90.00
385	45	45	60	210	360.46	88.49	6.62	191.68	10.04	4.80	3.00	16.50	-15.00	17.00	-90.00	90.00
386	45	60	60	90	30.22	87.71	1.54	49.53	8.94	3.23	3.00	14.48	-15.00	16.00	-22.50	22.50
387	45	60	60	120	30.22	66.67	0.91	35.97	7.47	4.98	3.68	11.10	-14.00	15.00	-45.00	45.00
388	45	60	60	120	45.17	84.35	2.61	80.32	8.79	3.34	3.00	13.80	-15.00	16.00	-45.00	45.00
389	45	60	60	150	30.22	55.75	0.21	12.14	6.48	6.00	5.03	7.73	-2.00	14.00	-33.75	33.75
390	45	60	60	150	45.17	63.87	1.11	40.40	7.84	5.70	4.35	11.10	-12.00	15.00	-45.00	45.00
391	45	60	60	150	60.43	72.92	2.36	77.45	8.64	4.25	3.68	13.13	-14.00	16.00	-56.25	56.25
392	45	60	60	180	45.17	55.58	0.30	17.68	6.92	5.68	5.03	8.40	-2.00	14.00	-45.00	45.00
393	45	60	60	180	60.43	60.39	1.01	39.72	7.76	5.77	4.35	10.43	-3.00	15.00	-56.25	56.25
394	45	60	60	180	120.25	79.42	4.60	133.74	9.66	3.74	3.68	15.15	-14.00	16.00	-67.50	67.50
395	45	60	60	180	150.16	89.09	6.29	173.92	10.24	3.20	3.00	16.50	-15.00	17.00	-67.50	67.50
396	45	60	60	180	180.38	98.47	7.61	201.51	10.71	2.94	3.00	17.85	-15.00	17.00	-67.50	67.50
397	45	60	60	210	60.43	54.18	0.26	18.01	7.04	5.13	5.70	8.40	-2.00	13.00	-56.25	56.25
398	45	60	60	210	120.25	65.30	2.87	92.84	8.87	5.37	4.35	13.13	-4.00	16.00	-78.75	78.75
399	45	60	60	210	150.16	70.46	4.27	132.04	9.35	4.77	3.68	14.48	-13.00	16.00	-90.00	90.00
400	45	60	60	210	180.38	75.32	5.59	165.01	9.68	4.15	3.68	15.15	-14.00	16.00	-90.00	90.00

Table 38 Prostate simulations parameters and results for Tests 401-450.

Test #	Q1 (W)	Q2 (W)	Q3 (W)	Angle (deg)	Heat Time (s)	Tmax (^{o}C)	Vnecr (cm^3)	Surf Area (cm^2)	r centroid (mm)	z centroid (mm)	r min (mm)	r max (mm)	z min (mm)	z max (mm)	theta min (deg)	theta max (deg)
401	45	60	60	210	210.29	79.73	6.72	190.77	9.98	3.68	3.68	15.83	-14.00	16.00	-90.00	90.00
402	45	60	60	210	240.20	83.73	7.63	209.76	10.20	3.47	3.00	16.50	-14.00	17.00	-90.00	90.00
403	45	60	60	210	270.42	87.44	8.43	226.45	10.39	3.33	3.00	16.50	-15.00	17.00	-90.00	90.00
404	45	60	60	210	300.33	90.76	9.13	241.84	10.57	3.19	3.00	17.18	-15.00	17.00	-90.00	90.00
405	45	60	60	210	360.46	96.33	10.19	265.38	10.81	2.96	3.00	17.85	-15.00	17.00	-90.00	90.00
406	60	30	60	90	30.22	87.54	1.26	38.33	9.18	0.00	3.00	14.48	-16.00	16.00	-22.50	22.50
407	60	30	60	120	30.22	66.56	0.83	30.68	7.51	0.00	3.68	11.10	-15.00	15.00	-45.00	45.00
408	60	30	60	120	45.17	83.78	2.07	61.34	8.94	0.00	3.00	13.80	-16.00	16.00	-45.00	45.00
409	60	30	60	150	30.22	55.68	0.21	12.14	6.48	0.00	5.03	7.73	-14.00	14.00	-33.75	33.75
410	60	30	60	150	45.17	63.55	1.00	35.22	7.80	0.00	4.35	11.10	-15.00	15.00	-45.00	45.00
411	60	30	60	150	60.43	72.06	1.95	61.45	8.70	0.00	3.68	13.13	-16.00	16.00	-56.25	56.25
412	60	30	60	180	45.17	55.36	0.29	17.10	6.90	0.00	5.03	8.40	-14.00	14.00	-45.00	45.00
413	60	30	60	180	60.43	59.85	0.93	36.57	7.74	0.00	4.35	10.43	-15.00	15.00	-56.25	56.25
414	60	30	60	180	120.25	76.36	3.34	97.05	9.58	0.00	3.68	14.48	-16.00	16.00	-67.50	67.50
415	60	30	60	180	150.16	84.13	4.33	122.03	10.11	0.00	3.00	15.83	-17.00	17.00	-67.50	67.50
416	60	30	60	180	180.38	91.57	5.29	145.91	10.50	0.00	3.00	16.50	-17.00	17.00	-67.50	67.50
417	60	30	60	180	210.29	98.22	6.11	173.23	10.78	0.00	3.00	17.18	-17.00	17.00	-67.50	67.50
418	60	30	60	210	60.43	53.79	0.18	13.08	6.99	0.00	5.70	8.40	-13.00	13.00	-56.25	56.25
419	60	30	60	210	120.25	63.30	2.29	76.45	8.66	0.00	4.35	12.45	-15.00	15.00	-78.75	78.75
420	60	30	60	210	150.16	67.40	3.13	96.14	9.10	0.00	3.68	13.80	-16.00	16.00	-78.75	78.75
421	60	30	60	210	180.38	71.14	3.84	112.95	9.47	0.00	3.68	14.48	-16.00	16.00	-90.00	90.00
422	60	30	60	210	210.29	74.46	4.49	129.58	9.71	0.00	3.68	15.15	-16.00	16.00	-90.00	90.00
423	60	30	60	210	240.20	77.41	5.06	141.99	9.95	0.00	3.68	15.15	-17.00	17.00	-90.00	90.00
424	60	30	60	210	270.42	80.06	5.50	153.86	10.07	0.00	3.68	15.83	-17.00	17.00	-90.00	90.00
425	60	30	60	210	300.33	82.38	5.97	165.29	10.21	0.00	3.00	15.83	-17.00	17.00	-90.00	90.00
426	60	30	60	210	360.46	86.48	6.70	183.00	10.48	0.00	3.00	16.50	-17.00	17.00	-90.00	90.00
427	60	45	60	90	30.22	87.57	1.52	48.54	8.94	0.00	3.00	14.48	-16.00	16.00	-22.50	22.50
428	60	45	60	120	30.22	66.58	0.88	34.72	7.46	0.00	3.68	11.10	-15.00	15.00	-45.00	45.00
429	60	45	60	120	45.17	83.89	2.53	78.40	8.76	0.00	3.00	13.80	-16.00	16.00	-45.00	45.00
430	60	45	60	150	30.22	55.69	0.21	12.14	6.48	0.00	5.03	7.73	-14.00	14.00	-33.75	33.75
431	60	45	60	150	45.17	63.62	1.06	39.09	7.84	0.00	4.35	11.10	-15.00	15.00	-45.00	45.00
432	60	45	60	150	60.43	72.23	2.27	74.99	8.58	0.00	3.68	13.13	-16.00	16.00	-56.25	56.25
433	60	45	60	180	45.17	55.41	0.29	17.23	6.91	0.00	5.03	8.40	-14.00	14.00	-45.00	45.00
434	60	45	60	180	60.43	59.96	0.95	37.41	7.73	0.00	4.35	10.43	-15.00	15.00	-56.25	56.25
435	60	45	60	180	120.25	76.96	4.32	132.99	9.47	0.00	3.68	15.15	-16.00	16.00	-67.50	67.50
436	60	45	60	180	150.16	85.11	5.99	171.26	9.96	0.00	3.00	15.83	-17.00	17.00	-67.50	67.50
437	60	45	60	180	180.38	92.95	7.38	199.55	10.40	0.00	3.00	17.18	-17.00	17.00	-67.50	67.50
438	60	45	60	210	60.43	53.87	0.21	14.90	6.94	0.00	5.70	8.40	-13.00	13.00	-56.25	56.25
439	60	45	60	210	120.25	63.69	2.51	86.01	8.68	0.00	4.35	12.45	-15.00	15.00	-78.75	78.75
440	60	45	60	210	150.16	68.00	3.80	124.29	9.06	0.00	3.68	13.80	-16.00	16.00	-78.75	78.75
441	60	45	60	210	180.38	71.97	5.05	158.06	9.41	0.00	3.68	14.48	-16.00	16.00	-90.00	90.00
442	60	45	60	210	210.29	75.52	6.21	184.77	9.63	0.00	3.68	15.15	-16.00	16.00	-90.00	90.00
443	60	45	60	210	240.20	78.70	7.11	205.02	9.84	0.00	3.68	15.83	-17.00	17.00	-90.00	90.00
444	60	45	60	210	270.42	81.56	7.93	222.36	10.01	0.00	3.68	15.83	-17.00	17.00	-90.00	90.00
445	60	45	60	210	300.33	84.12	8.63	237.07	10.15	0.00	3.00	16.50	-17.00	17.00	-90.00	90.00
446	60	45	60	210	360.46	88.57	9.76	259.48	10.40	0.00	3.00	16.50	-17.00	17.00	-90.00	90.00
447	60	60	60	90	30.22	87.74	1.97	60.81	9.16	0.00	3.00	14.48	-16.00	16.00	-22.50	22.50
448	60	60	60	120	30.22	66.69	1.31	48.50	7.50	0.00	3.68	11.10	-15.00	15.00	-45.00	45.00
449	60	60	60	120	45.17	84.47	3.38	99.38	8.98	0.00	3.00	14.48	-16.00	16.00	-45.00	45.00
450	60	60	60	150	30.22	55.76	0.31	18.21	6.48	0.00	5.03	7.73	-14.00	14.00	-33.75	33.75

Table 39 Prostate simulations parameters and results for Tests 451-465.

Test #	Q1 (W)	Q2 (W)	Q3 (W)	Angle (deg)	Heat Time (s)	Tmax (^{o}C)	Vnecr (cm^3)	Surf Area (cm^2)	r centroid (mm)	z centroid (mm)	r min (mm)	r max (mm)	z min (mm)	z max (mm)	theta min (deg)	theta max (deg)
451	60	60	60	150	45.17	63.94	1.66	59.24	7.84	0.00	4.35	11.10	-15.00	15.00	-45.00	45.00
452	60	60	60	150	60.43	73.11	3.24	102.16	8.75	0.00	3.68	13.13	-16.00	16.00	-56.25	56.25
453	60	60	60	180	45.17	55.62	0.45	26.34	6.93	0.00	5.03	8.40	-14.00	14.00	-45.00	45.00
454	60	60	60	180	60.43	60.50	1.53	60.36	7.78	0.00	4.35	11.10	-15.00	15.00	-56.25	56.25
455	60	60	60	180	120.25	80.20	6.23	170.36	9.84	0.00	3.68	15.83	-16.00	16.00	-67.50	67.50
456	60	60	60	180	150.16	90.48	8.16	212.19	10.49	0.00	3.00	17.18	-17.00	17.00	-67.50	67.50
457	60	60	60	210	60.43	54.26	0.38	26.60	7.05	0.00	5.70	8.40	-13.00	13.00	-56.25	56.25
458	60	60	60	210	120.25	65.78	4.32	140.55	8.86	0.00	4.35	13.13	-16.00	16.00	-78.75	78.75
459	60	60	60	210	150.16	71.25	6.25	184.30	9.41	0.00	3.68	14.48	-16.00	16.00	-90.00	90.00
460	60	60	60	210	180.38	76.48	7.84	215.84	9.81	0.00	3.68	15.15	-16.00	16.00	-90.00	90.00
461	60	60	60	210	210.29	81.29	9.08	239.56	10.17	0.00	3.68	15.83	-16.00	16.00	-90.00	90.00
462	60	60	60	210	240.20	85.68	10.22	264.16	10.44	0.00	3.00	16.50	-17.00	17.00	-90.00	90.00
463	60	60	60	210	270.42	89.86	11.14	284.13	10.67	0.00	3.00	17.18	-17.00	17.00	-90.00	90.00
464	60	60	60	210	300.33	93.55	11.87	300.48	10.85	0.00	3.00	17.18	-17.00	17.00	-90.00	90.00
465	60	60	60	210	360.46	99.77	13.07	326.12	11.14	0.00	3.00	17.85	-17.00	17.00	-90.00	90.00

Appendix B: Prostate Largest Tumor Necrosed Results

Results of the studies which predicted the largest tumor which could be necrosed are displayed in Table 40 – Table 42.

*1 – tumor centered halfway between r-min and r-centroid.
2 – tumor centered at r-centroid.
3 – tumor centered halfway between r-centroid and r-max.

**The largest spherical tumor which can be necrosed at each location.

***(largest tumor radius)/(equivalent necrosed radius)

Table 40 Largest necrosed tumor results for $\Theta = 90^{o}$.

Q1 (W)	Q2 (W)	Q3 (W)	Heat Time (s)	Angle (deg)	largest tumors necrosed			
					1*	2*	3*	
0	60	0	16.18	90	5.45	6.54	7.81	r-Coordinate (mm)
					1.00	1.00	1.00	Tumor Radius (mm)**
					0.41	0.41	0.41	r-Ratio***
0	60	0	30.39	90	5.95	8.89	12.02	r-Coordinate (mm)
					2.00	3.00	2.00	Tumor Radius (mm)**
					0.31	0.47	0.31	r-Ratio***
0	45	0	30.39	90	5.95	7.56	9.33	r-Coordinate (mm)
					2.00	2.00	1.00	Tumor Radius (mm)**
					0.41	0.41	0.20	r-Ratio***
0	45	0	55.35	90	6.42	9.84	13.17	r-Coordinate (mm)
					2.00	3.00	3.00	Tumor Radius (mm)**
					0.32	0.49	0.49	r-Ratio***
0	30	0	60.77	90	7.08	8.47	10.46	r-Coordinate (mm)
					2.00	1.00	1.00	Tumor Radius (mm)**
					0.45	0.23	0.23	r-Ratio***
0	30	0	120.46	90	7.15	9.96	13.23	r-Coordinate (mm)
					3.00	3.00	2.00	Tumor Radius (mm)**
					0.45	0.45	0.30	r-Ratio***
0	30	0	200.76	90	6.85	10.70	14.95	r-Coordinate (mm)
					3.00	3.00	3.00	Tumor Radius (mm)**
					0.39	0.39	0.39	r-Ratio***

Table 41 Largest necrosed tumor results for $\Theta = 120^{\circ}$ and 150°.

Q1 (W)	Q2 (W)	Q3 (W)	Heat Time (s)	Angle (deg)	largest tumors necrosed			
					1*	2*	3*	
0	60	0	30.39	120	5.37	7.07	8.75	r-Coordinate (mm)
					2.00	2.00	2.00	Tumor Radius (mm)**
					0.00	0.00	0.00	r-Ratio***
0	60	0	60.43	120	6.05	9.11	12.80	r-Coordinate (mm)
					3.00	3.00	2.00	Tumor Radius (mm)**
					0.00	0.00	0.00	r-Ratio***
0	45	0	60.43	120	5.78	7.88	10.17	r-Coordinate (mm)
					2.00	3.00	2.00	Tumor Radius (mm)**
					0.00	0.00	0.00	r-Ratio***
0	45	0	120.25	120	6.31	9.62	13.40	r-Coordinate (mm)
					3.00	4.00	2.00	Tumor Radius (mm)**
					0.00	0.00	0.00	r-Ratio***
0	30	0	120.25	120	6.55	8.08	9.59	r-Coordinate (mm)
					1.00	1.00	1.00	Tumor Radius (mm)**
					0.00	0.00	0.00	r-Ratio***
0	30	0	150.16	120	6.68	8.34	10.06	r-Coordinate (mm)
					1.00	2.00	1.00	Tumor Radius (mm)**
					0.00	0.00	0.00	r-Ratio***
0	30	0	180.38	120	6.76	8.49	10.47	r-Coordinate (mm)
					2.00	2.00	2.00	Tumor Radius (mm)**
					0.00	0.00	0.00	r-Ratio***
0	30	0	210.29	120	6.56	8.77	10.95	r-Coordinate (mm)
					1.00	2.00	2.00	Tumor Radius (mm)**
					0.00	0.00	0.00	r-Ratio***
0	30	0	240.2	120	6.50	8.65	11.22	r-Coordinate (mm)
					1.00	2.00	2.00	Tumor Radius (mm)**
					0.00	0.00	0.00	r-Ratio***
0	60	0	60.43	150	5.84	8.00	10.56	r-Coordinate (mm)
					2.00	3.00	2.00	Tumor Radius (mm)**
					0.00	0.00	0.00	r-Ratio***
0	60	0	105.3	150	6.16	9.31	12.91	r-Coordinate (mm)
					3.00	4.00	3.00	Tumor Radius (mm)**
					0.00	0.00	0.00	r-Ratio***
0	45	0	120.25	150	6.38	8.42	10.77	r-Coordinate (mm)
					2.00	3.00	2.00	Tumor Radius (mm)**
					0.00	0.00	0.00	r-Ratio***
0	45	0	150.16	150	6.21	8.74	11.61	r-Coordinate (mm)
					2.00	3.00	2.00	Tumor Radius (mm)**
					0.00	0.00	0.00	r-Ratio***
0	45	0	210.29	150	6.42	9.17	12.50	r-Coordinate (mm)
					3.00	3.00	2.00	Tumor Radius (mm)**
					0.00	0.00	0.00	r-Ratio***

Table 42 Largest necrosed tumor results for Θ = 180°.

Q1 (W)	Q2 (W)	Q3 (W)	Heat Time (s)	Angle (deg)	largest tumors necrosed			
					1*	2*	3*	
0	60	0	60.43	180	5.84	7.33	8.88	r-Coordinate (mm)
					1.00	2.00	1.00	Tumor Radius (mm)**
					0.00	0.00	0.00	r-Ratio***
0	60	0	120.25	180	6.19	8.70	11.59	r-Coordinate (mm)
					2.00	3.00	2.00	Tumor Radius (mm)**
					0.00	0.00	0.00	r-Ratio***
0	60	0	150.16	180	6.02	9.04	12.43	r-Coordinate (mm)
					3.00	3.00	2.00	Tumor Radius (mm)**
					0.00	0.00	0.00	r-Ratio***
0	60	0	180.38	180	6.16	9.31	12.91	r-Coordinate (mm)
					3.00	4.00	3.00	Tumor Radius (mm)**
					0.00	0.00	0.00	r-Ratio***
0	60	0	210.29	180	6.29	9.59	13.38	r-Coordinate (mm)
					3.00	4.00	3.00	Tumor Radius (mm)**
					0.00	0.00	0.00	r-Ratio***
0	45	0	120.25	180	6.32	7.61	9.02	r-Coordinate (mm)
					1.00	1.00	1.00	Tumor Radius (mm)**
					0.00	0.00	0.00	r-Ratio***
0	45	0	150.16	180	6.49	7.96	9.53	r-Coordinate (mm)
					1.00	2.00	1.00	Tumor Radius (mm)**
					0.00	0.00	0.00	r-Ratio***
0	45	0	180.38	180	6.59	8.16	9.97	r-Coordinate (mm)
					1.00	2.00	1.00	Tumor Radius (mm)**
					0.00	0.00	0.00	r-Ratio***
0	45	0	210.29	180	6.34	8.33	10.39	r-Coordinate (mm)
					1.00	2.00	2.00	Tumor Radius (mm)**
					0.00	0.00	0.00	r-Ratio***
0	45	0	240.2	180	6.35	8.36	10.74	r-Coordinate (mm)
					2.00	2.00	2.00	Tumor Radius (mm)**
					0.00	0.00	0.00	r-Ratio***
0	45	0	270.42	180	6.38	8.41	10.77	r-Coordinate (mm)
					2.00	2.00	2.00	Tumor Radius (mm)**
					0.00	0.00	0.00	r-Ratio***
0	45	0	300.33	180	6.44	8.53	11.16	r-Coordinate (mm)
					2.00	3.00	2.00	Tumor Radius (mm)**
					0.00	0.00	0.00	r-Ratio***

Appendix C: Breast Focal Point Location Simulations Results

Results from the simulations of the heat generation produced from HIFU for breast cancer are displayed in Table 43 – Table 54.

Table 43 Breast focal point location simulations parameters and results for Tests 1-50.

Test #	Shape	# of ele/ row	# of rows	# of Trans	xn	zn	q''' Max (W/m^3)	x focus input (mm)	y focus input (mm)	z focus input (mm)	x focus output (mm)	y focus output (mm)	z focus output (mm)	distance apart (mm)	r nodes apart	th nodes apart	phi nodes apart
1	flat	41	20	1	1	1	2.59E+08	14.85	0.00	14.85	16.84	0.00	14.92	1.99	1	0	-1
2	flat	41	20	1	2	1	5.55E+08	29.22	0.00	15.34	29.22	0.00	15.34	0.00	0	0	0
3	flat	41	20	1	3	1	1.60E+09	44.39	0.00	13.83	44.39	0.00	13.83	0.00	0	0	0
4	flat	41	20	1	3	1	1.60E+09	44.39	0.00	13.83	44.39	0.00	13.83	0.00	0	0	0
5	flat	41	20	1	1	2	2.37E+08	13.54	0.00	30.09	17.85	0.00	29.52	4.34	1	0	-2
6	flat	41	20	1	2	2	4.54E+08	25.86	0.00	29.19	25.86	0.00	29.19	0.00	0	0	0
7	flat	41	20	1	3	2	1.06E+09	38.97	0.00	30.53	38.97	0.00	30.53	0.00	0	0	0
8	flat	41	20	1	1	3	2.09E+08	11.13	0.00	45.15	13.83	0.00	44.39	2.81	0	0	-1
9	flat	41	20	1	2	3	3.38E+08	20.32	0.00	45.14	23.70	0.00	45.16	3.39	1	0	-1
10	flat	41	20	1	3	3	6.11E+08	30.68	0.00	44.44	30.68	0.00	44.44	0.00	0	0	0
11	flat	41	20	2	1	1	5.90E+08	14.85	0.00	14.85	15.72	0.00	13.93	1.27	0	0	-1
12	flat	41	20	2	2	1	7.64E+08	29.22	0.00	15.34	30.55	0.00	16.03	1.50	1	0	0
13	flat	41	20	2	3	1	2.01E+09	44.39	0.00	13.83	44.39	0.00	13.83	0.00	0	0	0
14	flat	41	20	2	1	2	6.32E+08	13.54	0.00	30.09	13.54	0.00	30.09	0.00	0	0	0
15	flat	41	20	2	1	2	6.32E+08	13.54	0.00	30.09	13.54	0.00	30.09	0.00	0	0	0
16	flat	41	20	2	2	2	6.60E+08	25.86	0.00	29.19	25.86	0.00	29.19	0.00	0	0	0
17	flat	41	20	2	2	2	6.60E+08	25.86	0.00	29.19	25.86	0.00	29.19	0.00	0	0	0
18	flat	41	20	2	3	2	1.01E+09	38.97	0.00	30.53	40.15	0.00	31.45	1.50	1	0	0
19	flat	41	20	2	1	3	5.87E+08	11.13	0.00	45.15	11.13	0.00	45.15	0.00	0	0	0
20	flat	41	20	2	1	3	5.87E+08	11.13	0.00	45.15	11.13	0.00	45.15	0.00	0	0	0
21	flat	41	20	2	2	3	5.93E+08	20.32	0.00	45.14	19.70	0.00	43.77	1.50	-1	0	0
22	flat	41	20	2	3	3	1.16E+09	30.68	0.00	44.44	30.68	0.00	44.44	0.00	0	0	0
23	flat	41	20	3	1	1	1.11E+09	14.85	0.00	14.85	15.72	0.00	13.93	1.27	0	0	-1
24	flat	41	20	3	2	1	6.63E+08	29.22	0.00	15.34	29.22	0.00	15.34	0.00	0	0	0
25	flat	41	20	3	3	1	1.53E+09	44.39	0.00	13.83	45.83	0.00	14.28	1.50	1	0	0
26	flat	41	20	3	1	2	8.25E+08	13.54	0.00	30.09	14.12	-1.06	31.46	1.82	1	1	0
27	flat	41	20	3	2	2	1.07E+09	25.86	0.00	29.19	25.86	0.00	29.19	0.00	0	0	0
28	flat	41	20	3	3	2	1.06E+09	38.97	0.00	30.53	38.97	0.00	30.53	0.00	0	0	0
29	flat	41	20	3	1	3	1.20E+09	11.13	0.00	45.15	11.13	0.00	45.15	0.00	0	0	0
30	flat	41	20	3	1	3	1.20E+09	11.13	0.00	45.15	11.13	0.00	45.15	0.00	0	0	0
31	flat	41	20	3	2	3	7.16E+08	20.32	0.00	45.14	20.32	0.00	45.14	0.00	0	0	0
32	flat	41	20	3	3	3	1.41E+09	30.68	0.00	44.44	30.68	0.00	44.44	0.00	0	0	0
33	flat	41	30	1	1	1	3.88E+08	14.85	0.00	14.85	16.84	0.00	14.92	1.99	1	0	-1
34	flat	41	30	1	2	1	8.36E+08	29.22	0.00	15.34	29.22	0.00	15.34	0.00	0	0	0
35	flat	41	30	1	2	1	8.36E+08	29.22	0.00	15.34	29.22	0.00	15.34	0.00	0	0	0
36	flat	41	30	1	3	1	2.39E+09	44.39	0.00	13.83	44.39	0.00	13.83	0.00	0	0	0
37	flat	41	30	1	1	2	3.56E+08	13.54	0.00	30.09	17.85	0.00	29.52	4.34	1	0	-2
38	flat	41	30	1	2	2	6.80E+08	25.86	0.00	29.19	25.86	0.00	29.19	0.00	0	0	0
39	flat	41	30	1	2	2	6.80E+08	25.86	0.00	29.19	25.86	0.00	29.19	0.00	0	0	0
40	flat	41	30	1	3	2	1.59E+09	38.97	0.00	30.53	38.97	0.00	30.53	0.00	0	0	0
41	flat	41	30	1	1	3	3.11E+08	11.13	0.00	45.15	13.83	0.00	44.39	2.81	0	0	0
42	flat	41	30	1	1	3	3.11E+08	11.13	0.00	45.15	13.83	0.00	44.39	0.00	0	0	0
43	flat	41	30	1	2	3	5.10E+08	20.32	0.00	45.14	23.70	0.00	45.16	3.39	1	0	-1
44	flat	41	30	1	3	3	9.11E+08	30.68	0.00	44.44	30.68	0.00	44.44	0.00	0	0	0
45	flat	41	30	1	3	3	9.11E+08	30.68	0.00	44.44	30.68	0.00	44.44	0.00	0	0	0
46	flat	41	30	2	1	1	8.90E+08	14.85	0.00	14.85	15.72	0.00	13.93	1.27	0	0	-1
47	flat	41	30	2	2	1	1.23E+09	29.22	0.00	15.34	30.55	0.00	16.03	1.50	1	0	0
48	flat	41	30	2	3	1	2.80E+09	44.39	0.00	13.83	44.39	0.00	13.83	0.00	0	0	0
49	flat	41	30	2	1	2	9.57E+08	13.54	0.00	30.09	13.54	0.00	30.09	0.00	0	0	0
50	flat	41	30	2	2	2	9.11E+08	25.86	0.00	29.19	25.86	0.00	29.19	0.00	0	0	0

Table 44 Breast focal point location simulations parameters and results for Tests 51-100.

Test #	Shape	# of ele/ row	# of rows	# of Trans	xn	zn	q''' Max (W/m^3)	x focus input (mm)	y focus input (mm)	z focus input (mm)	x focus output (mm)	y focus output (mm)	z focus output (mm)	distance apart (mm)	r nodes apart	th nodes apart	phi nodes apart
51	flat	41	30	2	3	2	1.63E+09	38.97	0.00	30.53	40.15	0.00	31.45	1.50	1	0	0
52	flat	41	30	2	1	3	8.89E+08	11.13	0.00	45.15	11.13	0.00	45.15	0.00	0	0	0
53	flat	41	30	2	2	3	9.01E+08	20.32	0.00	45.14	19.70	0.00	43.77	1.50	-1	0	0
54	flat	41	30	2	3	3	1.68E+09	30.68	0.00	44.44	30.68	0.00	44.44	0.00	0	0	0
55	flat	41	30	3	1	1	1.68E+09	14.85	0.00	14.85	15.72	0.00	13.93	1.27	0	0	-1
56	flat	41	30	3	2	1	9.47E+08	29.22	0.00	15.34	29.22	0.00	15.34	0.00	0	0	0
57	flat	41	30	3	3	1	2.33E+09	44.39	0.00	13.83	45.83	0.00	14.28	1.50	1	0	0
58	flat	41	30	3	1	2	1.22E+09	13.54	0.00	30.09	14.12	-1.06	31.46	1.82	1	1	0
59	flat	41	30	3	2	2	1.53E+09	25.86	0.00	29.19	25.86	0.00	29.19	0.00	0	0	0
60	flat	41	30	3	3	2	1.53E+09	38.97	0.00	30.53	38.97	0.00	30.53	0.00	0	0	0
61	flat	41	30	3	1	3	1.81E+09	11.13	0.00	45.15	11.13	0.00	45.15	0.00	0	0	0
62	flat	41	30	3	1	3	1.81E+09	11.13	0.00	45.15	11.13	0.00	45.15	0.00	0	0	0
63	flat	41	30	3	2	3	1.04E+09	20.32	0.00	45.14	20.32	0.00	45.14	0.00	0	0	0
64	flat	41	30	3	2	3	1.04E+09	20.32	0.00	45.14	20.32	0.00	45.14	0.00	0	0	0
65	flat	41	30	3	3	3	2.20E+09	30.68	0.00	44.44	30.68	0.00	44.44	0.00	0	0	0
66	flat	41	40	1	1	1	5.21E+08	14.85	0.00	14.85	16.84	0.00	14.92	1.99	1	0	-1
67	flat	41	40	1	2	1	1.12E+09	29.22	0.00	15.34	29.22	0.00	15.34	0.00	0	0	0
68	flat	41	40	1	3	1	3.20E+09	44.39	0.00	13.83	44.39	0.00	13.83	0.00	0	0	0
69	flat	41	40	1	1	2	4.76E+08	13.54	0.00	30.09	16.03	0.00	30.55	2.53	1	0	-1
70	flat	41	40	1	2	2	9.07E+08	25.86	0.00	29.19	25.86	0.00	29.19	0.00	0	0	0
71	flat	41	40	1	3	2	2.14E+09	38.97	0.00	30.53	38.97	0.00	30.53	0.00	0	0	0
72	flat	41	40	1	1	3	4.14E+08	11.13	0.00	45.15	13.83	0.00	44.39	2.81	0	0	0
73	flat	41	40	1	1	3	4.14E+08	11.13	0.00	45.15	13.83	0.00	44.39	0.00	0	0	0
74	flat	41	40	1	2	3	6.81E+08	20.32	0.00	45.14	23.70	0.00	45.16	0.00	1	1	0
75	flat	41	40	1	2	3	6.81E+08	20.32	0.00	45.14	23.70	0.00	45.16	0.00	1	1	0
76	flat	41	40	1	3	3	1.23E+09	30.68	0.00	44.44	30.68	0.00	44.44	0.00	0	0	0
77	flat	41	40	1	3	3	1.23E+09	30.68	0.00	44.44	30.68	0.00	44.44	0.00	0	0	0
78	flat	41	40	2	1	1	1.18E+09	14.85	0.00	14.85	15.72	0.00	13.93	1.27	0	0	-1
79	flat	41	40	2	2	1	1.69E+09	29.22	0.00	15.34	30.55	0.00	16.03	1.50	1	0	0
80	flat	41	40	2	3	1	3.60E+09	44.39	0.00	13.83	44.39	0.00	13.83	0.00	0	0	0
81	flat	41	40	2	1	2	1.25E+09	13.54	0.00	30.09	13.54	0.00	30.09	0.00	0	0	0
82	flat	41	40	2	2	2	1.23E+09	25.86	0.00	29.19	26.86	0.00	30.31	1.50	1	0	0
83	flat	41	40	2	3	2	2.24E+09	38.97	0.00	30.53	38.97	0.00	30.53	0.00	0	0	0
84	flat	41	40	2	1	3	1.19E+09	11.13	0.00	45.15	11.13	0.00	45.15	0.00	0	0	0
85	flat	41	40	2	2	3	1.21E+09	20.32	0.00	45.14	19.70	0.00	43.77	1.50	-1	-1	0
86	flat	41	40	2	2	3	1.21E+09	20.32	0.00	45.14	19.70	0.00	43.77	0.00	-1	-1	0
87	flat	41	40	2	3	3	2.28E+09	30.68	0.00	44.44	30.68	0.00	44.44	0.00	0	0	0
88	flat	41	40	3	1	1	2.23E+09	14.85	0.00	14.85	15.72	0.00	13.93	1.27	0	0	0
89	flat	41	40	3	1	1	2.23E+09	14.85	0.00	14.85	15.72	0.00	13.93	0.00	0	0	0
90	flat	41	40	3	2	1	1.23E+09	29.22	0.00	15.34	29.22	0.00	15.34	0.00	0	0	0
91	flat	41	40	3	3	1	3.18E+09	44.39	0.00	13.83	45.83	0.00	14.28	1.50	1	0	0
92	flat	41	40	3	1	2	1.68E+09	13.54	0.00	30.09	14.12	-1.06	31.46	1.82	1	1	0
93	flat	41	40	3	2	2	1.99E+09	25.86	0.00	29.19	25.86	0.00	29.19	0.00	0	0	0
94	flat	41	40	3	3	2	2.26E+09	38.97	0.00	30.53	38.97	0.00	30.53	0.00	0	0	0
95	flat	41	40	3	1	3	2.42E+09	11.13	0.00	45.15	11.13	0.00	45.15	0.00	0	0	0
96	flat	41	40	3	1	3	2.42E+09	11.13	0.00	45.15	11.13	0.00	45.15	0.00	0	0	0
97	flat	41	40	3	2	3	1.36E+09	20.32	0.00	45.14	20.32	0.00	45.14	0.00	0	0	0
98	flat	41	40	3	3	3	2.69E+09	30.68	0.00	44.44	30.68	0.00	44.44	0.00	0	0	0
99	flat	51	20	1	1	1	2.88E+08	14.85	0.00	14.85	16.84	0.00	14.92	1.99	1	0	-1
100	flat	51	20	1	2	1	6.18E+08	29.22	0.00	15.34	29.22	0.00	15.34	0.00	0	0	0

Table 45 Breast focal point location simulations parameters and results for Tests 101-150.

Test #	Shape	# of ele/ row	# of rows	# of Trans	xn	zn	q''' Max (W/m^3)	x focus input (mm)	y focus input (mm)	z focus input (mm)	x focus output (mm)	y focus output (mm)	z focus output (mm)	distance apart (mm)	r nodes apart	th nodes apart	phi nodes apart
101	flat	51	20	1	3	1	1.67E+09	44.39	0.00	13.83	44.39	0.00	13.83	0.00	0	0	0
102	flat	51	20	1	1	2	2.61E+08	13.54	0.00	30.09	13.54	0.00	30.09	0.00	0	0	0
103	flat	51	20	1	2	2	5.10E+08	25.86	0.00	29.19	25.86	0.00	29.19	0.00	0	0	0
104	flat	51	20	1	3	2	1.14E+09	38.97	0.00	30.53	38.97	0.00	30.53	0.00	0	0	0
105	flat	51	20	1	1	3	2.30E+08	11.13	0.00	45.15	11.13	0.00	45.15	0.00	0	0	0
106	flat	51	20	1	2	3	3.73E+08	20.32	0.00	45.14	20.32	0.00	45.14	0.00	0	0	0
107	flat	51	20	1	3	3	6.77E+08	30.68	0.00	44.44	30.68	0.00	44.44	0.00	0	0	0
108	flat	51	20	1	3	3	6.77E+08	30.68	0.00	44.44	30.68	0.00	44.44	0.00	0	0	0
109	flat	51	20	2	1	1	6.14E+08	14.85	0.00	14.85	15.72	0.00	13.93	0.00	0	0	0
110	flat	51	20	2	1	1	6.14E+08	14.85	0.00	14.85	15.72	0.00	13.93	0.00	0	0	0
111	flat	51	20	2	2	1	9.29E+08	29.22	0.00	15.34	30.55	0.00	16.03	1.50	1	0	0
112	flat	51	20	2	3	1	2.42E+09	44.39	0.00	13.83	44.39	0.00	13.83	0.00	0	0	0
113	flat	51	20	2	1	2	5.79E+08	13.54	0.00	30.09	12.93	0.00	28.72	1.50	-1	-1	0
114	flat	51	20	2	1	2	5.79E+08	13.54	0.00	30.09	12.93	0.00	28.72	0.00	-1	-1	0
115	flat	51	20	2	2	2	1.01E+09	25.86	0.00	29.19	25.86	0.00	29.19	0.00	0	0	0
116	flat	51	20	2	2	2	1.01E+09	25.86	0.00	29.19	25.86	0.00	29.19	0.00	0	0	0
117	flat	51	20	2	3	2	1.14E+09	38.97	0.00	30.53	40.15	0.00	31.45	1.50	1	0	0
118	flat	51	20	2	1	3	6.90E+08	11.13	0.00	45.15	11.13	0.00	45.15	0.00	0	0	0
119	flat	51	20	2	1	3	6.90E+08	11.13	0.00	45.15	11.13	0.00	45.15	0.00	0	0	0
120	flat	51	20	2	2	3	6.65E+08	20.32	0.00	45.14	19.70	0.00	43.77	1.50	-1	0	0
121	flat	51	20	2	3	3	1.24E+09	30.68	0.00	44.44	30.68	0.00	44.44	0.00	0	0	0
122	flat	51	20	3	1	1	9.94E+08	14.85	0.00	14.85	14.85	0.00	14.85	0.00	0	0	0
123	flat	51	20	3	2	1	1.43E+09	29.22	0.00	15.34	30.55	0.00	16.03	1.50	1	0	0
124	flat	51	20	3	3	1	2.70E+09	44.39	0.00	13.83	44.39	0.00	13.83	0.00	0	0	0
125	flat	51	20	3	1	2	6.92E+08	13.54	0.00	30.09	13.51	-1.01	30.09	1.01	0	1	0
126	flat	51	20	3	2	2	1.51E+09	25.86	0.00	29.19	25.86	0.00	29.19	0.00	0	0	0
127	flat	51	20	3	2	2	1.51E+09	25.86	0.00	29.19	25.86	0.00	29.19	0.00	0	0	0
128	flat	51	20	3	3	2	1.24E+09	38.97	0.00	30.53	38.97	0.00	30.53	0.00	0	0	0
129	flat	51	20	3	1	3	8.52E+08	11.13	0.00	45.15	10.74	0.80	43.69	1.71	-1	1	0
130	flat	51	20	3	2	3	5.39E+08	20.32	0.00	45.14	20.32	0.00	45.14	0.00	0	0	0
131	flat	51	20	3	2	3	5.39E+08	20.32	0.00	45.14	20.32	0.00	45.14	0.00	0	0	0
132	flat	51	20	3	3	3	8.90E+08	30.68	0.00	44.44	30.68	0.00	44.44	0.00	0	0	0
133	flat	51	30	1	1	1	4.32E+08	14.85	0.00	14.85	16.84	0.00	14.92	1.99	1	0	-1
134	flat	51	30	1	2	1	9.31E+08	29.22	0.00	15.34	29.22	0.00	15.34	0.00	0	0	0
135	flat	51	30	1	3	1	2.51E+09	44.39	0.00	13.83	44.39	0.00	13.83	0.00	0	0	0
136	flat	51	30	1	1	2	3.91E+08	13.54	0.00	30.09	13.54	0.00	30.09	0.00	0	0	0
137	flat	51	30	1	2	2	7.65E+08	25.86	0.00	29.19	25.86	0.00	29.19	0.00	0	0	0
138	flat	51	30	1	3	2	1.71E+09	38.97	0.00	30.53	38.97	0.00	30.53	0.00	0	0	0
139	flat	51	30	1	1	3	3.46E+08	11.13	0.00	45.15	11.13	0.00	45.15	0.00	0	0	0
140	flat	51	30	1	2	3	5.61E+08	20.32	0.00	45.14	20.32	0.00	45.14	0.00	0	0	0
141	flat	51	30	1	2	3	5.61E+08	20.32	0.00	45.14	20.32	0.00	45.14	0.00	0	0	0
142	flat	51	30	1	3	3	1.01E+09	30.68	0.00	44.44	30.68	0.00	44.44	0.00	0	0	0
143	flat	51	30	2	1	1	9.05E+08	14.85	0.00	14.85	15.72	0.00	13.93	1.27	0	0	-1
144	flat	51	30	2	2	1	1.45E+09	29.22	0.00	15.34	30.55	0.00	16.03	1.50	1	0	0
145	flat	51	30	2	3	1	3.51E+09	44.39	0.00	13.83	44.39	0.00	13.83	0.00	0	0	0
146	flat	51	30	2	1	2	8.87E+08	13.54	0.00	30.09	13.54	0.00	30.09	0.00	0	0	0
147	flat	51	30	2	2	2	1.46E+09	25.86	0.00	29.19	25.86	0.00	29.19	0.00	0	0	0
148	flat	51	30	2	2	2	1.46E+09	25.86	0.00	29.19	25.86	0.00	29.19	0.00	0	0	0
149	flat	51	30	2	3	2	1.80E+09	38.97	0.00	30.53	40.15	0.00	31.45	1.50	1	0	0
150	flat	51	30	2	1	3	1.03E+09	11.13	0.00	45.15	11.13	0.00	45.15	0.00	0	0	0

Table 46 Breast focal point location simulations parameters and results for Tests 151-200.

Test #	Shape	# of ele/ row	# of rows	# of Trans	xn	zn	q''' Max (W/m^3)	x focus input (mm)	y focus input (mm)	z focus input (mm)	x focus output (mm)	y focus output (mm)	z focus output (mm)	distance apart (mm)	r nodes apart	th nodes apart	phi nodes apart
151	flat	51	30	2	1	3	1.03E+09	11.13	0.00	45.15	11.13	0.00	45.15	0.00	0	0	0
152	flat	51	30	2	2	3	9.79E+08	20.32	0.00	45.14	19.70	0.00	43.77	0.00	-1	-1	0
153	flat	51	30	2	2	3	9.79E+08	20.32	0.00	45.14	19.70	0.00	43.77	0.00	-1	-1	0
154	flat	51	30	2	3	3	1.97E+09	30.68	0.00	44.44	30.68	0.00	44.44	0.00	0	0	0
155	flat	51	30	3	1	1	1.54E+09	14.85	0.00	14.85	14.85	0.00	14.85	0.00	0	0	0
156	flat	51	30	3	2	1	2.22E+09	29.22	0.00	15.34	30.55	0.00	16.03	1.50	1	0	0
157	flat	51	30	3	3	1	3.81E+09	44.39	0.00	13.83	44.39	0.00	13.83	0.00	0	0	0
158	flat	51	30	3	1	2	1.05E+09	13.54	0.00	30.09	13.54	0.00	30.09	0.00	0	0	0
159	flat	51	30	3	1	2	1.05E+09	13.54	0.00	30.09	13.54	0.00	30.09	0.00	0	0	0
160	flat	51	30	3	2	2	2.18E+09	25.86	0.00	29.19	25.86	0.00	29.19	0.00	0	0	0
161	flat	51	30	3	3	2	1.78E+09	38.97	0.00	30.53	38.97	0.00	30.53	0.00	0	0	0
162	flat	51	30	3	1	3	1.28E+09	11.13	0.00	45.15	11.46	-0.86	46.61	1.72	1	1	0
163	flat	51	30	3	2	3	7.66E+08	20.32	0.00	45.14	20.32	0.00	45.14	0.00	0	0	0
164	flat	51	30	3	3	3	1.35E+09	30.68	0.00	44.44	30.68	0.00	44.44	0.00	0	0	0
165	flat	51	40	1	1	1	5.79E+08	14.85	0.00	14.85	16.84	0.00	14.92	1.99	1	1	0
166	flat	51	40	1	1	1	5.79E+08	14.85	0.00	14.85	16.84	0.00	14.92	0.00	1	1	0
167	flat	51	40	1	2	1	1.24E+09	29.22	0.00	15.34	29.22	0.00	15.34	0.00	0	0	0
168	flat	51	40	1	3	1	3.35E+09	44.39	0.00	13.83	44.39	0.00	13.83	0.00	0	0	0
169	flat	51	40	1	1	2	5.23E+08	13.54	0.00	30.09	13.54	0.00	30.09	0.00	0	0	0
170	flat	51	40	1	2	2	1.02E+09	25.86	0.00	29.19	25.86	0.00	29.19	0.00	0	0	0
171	flat	51	40	1	3	2	2.29E+09	38.97	0.00	30.53	38.97	0.00	30.53	0.00	0	0	0
172	flat	51	40	1	1	3	4.62E+08	11.13	0.00	45.15	11.13	0.00	45.15	0.00	0	0	0
173	flat	51	40	1	2	3	7.48E+08	20.32	0.00	45.14	20.32	0.00	45.14	0.00	0	0	0
174	flat	51	40	1	3	3	1.36E+09	30.68	0.00	44.44	30.68	0.00	44.44	0.00	0	0	0
175	flat	51	40	1	3	3	1.36E+09	30.68	0.00	44.44	30.68	0.00	44.44	0.00	0	0	0
176	flat	51	40	2	1	1	1.20E+09	14.85	0.00	14.85	15.72	0.00	13.93	0.00	0	0	0
177	flat	51	40	2	1	1	1.20E+09	14.85	0.00	14.85	15.72	0.00	13.93	0.00	0	0	0
178	flat	51	40	2	2	1	1.95E+09	29.22	0.00	15.34	30.55	0.00	16.03	1.50	1	0	0
179	flat	51	40	2	3	1	4.60E+09	44.39	0.00	13.83	44.39	0.00	13.83	0.00	0	0	0
180	flat	51	40	2	1	2	1.17E+09	13.54	0.00	30.09	12.93	0.00	28.72	1.50	-1	0	0
181	flat	51	40	2	2	2	1.90E+09	25.86	0.00	29.19	25.86	0.00	29.19	0.00	0	0	0
182	flat	51	40	2	3	2	2.35E+09	38.97	0.00	30.53	38.97	0.00	30.53	0.00	0	0	0
183	flat	51	40	2	1	3	1.37E+09	11.13	0.00	45.15	11.13	0.00	45.15	0.00	0	0	0
184	flat	51	40	2	1	3	1.37E+09	11.13	0.00	45.15	11.13	0.00	45.15	0.00	0	0	0
185	flat	51	40	2	2	3	1.29E+09	20.32	0.00	45.14	19.70	0.00	43.77	1.50	-1	0	0
186	flat	51	40	2	3	3	2.36E+09	30.68	0.00	44.44	30.68	0.00	44.44	0.00	0	0	0
187	flat	51	40	3	1	1	2.09E+09	14.85	0.00	14.85	14.85	0.00	14.85	0.00	0	0	0
188	flat	51	40	3	1	1	2.09E+09	14.85	0.00	14.85	14.85	0.00	14.85	0.00	0	0	0
189	flat	51	40	3	2	1	3.00E+09	29.22	0.00	15.34	30.55	0.00	16.03	1.50	1	0	0
190	flat	51	40	3	3	1	4.93E+09	44.39	0.00	13.83	44.39	0.00	13.83	0.00	0	0	0
191	flat	51	40	3	1	2	1.44E+09	13.54	0.00	30.09	13.51	-1.01	30.09	1.01	0	1	0
192	flat	51	40	3	2	2	2.86E+09	25.86	0.00	29.19	25.86	0.00	29.19	0.00	0	0	0
193	flat	51	40	3	3	2	2.70E+09	38.97	0.00	30.53	38.97	0.00	30.53	0.00	0	0	0
194	flat	51	40	3	1	3	1.72E+09	11.13	0.00	45.15	11.46	-0.86	46.61	1.72	1	1	0
195	flat	51	40	3	2	3	9.95E+08	20.32	0.00	45.14	20.32	0.00	45.14	0.00	0	0	0
196	flat	51	40	3	3	3	1.73E+09	30.68	0.00	44.44	30.68	0.00	44.44	0.00	0	0	0
197	flat	61	20	1	1	1	3.07E+08	14.85	0.00	14.85	14.85	0.00	14.85	0.00	0	0	0
198	flat	61	20	1	2	1	6.58E+08	29.22	0.00	15.34	29.22	0.00	15.34	0.00	0	0	0
199	flat	61	20	1	3	1	1.69E+09	44.39	0.00	13.83	44.39	0.00	13.83	0.00	0	0	0
200	flat	61	20	1	1	2	2.87E+08	13.54	0.00	30.09	13.54	0.00	30.09	0.00	0	0	0

Table 47 Breast focal point location simulations parameters and results for Tests 201-250.

Test #	Shape	# of ele/ row	# of rows	# of Trans	xn	zn	q''' Max (W/m^3)	x focus input (mm)	y focus input (mm)	z focus input (mm)	x focus output (mm)	y focus output (mm)	z focus output (mm)	distance apart (mm)	r nodes apart	th nodes apart	phi nodes apart
201	flat	61	20	1	2	2	5.48E+08	25.86	0.00	29.19	25.86	0.00	29.19	0.00	0	0	0
202	flat	61	20	1	3	2	1.18E+09	38.97	0.00	30.53	38.97	0.00	30.53	0.00	0	0	0
203	flat	61	20	1	3	2	1.18E+09	38.97	0.00	30.53	38.97	0.00	30.53	0.00	0	0	0
204	flat	61	20	1	1	3	2.55E+08	11.13	0.00	45.15	11.13	0.00	45.15	0.00	0	0	0
205	flat	61	20	1	2	3	4.06E+08	20.32	0.00	45.14	20.32	0.00	45.14	0.00	0	0	0
206	flat	61	20	1	3	3	7.18E+08	30.68	0.00	44.44	30.68	0.00	44.44	0.00	0	0	0
207	flat	61	20	2	1	1	6.77E+08	14.85	0.00	14.85	14.85	0.00	14.85	0.00	0	0	0
208	flat	61	20	2	1	1	6.77E+08	14.85	0.00	14.85	14.85	0.00	14.85	0.00	0	0	0
209	flat	61	20	2	2	1	9.19E+08	29.22	0.00	15.34	30.55	0.00	16.03	1.50	1	0	0
210	flat	61	20	2	3	1	2.51E+09	44.39	0.00	13.83	44.39	0.00	13.83	0.00	0	0	0
211	flat	61	20	2	1	2	6.48E+08	13.54	0.00	30.09	12.93	0.00	28.72	1.50	-1	0	0
212	flat	61	20	2	2	2	1.15E+09	25.86	0.00	29.19	25.86	0.00	29.19	0.00	0	0	0
213	flat	61	20	2	3	2	1.34E+09	38.97	0.00	30.53	40.15	0.00	31.45	1.50	1	0	0
214	flat	61	20	2	1	3	6.96E+08	11.13	0.00	45.15	11.13	0.00	45.15	0.00	0	0	0
215	flat	61	20	2	2	3	6.37E+08	20.32	0.00	45.14	19.70	0.00	43.77	1.50	-1	0	0
216	flat	61	20	2	3	3	1.37E+09	30.68	0.00	44.44	30.68	0.00	44.44	0.00	0	0	0
217	flat	61	20	3	1	1	9.54E+08	14.85	0.00	14.85	14.81	1.11	14.85	1.11	0	1	0
218	flat	61	20	3	2	1	8.55E+08	29.22	0.00	15.34	29.22	0.00	15.34	0.00	0	0	0
219	flat	61	20	3	3	1	3.60E+09	44.39	0.00	13.83	44.39	0.00	13.83	0.00	0	0	0
220	flat	61	20	3	1	2	1.27E+09	13.54	0.00	30.09	12.93	0.00	28.72	1.50	-1	0	0
221	flat	61	20	3	2	2	8.56E+08	25.86	0.00	29.19	26.86	0.00	30.31	1.50	1	0	0
222	flat	61	20	3	3	2	1.18E+09	38.97	0.00	30.53	37.78	0.00	29.60	1.50	-1	0	0
223	flat	61	20	3	1	3	1.46E+09	11.13	0.00	45.15	11.13	0.00	45.15	0.00	0	0	0
224	flat	61	20	3	1	3	1.46E+09	11.13	0.00	45.15	11.13	0.00	45.15	0.00	0	0	0
225	flat	61	20	3	2	3	6.49E+08	20.32	0.00	45.14	20.32	0.00	45.14	0.00	0	0	0
226	flat	61	20	3	3	3	1.78E+09	30.68	0.00	44.44	30.68	0.00	44.44	0.00	0	0	0
227	flat	61	30	1	1	1	4.59E+08	14.85	0.00	14.85	14.85	0.00	14.85	0.00	0	0	0
228	flat	61	30	1	2	1	9.91E+08	29.22	0.00	15.34	29.22	0.00	15.34	0.00	0	0	0
229	flat	61	30	1	3	1	2.54E+09	44.39	0.00	13.83	44.39	0.00	13.83	0.00	0	0	0
230	flat	61	30	1	1	2	4.31E+08	13.54	0.00	30.09	13.54	0.00	30.09	0.00	0	0	0
231	flat	61	30	1	1	2	4.31E+08	13.54	0.00	30.09	13.54	0.00	30.09	0.00	0	0	0
232	flat	61	30	1	2	2	8.22E+08	25.86	0.00	29.19	25.86	0.00	29.19	0.00	0	0	0
233	flat	61	30	1	2	2	8.22E+08	25.86	0.00	29.19	25.86	0.00	29.19	0.00	0	0	0
234	flat	61	30	1	3	2	1.76E+09	38.97	0.00	30.53	38.97	0.00	30.53	0.00	0	0	0
235	flat	61	30	1	1	3	3.83E+08	11.13	0.00	45.15	11.13	0.00	45.15	0.00	0	0	0
236	flat	61	30	1	2	3	6.10E+08	20.32	0.00	45.14	20.32	0.00	45.14	0.00	0	0	0
237	flat	61	30	1	3	3	1.07E+09	30.68	0.00	44.44	30.68	0.00	44.44	0.00	0	0	0
238	flat	61	30	1	3	3	1.07E+09	30.68	0.00	44.44	30.68	0.00	44.44	0.00	0	0	0
239	flat	61	30	2	1	1	1.04E+09	14.85	0.00	14.85	14.85	0.00	14.85	0.00	0	0	0
240	flat	61	30	2	2	1	1.43E+09	29.22	0.00	15.34	30.55	0.00	16.03	1.50	1	0	0
241	flat	61	30	2	3	1	3.84E+09	44.39	0.00	13.83	44.39	0.00	13.83	0.00	0	0	0
242	flat	61	30	2	1	2	9.74E+08	13.54	0.00	30.09	12.93	0.00	28.72	1.50	-1	-1	0
243	flat	61	30	2	1	2	9.74E+08	13.54	0.00	30.09	12.93	0.00	28.72	0.00	-1	-1	0
244	flat	61	30	2	2	2	1.68E+09	25.86	0.00	29.19	25.86	0.00	29.19	0.00	0	0	0
245	flat	61	30	2	2	2	1.68E+09	25.86	0.00	29.19	25.86	0.00	29.19	0.00	0	0	0
246	flat	61	30	2	3	2	2.03E+09	38.97	0.00	30.53	40.15	0.00	31.45	1.50	1	0	0
247	flat	61	30	2	1	3	1.03E+09	11.13	0.00	45.15	11.13	0.00	45.15	0.00	0	0	0
248	flat	61	30	2	2	3	9.29E+08	20.32	0.00	45.14	19.70	0.00	43.77	1.50	-1	0	0
249	flat	61	30	2	3	3	2.14E+09	30.68	0.00	44.44	30.68	0.00	44.44	0.00	0	0	0
250	flat	61	30	3	1	1	1.40E+09	14.85	0.00	14.85	14.81	1.11	14.85	1.11	0	1	0

Table 48 Breast focal point location simulations parameters and results for Tests 251-300.

Test #	Shape	# of ele/ row	# of rows	# of Trans	xn	zn	q''' Max (W/m^3)	x focus input (mm)	y focus input (mm)	z focus input (mm)	x focus output (mm)	y focus output (mm)	z focus output (mm)	distance apart (mm)	r nodes apart	th nodes apart	phi nodes apart
251	flat	61	30	3	2	1	1.20E+09	29.22	0.00	15.34	29.22	0.00	15.34	0.00	0	0	0
252	flat	61	30	3	3	1	5.49E+09	44.39	0.00	13.83	44.39	0.00	13.83	0.00	0	0	0
253	flat	61	30	3	1	2	1.91E+09	13.54	0.00	30.09	12.93	0.00	28.72	1.50	-1	-1	0
254	flat	61	30	3	1	2	1.91E+09	13.54	0.00	30.09	12.93	0.00	28.72	0.00	-1	-1	0
255	flat	61	30	3	2	2	1.35E+09	25.86	0.00	29.19	26.86	0.00	30.31	1.50	1	0	0
256	flat	61	30	3	3	2	1.84E+09	38.97	0.00	30.53	37.78	0.00	29.60	1.50	-1	0	0
257	flat	61	30	3	1	3	2.17E+09	11.13	0.00	45.15	11.13	0.00	45.15	0.00	0	0	0
258	flat	61	30	3	1	3	2.17E+09	11.13	0.00	45.15	11.13	0.00	45.15	0.00	0	0	0
259	flat	61	30	3	2	3	9.21E+08	20.32	0.00	45.14	20.32	0.00	45.14	0.00	0	0	0
260	flat	61	30	3	3	3	2.78E+09	30.68	0.00	44.44	30.68	0.00	44.44	0.00	0	0	0
261	flat	61	40	1	1	1	6.15E+08	14.85	0.00	14.85	14.85	0.00	14.85	0.00	0	0	0
262	flat	61	40	1	2	1	1.32E+09	29.22	0.00	15.34	29.22	0.00	15.34	0.00	0	0	0
263	flat	61	40	1	3	1	3.39E+09	44.39	0.00	13.83	44.39	0.00	13.83	0.00	0	0	0
264	flat	61	40	1	1	2	5.76E+08	13.54	0.00	30.09	13.54	0.00	30.09	0.00	0	0	0
265	flat	61	40	1	2	2	1.10E+09	25.86	0.00	29.19	25.86	0.00	29.19	0.00	0	0	0
266	flat	61	40	1	3	2	2.37E+09	38.97	0.00	30.53	38.97	0.00	30.53	0.00	0	0	0
267	flat	61	40	1	1	3	5.11E+08	11.13	0.00	45.15	11.13	0.00	45.15	0.00	0	0	0
268	flat	61	40	1	2	3	8.14E+08	20.32	0.00	45.14	20.32	0.00	45.14	0.00	0	0	0
269	flat	61	40	1	3	3	1.44E+09	30.68	0.00	44.44	30.68	0.00	44.44	0.00	0	0	0
270	flat	61	40	2	1	1	1.41E+09	14.85	0.00	14.85	14.85	0.00	14.85	0.00	0	0	0
271	flat	61	40	2	1	1	1.41E+09	14.85	0.00	14.85	14.85	0.00	14.85	0.00	0	0	0
272	flat	61	40	2	2	1	1.93E+09	29.22	0.00	15.34	30.55	0.00	16.03	1.50	1	0	0
273	flat	61	40	2	3	1	5.17E+09	44.39	0.00	13.83	44.39	0.00	13.83	0.00	0	0	0
274	flat	61	40	2	1	2	1.29E+09	13.54	0.00	30.09	12.93	0.00	28.72	1.50	-1	0	0
275	flat	61	40	2	2	2	2.21E+09	25.86	0.00	29.19	25.86	0.00	29.19	0.00	0	0	0
276	flat	61	40	2	3	2	2.59E+09	38.97	0.00	30.53	40.15	0.00	31.45	1.50	1	0	0
277	flat	61	40	2	1	3	1.36E+09	11.13	0.00	45.15	11.13	0.00	45.15	0.00	0	0	0
278	flat	61	40	2	2	3	1.22E+09	20.32	0.00	45.14	19.70	0.00	43.77	1.50	-1	-1	0
279	flat	61	40	2	2	3	1.22E+09	20.32	0.00	45.14	19.70	0.00	43.77	0.00	-1	-1	0
280	flat	61	40	2	3	3	2.64E+09	30.68	0.00	44.44	30.68	0.00	44.44	0.00	0	0	0
281	flat	61	40	3	1	1	1.84E+09	14.85	0.00	14.85	14.81	1.11	14.85	1.11	0	1	0
282	flat	61	40	3	2	1	1.56E+09	29.22	0.00	15.34	29.22	0.00	15.34	0.00	0	0	0
283	flat	61	40	3	3	1	7.37E+09	44.39	0.00	13.83	44.39	0.00	13.83	0.00	0	0	0
284	flat	61	40	3	1	2	2.54E+09	13.54	0.00	30.09	12.93	0.00	28.72	1.50	-1	-1	0
285	flat	61	40	3	1	2	2.54E+09	13.54	0.00	30.09	12.93	0.00	28.72	0.00	-1	-1	0
286	flat	61	40	3	2	2	1.85E+09	25.86	0.00	29.19	26.86	0.00	30.31	1.50	1	0	0
287	flat	61	40	3	3	2	2.32E+09	38.97	0.00	30.53	40.15	0.00	31.45	1.50	1	0	0
288	flat	61	40	3	1	3	2.88E+09	11.13	0.00	45.15	11.13	0.00	45.15	0.00	0	0	0
289	flat	61	40	3	1	3	2.88E+09	11.13	0.00	45.15	11.13	0.00	45.15	0.00	0	0	0
290	flat	61	40	3	2	3	1.19E+09	20.32	0.00	45.14	20.32	0.00	45.14	0.00	0	0	0
291	flat	61	40	3	3	3	3.43E+09	30.68	0.00	44.44	30.68	0.00	44.44	0.00	0	0	0
292	curved	41	20	1	1	1	2.56E+08	14.85	0.00	14.85	16.84	0.00	14.92	1.99	1	0	-1
293	curved	41	20	1	2	1	5.51E+08	29.22	0.00	15.34	29.22	0.00	15.34	0.00	0	0	0
294	curved	41	20	1	3	1	1.57E+09	44.39	0.00	13.83	44.39	0.00	13.83	0.00	0	0	0
295	curved	41	20	1	3	1	1.57E+09	44.39	0.00	13.83	44.39	0.00	13.83	0.00	0	0	0
296	curved	41	20	1	1	2	2.32E+08	13.54	0.00	30.09	16.03	0.00	30.55	2.53	1	0	-1
297	curved	41	20	1	2	2	4.51E+08	25.86	0.00	29.19	25.86	0.00	29.19	0.00	0	0	0
298	curved	41	20	1	3	2	1.05E+09	38.97	0.00	30.53	38.97	0.00	30.53	0.00	0	0	0
299	curved	41	20	1	3	2	1.05E+09	38.97	0.00	30.53	38.97	0.00	30.53	0.00	0	0	0
300	curved	41	20	1	1	3	2.05E+08	11.13	0.00	45.15	13.83	0.00	44.39	2.81	0	0	-1

Table 49 Breast focal point location simulations parameters and results for Tests 301-350.

Test #	Shape	# of ele/ row	# of rows	# of Trans	xn	zn	q''' Max (W/m^3)	x focus input (mm)	y focus input (mm)	z focus input (mm)	x focus output (mm)	y focus output (mm)	z focus output (mm)	distance apart (mm)	r nodes apart	th nodes apart	phi nodes apart
301	curved	41	20	1	2	3	3.26E+08	20.32	0.00	45.14	20.32	0.00	45.14	0.00	0	0	0
302	curved	41	20	1	3	3	6.06E+08	30.68	0.00	44.44	30.68	0.00	44.44	0.00	0	0	0
303	curved	41	20	1	3	3	6.06E+08	30.68	0.00	44.44	30.68	0.00	44.44	0.00	0	0	0
304	curved	41	20	2	1	1	5.84E+08	14.85	0.00	14.85	15.72	0.00	13.93	0.00	0	0	0
305	curved	41	20	2	1	1	5.84E+08	14.85	0.00	14.85	15.72	0.00	13.93	0.00	0	0	0
306	curved	41	20	2	2	1	7.92E+08	29.22	0.00	15.34	30.55	0.00	16.03	1.50	1	0	0
307	curved	41	20	2	3	1	2.16E+09	44.39	0.00	13.83	44.39	0.00	13.83	0.00	0	0	0
308	curved	41	20	2	1	2	5.99E+08	13.54	0.00	30.09	13.54	0.00	30.09	0.00	0	0	0
309	curved	41	20	2	2	2	7.44E+08	25.86	0.00	29.19	25.86	0.00	29.19	0.00	0	0	0
310	curved	41	20	2	3	2	1.03E+09	38.97	0.00	30.53	40.15	0.00	31.45	1.50	1	0	0
311	curved	41	20	2	1	3	6.02E+08	11.13	0.00	45.15	11.13	0.00	45.15	0.00	0	0	0
312	curved	41	20	2	2	3	6.07E+08	20.32	0.00	45.14	19.70	0.00	43.77	1.50	-1	-1	0
313	curved	41	20	2	2	3	6.07E+08	20.32	0.00	45.14	19.70	0.00	43.77	0.00	-1	-1	0
314	curved	41	20	2	3	3	1.14E+09	30.68	0.00	44.44	30.68	0.00	44.44	0.00	0	0	0
315	curved	41	20	3	1	1	9.61E+08	14.85	0.00	14.85	14.81	1.11	14.85	1.11	0	1	0
316	curved	41	20	3	2	1	1.28E+09	29.22	0.00	15.34	30.55	0.00	16.03	1.50	1	0	0
317	curved	41	20	3	3	1	2.66E+09	44.39	0.00	13.83	44.39	0.00	13.83	0.00	0	0	0
318	curved	41	20	3	1	2	8.98E+08	13.54	0.00	30.09	13.54	0.00	30.09	0.00	0	0	0
319	curved	41	20	3	2	2	9.27E+08	25.86	0.00	29.19	26.86	0.00	30.31	1.50	1	0	0
320	curved	41	20	3	3	2	1.57E+09	38.97	0.00	30.53	40.15	0.00	31.45	1.50	1	0	0
321	curved	41	20	3	1	3	8.72E+08	11.13	0.00	45.15	11.13	0.00	45.15	0.00	0	0	0
322	curved	41	20	3	1	3	8.72E+08	11.13	0.00	45.15	11.13	0.00	45.15	0.00	0	0	0
323	curved	41	20	3	2	3	5.67E+08	20.32	0.00	45.14	19.70	0.00	43.77	0.00	-1	-1	0
324	curved	41	20	3	2	3	5.67E+08	20.32	0.00	45.14	19.70	0.00	43.77	0.00	-1	-1	0
325	curved	41	20	3	3	3	1.12E+09	30.68	0.00	44.44	30.68	0.00	44.44	0.00	0	0	0
326	curved	41	30	1	1	1	3.84E+08	14.85	0.00	14.85	16.84	0.00	14.92	1.99	1	0	-1
327	curved	41	30	1	2	1	8.29E+08	29.22	0.00	15.34	29.22	0.00	15.34	0.00	0	0	0
328	curved	41	30	1	2	1	8.29E+08	29.22	0.00	15.34	29.22	0.00	15.34	0.00	0	0	0
329	curved	41	30	1	3	1	2.35E+09	44.39	0.00	13.83	44.39	0.00	13.83	0.00	0	0	0
330	curved	41	30	1	3	1	2.35E+09	44.39	0.00	13.83	44.39	0.00	13.83	0.00	0	0	0
331	curved	41	30	1	1	2	3.47E+08	13.54	0.00	30.09	16.03	0.00	30.55	0.00	1	1	0
332	curved	41	30	1	1	2	3.47E+08	13.54	0.00	30.09	16.03	0.00	30.55	0.00	1	1	0
333	curved	41	30	1	2	2	6.76E+08	25.86	0.00	29.19	25.86	0.00	29.19	0.00	0	0	0
334	curved	41	30	1	3	2	1.57E+09	38.97	0.00	30.53	38.97	0.00	30.53	0.00	0	0	0
335	curved	41	30	1	1	3	3.07E+08	11.13	0.00	45.15	13.83	0.00	44.39	2.81	0	0	0
336	curved	41	30	1	1	3	3.07E+08	11.13	0.00	45.15	13.83	0.00	44.39	0.00	0	0	0
337	curved	41	30	1	2	3	4.90E+08	20.32	0.00	45.14	20.32	0.00	45.14	0.00	0	0	0
338	curved	41	30	1	2	3	4.90E+08	20.32	0.00	45.14	20.32	0.00	45.14	0.00	0	0	0
339	curved	41	30	1	3	3	9.04E+08	30.68	0.00	44.44	30.68	0.00	44.44	0.00	0	0	0
340	curved	41	30	2	1	1	8.73E+08	14.85	0.00	14.85	15.72	0.00	13.93	1.27	0	0	-1
341	curved	41	30	2	2	1	1.26E+09	29.22	0.00	15.34	30.55	0.00	16.03	1.50	1	0	0
342	curved	41	30	2	3	1	3.07E+09	44.39	0.00	13.83	44.39	0.00	13.83	0.00	0	0	0
343	curved	41	30	2	1	2	9.13E+08	13.54	0.00	30.09	13.54	0.00	30.09	0.00	0	0	0
344	curved	41	30	2	2	2	1.04E+09	25.86	0.00	29.19	25.86	0.00	29.19	0.00	0	0	0
345	curved	41	30	2	3	2	1.65E+09	38.97	0.00	30.53	40.15	0.00	31.45	1.50	1	0	0
346	curved	41	30	2	1	3	9.08E+08	11.13	0.00	45.15	11.13	0.00	45.15	0.00	0	0	0
347	curved	41	30	2	2	3	9.13E+08	20.32	0.00	45.14	19.70	0.00	43.77	1.50	-1	0	0
348	curved	41	30	2	3	3	1.70E+09	30.68	0.00	44.44	30.68	0.00	44.44	0.00	0	0	0
349	curved	41	30	3	1	1	1.43E+09	14.85	0.00	14.85	14.81	1.11	14.85	1.11	0	1	0
350	curved	41	30	3	2	1	2.01E+09	29.22	0.00	15.34	30.55	0.00	16.03	1.50	1	0	0

Table 50 Breast focal point location simulations parameters and results for Tests 351-400.

Test #	Shape	# of ele/ row	# of rows	# of Trans	xn	zn	q''' Max (W/m^3)	x focus input (mm)	y focus input (mm)	z focus input (mm)	x focus output (mm)	y focus output (mm)	z focus output (mm)	distance apart (mm)	r nodes apart	th nodes apart	phi nodes apart
351	curved	41	30	3	3	1	3.92E+09	44.39	0.00	13.83	44.39	0.00	13.83	0.00	0	0	0
352	curved	41	30	3	1	2	1.37E+09	13.54	0.00	30.09	13.54	0.00	30.09	0.00	0	0	0
353	curved	41	30	3	2	2	1.47E+09	25.86	0.00	29.19	26.86	0.00	30.31	1.50	1	0	0
354	curved	41	30	3	3	2	2.49E+09	38.97	0.00	30.53	40.15	0.00	31.45	1.50	1	0	0
355	curved	41	30	3	1	3	1.31E+09	11.13	0.00	45.15	11.13	0.00	45.15	0.00	0	0	0
356	curved	41	30	3	1	3	1.31E+09	11.13	0.00	45.15	11.13	0.00	45.15	0.00	0	0	0
357	curved	41	30	3	2	3	8.52E+08	20.32	0.00	45.14	19.70	0.00	43.77	1.50	-1	0	0
358	curved	41	30	3	3	3	1.55E+09	30.68	0.00	44.44	30.68	0.00	44.44	0.00	0	0	0
359	curved	41	40	1	1	1	5.15E+08	14.85	0.00	14.85	16.84	0.00	14.92	1.99	1	0	-1
360	curved	41	40	1	2	1	1.11E+09	29.22	0.00	15.34	29.22	0.00	15.34	0.00	0	0	0
361	curved	41	40	1	2	1	1.11E+09	29.22	0.00	15.34	29.22	0.00	15.34	0.00	0	0	0
362	curved	41	40	1	3	1	3.15E+09	44.39	0.00	13.83	44.39	0.00	13.83	0.00	0	0	0
363	curved	41	40	1	1	2	4.68E+08	13.54	0.00	30.09	16.03	0.00	30.55	2.53	1	0	-1
364	curved	41	40	1	2	2	9.01E+08	25.86	0.00	29.19	25.86	0.00	29.19	0.00	0	0	0
365	curved	41	40	1	3	2	2.11E+09	38.97	0.00	30.53	38.97	0.00	30.53	0.00	0	0	0
366	curved	41	40	1	1	3	4.08E+08	11.13	0.00	45.15	13.83	0.00	44.39	2.81	0	0	0
367	curved	41	40	1	1	3	4.08E+08	11.13	0.00	45.15	13.83	0.00	44.39	0.00	0	0	0
368	curved	41	40	1	2	3	6.54E+08	20.32	0.00	45.14	23.70	0.00	45.16	3.39	1	0	-1
369	curved	41	40	1	3	3	1.22E+09	30.68	0.00	44.44	30.68	0.00	44.44	0.00	0	0	0
370	curved	41	40	1	3	3	1.22E+09	30.68	0.00	44.44	30.68	0.00	44.44	0.00	0	0	0
371	curved	41	40	2	1	1	1.16E+09	14.85	0.00	14.85	15.72	0.00	13.93	0.00	0	0	0
372	curved	41	40	2	1	1	1.16E+09	14.85	0.00	14.85	15.72	0.00	13.93	0.00	0	0	0
373	curved	41	40	2	2	1	1.72E+09	29.22	0.00	15.34	30.55	0.00	16.03	1.50	1	0	0
374	curved	41	40	2	3	1	3.99E+09	44.39	0.00	13.83	44.39	0.00	13.83	0.00	0	0	0
375	curved	41	40	2	1	2	1.17E+09	13.54	0.00	30.09	13.54	0.00	30.09	0.00	0	0	0
376	curved	41	40	2	1	2	1.17E+09	13.54	0.00	30.09	13.54	0.00	30.09	0.00	0	0	0
377	curved	41	40	2	2	2	1.34E+09	25.86	0.00	29.19	25.86	0.00	29.19	0.00	0	0	0
378	curved	41	40	2	3	2	2.09E+09	38.97	0.00	30.53	38.97	0.00	30.53	0.00	0	0	0
379	curved	41	40	2	1	3	1.21E+09	11.13	0.00	45.15	11.13	0.00	45.15	0.00	0	0	0
380	curved	41	40	2	1	3	1.21E+09	11.13	0.00	45.15	11.13	0.00	45.15	0.00	0	0	0
381	curved	41	40	2	2	3	1.22E+09	20.32	0.00	45.14	19.70	0.00	43.77	1.50	-1	0	0
382	curved	41	40	2	3	3	2.22E+09	30.68	0.00	44.44	30.68	0.00	44.44	0.00	0	0	0
383	curved	41	40	3	1	1	1.91E+09	14.85	0.00	14.85	14.81	1.11	14.85	1.11	0	1	0
384	curved	41	40	3	2	1	2.74E+09	29.22	0.00	15.34	30.55	0.00	16.03	1.50	1	0	0
385	curved	41	40	3	3	1	5.17E+09	44.39	0.00	13.83	44.39	0.00	13.83	0.00	0	0	0
386	curved	41	40	3	1	2	1.80E+09	13.54	0.00	30.09	12.93	0.00	28.72	1.50	-1	-1	0
387	curved	41	40	3	1	2	1.80E+09	13.54	0.00	30.09	12.93	0.00	28.72	0.00	-1	-1	0
388	curved	41	40	3	2	2	2.02E+09	25.86	0.00	29.19	26.86	0.00	30.31	1.50	1	0	0
389	curved	41	40	3	3	2	2.81E+09	38.97	0.00	30.53	40.15	0.00	31.45	1.50	1	0	0
390	curved	41	40	3	1	3	1.75E+09	11.13	0.00	45.15	11.13	0.00	45.15	0.00	0	0	0
391	curved	41	40	3	1	3	1.75E+09	11.13	0.00	45.15	11.13	0.00	45.15	0.00	0	0	0
392	curved	41	40	3	2	3	1.13E+09	20.32	0.00	45.14	19.70	0.00	43.77	1.50	-1	0	0
393	curved	41	40	3	3	3	2.27E+09	30.68	0.00	44.44	30.68	0.00	44.44	0.00	0	0	0
394	curved	51	20	1	1	1	2.80E+08	14.85	0.00	14.85	16.84	0.00	14.92	1.99	1	0	-1
395	curved	51	20	1	2	1	6.09E+08	29.22	0.00	15.34	29.22	0.00	15.34	0.00	0	0	0
396	curved	51	20	1	3	1	1.63E+09	44.39	0.00	13.83	44.39	0.00	13.83	0.00	0	0	0
397	curved	51	20	1	3	1	1.63E+09	44.39	0.00	13.83	44.39	0.00	13.83	0.00	0	0	0
398	curved	51	20	1	1	2	2.59E+08	13.54	0.00	30.09	13.54	0.00	30.09	0.00	0	0	0
399	curved	51	20	1	2	2	5.04E+08	25.86	0.00	29.19	25.86	0.00	29.19	0.00	0	0	0
400	curved	51	20	1	3	2	1.11E+09	38.97	0.00	30.53	38.97	0.00	30.53	0.00	0	0	0

Table 51 Breast focal point location simulations parameters and results for Tests 401-450.

Test #	Shape	# of ele/ row	# of rows	# of Trans	xn	zn	q''' Max (W/m^3)	x focus input (mm)	y focus input (mm)	z focus input (mm)	x focus output (mm)	y focus output (mm)	z focus output (mm)	distance apart (mm)	r nodes apart	th nodes apart	phi nodes apart
401	curved	51	20	1	1	3	2.30E+08	11.13	0.00	45.15	11.13	0.00	45.15	0.00	0	0	0
402	curved	51	20	1	1	3	2.30E+08	11.13	0.00	45.15	11.13	0.00	45.15	0.00	0	0	0
403	curved	51	20	1	2	3	3.70E+08	20.32	0.00	45.14	20.32	0.00	45.14	0.00	0	0	0
404	curved	51	20	1	3	3	6.67E+08	30.68	0.00	44.44	30.68	0.00	44.44	0.00	0	0	0
405	curved	51	20	1	3	3	6.67E+08	30.68	0.00	44.44	30.68	0.00	44.44	0.00	0	0	0
406	curved	51	20	2	1	1	5.60E+08	14.85	0.00	14.85	15.72	0.00	13.93	0.00	0	0	0
407	curved	51	20	2	1	1	5.60E+08	14.85	0.00	14.85	15.72	0.00	13.93	0.00	0	0	0
408	curved	51	20	2	2	1	8.50E+08	29.22	0.00	15.34	30.55	0.00	16.03	1.50	1	0	0
409	curved	51	20	2	3	1	2.25E+09	44.39	0.00	13.83	44.39	0.00	13.83	0.00	0	0	0
410	curved	51	20	2	1	2	5.87E+08	13.54	0.00	30.09	12.93	0.00	28.72	1.50	-1	0	0
411	curved	51	20	2	2	2	1.00E+09	25.86	0.00	29.19	25.86	0.00	29.19	0.00	0	0	0
412	curved	51	20	2	3	2	1.27E+09	38.97	0.00	30.53	40.15	0.00	31.45	1.50	1	0	0
413	curved	51	20	2	1	3	6.55E+08	11.13	0.00	45.15	11.13	0.00	45.15	0.00	0	0	0
414	curved	51	20	2	1	3	6.55E+08	11.13	0.00	45.15	11.13	0.00	45.15	0.00	0	0	0
415	curved	51	20	2	2	3	6.23E+08	20.32	0.00	45.14	19.70	0.00	43.77	0.00	-1	-1	0
416	curved	51	20	2	2	3	6.23E+08	20.32	0.00	45.14	19.70	0.00	43.77	0.00	-1	-1	0
417	curved	51	20	2	3	3	1.28E+09	30.68	0.00	44.44	30.68	0.00	44.44	0.00	0	0	0
418	curved	51	20	3	1	1	9.62E+08	14.85	0.00	14.85	15.72	0.00	13.93	1.27	0	0	0
419	curved	51	20	3	1	1	9.62E+08	14.85	0.00	14.85	15.72	0.00	13.93	0.00	0	0	0
420	curved	51	20	3	2	1	1.33E+09	29.22	0.00	15.34	30.55	0.00	16.03	1.50	1	0	0
421	curved	51	20	3	3	1	2.66E+09	44.39	0.00	13.83	44.39	0.00	13.83	0.00	0	0	0
422	curved	51	20	3	1	2	8.24E+08	13.54	0.00	30.09	14.12	-1.06	31.46	1.82	1	1	0
423	curved	51	20	3	2	2	1.69E+09	25.86	0.00	29.19	25.86	0.00	29.19	0.00	0	0	0
424	curved	51	20	3	3	2	1.20E+09	38.97	0.00	30.53	38.97	0.00	30.53	0.00	0	0	0
425	curved	51	20	3	1	3	1.19E+09	11.13	0.00	45.15	11.13	0.00	45.15	0.00	0	0	0
426	curved	51	20	3	2	3	1.19E+09	20.32	0.00	45.14	19.70	0.00	43.77	1.50	-1	-1	0
427	curved	51	20	3	2	3	1.19E+09	20.32	0.00	45.14	19.70	0.00	43.77	0.00	-1	-1	0
428	curved	51	20	3	3	3	1.26E+09	30.68	0.00	44.44	30.68	0.00	44.44	0.00	0	0	0
429	curved	51	30	1	1	1	4.19E+08	14.85	0.00	14.85	16.84	0.00	14.92	1.99	1	1	0
430	curved	51	30	1	1	1	4.19E+08	14.85	0.00	14.85	16.84	0.00	14.92	0.00	1	1	0
431	curved	51	30	1	2	1	9.18E+08	29.22	0.00	15.34	29.22	0.00	15.34	0.00	0	0	0
432	curved	51	30	1	2	1	9.18E+08	29.22	0.00	15.34	29.22	0.00	15.34	0.00	0	0	0
433	curved	51	30	1	3	1	2.44E+09	44.39	0.00	13.83	44.39	0.00	13.83	0.00	0	0	0
434	curved	51	30	1	1	2	3.89E+08	13.54	0.00	30.09	13.54	0.00	30.09	0.00	0	0	0
435	curved	51	30	1	1	2	3.89E+08	13.54	0.00	30.09	13.54	0.00	30.09	0.00	0	0	0
436	curved	51	30	1	2	2	7.56E+08	25.86	0.00	29.19	25.86	0.00	29.19	0.00	0	0	0
437	curved	51	30	1	3	2	1.67E+09	38.97	0.00	30.53	38.97	0.00	30.53	0.00	0	0	0
438	curved	51	30	1	1	3	3.45E+08	11.13	0.00	45.15	11.13	0.00	45.15	0.00	0	0	0
439	curved	51	30	1	1	3	3.45E+08	11.13	0.00	45.15	11.13	0.00	45.15	0.00	0	0	0
440	curved	51	30	1	2	3	5.56E+08	20.32	0.00	45.14	20.32	0.00	45.14	0.00	0	0	0
441	curved	51	30	1	3	3	9.96E+08	30.68	0.00	44.44	30.68	0.00	44.44	0.00	0	0	0
442	curved	51	30	2	1	1	8.59E+08	14.85	0.00	14.85	14.85	0.00	14.85	0.00	0	0	0
443	curved	51	30	2	1	1	8.59E+08	14.85	0.00	14.85	14.85	0.00	14.85	0.00	0	0	0
444	curved	51	30	2	2	1	1.33E+09	29.22	0.00	15.34	30.55	0.00	16.03	1.50	1	0	0
445	curved	51	30	2	3	1	3.50E+09	44.39	0.00	13.83	44.39	0.00	13.83	0.00	0	0	0
446	curved	51	30	2	1	2	8.78E+08	13.54	0.00	30.09	12.93	0.00	28.72	1.50	-1	-1	0
447	curved	51	30	2	1	2	8.78E+08	13.54	0.00	30.09	12.93	0.00	28.72	0.00	-1	-1	0
448	curved	51	30	2	2	2	1.45E+09	25.86	0.00	29.19	25.86	0.00	29.19	0.00	0	0	0
449	curved	51	30	2	2	2	1.45E+09	25.86	0.00	29.19	25.86	0.00	29.19	0.00	0	0	0
450	curved	51	30	2	3	2	1.91E+09	38.97	0.00	30.53	40.15	0.00	31.45	1.50	1	0	0

Table 52 Breast focal point location simulations parameters and results for Tests 451-500.

Test #	Shape	# of ele/ row	# of rows	# of Trans	xn	zn	q''' Max (W/m^3)	x focus input (mm)	y focus input (mm)	z focus input (mm)	x focus output (mm)	y focus output (mm)	z focus output (mm)	distance apart (mm)	r nodes apart	th nodes apart	phi nodes apart
451	curved	51	30	2	1	3	9.71E+08	11.13	0.00	45.15	11.13	0.00	45.15	0.00	0	0	0
452	curved	51	30	2	1	3	9.71E+08	11.13	0.00	45.15	11.13	0.00	45.15	0.00	0	0	0
453	curved	51	30	2	2	3	9.12E+08	20.32	0.00	45.14	19.70	0.00	43.77	1.50	-1	0	0
454	curved	51	30	2	3	3	1.95E+09	30.68	0.00	44.44	30.68	0.00	44.44	0.00	0	0	0
455	curved	51	30	3	1	1	1.42E+09	14.85	0.00	14.85	15.72	0.00	13.93	1.27	0	0	-1
456	curved	51	30	3	2	1	2.06E+09	29.22	0.00	15.34	30.55	0.00	16.03	1.50	1	0	0
457	curved	51	30	3	3	1	4.19E+09	44.39	0.00	13.83	44.39	0.00	13.83	0.00	0	0	0
458	curved	51	30	3	1	2	1.25E+09	13.54	0.00	30.09	14.12	-1.06	31.46	1.82	1	1	0
459	curved	51	30	3	2	2	2.48E+09	25.86	0.00	29.19	25.86	0.00	29.19	0.00	0	0	0
460	curved	51	30	3	2	2	2.48E+09	25.86	0.00	29.19	25.86	0.00	29.19	0.00	0	0	0
461	curved	51	30	3	3	2	1.67E+09	38.97	0.00	30.53	38.97	0.00	30.53	0.00	0	0	0
462	curved	51	30	3	1	3	1.77E+09	11.13	0.00	45.15	11.13	0.00	45.15	0.00	0	0	0
463	curved	51	30	3	1	3	1.77E+09	11.13	0.00	45.15	11.13	0.00	45.15	0.00	0	0	0
464	curved	51	30	3	2	3	1.76E+09	20.32	0.00	45.14	19.70	0.00	43.77	1.50	-1	0	0
465	curved	51	30	3	3	3	1.88E+09	30.68	0.00	44.44	30.68	0.00	44.44	0.00	0	0	0
466	curved	51	40	1	1	1	5.61E+08	14.85	0.00	14.85	16.84	0.00	14.92	1.99	1	0	-1
467	curved	51	40	1	2	1	1.23E+09	29.22	0.00	15.34	29.22	0.00	15.34	0.00	0	0	0
468	curved	51	40	1	3	1	3.26E+09	44.39	0.00	13.83	44.39	0.00	13.83	0.00	0	0	0
469	curved	51	40	1	1	2	5.20E+08	13.54	0.00	30.09	13.54	0.00	30.09	0.00	0	0	0
470	curved	51	40	1	1	2	5.20E+08	13.54	0.00	30.09	13.54	0.00	30.09	0.00	0	0	0
471	curved	51	40	1	2	2	1.01E+09	25.86	0.00	29.19	25.86	0.00	29.19	0.00	0	0	0
472	curved	51	40	1	3	2	2.24E+09	38.97	0.00	30.53	38.97	0.00	30.53	0.00	0	0	0
473	curved	51	40	1	3	2	2.24E+09	38.97	0.00	30.53	38.97	0.00	30.53	0.00	0	0	0
474	curved	51	40	1	1	3	4.60E+08	11.13	0.00	45.15	11.13	0.00	45.15	0.00	0	0	0
475	curved	51	40	1	2	3	7.42E+08	20.32	0.00	45.14	20.32	0.00	45.14	0.00	0	0	0
476	curved	51	40	1	3	3	1.34E+09	30.68	0.00	44.44	30.68	0.00	44.44	0.00	0	0	0
477	curved	51	40	2	1	1	1.17E+09	14.85	0.00	14.85	14.85	0.00	14.85	0.00	0	0	0
478	curved	51	40	2	2	1	1.81E+09	29.22	0.00	15.34	30.55	0.00	16.03	1.50	1	0	0
479	curved	51	40	2	3	1	4.75E+09	44.39	0.00	13.83	44.39	0.00	13.83	0.00	0	0	0
480	curved	51	40	2	1	2	1.18E+09	13.54	0.00	30.09	12.93	0.00	28.72	1.50	-1	-1	0
481	curved	51	40	2	1	2	1.18E+09	13.54	0.00	30.09	12.93	0.00	28.72	0.00	-1	-1	0
482	curved	51	40	2	2	2	1.90E+09	25.86	0.00	29.19	25.86	0.00	29.19	0.00	0	0	0
483	curved	51	40	2	3	2	2.49E+09	38.97	0.00	30.53	40.15	0.00	31.45	1.50	1	0	0
484	curved	51	40	2	1	3	1.29E+09	11.13	0.00	45.15	11.13	0.00	45.15	0.00	0	0	0
485	curved	51	40	2	2	3	1.20E+09	20.32	0.00	45.14	19.70	0.00	43.77	1.50	-1	-1	0
486	curved	51	40	2	2	3	1.20E+09	20.32	0.00	45.14	19.70	0.00	43.77	0.00	-1	-1	0
487	curved	51	40	2	3	3	2.48E+09	30.68	0.00	44.44	30.68	0.00	44.44	0.00	0	0	0
488	curved	51	40	3	1	1	1.87E+09	14.85	0.00	14.85	15.72	0.00	13.93	1.27	0	0	0
489	curved	51	40	3	1	1	1.87E+09	14.85	0.00	14.85	15.72	0.00	13.93	0.00	0	0	0
490	curved	51	40	3	2	1	2.78E+09	29.22	0.00	15.34	30.55	0.00	16.03	1.50	1	0	0
491	curved	51	40	3	3	1	5.72E+09	44.39	0.00	13.83	44.39	0.00	13.83	0.00	0	0	0
492	curved	51	40	3	1	2	1.62E+09	13.54	0.00	30.09	14.12	-1.06	31.46	1.82	1	1	0
493	curved	51	40	3	2	2	3.25E+09	25.86	0.00	29.19	25.86	0.00	29.19	0.00	0	0	0
494	curved	51	40	3	3	2	2.70E+09	38.97	0.00	30.53	38.97	0.00	30.53	0.00	0	0	0
495	curved	51	40	3	1	3	2.35E+09	11.13	0.00	45.15	11.13	0.00	45.15	0.00	0	0	0
496	curved	51	40	3	1	3	2.35E+09	11.13	0.00	45.15	11.13	0.00	45.15	0.00	0	0	0
497	curved	51	40	3	2	3	2.32E+09	20.32	0.00	45.14	19.70	0.00	43.77	0.00	-1	-1	0
498	curved	51	40	3	2	3	2.32E+09	20.32	0.00	45.14	19.70	0.00	43.77	0.00	-1	-1	0
499	curved	51	40	3	3	3	2.49E+09	30.68	0.00	44.44	30.68	0.00	44.44	0.00	0	0	0
500	curved	61	20	1	1	1	3.04E+08	14.85	0.00	14.85	14.85	0.00	14.85	0.00	0	0	0

Table 53 Breast focal point location simulations parameters and results for Tests 501-550.

Test #	Shape	# of ele/ row	# of rows	# of Trans	xn	zn	q''' Max (W/m^3)	x focus input (mm)	y focus input (mm)	z focus input (mm)	x focus output (mm)	y focus output (mm)	z focus output (mm)	distance apart (mm)	r nodes apart	th nodes apart	phi nodes apart
501	curved	61	20	1	2	1	6.44E+08	29.22	0.00	15.34	29.22	0.00	15.34	0.00	0	0	0
502	curved	61	20	1	3	1	1.62E+09	44.39	0.00	13.83	44.39	0.00	13.83	0.00	0	0	0
503	curved	61	20	1	1	2	2.85E+08	13.54	0.00	30.09	13.54	0.00	30.09	0.00	0	0	0
504	curved	61	20	1	1	2	2.85E+08	13.54	0.00	30.09	13.54	0.00	30.09	0.00	0	0	0
505	curved	61	20	1	2	2	5.38E+08	25.86	0.00	29.19	25.86	0.00	29.19	0.00	0	0	0
506	curved	61	20	1	3	2	1.14E+09	38.97	0.00	30.53	38.97	0.00	30.53	0.00	0	0	0
507	curved	61	20	1	1	3	2.53E+08	11.13	0.00	45.15	11.13	0.00	45.15	0.00	0	0	0
508	curved	61	20	1	1	3	2.53E+08	11.13	0.00	45.15	11.13	0.00	45.15	0.00	0	0	0
509	curved	61	20	1	2	3	4.00E+08	20.32	0.00	45.14	20.32	0.00	45.14	0.00	0	0	0
510	curved	61	20	1	3	3	7.01E+08	30.68	0.00	44.44	30.68	0.00	44.44	0.00	0	0	0
511	curved	61	20	2	1	1	6.86E+08	14.85	0.00	14.85	14.85	0.00	14.85	0.00	0	0	0
512	curved	61	20	2	2	1	7.42E+08	29.22	0.00	15.34	29.22	0.00	15.34	0.00	0	0	0
513	curved	61	20	2	3	1	1.64E+09	44.39	0.00	13.83	45.83	0.00	14.28	1.50	1	0	0
514	curved	61	20	2	1	2	6.31E+08	13.54	0.00	30.09	12.93	0.00	28.72	1.50	-1	0	0
515	curved	61	20	2	2	2	9.23E+08	25.86	0.00	29.19	25.86	0.00	29.19	0.00	0	0	0
516	curved	61	20	2	3	2	1.05E+09	38.97	0.00	30.53	37.78	0.00	29.60	1.50	-1	0	0
517	curved	61	20	2	1	3	6.63E+08	11.13	0.00	45.15	11.13	0.00	45.15	0.00	0	0	0
518	curved	61	20	2	1	3	6.63E+08	11.13	0.00	45.15	11.13	0.00	45.15	0.00	0	0	0
519	curved	61	20	2	2	3	6.66E+08	20.32	0.00	45.14	19.70	0.00	43.77	1.50	-1	0	0
520	curved	61	20	2	3	3	1.34E+09	30.68	0.00	44.44	30.68	0.00	44.44	0.00	0	0	0
521	curved	61	20	3	1	1	1.09E+09	14.85	0.00	14.85	15.72	0.00	13.93	1.27	0	0	0
522	curved	61	20	3	1	1	1.09E+09	14.85	0.00	14.85	15.72	0.00	13.93	0.00	0	0	0
523	curved	61	20	3	2	1	8.94E+08	29.22	0.00	15.34	30.55	0.00	16.03	1.50	1	0	0
524	curved	61	20	3	3	1	2.09E+09	44.39	0.00	13.83	45.83	0.00	14.28	1.50	1	0	0
525	curved	61	20	3	1	2	1.15E+09	13.54	0.00	30.09	13.51	-1.01	30.09	1.01	0	1	0
526	curved	61	20	3	2	2	5.19E+08	25.86	0.00	29.19	26.86	0.00	30.31	1.50	1	0	0
527	curved	61	20	3	3	2	1.44E+09	38.97	0.00	30.53	38.97	0.00	30.53	0.00	0	0	0
528	curved	61	20	3	1	3	9.66E+08	11.13	0.00	45.15	11.46	-0.86	46.61	1.72	1	1	0
529	curved	61	20	3	2	3	8.52E+08	20.32	0.00	45.14	19.70	0.00	43.77	1.50	-1	0	0
530	curved	61	20	3	3	3	1.21E+09	30.68	0.00	44.44	30.68	0.00	44.44	0.00	0	0	0
531	curved	61	30	1	1	1	4.55E+08	14.85	0.00	14.85	14.85	0.00	14.85	0.00	0	0	0
532	curved	61	30	1	2	1	9.69E+08	29.22	0.00	15.34	29.22	0.00	15.34	0.00	0	0	0
533	curved	61	30	1	3	1	2.43E+09	44.39	0.00	13.83	44.39	0.00	13.83	0.00	0	0	0
534	curved	61	30	1	1	2	4.27E+08	13.54	0.00	30.09	13.54	0.00	30.09	0.00	0	0	0
535	curved	61	30	1	1	2	4.27E+08	13.54	0.00	30.09	13.54	0.00	30.09	0.00	0	0	0
536	curved	61	30	1	2	2	8.06E+08	25.86	0.00	29.19	25.86	0.00	29.19	0.00	0	0	0
537	curved	61	30	1	3	2	1.71E+09	38.97	0.00	30.53	38.97	0.00	30.53	0.00	0	0	0
538	curved	61	30	1	1	3	3.81E+08	11.13	0.00	45.15	11.13	0.00	45.15	0.00	0	0	0
539	curved	61	30	1	1	3	3.81E+08	11.13	0.00	45.15	11.13	0.00	45.15	0.00	0	0	0
540	curved	61	30	1	2	3	6.01E+08	20.32	0.00	45.14	20.32	0.00	45.14	0.00	0	0	0
541	curved	61	30	1	3	3	1.05E+09	30.68	0.00	44.44	30.68	0.00	44.44	0.00	0	0	0
542	curved	61	30	1	3	3	1.05E+09	30.68	0.00	44.44	30.68	0.00	44.44	0.00	0	0	0
543	curved	61	30	2	1	1	1.06E+09	14.85	0.00	14.85	14.85	0.00	14.85	0.00	0	0	0
544	curved	61	30	2	2	1	1.02E+09	29.22	0.00	15.34	29.22	0.00	15.34	0.00	0	0	0
545	curved	61	30	2	3	1	2.44E+09	44.39	0.00	13.83	45.83	0.00	14.28	1.50	1	0	0
546	curved	61	30	2	1	2	9.50E+08	13.54	0.00	30.09	12.93	0.00	28.72	1.50	-1	0	0
547	curved	61	30	2	2	2	1.32E+09	25.86	0.00	29.19	25.86	0.00	29.19	0.00	0	0	0
548	curved	61	30	2	3	2	1.65E+09	38.97	0.00	30.53	38.97	0.00	30.53	0.00	0	0	0
549	curved	61	30	2	1	3	9.78E+08	11.13	0.00	45.15	11.13	0.00	45.15	0.00	0	0	0
550	curved	61	30	2	1	3	9.78E+08	11.13	0.00	45.15	11.13	0.00	45.15	0.00	0	0	0

Table 54 Breast focal point location simulations parameters and results for Tests 551-593.

Test #	Shape	# of ele/ row	# of rows	# of Trans	xn	zn	q''' Max (W/m^3)	x focus input (mm)	y focus input (mm)	z focus input (mm)	x focus output (mm)	y focus output (mm)	z focus output (mm)	distance apart (mm)	r nodes apart	th nodes apart	phi nodes apart
551	curved	61	30	2	2	3	9.76E+08	20.32	0.00	45.14	19.70	0.00	43.77	1.50	-1	0	0
552	curved	61	30	2	3	3	1.80E+09	30.68	0.00	44.44	30.68	0.00	44.44	0.00	0	0	0
553	curved	61	30	3	1	1	1.60E+09	14.85	0.00	14.85	15.72	0.00	13.93	1.27	0	0	0
554	curved	61	30	3	1	1	1.60E+09	14.85	0.00	14.85	15.72	0.00	13.93	0.00	0	0	0
555	curved	61	30	3	2	1	1.42E+09	29.22	0.00	15.34	30.55	0.00	16.03	1.50	1	0	0
556	curved	61	30	3	3	1	3.11E+09	44.39	0.00	13.83	45.83	0.00	14.28	1.50	1	0	0
557	curved	61	30	3	1	2	1.70E+09	13.54	0.00	30.09	13.51	-1.01	30.09	1.01	0	1	0
558	curved	61	30	3	2	2	8.20E+08	25.86	0.00	29.19	26.86	0.00	30.31	1.50	1	0	0
559	curved	61	30	3	3	2	2.37E+09	38.97	0.00	30.53	38.97	0.00	30.53	0.00	0	0	0
560	curved	61	30	3	1	3	1.45E+09	11.13	0.00	45.15	11.46	-0.86	46.61	1.72	1	1	0
561	curved	61	30	3	2	3	1.24E+09	20.32	0.00	45.14	19.70	0.00	43.77	1.50	-1	0	0
562	curved	61	30	3	3	3	2.00E+09	30.68	0.00	44.44	31.53	0.00	45.68	1.50	1	0	0
563	curved	61	40	1	1	1	6.09E+08	14.85	0.00	14.85	14.85	0.00	14.85	0.00	0	0	0
564	curved	61	40	1	2	1	1.29E+09	29.22	0.00	15.34	29.22	0.00	15.34	0.00	0	0	0
565	curved	61	40	1	2	1	1.29E+09	29.22	0.00	15.34	29.22	0.00	15.34	0.00	0	0	0
566	curved	61	40	1	3	1	3.26E+09	44.39	0.00	13.83	44.39	0.00	13.83	0.00	0	0	0
567	curved	61	40	1	1	2	5.71E+08	13.54	0.00	30.09	13.54	0.00	30.09	0.00	0	0	0
568	curved	61	40	1	2	2	1.07E+09	25.86	0.00	29.19	25.86	0.00	29.19	0.00	0	0	0
569	curved	61	40	1	3	2	2.29E+09	38.97	0.00	30.53	38.97	0.00	30.53	0.00	0	0	0
570	curved	61	40	1	3	2	2.29E+09	38.97	0.00	30.53	38.97	0.00	30.53	0.00	0	0	0
571	curved	61	40	1	1	3	5.08E+08	11.13	0.00	45.15	11.13	0.00	45.15	0.00	0	0	0
572	curved	61	40	1	2	3	8.03E+08	20.32	0.00	45.14	20.32	0.00	45.14	0.00	0	0	0
573	curved	61	40	1	3	3	1.41E+09	30.68	0.00	44.44	30.68	0.00	44.44	0.00	0	0	0
574	curved	61	40	2	1	1	1.43E+09	14.85	0.00	14.85	14.85	0.00	14.85	0.00	0	0	0
575	curved	61	40	2	2	1	1.31E+09	29.22	0.00	15.34	28.24	0.00	17.07	1.99	0	0	1
576	curved	61	40	2	3	1	3.24E+09	44.39	0.00	13.83	45.83	0.00	14.28	1.50	1	0	0
577	curved	61	40	2	1	2	1.25E+09	13.54	0.00	30.09	12.93	0.00	28.72	1.50	-1	-1	0
578	curved	61	40	2	1	2	1.25E+09	13.54	0.00	30.09	12.93	0.00	28.72	0.00	-1	-1	0
579	curved	61	40	2	2	2	1.71E+09	25.86	0.00	29.19	25.86	0.00	29.19	0.00	0	0	0
580	curved	61	40	2	3	2	2.21E+09	38.97	0.00	30.53	37.78	0.00	29.60	1.50	-1	0	0
581	curved	61	40	2	1	3	1.29E+09	11.13	0.00	45.15	11.13	0.00	45.15	0.00	0	0	0
582	curved	61	40	2	2	3	1.29E+09	20.32	0.00	45.14	19.70	0.00	43.77	1.50	-1	0	0
583	curved	61	40	2	3	3	2.76E+09	30.68	0.00	44.44	30.68	0.00	44.44	0.00	0	0	0
584	curved	61	40	3	1	1	2.12E+09	14.85	0.00	14.85	15.72	0.00	13.93	1.27	0	0	0
585	curved	61	40	3	1	1	2.12E+09	14.85	0.00	14.85	15.72	0.00	13.93	0.00	0	0	0
586	curved	61	40	3	2	1	1.94E+09	29.22	0.00	15.34	30.55	0.00	16.03	1.50	1	0	0
587	curved	61	40	3	3	1	4.11E+09	44.39	0.00	13.83	45.83	0.00	14.28	1.50	1	0	0
588	curved	61	40	3	1	2	2.32E+09	13.54	0.00	30.09	13.51	-1.01	30.09	1.01	0	1	0
589	curved	61	40	3	2	2	1.12E+09	25.86	0.00	29.19	26.86	0.00	30.31	1.50	1	0	0
590	curved	61	40	3	3	2	2.70E+09	38.97	0.00	30.53	37.78	0.00	29.60	1.50	-1	0	0
591	curved	61	40	3	1	3	1.93E+09	11.13	0.00	45.15	11.46	-0.86	46.61	1.72	1	1	0
592	curved	61	40	3	2	3	1.62E+09	20.32	0.00	45.14	19.70	0.00	43.77	1.50	-1	0	0
593	curved	61	40	3	3	3	2.47E+09	30.68	0.00	44.44	30.68	0.00	44.44	0.00	0	0	0

Appendix D: Breast Necrosis Simulations Results

Results from the simulations of the US propagation and resulting tissue necrosis produced from HIFU for breast cancer are displayed in Table 55 – Table 64.

Table 55 Breast necrosis simulations parameters and results for Tests 1-50.

Test #	Shape	# of ele/ row	# of rows	Q(W)	xn	zn	Vnecr (m^3)	Heat Time (s)
1	flat	41	50	20	1	1	1.38E-06	2.64
2	flat	41	50	20	2	1	2.36E-07	0.87
3	flat	41	50	20	3	1	7.13E-08	0.25
4	flat	41	50	20	1	2	2.01E-06	2.99
5	flat	41	50	20	2	2	2.99E-07	1.10
6	flat	41	50	20	3	2	9.59E-08	0.39
7	flat	41	50	20	1	3	3.00E-06	3.69
8	flat	41	50	20	2	3	6.81E-07	1.69
9	flat	41	50	20	3	3	1.92E-07	0.76
10	flat	41	75	20	1	1	1.11E-06	1.62
11	flat	41	75	20	2	1	2.28E-07	0.56
12	flat	41	75	20	3	1	7.13E-08	0.17
13	flat	41	75	20	1	2	1.59E-06	1.81
14	flat	41	75	20	2	2	2.89E-07	0.71
15	flat	41	75	20	3	2	9.59E-08	0.26
16	flat	41	75	20	1	3	2.57E-06	2.20
17	flat	41	75	20	2	3	5.91E-07	1.06
18	flat	41	75	20	3	3	1.19E-07	0.49
19	flat	41	100	20	1	1	1.05E-06	1.16
20	flat	41	100	20	2	1	2.28E-07	0.41
21	flat	41	100	20	3	1	7.13E-08	0.13
22	flat	41	100	20	1	2	1.34E-06	1.30
23	flat	41	100	20	2	2	2.82E-07	0.52
24	flat	41	100	20	3	2	9.59E-08	0.19
25	flat	41	100	20	1	3	2.28E-06	1.56
26	flat	41	100	20	2	3	5.91E-07	0.77
27	flat	41	100	20	3	3	1.19E-07	0.37
28	flat	41	50	30	1	1	1.16E-06	1.62
29	flat	41	50	30	2	1	2.27E-07	0.56
30	flat	41	50	30	3	1	7.13E-08	0.17
31	flat	41	50	30	1	2	1.52E-06	1.82
32	flat	41	50	30	2	2	2.89E-07	0.71
33	flat	41	50	30	3	2	9.59E-08	0.26
34	flat	41	50	30	1	3	2.44E-06	2.20
35	flat	41	50	30	2	3	5.92E-07	1.05
36	flat	41	50	30	3	3	1.52E-07	0.50
37	flat	41	75	30	1	1	1.03E-06	1.02
38	flat	41	75	30	2	1	2.19E-07	0.36
39	flat	41	75	30	3	1	7.13E-08	0.11
40	flat	41	75	30	1	2	1.26E-06	1.13
41	flat	41	75	30	2	2	2.82E-07	0.46
42	flat	41	75	30	3	2	9.59E-08	0.17
43	flat	41	75	30	1	3	2.06E-06	1.36
44	flat	41	75	30	2	3	5.36E-07	0.67
45	flat	41	75	30	3	3	1.19E-07	0.33
46	flat	41	100	30	1	1	9.55E-07	0.74
47	flat	41	100	30	2	1	1.99E-07	0.27
48	flat	41	100	30	3	1	7.13E-08	0.09
49	flat	41	100	30	1	2	1.19E-06	0.82
50	flat	41	100	30	2	2	2.82E-07	0.34

Table 56 Breast necrosis simulations parameters and results for Tests 51-100.

Test #	Shape	# of ele/ row	# of rows	Q(W)	xn	zn	Vnecr (m^3)	Heat Time (s)
51	flat	41	100	30	3	2	9.59E-08	0.13
52	flat	41	100	30	1	3	1.92E-06	0.98
53	flat	41	100	30	2	3	4.81E-07	0.49
54	flat	41	100	30	3	3	1.19E-07	0.24
55	flat	41	50	40	1	1	1.01E-06	1.15
56	flat	41	50	40	2	1	2.08E-07	0.41
57	flat	41	50	40	3	1	7.13E-08	0.13
58	flat	41	50	40	1	2	1.39E-06	1.31
59	flat	41	50	40	2	2	2.82E-07	0.52
60	flat	41	50	40	3	2	9.59E-08	0.19
61	flat	41	50	40	1	3	2.14E-06	1.56
62	flat	41	50	40	2	3	5.05E-07	0.76
63	flat	41	50	40	3	3	1.19E-07	0.36
64	flat	41	75	40	1	1	9.40E-07	0.73
65	flat	41	75	40	2	1	1.72E-07	0.27
66	flat	41	75	40	3	1	7.13E-08	0.09
67	flat	41	75	40	1	2	1.25E-06	0.83
68	flat	41	75	40	2	2	2.82E-07	0.34
69	flat	41	75	40	3	2	9.59E-08	0.13
70	flat	41	75	40	1	3	1.90E-06	0.98
71	flat	41	75	40	2	3	4.81E-07	0.49
72	flat	41	75	40	3	3	1.19E-07	0.24
73	flat	41	100	40	1	1	8.51E-07	0.53
74	flat	41	100	40	2	1	1.72E-07	0.20
75	flat	41	100	40	3	1	7.13E-08	0.06
76	flat	41	100	40	1	2	1.17E-06	0.60
77	flat	41	100	40	2	2	2.63E-07	0.25
78	flat	41	100	40	3	2	9.59E-08	0.10
79	flat	41	100	40	1	3	1.78E-06	0.71
80	flat	41	100	40	2	3	4.35E-07	0.36
81	flat	41	100	40	3	3	1.10E-07	0.18
82	flat	51	50	20	1	1	1.29E-06	2.63
83	flat	51	50	20	2	1	1.52E-07	0.79
84	flat	51	50	20	3	1	4.27E-08	0.24
85	flat	51	50	20	1	2	1.91E-06	3.11
86	flat	51	50	20	2	2	2.39E-07	1.04
87	flat	51	50	20	3	2	6.84E-08	0.37
88	flat	51	50	20	1	3	3.22E-06	3.94
89	flat	51	50	20	2	3	7.01E-07	1.74
90	flat	51	50	20	3	3	1.91E-07	0.70
91	flat	51	75	20	1	1	1.10E-06	1.58
92	flat	51	75	20	2	1	1.52E-07	0.51
93	flat	51	75	20	3	1	4.27E-08	0.16
94	flat	51	75	20	1	2	1.48E-06	1.84
95	flat	51	75	20	2	2	2.33E-07	0.67
96	flat	51	75	20	3	2	6.84E-08	0.24
97	flat	51	75	20	1	3	2.59E-06	2.26
98	flat	51	75	20	2	3	6.39E-07	1.08
99	flat	51	75	20	3	3	1.64E-07	0.45
100	flat	51	100	20	1	1	9.44E-07	1.12

Table 57 Breast necrosis simulations parameters and results for Tests 101-150.

Test #	Shape	# of ele/ row	# of rows	Q(W)	xn	zn	Vnecr (m^3)	Heat Time (s)
100	flat	51	100	20	1	1	9.44E-07	1.12
101	flat	51	100	20	2	1	1.52E-07	0.38
102	flat	51	100	20	3	1	4.27E-08	0.12
103	flat	51	100	20	1	2	1.28E-06	1.30
104	flat	51	100	20	2	2	2.33E-07	0.49
105	flat	51	100	20	3	2	6.84E-08	0.18
106	flat	51	100	20	1	3	2.42E-06	1.58
107	flat	51	100	20	2	3	5.40E-07	0.78
108	flat	51	100	20	3	3	1.21E-07	0.34
109	flat	51	50	30	1	1	1.11E-06	1.58
110	flat	51	50	30	2	1	1.46E-07	0.51
111	flat	51	50	30	3	1	4.27E-08	0.16
112	flat	51	50	30	1	2	1.44E-06	1.84
113	flat	51	50	30	2	2	2.33E-07	0.67
114	flat	51	50	30	3	2	6.84E-08	0.24
115	flat	51	50	30	1	3	2.56E-06	2.27
116	flat	51	50	30	2	3	6.37E-07	1.07
117	flat	51	50	30	3	3	1.49E-07	0.46
118	flat	51	75	30	1	1	9.44E-07	0.98
119	flat	51	75	30	2	1	1.46E-07	0.33
120	flat	51	75	30	3	1	4.27E-08	0.11
121	flat	51	75	30	1	2	1.20E-06	1.13
122	flat	51	75	30	2	2	2.33E-07	0.43
123	flat	51	75	30	3	2	6.84E-08	0.16
124	flat	51	75	30	1	3	2.19E-06	1.38
125	flat	51	75	30	2	3	5.05E-07	0.68
126	flat	51	75	30	3	3	1.10E-07	0.30
127	flat	51	100	30	1	1	8.39E-07	0.71
128	flat	51	100	30	2	1	1.46E-07	0.24
129	flat	51	100	30	3	1	4.27E-08	0.08
130	flat	51	100	30	1	2	1.07E-06	0.81
131	flat	51	100	30	2	2	2.23E-07	0.31
132	flat	51	100	30	3	2	6.84E-08	0.12
133	flat	51	100	30	1	3	1.94E-06	0.98
134	flat	51	100	30	2	3	4.17E-07	0.49
135	flat	51	100	30	3	3	1.10E-07	0.22
136	flat	51	50	40	1	1	9.78E-07	1.12
137	flat	51	50	40	2	1	1.46E-07	0.37
138	flat	51	50	40	3	1	4.27E-08	0.12
139	flat	51	50	40	1	2	1.25E-06	1.28
140	flat	51	50	40	2	2	2.33E-07	0.49
141	flat	51	50	40	3	2	5.33E-08	0.18
142	flat	51	50	40	1	3	2.23E-06	1.59
143	flat	51	50	40	2	3	5.15E-07	0.77
144	flat	51	50	40	3	3	1.64E-07	0.33
145	flat	51	75	40	1	1	8.17E-07	0.70
146	flat	51	75	40	2	1	1.41E-07	0.24
147	flat	51	75	40	3	1	4.27E-08	0.08
148	flat	51	75	40	1	2	1.08E-06	0.80
149	flat	51	75	40	2	2	2.23E-07	0.31
150	flat	51	75	40	3	2	5.33E-08	0.12

Table 58 Breast necrosis simulations parameters and results for Tests 151-200.

Test #	Shape	# of ele/ row	# of rows	Q(W)	xn	zn	Vnecr (m^3)	Heat Time (s)
151	flat	51	75	40	1	3	1.97E-06	0.99
152	flat	51	75	40	2	3	4.54E-07	0.49
153	flat	51	75	40	3	3	1.21E-07	0.22
154	flat	51	100	40	1	1	7.62E-07	0.51
155	flat	51	100	40	2	1	1.25E-07	0.18
156	flat	51	100	40	3	1	4.27E-08	0.06
157	flat	51	100	40	1	2	1.01E-06	0.58
158	flat	51	100	40	2	2	1.96E-07	0.23
159	flat	51	100	40	3	2	5.33E-08	0.09
160	flat	51	100	40	1	3	1.79E-06	0.71
161	flat	51	100	40	2	3	3.59E-07	0.35
162	flat	51	100	40	3	3	1.10E-07	0.16
163	flat	61	50	20	1	1	1.33E-06	2.67
164	flat	61	50	20	2	1	1.36E-07	0.76
165	flat	61	50	20	3	1	4.27E-08	0.24
166	flat	61	50	20	1	2	1.92E-06	3.23
167	flat	61	50	20	2	2	2.34E-07	1.00
168	flat	61	50	20	3	2	4.10E-08	0.36
169	flat	61	50	20	1	3	3.26E-06	4.14
170	flat	61	50	20	2	3	6.16E-07	1.66
171	flat	61	50	20	3	3	1.62E-07	0.67
172	flat	61	75	20	1	1	1.03E-06	1.58
173	flat	61	75	20	2	1	1.36E-07	0.49
174	flat	61	75	20	3	1	4.27E-08	0.16
175	flat	61	75	20	1	2	1.42E-06	1.87
176	flat	61	75	20	2	2	2.23E-07	0.64
177	flat	61	75	20	3	2	4.10E-08	0.24
178	flat	61	75	20	1	3	2.64E-06	2.33
179	flat	61	75	20	2	3	5.24E-07	1.02
180	flat	61	75	20	3	3	1.34E-07	0.44
181	flat	61	100	20	1	1	9.23E-07	1.11
182	flat	61	100	20	2	1	1.22E-07	0.36
183	flat	61	100	20	3	1	4.27E-08	0.12
184	flat	61	100	20	1	2	1.31E-06	1.31
185	flat	61	100	20	2	2	2.04E-07	0.46
186	flat	61	100	20	3	2	4.10E-08	0.18
187	flat	61	100	20	1	3	2.29E-06	1.62
188	flat	61	100	20	2	3	4.06E-07	0.73
189	flat	61	100	20	3	3	1.34E-07	0.32
190	flat	61	50	30	1	1	1.09E-06	1.58
191	flat	61	50	30	2	1	1.36E-07	0.49
192	flat	61	50	30	3	1	4.27E-08	0.16
193	flat	61	50	30	1	2	1.41E-06	1.87
194	flat	61	50	30	2	2	2.23E-07	0.64
195	flat	61	50	30	3	2	4.10E-08	0.24
196	flat	61	50	30	1	3	2.56E-06	2.34
197	flat	61	50	30	2	3	5.26E-07	1.02
198	flat	61	50	30	3	3	1.34E-07	0.44
199	flat	61	75	30	1	1	9.55E-07	0.97
200	flat	61	75	30	2	1	1.22E-07	0.32

Table 59 Breast necrosis simulations parameters and results for Tests 201-250.

Test #	Shape	# of ele/ row	# of rows	Q(W)	xn	zn	Vnecr (m^3)	Heat Time (s)
201	flat	61	75	30	3	1	4.27E-08	0.11
202	flat	61	75	30	1	2	1.25E-06	1.13
203	flat	61	75	30	2	2	2.04E-07	0.41
204	flat	61	75	30	3	2	4.10E-08	0.16
205	flat	61	75	30	1	3	2.11E-06	1.40
206	flat	61	75	30	2	3	3.56E-07	0.64
207	flat	61	75	30	3	3	1.34E-07	0.28
208	flat	61	100	30	1	1	8.02E-07	0.70
209	flat	61	100	30	2	1	1.22E-07	0.23
210	flat	61	100	30	3	1	4.27E-08	0.08
211	flat	61	100	30	1	2	1.04E-06	0.81
212	flat	61	100	30	2	2	1.63E-07	0.30
213	flat	61	100	30	3	2	4.10E-08	0.12
214	flat	61	100	30	1	3	1.93E-06	0.98
215	flat	61	100	30	2	3	3.33E-07	0.46
216	flat	61	100	30	3	3	1.21E-07	0.21
217	flat	61	50	40	1	1	8.33E-07	1.11
218	flat	61	50	40	2	1	1.27E-07	0.36
219	flat	61	50	40	3	1	4.27E-08	0.12
220	flat	61	50	40	1	2	1.26E-06	1.30
221	flat	61	50	40	2	2	2.04E-07	0.46
222	flat	61	50	40	3	2	4.10E-08	0.18
223	flat	61	50	40	1	3	2.21E-06	1.62
224	flat	61	50	40	2	3	3.85E-07	0.73
225	flat	61	50	40	3	3	1.34E-07	0.32
226	flat	61	75	40	1	1	7.56E-07	0.69
227	flat	61	75	40	2	1	1.22E-07	0.23
228	flat	61	75	40	3	1	4.27E-08	0.08
229	flat	61	75	40	1	2	1.03E-06	0.80
230	flat	61	75	40	2	2	1.63E-07	0.30
231	flat	61	75	40	3	2	4.10E-08	0.12
232	flat	61	75	40	1	3	1.79E-06	0.98
233	flat	61	75	40	2	3	3.56E-07	0.46
234	flat	61	75	40	3	3	1.34E-07	0.21
235	flat	61	100	40	1	1	6.54E-07	0.50
236	flat	61	100	40	2	1	1.22E-07	0.17
237	flat	61	100	40	3	1	4.27E-08	0.06
238	flat	61	100	40	1	2	9.31E-07	0.57
239	flat	61	100	40	2	2	1.63E-07	0.22
240	flat	61	100	40	3	2	4.10E-08	0.09
241	flat	61	100	40	1	3	1.54E-06	0.70
242	flat	61	100	40	2	3	2.89E-07	0.33
243	flat	61	100	40	3	3	1.21E-07	0.15
244	curved	41	50	20	1	1	1.42E-06	2.79
245	curved	41	50	20	2	1	2.14E-07	0.87
246	curved	41	50	20	3	1	7.13E-08	0.25
247	curved	41	50	20	1	2	2.07E-06	3.18
248	curved	41	50	20	2	2	2.89E-07	1.15
249	curved	41	50	20	3	2	9.59E-08	0.39
250	curved	41	50	20	1	3	3.34E-06	4.05

Table 60 Breast necrosis simulations parameters and results for Tests 251-300.

Test #	Shape	# of ele/ row	# of rows	Q(W)	xn	zn	Vnecr (m^3)	Heat Time (s)
251	curved	41	50	20	2	3	6.83E-07	1.77
252	curved	41	50	20	3	3	1.21E-07	0.77
253	curved	41	75	20	1	1	1.11E-06	1.70
254	curved	41	75	20	2	1	1.95E-07	0.57
255	curved	41	75	20	3	1	7.13E-08	0.17
256	curved	41	75	20	1	2	1.62E-06	1.92
257	curved	41	75	20	2	2	2.89E-07	0.74
258	curved	41	75	20	3	2	9.59E-08	0.26
259	curved	41	75	20	1	3	2.61E-06	2.40
260	curved	41	75	20	2	3	5.78E-07	1.11
261	curved	41	75	20	3	3	1.10E-07	0.50
262	curved	41	100	20	1	1	9.88E-07	1.22
263	curved	41	100	20	2	1	1.49E-07	0.42
264	curved	41	100	20	3	1	7.13E-08	0.13
265	curved	41	100	20	1	2	1.49E-06	1.37
266	curved	41	100	20	2	2	2.71E-07	0.54
267	curved	41	100	20	3	2	9.59E-08	0.19
268	curved	41	100	20	1	3	2.34E-06	1.70
269	curved	41	100	20	2	3	5.40E-07	0.81
270	curved	41	100	20	3	3	1.10E-07	0.37
271	curved	41	50	30	1	1	1.22E-06	1.70
272	curved	41	50	30	2	1	1.73E-07	0.56
273	curved	41	50	30	3	1	5.88E-08	0.17
274	curved	41	50	30	1	2	1.57E-06	1.92
275	curved	41	50	30	2	2	2.89E-07	0.74
276	curved	41	50	30	3	2	9.59E-08	0.26
277	curved	41	50	30	1	3	2.54E-06	2.39
278	curved	41	50	30	2	3	5.44E-07	1.10
279	curved	41	50	30	3	3	1.10E-07	0.50
280	curved	41	75	30	1	1	1.05E-06	1.06
281	curved	41	75	30	2	1	1.73E-07	0.37
282	curved	41	75	30	3	1	5.88E-08	0.12
283	curved	41	75	30	1	2	1.35E-06	1.19
284	curved	41	75	30	2	2	2.47E-07	0.48
285	curved	41	75	30	3	2	9.59E-08	0.17
286	curved	41	75	30	1	3	2.20E-06	1.48
287	curved	41	75	30	2	3	5.39E-07	0.70
288	curved	41	75	30	3	3	1.10E-07	0.33
289	curved	41	100	30	1	1	9.45E-07	0.77
290	curved	41	100	30	2	1	1.43E-07	0.27
291	curved	41	100	30	3	1	5.88E-08	0.09
292	curved	41	100	30	1	2	1.22E-06	0.86
293	curved	41	100	30	2	2	2.25E-07	0.35
294	curved	41	100	30	3	2	9.59E-08	0.13
295	curved	41	100	30	1	3	2.11E-06	1.06
296	curved	41	100	30	2	3	4.78E-07	0.51
297	curved	41	100	30	3	3	1.10E-07	0.24
298	curved	41	50	40	1	1	9.75E-07	1.21
299	curved	41	50	40	2	1	1.68E-07	0.41
300	curved	41	50	40	3	1	7.13E-08	0.13

Table 61 Breast necrosis simulations parameters and results for Tests 301-350.

Test #	Shape	# of ele/ row	# of rows	Q(W)	xn	zn	Vnecr (m^3)	Heat Time (s)
301	curved	41	50	40	1	2	1.48E-06	1.38
302	curved	41	50	40	2	2	2.71E-07	0.54
303	curved	41	50	40	3	2	9.59E-08	0.19
304	curved	41	50	40	1	3	2.28E-06	1.69
305	curved	41	50	40	2	3	5.44E-07	0.80
306	curved	41	50	40	3	3	1.10E-07	0.37
307	curved	41	75	40	1	1	8.63E-07	0.77
308	curved	41	75	40	2	1	1.48E-07	0.27
309	curved	41	75	40	3	1	7.13E-08	0.09
310	curved	41	75	40	1	2	1.17E-06	0.87
311	curved	41	75	40	2	2	2.25E-07	0.35
312	curved	41	75	40	3	2	9.59E-08	0.13
313	curved	41	75	40	1	3	2.06E-06	1.06
314	curved	41	75	40	2	3	5.04E-07	0.51
315	curved	41	75	40	3	3	1.10E-07	0.24
316	curved	41	100	40	1	1	8.02E-07	0.56
317	curved	41	100	40	2	1	1.39E-07	0.20
318	curved	41	100	40	3	1	7.13E-08	0.07
319	curved	41	100	40	1	2	9.91E-07	0.63
320	curved	41	100	40	2	2	2.25E-07	0.26
321	curved	41	100	40	3	2	9.59E-08	0.10
322	curved	41	100	40	1	3	1.94E-06	0.77
323	curved	41	100	40	2	3	4.39E-07	0.38
324	curved	41	100	40	3	3	1.10E-07	0.18
325	curved	51	50	20	1	1	1.21E-06	2.78
326	curved	51	50	20	2	1	1.41E-07	0.81
327	curved	51	50	20	3	1	4.27E-08	0.25
328	curved	51	50	20	1	2	1.87E-06	3.34
329	curved	51	50	20	2	2	1.98E-07	1.06
330	curved	51	50	20	3	2	5.33E-08	0.37
331	curved	51	50	20	1	3	3.02E-06	4.27
332	curved	51	50	20	2	3	6.37E-07	1.78
333	curved	51	50	20	3	3	1.34E-07	0.71
334	curved	51	75	20	1	1	9.86E-07	1.66
335	curved	51	75	20	2	1	1.41E-07	0.52
336	curved	51	75	20	3	1	4.27E-08	0.17
337	curved	51	75	20	1	2	1.39E-06	1.95
338	curved	51	75	20	2	2	1.82E-07	0.68
339	curved	51	75	20	3	2	5.33E-08	0.25
340	curved	51	75	20	1	3	2.40E-06	2.42
341	curved	51	75	20	2	3	5.10E-07	1.09
342	curved	51	75	20	3	3	1.21E-07	0.46
343	curved	51	100	20	1	1	8.96E-07	1.17
344	curved	51	100	20	2	1	1.41E-07	0.38
345	curved	51	100	20	3	1	4.27E-08	0.13
346	curved	51	100	20	1	2	1.19E-06	1.38
347	curved	51	100	20	2	2	1.82E-07	0.49
348	curved	51	100	20	3	2	5.33E-08	0.19
349	curved	51	100	20	1	3	2.21E-06	1.68
350	curved	51	100	20	2	3	3.83E-07	0.79

Table 62 Breast necrosis simulations parameters and results for Tests 351-400.

Test #	Shape	# of ele/ row	# of rows	Q(W)	xn	zn	Vnecr (m^3)	Heat Time (s)
351	curved	51	100	20	3	3	1.10E-07	0.34
352	curved	51	50	30	1	1	1.04E-06	1.66
353	curved	51	50	30	2	1	1.41E-07	0.52
354	curved	51	50	30	3	1	4.27E-08	0.17
355	curved	51	50	30	1	2	1.39E-06	1.96
356	curved	51	50	30	2	2	1.82E-07	0.68
357	curved	51	50	30	3	2	5.33E-08	0.25
358	curved	51	50	30	1	3	2.46E-06	2.43
359	curved	51	50	30	2	3	4.40E-07	1.09
360	curved	51	50	30	3	3	1.21E-07	0.47
361	curved	51	75	30	1	1	8.57E-07	1.02
362	curved	51	75	30	2	1	1.19E-07	0.34
363	curved	51	75	30	3	1	4.27E-08	0.11
364	curved	51	75	30	1	2	1.12E-06	1.20
365	curved	51	75	30	2	2	1.63E-07	0.44
366	curved	51	75	30	3	2	5.33E-08	0.17
367	curved	51	75	30	1	3	1.98E-06	1.46
368	curved	51	75	30	2	3	3.71E-07	0.69
369	curved	51	75	30	3	3	1.10E-07	0.30
370	curved	51	100	30	1	1	7.93E-07	0.73
371	curved	51	100	30	2	1	1.19E-07	0.25
372	curved	51	100	30	3	1	4.27E-08	0.09
373	curved	51	100	30	1	2	9.94E-07	0.86
374	curved	51	100	30	2	2	1.63E-07	0.32
375	curved	51	100	30	3	2	4.10E-08	0.12
376	curved	51	100	30	1	3	1.78E-06	1.04
377	curved	51	100	30	2	3	3.26E-07	0.50
378	curved	51	100	30	3	3	1.10E-07	0.22
379	curved	51	50	40	1	1	8.41E-07	1.17
380	curved	51	50	40	2	1	1.36E-07	0.38
381	curved	51	50	40	3	1	4.27E-08	0.13
382	curved	51	50	40	1	2	1.19E-06	1.36
383	curved	51	50	40	2	2	1.82E-07	0.50
384	curved	51	50	40	3	2	4.10E-08	0.18
385	curved	51	50	40	1	3	2.11E-06	1.69
386	curved	51	50	40	2	3	4.03E-07	0.78
387	curved	51	50	40	3	3	1.21E-07	0.34
388	curved	51	75	40	1	1	7.48E-07	0.73
389	curved	51	75	40	2	1	1.19E-07	0.25
390	curved	51	75	40	3	1	4.27E-08	0.08
391	curved	51	75	40	1	2	1.01E-06	0.85
392	curved	51	75	40	2	2	1.63E-07	0.32
393	curved	51	75	40	3	2	4.10E-08	0.12
394	curved	51	75	40	1	3	1.74E-06	1.04
395	curved	51	75	40	2	3	3.26E-07	0.50
396	curved	51	75	40	3	3	1.10E-07	0.22
397	curved	51	100	40	1	1	6.68E-07	0.53
398	curved	51	100	40	2	1	1.19E-07	0.18
399	curved	51	100	40	3	1	4.27E-08	0.06
400	curved	51	100	40	1	2	8.74E-07	0.61

Table 63 Breast necrosis simulations parameters and results for Tests 401-450.

Test #	Shape	# of ele/ row	# of rows	Q(W)	xn	zn	Vnecr (m^3)	Heat Time (s)
401	curved	51	100	40	2	2	1.63E-07	0.23
402	curved	51	100	40	3	2	4.10E-08	0.09
403	curved	51	100	40	1	3	1.56E-06	0.75
404	curved	51	100	40	2	3	2.85E-07	0.36
405	curved	51	100	40	3	3	1.10E-07	0.17
406	curved	61	50	20	1	1	1.13E-06	2.97
407	curved	61	50	20	2	1	1.15E-07	0.79
408	curved	61	50	20	3	1	4.27E-08	0.25
409	curved	61	50	20	1	2	1.60E-06	3.44
410	curved	61	50	20	2	2	1.91E-07	1.03
411	curved	61	50	20	3	2	4.10E-08	0.37
412	curved	61	50	20	1	3	3.34E-06	4.73
413	curved	61	50	20	2	3	4.72E-07	1.72
414	curved	61	50	20	3	3	1.31E-07	0.70
415	curved	61	75	20	1	1	8.40E-07	1.72
416	curved	61	75	20	2	1	9.86E-08	0.50
417	curved	61	75	20	3	1	4.27E-08	0.17
418	curved	61	75	20	1	2	1.15E-06	1.94
419	curved	61	75	20	2	2	1.40E-07	0.65
420	curved	61	75	20	3	2	4.10E-08	0.25
421	curved	61	75	20	1	3	2.21E-06	2.47
422	curved	61	75	20	2	3	3.76E-07	1.05
423	curved	61	75	20	3	3	1.10E-07	0.45
424	curved	61	100	20	1	1	7.15E-07	1.20
425	curved	61	100	20	2	1	8.78E-08	0.37
426	curved	61	100	20	3	1	4.27E-08	0.13
427	curved	61	100	20	1	2	9.71E-07	1.35
428	curved	61	100	20	2	2	1.40E-07	0.48
429	curved	61	100	20	3	2	4.10E-08	0.18
430	curved	61	100	20	1	3	1.78E-06	1.68
431	curved	61	100	20	2	3	3.14E-07	0.75
432	curved	61	100	20	3	3	1.10E-07	0.33
433	curved	61	50	30	1	1	8.83E-07	1.72
434	curved	61	50	30	2	1	9.86E-08	0.50
435	curved	61	50	30	3	1	4.27E-08	0.17
436	curved	61	50	30	1	2	1.15E-06	1.94
437	curved	61	50	30	2	2	1.40E-07	0.65
438	curved	61	50	30	3	2	4.10E-08	0.25
439	curved	61	50	30	1	3	2.10E-06	2.47
440	curved	61	50	30	2	3	3.56E-07	1.04
441	curved	61	50	30	3	3	1.10E-07	0.45
442	curved	61	75	30	1	1	7.36E-07	1.04
443	curved	61	75	30	2	1	8.78E-08	0.32
444	curved	61	75	30	3	1	4.27E-08	0.11
445	curved	61	75	30	1	2	9.03E-07	1.17
446	curved	61	75	30	2	2	1.30E-07	0.42
447	curved	61	75	30	3	2	4.10E-08	0.16
448	curved	61	75	30	1	3	1.56E-06	1.44
449	curved	61	75	30	2	3	2.72E-07	0.65
450	curved	61	75	30	3	3	8.54E-08	0.29

Table 64 Breast necrosis simulations parameters and results for Tests 451-486.

Test #	Shape	# of ele/ row	# of rows	Q(W)	xn	zn	Vnecr (m^3)	Heat Time (s)
451	curved	61	100	30	1	1	6.61E-07	0.74
452	curved	61	100	30	2	1	8.78E-08	0.24
453	curved	61	100	30	3	1	4.27E-08	0.08
454	curved	61	100	30	1	2	7.82E-07	0.83
455	curved	61	100	30	2	2	1.30E-07	0.30
456	curved	61	100	30	3	2	4.10E-08	0.12
457	curved	61	100	30	1	3	1.24E-06	1.01
458	curved	61	100	30	2	3	2.61E-07	0.47
459	curved	61	100	30	3	3	8.54E-08	0.22
460	curved	61	50	40	1	1	7.19E-07	1.20
461	curved	61	50	40	2	1	8.78E-08	0.37
462	curved	61	50	40	3	1	4.27E-08	0.13
463	curved	61	50	40	1	2	1.00E-06	1.34
464	curved	61	50	40	2	2	1.40E-07	0.48
465	curved	61	50	40	3	2	4.10E-08	0.18
466	curved	61	50	40	1	3	1.61E-06	1.67
467	curved	61	50	40	2	3	2.85E-07	0.75
468	curved	61	50	40	3	3	1.10E-07	0.33
469	curved	61	75	40	1	1	6.31E-07	0.74
470	curved	61	75	40	2	1	8.78E-08	0.24
471	curved	61	75	40	3	1	4.27E-08	0.08
472	curved	61	75	40	1	2	7.52E-07	0.82
473	curved	61	75	40	2	2	1.30E-07	0.30
474	curved	61	75	40	3	2	4.10E-08	0.12
475	curved	61	75	40	1	3	1.19E-06	1.01
476	curved	61	75	40	2	3	2.61E-07	0.47
477	curved	61	75	40	3	3	8.54E-08	0.21
478	curved	61	100	40	1	1	5.61E-07	0.53
479	curved	61	100	40	2	1	8.78E-08	0.18
480	curved	61	100	40	3	1	4.27E-08	0.06
481	curved	61	100	40	1	2	6.50E-07	0.59
482	curved	61	100	40	2	2	1.30E-07	0.22
483	curved	61	100	40	3	2	4.10E-08	0.09
484	curved	61	100	40	1	3	1.07E-06	0.71
485	curved	61	100	40	2	3	2.47E-07	0.34
486	curved	61	100	40	3	3	8.54E-08	0.16

Appendix E: Heating Time v. Power for Breast US Simulations

Graphs of the heating time versus the transducer power for different transducer parameters and focus locations are displayed in Figure 128 and Figure 129.

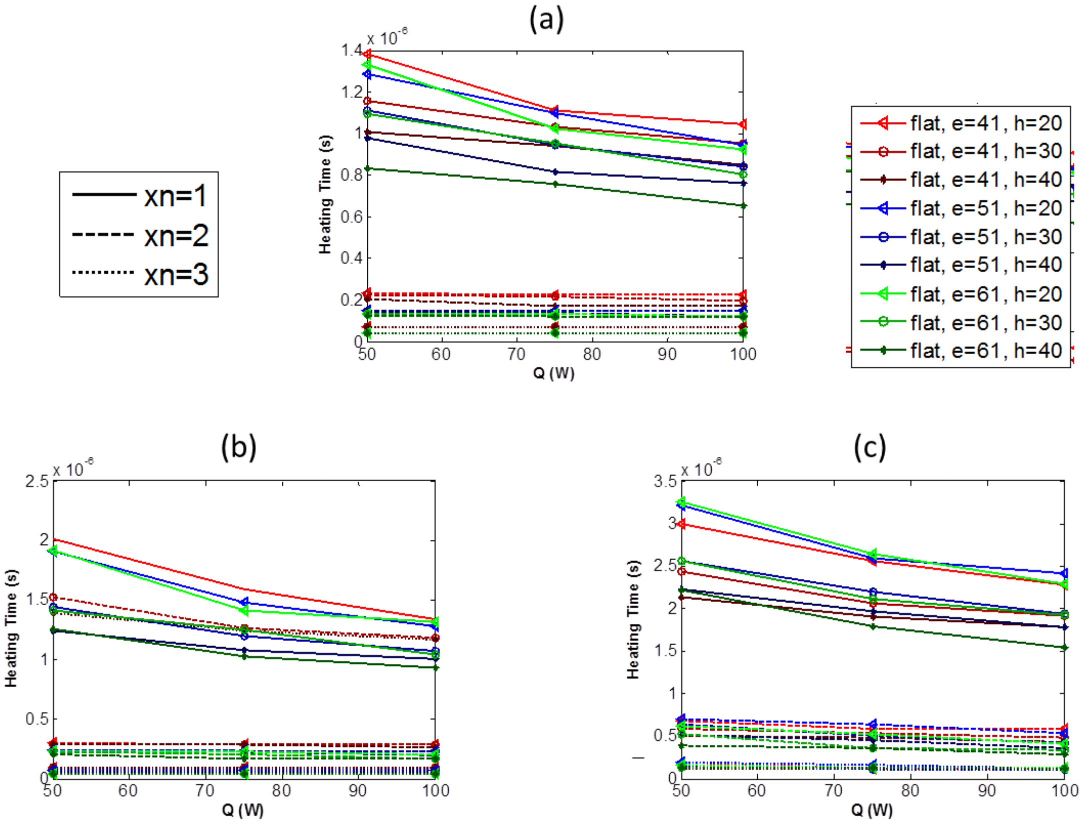

Figure 128 Heating time versus transducer power for flat transducers focused at (a) zn=1, (b) zn=2, (c) zn=3 for different values of xn (distinguished by line type) and transducer parameters (distinguished by color).

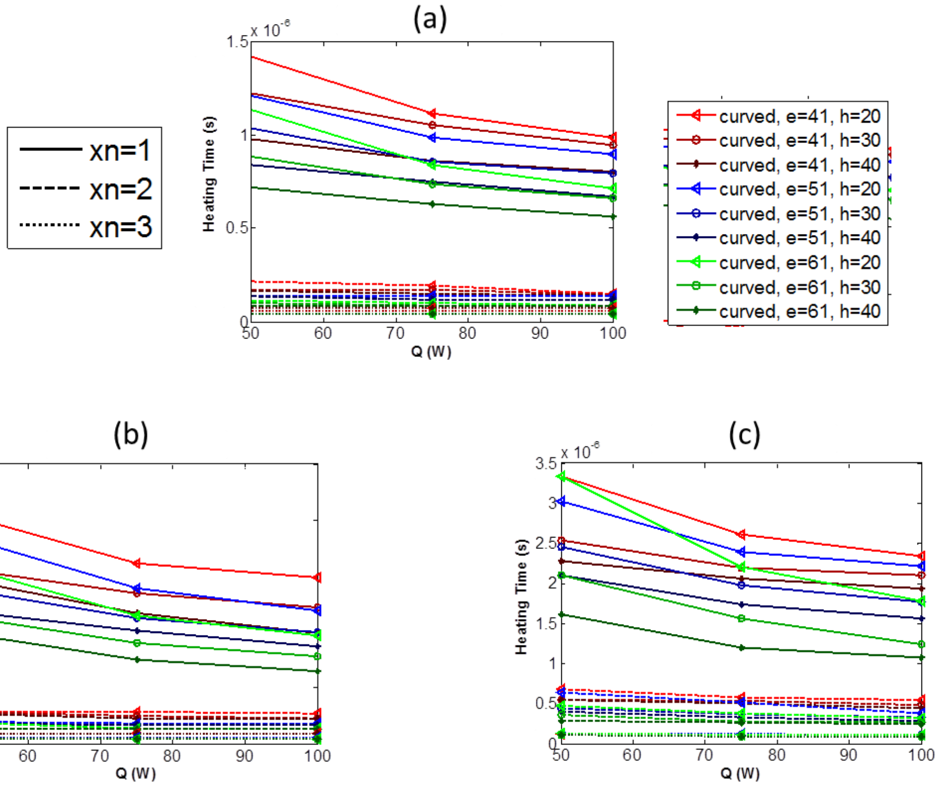

Figure 129 Heating time versus transducer power for curved transducers focused at (a) zn=1, (b) zn=2, (c) zn=3 for different values of xn (distinguished by line type) and transducer parameters (distinguished by color).

Appendix F: Heater Assembly Technical Drawings

Technical drawings of the heater assembly components not purchased are shown in Figure 130 – Figure 135.

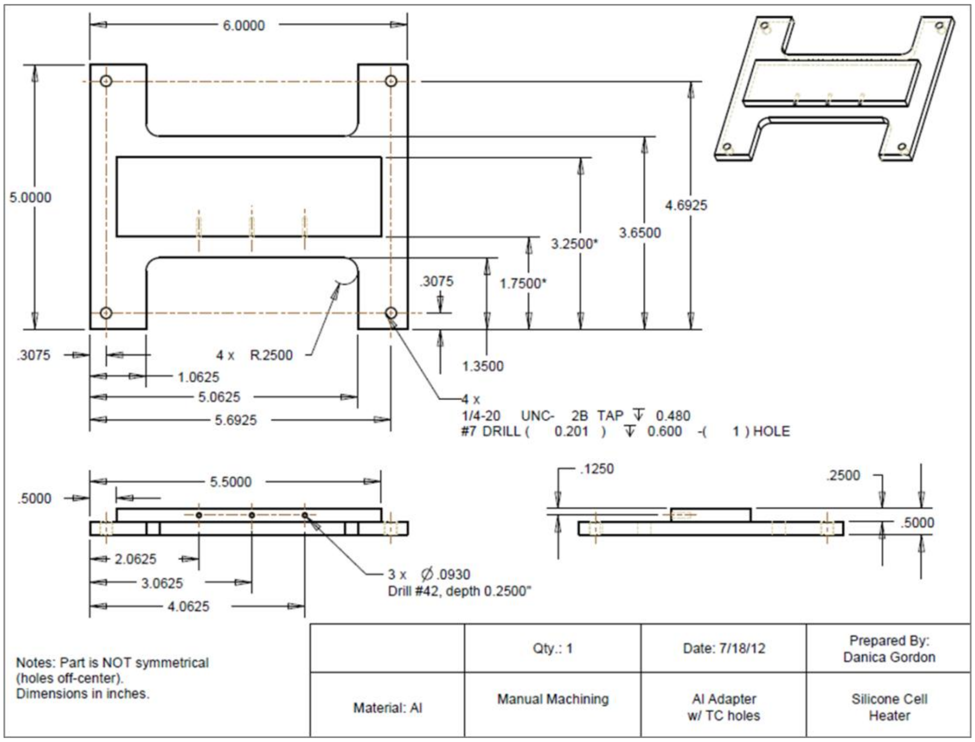

Figure 130 Technical drawing of aluminum adapter.

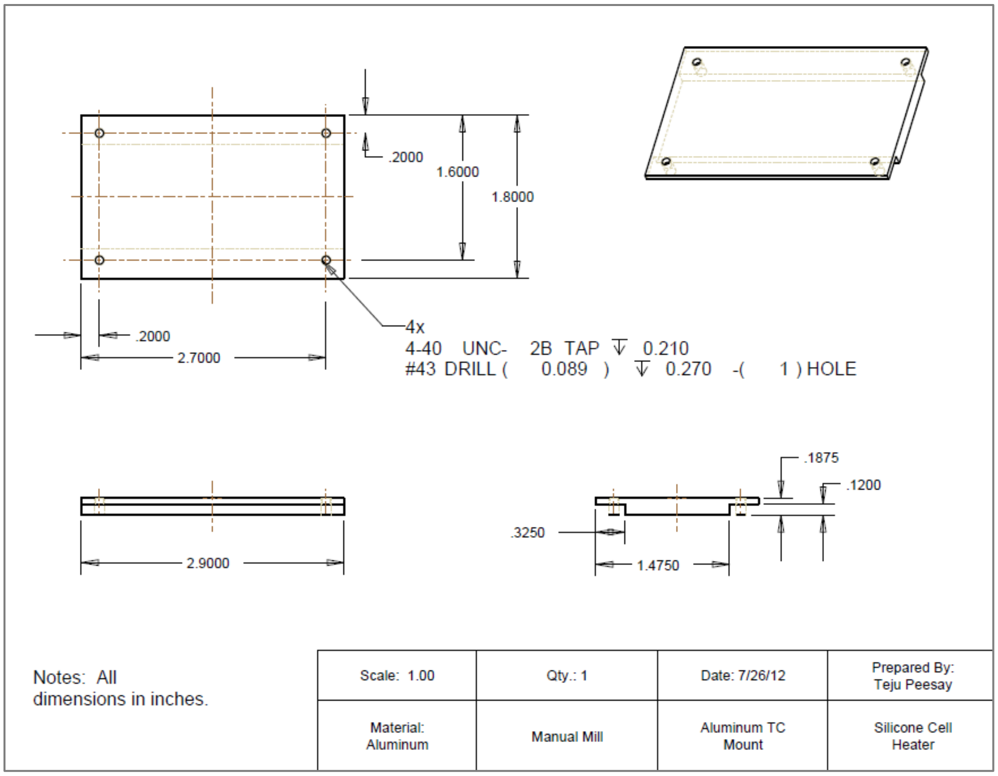

Figure 131 Technical drawing of aluminum top piece.

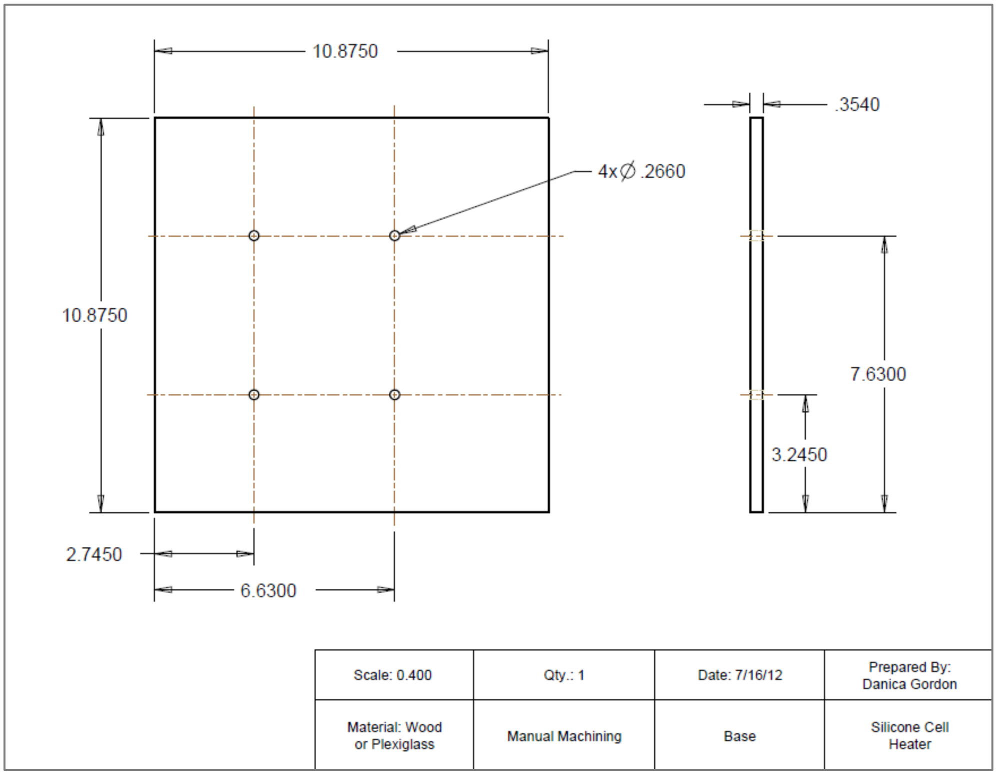

Figure 132 Technical drawing of base.

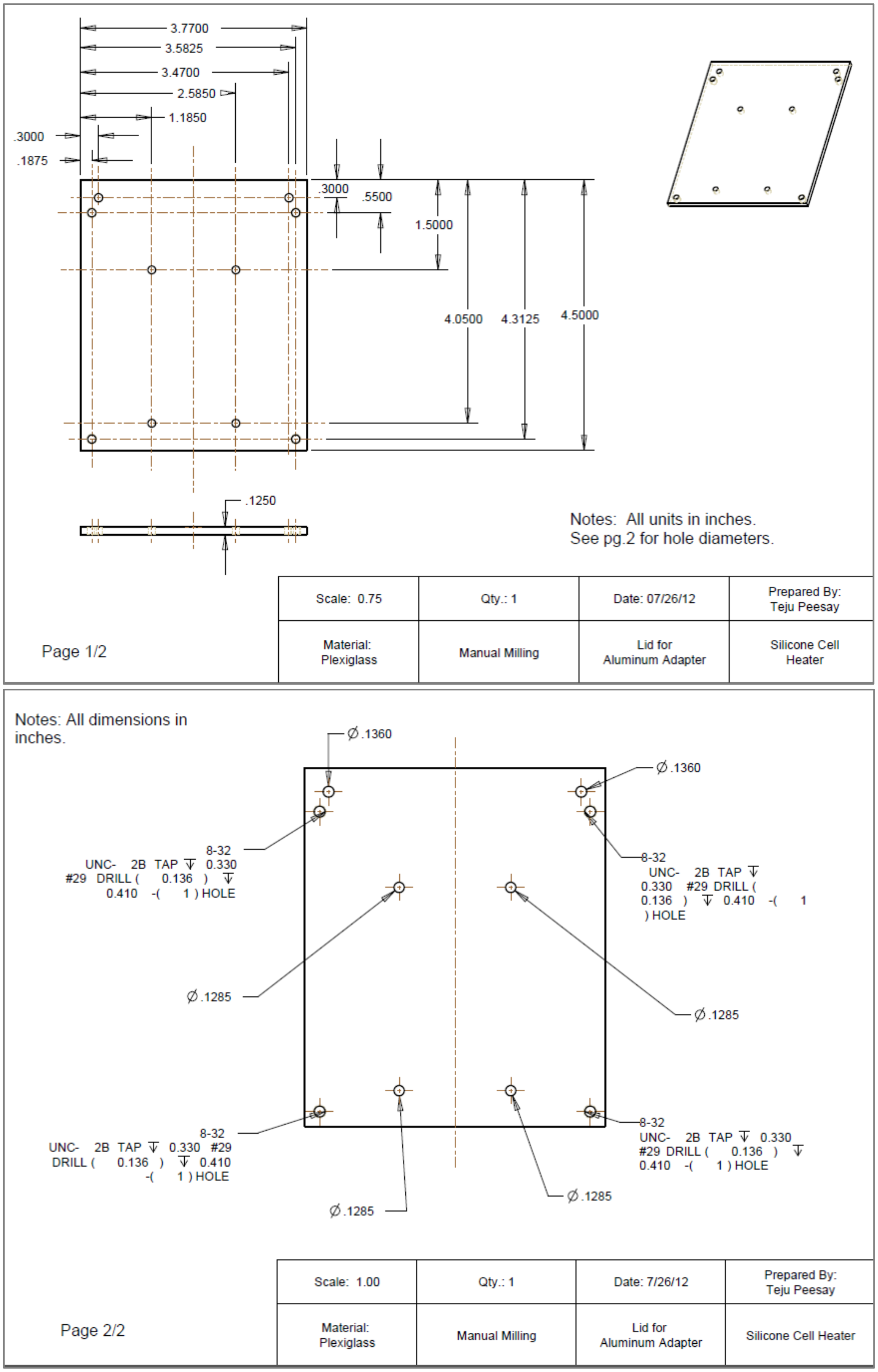

Figure 133 Technical drawing of top.

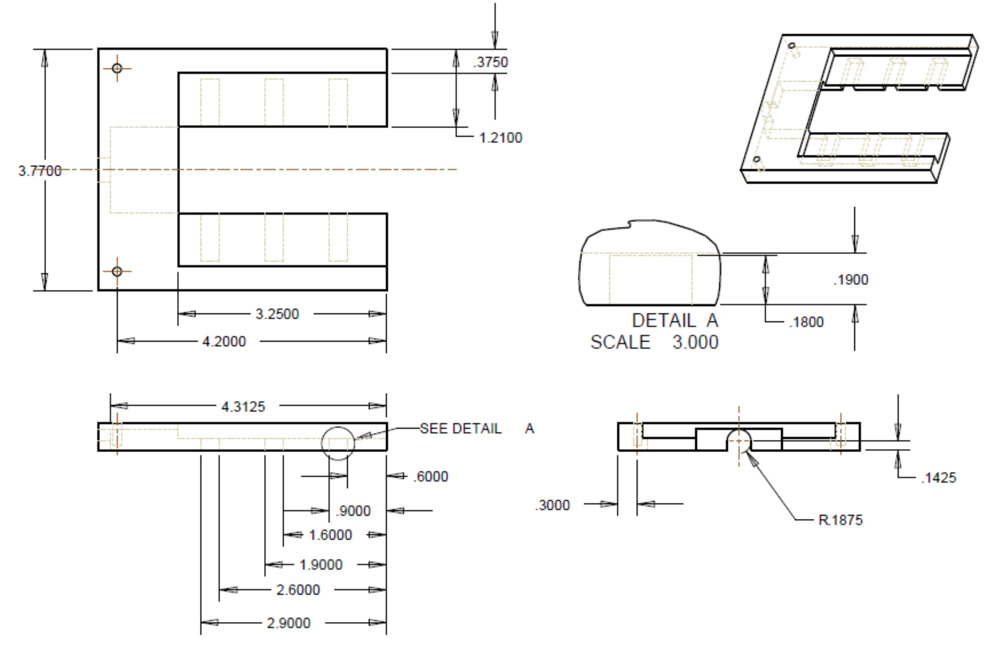

Piece symmetrical about centerline. All dimensions in inches.

Scale 0.750	Qty.: 1	Date: 7/18/12	Prepared By: Danica Gordon
Material: ABS Plastic	Rapid Prototype	Plastic Slide Heater	Silicone Cell Heater

Figure 134 Technical drawing of plastic slide holder.

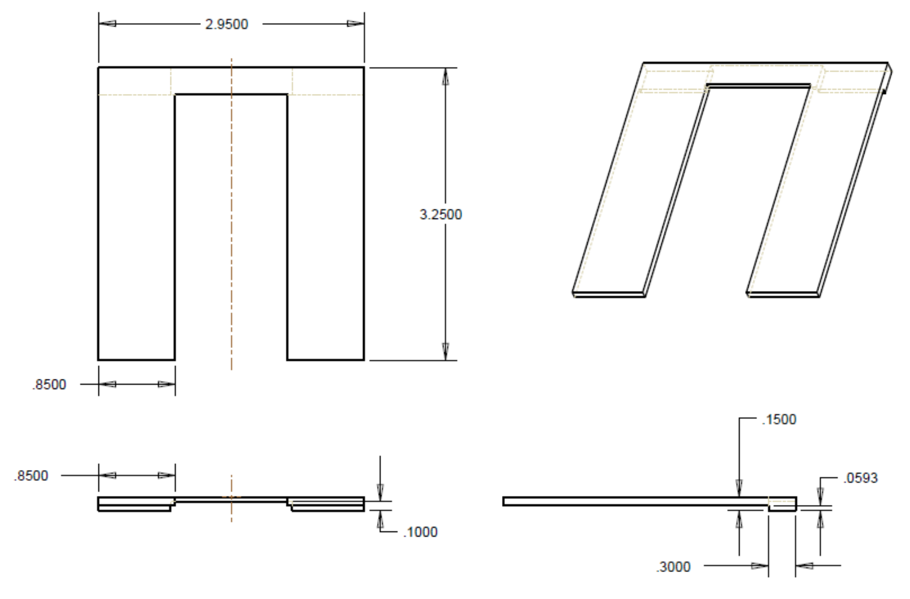

Part symmetrical about centerline. All dimensions in inches.

	Qty.: 1	Date: 7/18/12	Prepared By: Danica Gordon
Material: ABS Plastic	Rapid Prototyped	U-Aligner	Silicone Cell Heater

Figure 135 Technical drawing of U-aligner.

Appendix G: Cell Viabilities from Cell Experiments

The graphs of the temperatures measured by the thermocouples in the DAQ are shown in Table 65 – Table 104.

MCF-7 Viability Data

Table 65 Raw data from MCF-7 test at 49oC for 14min.

		Initial			Post-Heat		
Slide	**Picture #**	**Live**	**Dead**	**% Viable**	**Live**	**Dead**	**% Viable**
Control 37	1	69	4	94.52055	52	5	91.22807
	2	156	13	92.30769	40	6	86.95652
	3	76	4	95	151	11	93.20988
Control Var	1	59	13	81.94444	120	10	92.30769
	2	83	8	91.20879	65	17	79.26829
	3	61	16	79.22078	88	5	94.62366
One	1	98	16	85.96491	88	11	88.88889
	2	96	9	91.42857	48	17	73.84615
	3	118	7	94.4	75	20	78.94737
Two	1	110	9	92.43697	59	23	71.95122
	2	100	19	84.03361	78	16	82.97872
	3	105	6	94.59459	58	5	92.06349
Three	1	112	14	88.88889	61	24	71.76471
	2	138	13	91.39073	114	18	86.36364
	3	81	12	87.09677	66	13	83.5443

Table 66 Raw data from MCF-7 test at 49oC for 16min.

		Initial			Post-Heat		
Slide	**Picture #**	**Live**	**Dead**	**% Viable**	**Live**	**Dead**	**% Viable**
Control 37	1	41	5	89.13043	35	8	81.39535
	2	38	8	82.6087	96	15	86.48649
	3	29	5	85.29412	57	16	78.08219
Control Var	1	37	8	82.22222	31	11	73.80952
	2	33	9	78.57143	37	12	75.5102
	3	21	4	84	55	15	78.57143
One	1	82	10	89.13043	52	8	86.66667
	2	51	14	78.46154	40	22	64.51613
	3	72	11	86.74699	19	61	23.75
Two	1	63	7	90	38	13	74.5098
	2	54	10	84.375	44	15	74.57627
	3	53	8	86.88525	32	47	40.50633
Three	1	100	12	89.28571	45	36	55.55556
	2	67	4	94.3662	51	48	51.51515
	3	64	13	83.11688	26	17	60.46512

Table 67 Raw data from MCF-7 test at 49oC for 18min.

		Initial			Post-Heat		
Slide	Picture #	Live	Dead	% Viable	Live	Dead	% Viable
Control 37	1	86	10	89.58333	90	12	88.23529
	2	99	9	91.66667	120	12	90.90909
	3	82	5	94.25287	61	14	81.33333
Control Var	1	126	11	91.9708	143	25	85.11905
	2	63	11	85.13514	98	13	88.28829
	3	103	19	84.42623	83	7	92.22222
One	1	117	17	87.31343	73	19	79.34783
	2	90	16	84.90566	60	20	75
	3	86	11	88.65979	84	38	68.85246
Two	1	83	10	89.24731	64	17	79.01235
	2	113	10	91.86992	140	18	88.60759
	3	77	11	87.5	38	59	39.17526
Three	1	68	11	86.07595	57	40	58.76289
	2	70	10	87.5	97	28	77.6
	3	82	5	94.25287	85	35	70.83333

Table 68 Raw data from MCF-7 test at 49oC for 20min.

		Initial			Post-Heat		
Slide	Picture #	Live	Dead	% Viable	Live	Dead	% Viable
Control 37	1	81	12	87.09677	95	19	83.33333
	2	100	11	90.09009	106	11	90.59829
	3	108	9	92.30769	128	9	93.43066
Control Var	1	72	8	90	53	14	79.10448
	2	96	10	90.56604	59	22	72.83951
	3	53	14	79.10448	53	8	86.88525
One	1	80	10	88.88889	11	24	31.42857
	2	66	3	95.65217	24	97	19.83471
	3	109	11	90.83333	62	46	57.40741
Two	1	92	15	85.98131	49	19	72.05882
	2	80	21	79.20792	58	61	48.7395
	3	120	17	87.59124	100	46	68.49315
Three	1	81	16	83.50515	37	94	28.24427
	2	123	22	84.82759	21	67	23.86364
	3	70	15	82.35294	21	64	24.70588

Table 69 Raw data from MCF-7 test at 49oC for 22min.

		Initial			Post-Heat		
Slide	**Picture #**	**Live**	**Dead**	**% Viable**	**Live**	**Dead**	**% Viable**
Control 37	1	60	16	78.94737	63	18	77.77778
	2	77	5	93.90244	47	5	90.38462
	3	91	11	89.21569	82	14	85.41667
Control Var	1	45	11	80.35714	37	7	84.09091
	2	68	10	87.17949	77	12	86.51685
	3	56	11	83.58209	52	13	80
One	1	45	8	84.90566	87	86	50.28902
	2	183	25	87.98077	3	87	3.333333
	3	115	24	82.73381	66	77	46.15385
Two	1	15	14	51.72414	46	45	50.54945
	2	27	9	75	0	23	0
	3	54	14	79.41176	0	72	0
Three	1	78	15	83.87097	102	36	73.91304
	2	75	6	92.59259	29	77	27.35849
	3	35	12	74.46809	38	35	52.05479

Table 70 Raw data from MCF-7 test at 53oC for 8min.

		Initial			Post-Heat		
Slide	**Picture #**	**Live**	**Dead**	**% Viable**	**Live**	**Dead**	**% Viable**
Control 37	1	78	11	87.64045	56	17	76.71233
	2	44	4	91.66667	111	12	90.2439
	3	148	4	97.36842	51	10	83.60656
Control Var	1	75	10	88.23529	50	16	75.75758
	2	120	24	83.33333	33	19	63.46154
	3	95	15	86.36364	86	22	79.62963
One	1	115	19	85.8209	41	70	36.93694
	2	162	21	88.52459	36	67	34.95146
	3	119	18	86.86131	44	83	34.64567
Two	1	41	8	83.67347	73	77	48.66667
	2	170	16	91.39785	39	72	35.13514
	3	156	34	82.10526	50	57	46.72897
Three	1	176	28	86.27451	65	64	50.3876
	2	175	16	91.62304	56	66	45.90164
	3	164	17	90.60773	43	92	31.85185

Table 71 Raw data from MCF-7 test at 53oC for 11min.

		Initial			Post-Heat		
Slide	**Picture #**	**Live**	**Dead**	**% Viable**	**Live**	**Dead**	**% Viable**
Control 37	1	131	16	89.11565	107	25	81.06061
	2	77	14	84.61538	105	18	85.36585
	3	143	18	88.81988	80	13	86.02151
Control Var	1	113	9	92.62295	33	14	70.21277
	2	125	4	96.89922	42	15	73.68421
	3	48	20	70.58824	165	19	89.67391
One	1	118	29	80.27211	64	80	44.44444
	2	112	17	86.82171	24	59	28.91566
	3	130	12	91.5493	39	79	33.05085
Two	1	145	19	88.41463	31	90	25.61983
	2	134	25	84.27673	35	91	27.77778
	3	112	18	86.15385	48	84	36.36364
Three	1	117	18	86.66667	61	57	51.69492
	2	119	13	90.15152	35	59	37.23404
	3	161	23	87.5	26	53	32.91139

Table 72 Raw data from MCF-7 test at 53oC for 14min.

		Initial			Post-Heat		
Slide	**Picture #**	**Live**	**Dead**	**% Viable**	**Live**	**Dead**	**% Viable**
Control 37	1	45	6	88.23529	39	0	100
	2	29	2	93.54839	28	7	80
	3	53	2	96.36364	40	18	68.96552
Control Var	1	43	1	97.72727	49	2	96.07843
	2	35	0	100	61	2	96.8254
	3	36	2	94.73684	38	1	97.4359
One	1	40	5	88.88889	52	21	71.23288
	2	43	2	95.55556	42	14	75
	3	40	2	95.2381	17	11	60.71429
Two	1	35	3	92.10526	20	11	64.51613
	2	56	5	91.80328	35	13	72.91667
	3	60	1	98.36066	45	16	73.77049
Three	1	41	7	85.41667	32	34	48.48485
	2	55	2	96.49123	25	40	38.46154
	3	38	5	88.37209	12	35	25.53191

Table 73 Raw data from MCF-7 test at 53oC for 16.5min.

		Initial			Post-Heat		
Slide	**Picture #**	**Live**	**Dead**	**% Viable**	**Live**	**Dead**	**% Viable**
Control 37	1	46	4	92	12	5	70.58824
	2	45	5	90	46	7	86.79245
	3	41	4	91.11111	48	5	90.56604
Control Var	1	31	16	65.95745	39	0	100
	2	41	3	93.18182	26	1	96.2963
	3	31	3	91.17647	40	1	97.56098
One	1	35	5	87.5	31	32	49.20635
	2	26	1	96.2963	49	30	62.02532
	3	23	0	100	18	20	47.36842
Two	1	14	2	87.5	0	19	0
	2	19	9	67.85714	1	34	2.857143
	3	35	0	100	0	22	0
Three	1	32	1	96.9697	18	31	36.73469
	2	54	3	94.73684	13	26	33.33333
	3	18	7	72	23	24	48.93617

Table 74 Raw data from MCF-7 test at 53oC for 18min.

		Initial			Post-Heat		
Slide	**Picture #**	**Live**	**Dead**	**% Viable**	**Live**	**Dead**	**% Viable**
Control 37	1	21	2	91.30435	23	3	88.46154
	2	35	0	100	22	1	95.65217
	3	42	0	100	33	2	94.28571
Control Var	1	28	0	100	32	1	96.9697
	2	13	0	100	30	0	100
	3	27	0	100	16	0	100
One	1	36	0	100	0	9	0
	2	15	0	100	0	8	0
	3	9	0	100	1	9	10
Two	1	34	31	52.30769	5	27	15.625
	2	31	7	81.57895	4	26	13.33333
	3	31	8	79.48718	12	41	22.64151
Three	1	23	1	95.83333	0	23	0
	2	7	8	46.66667	2	46	4.166667
	3	37	4	90.2439	1	33	2.941176

Table 75 Raw data from MCF-7 test at 55oC for 2min.

		Initial			Post-Heat		
Slide	Picture #	Live	Dead	% Viable	Live	Dead	% Viable
Control 37	1	105	15	87.5	139	24	85.27607
	2	168	24	87.5	116	19	85.92593
	3	126	14	90	108	16	87.09677
Control Var	1	124	11	91.85185	108	13	89.2562
	2	144	19	88.34356	131	9	93.57143
	3	108	22	83.07692	63	20	75.90361
One	1	175	14	92.59259	98	16	85.96491
	2	140	13	91.50327	140	39	78.21229
	3	193	29	86.93694	79	33	70.53571
Two	1	128	25	83.66013	52	35	59.77011
	2	120	11	91.60305	49	24	67.12329
	3	129	15	89.58333	85	50	62.96296
Three	1	64	10	86.48649	10	24	29.41176
	2	41	2	95.34884	17	11	60.71429
	3	78	5	93.9759	35	33	51.47059

Table 76 Raw data from MCF-7 test at 55oC for 4min.

		Initial			Post-Heat		
Slide	Picture #	Live	Dead	% Viable	Live	Dead	% Viable
Control 37	1	72	9	88.88889	35	1	97.22222
	2	65	11	85.52632	62	2	96.875
	3	59	6	90.76923	69	9	88.46154
Control Var	1	141	5	96.57534	102	6	94.44444
	2	121	6	95.27559	132	12	91.66667
	3	101	2	98.05825	97	5	95.09804
One	1	58	6	90.625	98	53	64.90066
	2	77	4	95.06173	62	21	74.6988
	3	131	6	95.62044	66	21	75.86207
Two	1	70	2	97.22222	58	39	59.79381
	2	71	0	100	55	48	53.39806
	3	112	2	98.24561	36	49	42.35294
Three	1	88	7	92.63158	35	18	66.03774
	2	77	8	90.58824	58	31	65.16854
	3	68	4	94.44444	48	28	63.15789

Table 77 Raw data from MCF-7 test at 55oC for 5min.

		Initial			Post-Heat		
Slide	Picture #	Live	Dead	% Viable	Live	Dead	% Viable
Control 37	1	64	11	85.33333	85	5	94.44444
	2	48	8	85.71429	39	23	62.90323
	3	50	23	68.49315	20	15	57.14286
Control Var	1	62	9	87.32394	87	4	95.6044
	2	74	7	91.35802	94	6	94
	3	70	14	83.33333	56	19	74.66667
One	1	71	6	92.20779	41	36	53.24675
	2	83	11	88.29787	32	27	54.23729
	3	71	12	85.54217	61	42	59.2233
Two	1	38	11	77.55102	8	69	10.38961
	2	97	15	86.60714	49	64	43.36283
	3	48	8	85.71429	50	29	63.29114
Three	1	91	5	94.79167	71	29	71
	2	88	0	100	49	46	51.57895
	3	57	5	91.93548	114	30	79.16667

Table 78 Raw data from MCF-7 test at 55oC for 6min.

		Initial			Post-Heat		
Slide	Picture #	Live	Dead	% Viable	Live	Dead	% Viable
Control 37	1	106	9	92.17391	76	3	96.20253
	2	72	6	92.30769	124	4	96.875
	3	52	11	82.53968	68	8	89.47368
Control Var	1	32	7	82.05128	70	3	95.89041
	2	107	11	90.67797	116	3	97.47899
	3	82	4	95.34884	90	19	82.56881
One	1	88	3	96.7033	19	85	18.26923
	2	113	3	97.41379	23	85	21.2963
	3	59	3	95.16129	19	81	19
Two	1	63	6	91.30435	8	69	10.38961
	2	82	7	92.13483	14	41	25.45455
	3	41	10	80.39216	20	78	20.40816
Three	1	67	3	95.71429	39	48	44.82759
	2	66	3	95.65217	46	31	59.74026
	3	77	29	72.64151	31	17	64.58333

Table 79 Raw data from MCF-7 test at 55oC for 7min.

		Initial			Post-Heat		
Slide	**Picture #**	**Live**	**Dead**	**% Viable**	**Live**	**Dead**	**% Viable**
Control 37	1	79	11	87.77778	117	35	76.97368
	2	87	9	90.625	64	14	82.05128
	3	174	25	87.43719	48	10	82.75862
Control Var	1	126	9	93.33333	55	15	78.57143
	2	107	16	86.99187	73	12	85.88235
	3	5	16	23.80952	84	13	86.59794
One	1	123	16	88.48921	67	26	72.04301
	2	102	11	90.26549	20	51	28.16901
	3	82	10	89.13043	40	50	44.44444
Two	1	107	12	89.91597	28	125	18.30065
	2	132	12	91.66667	12	104	10.34483
	3	87	14	86.13861	6	94	6
Three	1	75	8	90.36145	1	45	2.173913
	2	123	21	85.41667	7	77	8.333333
	3	133	29	82.09877	17	61	21.79487

Table 80 Raw data from MCF-7 test at 57oC for 0.5min.

		Initial			Post-Heat		
Slide	**Picture #**	**Live**	**Dead**	**% Viable**	**Live**	**Dead**	**% Viable**
Control 37	1	51	0	100	46	13	77.9661
	2	129	5	96.26866	60	12	83.33333
	3	69	5	93.24324	36	6	85.71429
Control Var	1	201	21	90.54054	108	10	91.52542
	2	158	24	86.81319	96	13	88.07339
	3	145	7	95.39474	143	14	91.0828
One	1	97	6	94.17476	60	13	82.19178
	2	116	18	86.56716	44	14	75.86207
	3	85	6	93.40659	38	20	65.51724
Two	1	60	13	82.19178	29	6	82.85714
	2	99	10	90.82569	70	21	76.92308
	3	107	12	89.91597	71	22	76.34409
Three	1	77	11	87.5	98	29	77.16535
	2	76	13	85.39326	65	22	74.71264
	3	63	4	94.02985	121	43	73.78049

Table 81 Raw data from MCF-7 test at 57oC for 1min. The rows with dashes have data that was lost before it was able to be counted.

		Initial			Post-Heat		
Slide	**Picture #**	**Live**	**Dead**	**% Viable**	**Live**	**Dead**	**% Viable**
Control 37	1	35	16	68.62745	96	17	84.95575
	2	157	30	83.95722	69	11	86.25
	3	116	13	89.92248	93	11	89.42308
Control Var	1	19	5	79.16667	40	4	90.90909
	2	75	8	90.36145	71	12	85.54217
	3	43	7	86	44	14	75.86207
One	1	85	8	91.39785	73	30	70.87379
	2	--	--		170	62	73.27586
	3	--	--		37	16	69.81132
Two	1	41	8	83.67347	115	35	76.66667
	2	123	7	94.61538	77	30	71.96262
	3	175	18	90.67358	68	34	66.66667
Three	1	144	11	92.90323	108	36	75
	2	161	14	92	80	25	76.19048
	3	135	14	90.60403	111	25	81.61765

Table 82 Raw data from MCF-7 test at 57oC for 2min.

		Initial			Post-Heat		
Slide	**Picture #**	**Live**	**Dead**	**% Viable**	**Live**	**Dead**	**% Viable**
Control 37	1	126	10	92.64706	137	16	89.54248
	2	196	27	87.89238	110	18	85.9375
	3	123	9	93.18182	97	18	84.34783
Control Var	1	93	14	86.91589	36	4	90
	2	50	7	87.7193	114	24	82.6087
	3	137	17	88.96104	39	1	97.5
One	1	88	3	96.7033	57	43	57
	2	79	2	97.53086	64	31	67.36842
	3	99	8	92.52336	79	50	61.24031
Two	1	86	9	90.52632	72	43	62.6087
	2	112	12	90.32258	70	37	65.42056
	3	101	15	87.06897	55	45	55
Three	1	103	9	91.96429	41	46	47.12644
	2	130	20	86.66667	47	24	66.19718
	3	86	10	89.58333	47	37	55.95238

Table 83 Raw data from MCF-7 test at 57oC for 3min.

		Initial			Post-Heat		
Slide	**Picture #**	**Live**	**Dead**	**% Viable**	**Live**	**Dead**	**% Viable**
Control 37	1	83	6	93.25843	99	10	90.82569
	2	129	5	96.26866	107	5	95.53571
	3	93	7	93	157	17	90.22989
Control Var	1	137	13	91.33333	41	12	77.35849
	2	176	8	95.65217	118	8	93.65079
	3	122	4	96.8254	45	7	86.53846
One	1	113	11	91.12903	43	30	58.90411
	2	108	9	92.30769	74	40	64.91228
	3	103	4	96.26168	101	68	59.76331
Two	1	39	4	90.69767	28	27	50.90909
	2	163	11	93.67816	42	94	30.88235
	3	63	1	98.4375	16	28	36.36364
Three	1	138	6	95.83333	58	70	45.3125
	2	142	10	93.42105	73	82	47.09677
	3	142	9	94.03974	51	95	34.93151

Table 84 Raw data from MCF-7 test at 57oC for 5min.

		Initial			Post-Heat		
Slide	**Picture #**	**Live**	**Dead**	**% Viable**	**Live**	**Dead**	**% Viable**
Control 37	1	176	4	97.77778	77	12	86.51685
	2	98	26	79.03226	107	6	94.69027
	3	75	16	82.41758	40	3	93.02326
Control Var	1	91	4	95.78947	32	4	88.88889
	2	118	4	96.72131	32	8	80
	3	73	3	96.05263	88	12	88
One	1	124	13	90.51095	35	79	30.70175
	2	93	6	93.93939	21	117	15.21739
	3	135	13	91.21622	11	50	18.03279
Two	1	83	11	88.29787	59	123	32.41758
	2	122	6	95.3125	63	90	41.17647
	3	134	4	97.10145	45	78	36.58537
Three	1	125	14	89.92806	57	102	35.84906
	2	153	16	90.53254	20	92	17.85714
	3	31	45	40.78947	23	76	23.23232

T-47D Viability Data

Table 85 Raw data from T-47D test at 49oC for 20min.

		Initial			Post-Heat		
Slide	**Picture #**	**Live**	**Dead**	**% Viable**	**Live**	**Dead**	**% Viable**
Control 37	1	88	6	93.61702	113	14	88.97638
	2	127	10	92.70073	104	9	92.0354
	3	99	3	97.05882	95	6	94.05941
Control Var	1	117	7	94.35484	128	5	96.2406
	2	146	6	96.05263	118	8	93.65079
	3	66	4	94.28571	142	8	94.66667
One	1	110	6	94.82759	145	7	95.39474
	2	123	5	96.09375	102	5	95.3271
	3	73	3	96.05263	110	9	92.43697
Two	1	70	5	93.33333	95	7	93.13725
	2	75	1	98.68421	52	5	91.22807
	3	105	5	95.45455	98	6	94.23077
Three	1	94	4	95.91837	84	35	70.58824
	2	72	10	87.80488	101	19	84.16667
	3	75	1	98.68421	70	8	89.74359

Table 86 Raw data from T-47D test at 49oC for 24min.

		Initial			Post-Heat		
Slide	**Picture #**	**Live**	**Dead**	**% Viable**	**Live**	**Dead**	**% Viable**
Control 37	1	48	2	96	31	1	96.875
	2	67	2	97.10145	111	10	91.73554
	3	117	7	94.35484	54	3	94.73684
Control Var	1	169	11	93.88889	62	5	92.53731
	2	58	0	100	158	11	93.49112
	3	41	1	97.61905	136	10	93.15068
One	1	98	23	80.99174	29	37	43.93939
	2	79	5	94.04762	48	12	80
	3	65	4	94.2029	45	6	88.23529
Two	1	70	12	85.36585	96	7	93.20388
	2	107	5	95.53571	76	15	83.51648
	3	115	6	95.04132	36	15	70.58824
Three	1	66	3	95.65217	98	11	89.90826
	2	115	8	93.49593	16	18	47.05882
	3	123	6	95.34884	9	25	26.47059

Table 87 Raw data from T-47D test at 49oC for 28min.

		Initial			Post-Heat		
Slide	**Picture #**	**Live**	**Dead**	**% Viable**	**Live**	**Dead**	**% Viable**
Control 37	1	129	15	89.58333	145	6	96.02649
	2	161	11	93.60465	131	9	93.57143
	3	200	15	93.02326	104	11	90.43478
Control Var	1	114	11	91.2	123	7	94.61538
	2	159	15	91.37931	154	20	88.50575
	3	125	9	93.28358	219	14	93.99142
One	1	114	4	96.61017	84	20	80.76923
	2	139	7	95.20548	96	96	50
	3	122	11	91.72932	110	84	56.70103
Two	1	148	11	93.08176	76	76	50
	2	147	17	89.63415	101	59	63.125
	3	165	5	97.05882	127	68	65.12821
Three	1	54	5	91.52542	57	38	60
	2	34	0	100	62	68	47.69231
	3	57	2	96.61017	53	4	92.98246

Table 88 Raw data from T-47D test at 49oC for 32min.

		Initial			Post-Heat		
Slide	**Picture #**	**Live**	**Dead**	**% Viable**	**Live**	**Dead**	**% Viable**
Control 37	1	87	11	88.77551	49	4	92.45283
	2	83	5	94.31818	209	15	93.30357
	3	83	6	93.25843	15	2	88.23529
Control Var	1	129	10	92.80576	107	6	94.69027
	2	153	6	96.22642	129	9	93.47826
	3	147	27	84.48276	71	5	93.42105
One	1	114	7	94.21488	5	96	4.950495
	2	85	13	86.73469	0	133	0
	3	167	6	96.53179	73	25	74.4898
Two	1	148	15	90.79755	120	67	64.17112
	2	142	2	98.61111	113	47	70.625
	3	120	18	86.95652	125	43	74.40476
Three	1	132	7	94.96403	3	92	3.157895
	2	132	8	94.28571	24	129	15.68627
	3	162	15	91.52542	115	28	80.41958

Table 89 Raw data from T-47D test at 49oC for 34min.

		Initial			Post-Heat		
Slide	Picture #	Live	Dead	% Viable	Live	Dead	% Viable
Control 37	1	49	2	96.07843	238	8	96.74797
	2	197	5	97.52475	242	12	95.27559
	3	348	12	96.66667	301	7	97.72727
Control Var	1	219	15	93.58974	301	7	97.72727
	2	219	2	99.09502	315	32	90.7781
	3	354	5	98.60724	250	22	91.91176
One	1	193	5	97.47475	46	83	35.65891
	2	184	3	98.39572	4	93	4.123711
	3	90	11	89.10891	230	60	79.31034
Two	1	150	5	96.77419	21	9	70
	2	112	4	96.55172	18	51	26.08696
	3	184	7	96.33508	98	27	78.4
Three	1	114	7	94.21488	94	89	51.36612
	2	160	10	94.11765	135	25	84.375
	3	70	3	95.89041	74	96	43.52941

Table 90 Raw data from T-47D test at 52oC for 12min.

		Initial			Post-Heat		
Slide	Picture #	Live	Dead	% Viable	Live	Dead	% Viable
Control 37	1	522	8	98.49057	256	25	91.1032
	2	377	8	97.92208	274	12	95.8042
	3	126	5	96.18321	203	29	87.5
Control Var	1	213	12	94.66667	196	19	91.16279
	2	256	16	94.11765	234	11	95.5102
	3	264	11	96	396	17	95.88378
One	1	250	12	95.41985	226	33	87.25869
	2	335	23	93.57542	171	45	79.16667
	3	400	24	94.33962	288	39	88.07339
Two	1	332	10	97.07602	303	35	89.64497
	2	304	18	94.40994	283	28	90.99678
	3	385	29	92.99517	245	52	82.49158
Three	1	377	8	97.92208	214	37	85.25896
	2	316	10	96.93252	346	48	87.81726
	3	289	14	95.37954	208	30	87.39496

Table 91 Raw data from T-47D test at 52oC for 14min.

		Initial			Post-Heat		
Slide	**Picture #**	**Live**	**Dead**	**% Viable**	**Live**	**Dead**	**% Viable**
Control 37	1	361	12	96.78284	211	10	95.47511
	2	342	9	97.4359	179	14	92.74611
	3	236	12	95.16129	219	7	96.90265
Control Var	1	187	7	96.39175	181	7	96.2766
	2	203	11	94.85981	213	15	93.42105
	3	157	8	95.15152	191	28	87.21461
One	1	257	9	96.61654	168	17	90.81081
	2	299	9	97.07792	237	44	84.34164
	3	184	3	98.39572	314	24	92.89941
Two	1	156	9	94.54545	196	31	86.34361
	2	220	5	97.77778	178	26	87.2549
	3	267	2	99.25651	187	31	85.77982
Three	1	152	11	93.25153	155	25	86.11111
	2	225	5	97.82609	230	37	86.14232
	3	182	8	95.78947	147	27	84.48276

Table 92 Raw data from T-47D test at 52oC for 16min.

		Initial			Post-Heat		
Slide	**Picture #**	**Live**	**Dead**	**% Viable**	**Live**	**Dead**	**% Viable**
Control 37	1	225	10	95.74468	189	16	92.19512
	2	361	16	95.75597	218	17	92.76596
	3	361	22	94.25587	255	20	92.72727
Control Var	1	214	20	91.45299	285	9	96.93878
	2	324	17	95.01466	244	12	95.3125
	3	330	15	95.65217	209	10	95.43379
One	1	375	13	96.64948	208	29	87.76371
	2	307	14	95.63863	320	44	87.91209
	3	281	17	94.2953	263	33	88.85135
Two	1	165	18	90.16393	282	36	88.67925
	2	553	24	95.84055	244	66	78.70968
	3	331	22	93.76771	278	73	79.20228
Three	1	299	3	99.00662	172	56	75.4386
	2	161	15	91.47727	339	69	83.08824
	3	165	4	97.63314	370	46	88.94231

Table 93 Raw data from T-47D test at 52oC for 18min.

		Initial			Post-Heat		
Slide	**Picture #**	**Live**	**Dead**	**% Viable**	**Live**	**Dead**	**% Viable**
Control 37	1	134	11	92.41379	141	12	92.15686
	2	186	17	91.62562	156	23	87.15084
	3	172	10	94.50549	146	12	92.40506
Control Var	1	256	14	94.81481	243	17	93.46154
	2	204	10	95.3271	240	11	95.61753
	3	278	19	93.60269	192	6	96.9697
One	1	167	11	93.82022	71	100	41.52047
	2	172	20	89.58333	150	33	81.96721
	3	225	18	92.59259	254	45	84.94983
Two	1	199	17	92.12963	90	132	40.54054
	2	183	14	92.8934	104	117	47.05882
	3	182	14	92.85714	59	124	32.24044
Three	1	181	10	94.7644	31	93	25
	2	167	24	87.43455	0	181	0
	3	226	15	93.77593	84	122	40.7767

Table 94 Raw data from T-47D test at 52oC for 20min.

		Initial			Post-Heat		
Slide	**Picture #**	**Live**	**Dead**	**% Viable**	**Live**	**Dead**	**% Viable**
Control 37	1	158	9	94.61078	197	5	97.52475
	2	199	5	97.54902	304	10	96.81529
	3	186	9	95.38462	195	8	96.05911
Control Var	1	209	30	87.4477	185	16	92.0398
	2	187	18	91.21951	316	27	92.12828
	3	162	20	89.01099	200	58	77.51938
One	1	184	13	93.40102	363	145	71.45669
	2	143	5	96.62162	406	66	86.01695
	3	262	17	93.90681	240	109	68.76791
Two	1	176	6	96.7033	0	173	0
	2	140	7	95.2381	12	232	4.918033
	3	195	5	97.5	0	156	0
Three	1	161	7	95.83333	5	209	2.336449
	2	314	32	90.75145	0	167	0
	3	147	6	96.07843	63	194	24.51362

Table 95 Raw data from T-47D test at 54oC for 4min.

		Initial			Post-Heat		
Slide	Picture #	Live	Dead	% Viable	Live	Dead	% Viable
Control 37	1	90	28	76.27119	105	16	86.77686
	2	70	9	88.60759	76	13	85.39326
	3	21	3	87.5	90	16	84.90566
Control Var	1	103	16	86.55462	87	17	83.65385
	2	86	14	86	104	14	88.13559
	3	85	18	82.52427	156	29	84.32432
One	1	84	12	87.5	168	24	87.5
	2	72	16	81.81818	115	14	89.14729
	3	112	22	83.58209	51	11	82.25806
Two	1	165	27	85.9375	83	9	90.21739
	2	133	17	88.66667	128	10	92.75362
	3	69	11	86.25	132	16	89.18919
Three	1	87	11	88.77551	122	13	90.37037
	2	95	10	90.47619	81	8	91.01124
	3	46	6	88.46154	76	10	88.37209

Table 96 Raw data from T-47D test at 54oC for 6min.

		Initial			Post-Heat		
Slide	Picture #	Live	Dead	% Viable	Live	Dead	% Viable
Control 37	1	39	1	97.5	58	7	89.23077
	2	80	4	95.2381	61	10	85.91549
	3	40	2	95.2381	30	9	76.92308
Control Var	1	77	6	92.77108	53	3	94.64286
	2	63	4	94.02985	113	11	91.12903
	3	55	6	90.16393	53	4	92.98246
One	1	78	12	86.66667	56	17	76.71233
	2	76	4	95	40	20	66.66667
	3	116	2	98.30508	57	22	72.1519
Two	1	110	18	85.9375	45	28	61.64384
	2	91	23	79.82456	32	14	69.56522
	3	60	10	85.71429	73	37	66.36364
Three	1	79	14	84.94624	101	37	73.18841
	2	95	20	82.6087	47	11	81.03448
	3	116	15	88.54962	65	18	78.31325

Table 97 Raw data from T-47D test at 54oC for 8min.

		Initial			Post-Heat		
Slide	**Picture #**	**Live**	**Dead**	**% Viable**	**Live**	**Dead**	**% Viable**
Control 37	1	62	7	89.85507	107	9	92.24138
	2	166	21	88.77005	149	14	91.41104
	3	138	9	93.87755	57	7	89.0625
Control Var	1	61	5	92.42424	60	4	93.75
	2	121	2	98.37398	144	6	96
	3	58	3	95.08197	89	7	92.70833
One	1	70	6	92.10526	55	40	57.89474
	2	63	2	96.92308	19	17	52.77778
	3	78	5	93.9759	71	40	63.96396
Two	1	38	3	92.68293	47	31	60.25641
	2	41	3	93.18182	138	39	77.9661
	3	48	2	96	40	36	52.63158
Three	1	97	5	95.09804	77	35	68.75
	2	73	5	93.58974	28	22	56
	3	50	8	86.2069	93	37	71.53846

Table 98 Raw data from T-47D test at 54oC for 10min.

		Initial			Post-Heat		
Slide	**Picture #**	**Live**	**Dead**	**% Viable**	**Live**	**Dead**	**% Viable**
Control 37	1	79	13	85.86957	48	6	88.88889
	2	52	18	74.28571	66	4	94.28571
	3	98	14	87.5	63	5	92.64706
Control Var	1	68	23	74.72527	33	4	89.18919
	2	60	13	82.19178	41	12	77.35849
	3	57	9	86.36364	82	11	88.17204
One	1	54	22	71.05263	6	38	13.63636
	2	90	26	77.58621	79	121	39.5
	3	81	21	79.41176	6	51	10.52632
Two	1	43	14	75.4386	15	17	46.875
	2	80	12	86.95652	48	35	57.83133
	3	60	7	89.55224	0	58	0
Three	1	63	13	82.89474	8	58	12.12121
	2	43	7	86	2	42	4.545455
	3	28	2	93.33333	2	41	4.651163

Table 99 Raw data from T-47D test at 54oC for 12min.

		Initial			Post-Heat		
Slide	Picture #	Live	Dead	% Viable	Live	Dead	% Viable
Control 37	1	87	12	87.87879	86	8	91.48936
	2	99	6	94.28571	67	5	93.05556
	3	99	14	87.61062	134	7	95.03546
Control Var	1	79	3	96.34146	106	11	90.59829
	2	105	21	83.33333	108	6	94.73684
	3	92	7	92.92929	55	8	87.30159
One	1	88	7	92.63158	52	112	31.70732
	2	143	9	94.07895	41	86	32.28346
	3	114	17	87.0229	21	90	18.91892
Two	1	50	5	90.90909	5	51	8.928571
	2	41	0	100	0	30	0
	3	25	7	78.125	21	101	17.21311
Three	1	42	4	91.30435	117	122	48.95397
	2	43	6	87.7551	3	54	5.263158
	3	90	3	96.77419	8	78	9.302326

Table 100 Raw data from T-47D test at 57oC for 2min.

		Initial			Post-Heat		
Slide	Picture #	Live	Dead	% Viable	Live	Dead	% Viable
Control 37	1	277	42	86.83386	182	28	86.66667
	2	192	15	92.75362	193	46	80.75314
	3	276	16	94.52055	213	14	93.8326
Control Var	1	224	5	97.81659	272	12	95.77465
	2	232	14	94.30894	264	22	92.30769
	3	174	66	72.5	383	52	88.04598
One	1	403	50	88.96247	309	61	83.51351
	2	335	21	94.10112	237	33	87.77778
	3	173	8	95.58011	284	25	91.90939
Two	1	260	20	92.85714	332	64	83.83838
	2	356	18	95.18717	424	51	89.26316
	3	371	35	91.37931	242	47	83.73702
Three	1	415	66	86.27859	288	24	92.30769
	2	294	32	90.18405	263	39	87.08609
	3	428	53	88.98129	440	55	88.88889

Table 101 Raw data from T-47D test at 57oC for 3min.

		Initial			Post-Heat		
Slide	**Picture #**	**Live**	**Dead**	**% Viable**	**Live**	**Dead**	**% Viable**
Control 37	1	328	12	96.47059	309	21	93.63636
	2	362	16	95.7672	601	27	95.70064
	3	367	8	97.86667	350	13	96.41873
Control Va	1	310	14	95.67901	316	27	92.12828
	2	173	30	85.22167	315	13	96.03659
	3	365	22	94.31525	245	12	95.33074
One	1	716	23	96.88769	409	270	60.23564
	2	625	24	96.302	474	178	72.69939
	3	658	26	96.19883	431	182	70.30995
Two	1	595	22	96.43436	604	54	91.79331
	2	516	18	96.62921	449	45	90.89069
	3	616	31	95.20866	406	99	80.39604
Three	1	711	25	96.60326	436	76	85.15625
	2	512	10	98.08429	454	98	82.24638
	3	435	19	95.81498	530	63	89.37605

Table 102 Raw data from T-47D test at 57oC for 4.5min.

		Initial			Post-Heat		
Slide	**Picture #**	**Live**	**Dead**	**% Viable**	**Live**	**Dead**	**% Viable**
Control 37	1	147	9	94.23077	140	18	88.60759
	2	280	15	94.91525	143	18	88.81988
	3	148	5	96.73203	196	11	94.68599
Control Var	1	227	25	90.07937	200	7	96.61836
	2	162	19	89.50276	139	12	92.05298
	3	187	18	91.21951	103	10	91.15044
One	1	314	14	95.73171	61	248	19.7411
	2	380	15	96.20253	39	267	12.7451
	3	376	26	93.53234	80	242	24.84472
Two	1	547	19	96.64311	135	218	38.24363
	2	481	13	97.36842	296	197	60.04057
	3	376	14	96.41026	352	67	84.00955
Three	1	327	14	95.89443	254	50	83.55263
	2	282	11	96.24573	208	134	60.81871
	3	284	14	95.30201	213	66	76.34409

Table 103 Raw data from T-47D test at 57oC for 6min.

		Initial			Post-Heat		
Slide	Picture #	Live	Dead	% Viable	Live	Dead	% Viable
Control 37	1	155	11	93.37349	190	15	92.68293
	2	127	1	99.21875	151	17	89.88095
	3	190	7	96.4467	188	21	89.95215
Control Va	1	194	12	94.17476	198	10	95.19231
	2	190	13	93.59606	180	9	95.2381
	3	180	9	95.2381	199	10	95.21531
One	1	139	6	95.86207	140	18	88.60759
	2	162	10	94.18605	152	27	84.9162
	3	220	17	92.827	229	26	89.80392
Two	1	139	4	97.2028	0	175	0
	2	95	3	96.93878	0	108	0
	3	102	17	85.71429	0	84	0
Three	1	174	18	90.625	0	108	0
	2	102	8	92.72727	0	117	0
	3	139	25	84.7561	0	165	0

Table 104 Raw data from T-47D test at 57oC for 8min.

		Initial			Post-Heat		
Slide	Picture #	Live	Dead	% Viable	Live	Dead	% Viable
Control 37	1	412	23	94.71264	370	28	92.96482
	2	355	27	92.93194	241	19	92.69231
	3	257	22	92.1147	461	23	95.24793
Control Var	1	60	3	95.2381	94	6	94
	2	221	14	94.04255	117	8	93.6
	3	237	23	91.15385	152	15	91.01796
One	1	354	16	95.67568	0	399	0
	2	306	18	94.44444	15	295	4.83871
	3	408	19	95.55035	1	231	0.431034
Two	1	337	51	86.85567	2	234	0.847458
	2	371	20	94.88491	0	278	0
	3	314	18	94.57831	0	249	0
Three	1	288	18	94.11765	0	159	0
	2	265	10	96.36364	0	168	0
	3	365	22	94.31525	0	120	0

Appendix H: Data in Cell Survival Curves

Table 105 displays the means and confidence intervals of the viability percentages at each time and temperature trial for the treatment cells and when they are normalized to C-37 and C-Var.

Table 105 Viability percentage means and confidence intervals.

Cell Temp (°C)	Cell Line	Heating Time (min)	Alone			Normal to C-37			Normal to C-Var		
			Mean	CI low	CI high	Mean	CI low	CI high	Mean	CI low	CI high
50	*MCF-7*	*14*	89.1	83.6	94.5	92.2	86.8	97.6	94.1	89.1	99.1
		16	74.6	63.6	85.7	82.1	69.9	94.3	79.0	67.3	90.7
		18	84.5	76.2	92.7	88.8	80.8	96.8	90.3	82.4	98.2
		20	48.3	29.8	66.8	52.4	32.3	72.4	55.2	34.1	76.4
		22	39.6	13.9	65.4	42.9	15.0	70.8	44.7	15.6	73.7
	T-47D	*20*	96.4	93.7	99.2	98.5	96.2	100.8	97.8	95.3	100.3
		24	90.5	82.7	98.3	92.9	85.1	100.8	94.1	86.4	101.7
		28	59.5	52.3	66.6	62.0	54.5	69.4	62.6	55.1	70.1
		32	46.6	16.9	76.2	49.6	18.0	81.2	49.6	18.0	81.2
		34	55.0	32.8	77.3	55.7	33.2	78.3	57.8	34.4	81.1
52/53	*MCF-7 (53)*	*8*	46.4	40.1	52.7	51.3	44.3	58.2	54.7	47.3	62.2
		11	40.6	33.4	47.9	42.3	34.8	49.8	47.7	39.2	56.2
		14	63.3	47.0	79.6	67.9	50.4	85.4	63.7	47.3	80.2
		16.5	34.3	13.5	55.0	35.2	13.8	56.5	34.7	13.6	55.7
		18	13.8	-5.2	32.9	14.7	-5.6	34.9	14.1	-5.3	33.4
	T-47D (52)	*12*	90.7	87.7	93.7	96.4	93.5	99.2	94.6	91.6	97.7
		14	90.1	88.0	92.2	92.5	90.4	94.7	94.6	92.5	96.8
		16	88.8	84.6	93.0	91.4	87.1	95.7	92.6	88.2	96.9
		18	35.1	19.1	51.2	36.0	19.6	52.5	36.2	19.7	52.7
		20	5.6	-5.1	16.3	5.8	-5.3	16.9	6.2	-5.7	18.1
54/55.5	*MCF-7 (55.5)*	*2*	75.8	64.1	87.6	77.8	65.7	89.9	83.6	71.8	95.4
		4	66.4	57.1	75.7	70.5	60.7	80.4	68.5	58.9	78.0
		5	65.9	56.7	75.1	69.8	60.0	79.5	69.5	59.8	79.2
		6	35.2	17.6	52.8	37.4	18.7	56.0	37.0	18.5	55.4
		7	15.4	5.6	25.2	17.0	6.2	27.7	16.6	6.1	27.2
	T-47D (54)	*4*	91.9	88.8	94.9	100.0	100.0	100.0	95.7	93.6	97.9
		6	82.1	76.1	88.1	93.8	86.9	100.7	86.0	79.7	92.3
		8	66.9	59.4	74.4	71.3	63.3	79.3	68.9	61.1	76.6
		10	9.4	2.2	16.6	10.2	2.4	18.0	10.3	2.4	18.2
		12	19.4	8.4	30.4	20.8	9.0	32.7	20.0	8.6	31.4
57	*MCF-7 (57)*	*0.5*	85.3	80.5	90.1	97.4	93.5	101.4	91.4	86.4	96.4
		1	80.9	77.4	84.4	84.7	81.1	88.4	88.6	84.7	92.4
		2	65.4	59.9	70.8	68.9	63.1	74.6	69.7	63.9	75.5
		3	50.8	40.7	60.8	52.9	42.5	63.4	56.0	44.9	67.0
		5	30.3	22.5	38.1	33.1	24.6	41.6	34.0	25.3	42.7
	T-47D (57)	*2*	93.2	90.2	96.2	97.3	96.1	98.6	95.8	94.0	97.7
		3	85.9	78.8	93.0	87.2	80.0	94.4	89.4	82.0	96.7
		4.5	53.2	30.9	75.5	55.9	32.5	79.3	57.0	33.2	80.9
		6	0.0	0.0	0.0	0.0	0.0	0.0	0.0	0.0	0.0
		8	0.7	-0.6	2.0	0.7	-0.6	2.0	0.8	-0.6	2.1

Bibliography

[1] American Cancer Society, "What Are the Key Statistics About Prostate Cancer," 27 February 2012. [Online]. Available: http://www.cancer.org/Cancer/ProstateCancer/DetailedGuide/prostate-cancer-key-statistics. [Accessed 20 March 2012].

[2] American Cancer Society, "What Are the Key Statistics About Breast Cancer," 4 June 2012. [Online]. Available: http://www.cancer.org/Cancer/ProstateCancer /Detailed Guide/breast-cancer-key-statistics. [Accessed 4 June 2012].

[3] R. Diegel, N. D and A. Jemel, "Cancer Statistics, 2012," *CA: A Cancer Journal for Clinicians*, vol. 62, no. 1, pp. 10-29, 2012.

[4] National Cancer Institute, "Prostate Cancer Treatment," 21 September 2012. [Online]. Available: http://www.cancer.gov/cancertopics/pdq/treatment/prostate/Patient/page4. [Accessed 2012].

[5] R. Chopra, M. Burtnyk, M. A. Haider and M. J. Bronskill, "Method for MRI-Guided Conformal Thermal Therapy of Prostate with Planar Transurethral Ultrasound Heating Applicators," *Physics in Medicine and Biology*, vol. 50, pp. 4957-4975, 2005.

[6] K. Y. Saleh and N. B. Smith, "Two-Dimensional Ultrasound Phased Array Design for Tissue Ablation for Treatment of Benign Prostatic Hyperplasia," *International Journal of Hyperthermia*, vol. 20, no. 1, pp. 7-31, 2004.

[7] Y.-F. Zhou, "High Intensity Focused Ultrasound in Clinical Tumor Ablation," *World Journal of Clinical Oncology*, vol. 2, no. 1, pp. 8-27, 2011.

[8] E. B. Hutchinson and K. Hynynen, "Intracavitary Ultrasound Phased Arrays for Noninvasive Prostate Surgery," *IEEE Transactions on Ultrasonics, Ferroelectrics, and Frequency Control*, vol. 43, no. 6, pp. 1032-1042, 1996.

[9] BreastCancer.org, "Treatment & Side Effects," 29 April 2012. [Online]. Available: http://www.breastcancer.org/treatment/. [Accessed 2012].

[10] C.-P. Jen, C.-T. Huang and C.-H. Tsai, "Supraphysiological Thermal Injury in Different Human Bladder Carcinoma Cell Lines," *Annals of Biomedical Engineering*, vol. 37, no. 11, pp. 2407-2415, 2009.

[11] C.-T. Huang, Y.-H. Lu and C.-P. Jen, "Investigation on Supraphysiological Thermal Injury in Two Well-Differentiated Human Hepatoma Cell Lines, Hep G2 and Hep 3B," *Journal of Thermal Biology*, vol. 35, pp. 411-416, 2010.

[12] D. Gordon and C. Thamire, "Ultrasound Hyperthermia: Dose Estimation and Device Design," in *ASME 2012 International Mechanical Engineering Congress & Exposition*, Houston, 2012.

[13] G. T. Haar and C. Coussios, "High Intensity Focused Ultrasound: Physical Principles and Devices," *International Journal of Hyperthermia*, vol. 23, no. 2, pp. 89-104, 2007.

[14] P. Prakash and C. J. Diederich, "Considerations for Theoretical Modelling of Thermal Ablation with Catheter-Based Ultrasonic Sources: Implications for Treament Planning, Monitoring, and Control," *International Journal of Hyperthermia*, vol. 28, no. 1, pp. 69-86, 2012.

[15] C.-S. Ho, K.-C. Ju, T.-Y. Cheng, Y.-Y. Chen and W.-L. Lin, "Thermal Therapy for Breast Tumors by Using a Cylindrical Ultrasound Phased Array with Multifocus Pattern Scanning: a Preliminary Numerical Study," *Physics in Medicine and Biology*, vol. 52, pp. 4585-4599, 2007.

[16] C. J. Diederich, "Thermal Ablation and High-Temperature Thermal Therapy: Overview of Technology and Clinical Implementation," *International Journal of Hyperthermia*, vol. 21, no. 8, pp. 745-753, 2005.

[17] H. J. Jang, J.-Y. Lee, D.-H. Lee, W.-H. Kim and J. H. Hwang, "Current and Future Clinical Applications of High-Intensity Focused Ultrasound (HIFU) for Pancreatic Cancer," *Gut and Liver*, vol. 4, no. Suppl. 1, pp. 57-61, 2010.

[18] M. Malinen, T. Huttunen, J. P. Kaipio and K. Hynynen, "Scanning Path Optimization for Ultrasound Surgery," *Physics in Medicine and Biology*, vol. 50, no. 15, pp. 3473-3490, 2005.

[19] "Picture of the Prostate," 2009. [Online]. Available: http://men.webmd.com/picture-of-the-prostate. [Accessed April 2011].

[20] D. G. Bostwick, "Pathology of Benign Prostatic Hyperplasia," in *Textbook of Benign Prostatic Hyperplasia*, Oxford, Isis Medical Media Ltd, 1996, pp. 91-104.

[21] "File:Benign Prostatic Hyperplasia nci-vol-7137-300.jpg," [Online]. Available: http://en.wikipedia.org/wiki/File:Benign_Prostatic_Hyperplasia_nci-vol-7137-300.jpg. [Accessed April 2011].

[22] Susan G. Kolman for the Cure, "Structure and Function of the Breasts," 7 July 2012. [Online]. Available: http://ww5.komen.org/BreastCancer/TheBreast.html. [Accessed 2012].

[23] Mayo Clinic, "Slide s\Show: Female Breast Anatomy," 19 October 2011. [Online]. Available: http://www.mayoclinic.com/health/breast-cancer-early-stage/BC00001. [Accessed 2012].

[24] F. H. Netter, Atlas of Human Anatomy, Philadelphia: Saunders, 2011.

[25] J. W. Jenne, T. Preusser and M. Gunther, "High-Intensity Focused Ultrasound: Principles, Therapy Guidance, Simulations and Applications," *Zeitschrift fur Medizinische Physik*, pp. 1-12, 2012.

[26] K. H. Hynynen, "Fundamental Principles of Therapeutic Ultrasound," in *MRI-Guided Focused Ultrasound Surgery*, New York, Informa Healthcare, 2008, pp. 5-24.

[27] Y. Tang, *Cancer Therapy Combining Modalities of Hyperthermia and Chemotherapy: in vitro Cellular Response after Rapid Heat Accumulation in the Cancer Cell*, Miami: FIU Electronic Theses and Dissertations, 2010.

[28] X. He, S. Bhowmick and J. Boschof, "Thermal Therapy in Urologic Systems: A Comparison of Arrhenius and Thermal Isoeffective Dose Models in Predicting

Hyperthermic Injury," *Journal of Biomedical Engineering,* vol. 131, pp. 074507-1-074507-12, 2009.

[29] K.-C. Ju, L.-T. Tseng, Y.-Y. Chen and W.-L. Lin, "Investigation of a Scanned Cylindrical Ultrasound System for Breast Hyperthermia," *Physics in Medicine and Biology,* vol. 51, pp. 539-555, 2006.

[30] J. L. Rose, Basic Physics in Diagnostic Ultrasound, New York: John Wiley & Sons Inc., 1979.

[31] ElectronicsTeacher.com, "Light and Electromagnetic Waves: Dispersion of Light," [Online]. Available: http://www.electronicsteacher.com/succeed-in-physical-science/light-and-electromagnetic-waves/dispersion-of-light.php. [Accessed 2012].

[32] C. A. Damianou, N. T. Sanghvi, F. J. Fry and R. Maass-Moreno, "Dependence of Ultrasonic Attenuation and Absorption in Dog Soft Tissues on Temperature and Thermal Dose," *The Journal of the Acoustical Society of America,* vol. 102, no. 1, pp. 628-634, 1997.

[33] R. S. C. Cobbold, Foundations of Biomedical Ultrasound, Oxford: Oxford University Press, Inc., 2007.

[34] A. Lorincz, L. Csoka and L. Friedrich, "Modeling the Heat Effect of Ultrasound in the Irradiated Tissues," in *36th Ultrasonic Industry Association Symposium*, London, 2007.

[35] K. K. Shung and G. A. Thieme, Ultrasonic Scattering in Biological Tissues, Boca Raton: CRC Press, Inc., 1992.

[36] K. Hynynen, D. Shimm, D. Anhalt, B. Stea, H. Sykes, J. R. Cassady and R. B. Roemer, "Temperature Distributions During Clinical Scanned, Focussed Ultrasound Hyperthermia Treatments," *Internaltion Journal of Hyperthermia,* vol. 6, pp. 891-908, 1990.

[37] CliffsNotes, "Wave Optics," [Online]. Available: http://www.cliffsnotes.com/study_guide/Wave-Optics.topicArticleId-10453,articleId-10442.html. [Accessed 2012].

[38] Wikipedia, "Interference (wave propagation)," 4 September 2012. [Online]. Available: http://en.wikipedia.org/wiki/Interference_%28wave_propagation%29. [Accessed 2012].

[39] G. Mueller, *Chapter 17: Waves II,* Gainesville: University of Florida, 2008.

[40] M. A. Swartz and M. E. Fleury, "Interstitial Flow and its Effects in Soft Tissues," *Annual Review of Biomedical Engineering,* vol. 9, pp. 229-256, 2007.

[41] A. K. Datta and V. Rakesh, An Introduction to Modeling of Transport Processes: Applications to Biomedical Systems, Cambridge: Cambridge University Press, 2010.

[42] T. W. Davies, "Conduction," [Online]. Available: http://www.thermopedia.com/content/655/?tid=110&sn=7. [Accessed 2012].

[43] A.-R. A. Khaled and K. Vafai, "The role of Porous Media in Modeling Flow and Heat Transfer in Biological Tissues," *International Journal of Heat and*

Mass Transfer, vol. 46, pp. 4989-5003, 2003.

[44] S. E. Davis, C. Thamire and N. T. Wright, " Modeling of the local heating of non-perfused tissue with directionally dependent thermal diffusivity and heat-induced damage," *Advances in Heat and Mass Transfer in Biotechnology, ASME - HTD,* vol. 368, pp. 75-82, 2000.

[45] L. Zhu, L. Pang and L. X. Xu, "Simultaneous Measurements of Local Tissue Temperature and Blook Perfusion Rate in the Canine Prostate During Radio Frequency Thermal Therapy," *Biomechanics and Modeling in Mechanobiologuy,* vol. 4, pp. 1-9, 2005.

[46] P. Axelsson, "Computer Modelling of the Temperature Disctribution in High Intensity Focused Ultrasound Thermometry," Dept. of Biomedical Engineering, Lund University, Lund, 1999.

[47] J. Liu, L. Zhu and L. X. Xu, "Studies on the Three-Dimensional Temperature Transients in the Canine Prostate During Transurethral Microwave Thermal Therapy," *Journal of Biomedical Engineering,* vol. 122, no. 4, pp. 372-379, 2000.

[48] T.-C. Liang, W.-L. Lin, W.-C. Fan, J.-Y. Yen and Y.-Y. Chen, "SAR and Temperature Distributions of Cylindrical Ultrasound Transducers for Intracavitary Hyperthermia," in *20th Annual International Conference of the IEEE Engineering in Medicine and Biology Society,* Hong Kong, 1998.

[49] H. Wan and P. VanBaren, "Ultrasound Surgery: Comparison of Strategies Using Phased Array Systems," *IEEE Transactions on Ultrasonics, Ferroelectrics, and Frequency Control,* vol. 43, no. 6, pp. 1085-1098, 1996.

[50] J. L. Roti Roti, "Cellular responses to hyperthermia (40-46oC): Cell killing and molecular events," *International Journal of Hyperthermia,* vol. 24, no. 1, pp. 3-15, 2008.

[51] P. Schildkopf, O. Ott, B. Frey, M. Wadepohl, R. Sauer, R. Fietkau and U. Gaipl, "Biological Rationales and Clinical Applications of Temperature Controlled Hyperthermia - Implications for Multimodal Cancer Treatments," *Current Medicinal Chemistry,* vol. 17, pp. 3045-3057, 2010.

[52] X. He and J. C. Bischof, "Quantification of Temperature and Injury Response in Thermal Therapy and Cryosurgery," *Critical Reviews in Biomedical Engineering,* vol. 31, no. 5&6, pp. 355-421, 2003.

[53] M. W. Dewhirst, B. L. Vigilianti, M. Lora-Michiels, M. Hanson and P. J. Hoopes, "Basic Principles of Thermal Dosimetry and Thermal Thresholds for Tissue Damage from Hyperthermia," *International Journal of Hyperthermia,* vol. 19, no. 3, pp. 267-294, 2003.

[54] R. P. M. Dings, M. L. Loren, Y. Zhang, S. Mikkelson, K. H. Mayo, P. Corry and R. J. Griffin, "Tumor Thermotolerance, a Physiological Phenomenon Involving Vessel Normalisation," *International Journal of Hyperthermia,* vol. 27, no. 1, pp. 42-52, 2011.

[55] Y. Itoh, Y. Kazaoka, M. Nitta, Y. Yamada and N. Honda, "Combining Anti-Tumor Drugs with Mild Hyperthermia Increases the Cytotoxic Effects of Drugs on Human Leukemia Cells In Vitro," *Molecular Medicine Reports,* vol. 2, pp.

411-415, 2009.

[56] M. Urano, M. Kuroda and Y. Nishimura, "For the Clinical Application of Thermochemotherapy Given at Mild Temperatures," *International Journal of Hyperthermia,* vol. 15, pp. 79-107, 1999.

[57] H. Lee, S. Kim, B.-H. Choi, M.-T. Park, J. Lee, S.-Y. Jeong, E. K. Choi, B.-U. Lim, C. Kim and H. J. Park, "Hyperthermia Improves Therapeutic Efficacy of Doxorubicin Carried by Mesoporous Silica Nanocontainers in Human Lung Cancer Cells," *International Journal of Hyperthermia,* vol. 27, no. 7, pp. 698-707, 2011.

[58] M. H. Falk and R. D. Issels, "Hyperthermia in Oncology," *International Journal of Hyperthermia,* vol. 17, no. 1, pp. 1-18, 2001.

[59] D. R. Ciocca, S. A. W. Fuqua, S. Lock-Lim, D. O. Toft and W. J. Welch, "Response of Human Breast Cancer Cells to Heat Shock and Chemotherapeutic Drugs," *Cancer Research,* vol. 52, pp. 3648-3654, 1992.

[60] B. Hildebrandt, P. Wust, O. Ahlers, A. Dieing, G. Sreenivasa, T. Kerner, R. Felix and H. Riess, "The Cellular and Molecular Basis of Hyperthermia," *Critical Reviews in Oncology/Hematology,* vol. 43, pp. 33-56, 2002.

[61] R. D. Issels, "Hyperthermia Adds to Chemotherapy," *European Journal of Cancer,* vol. 44, pp. 2546-2554, 2008.

[62] Y. Feng, J. T. Oden and M. N. Rylander, "A Two-State Cell Damage Model Under Hyperthermic Conditions: Theory and In Vitro Experiments," *Journal of Biomedical Engineering,* vol. 130, pp. 041016-1-041016-10, 2008.

[63] D. P. O'Neill, T. Peng, P. Steigler, U. Mayrhauser, S. Koestenbauer, K. Tscheliessnigg and S. J. Payne, "A Three-State Mathematical Model of Hyperthermic Cell Death," *Annals of Biomedical Engineering,* vol. 39, no. 1, pp. 570-579, 2011.

[64] N. T. Wright, "On a Relationship Between the Arrhenius Parameters from Thermal Damage Studies," *Journal of Biomedical Engineering,* vol. 125, pp. 300-304, 2003.

[65] B. Shah and S. Showmick, "Evaluation of Imortant Treatment Parameters in Supraphysiological Thermal Therapy of Human Liver Cancer HepG2 Cells," *Annals of Biomedical Engineering,* vol. 34, no. 11, pp. 1745-1757, 2006.

[66] X. He and J. C. Bischof, "The Kinetics of Thermal Injury in Human Renal Carcinoma Cells," *Annals of Biomedical Engineering,* vol. 33, no. 4, pp. 502-510, 2005.

[67] C.-T. Huang, C.-H. Tsai and C.-P. Jen, "Effects of Supraphysiological Thermal Injury in Human Embryonic Kidney Cells," in *International Conference on BioMedical Engineering and Informatics*, Sanya, 2008.

[68] W. C. Dewey, L. E. Hopwood, S. A. Sapareto and L. E. Gerweck, "Cellular Responses to Combinations of Hyperthermia and Radiation," *Radiology,* vol. 123, no. 2, pp. 463-474, 1977.

[69] S. A. Sapareto and W. C. Dewey, "Thermal Dose Determination in Cancer Therapy," *International Journal of Radiation and Oncology Biology Physics,*

vol. 10, pp. 787-800, 1984.

[70] W. C. Dewey, "Arrhenius Relationships from the Molecule and Cell to the Clinic," *International Journal of Hyperthermia,* vol. 10, no. 4, pp. 457-483, 1994.

[71] X. Chen, C. J. Diederich, J. H. Wooton, J. Pouliot and I.-C. Hsu, "Optimisation-based thermal treatment planning for catheter-based ultrasound hyperthermia," *International Journal of Hyperthermia,* vol. 26, no. 1, pp. 39-55, 2010.

[72] T.-Y. Cheng, K.-C. Ju, C.-S. Ho, Y.-Y. Chen, H. Chang and W.-L. Lin, "Split-Focused Ultrasound Transducer with Multidirectional Heating for Breast Tumor Thermal Surgery," *Medical Physics,* vol. 35, no. 4, pp. 1387-1397, 2008.

[73] X. Fan and K. Hynynen, "Ultrasound Surgery Using Multiple Sonications - Treatment Time Considerations," *Ultrasound in Medicine and Biology,* vol. 22, no. 4, pp. 471-482, 1996.

[74] D. Tyreus, W. H. Nau and C. J. Diederich, "Effect of Applicator Diameter on Lesion Size from High Temperature Interstitial Ultrasound Thermal Therapy," *Medical Physics,* vol. 30, no. 7, pp. 1855-1863, 2003.

[75] D. Tyreus and C. J. Diederich, "Theoretical Model of Internally Cooled Interstitial Ultrasound Applicators for Thermal Therapy," *Physics in Medicine and Biology,* vol. 47, pp. 1073-1089, 2002.

[76] C. J. Diederich and K. Hynynen, "Induction of Hyperthermia Using an Intracavitary Multielement Ultrasonic Applicator," *IEEE Transactions on Biomedical Engineering,* vol. 36, no. 4, pp. 432-438, 1989.

[77] Y.-S. Huang, C.-S. Ho, M.-C. Hsu, Y.-Y. Chen and W.-L. Lin, "Investigation of Dual Curved Ultrasound Phased Arrays for Breat Tumor Thermal Therapy," in *IEEE Ultrasonics Symposium,* New York, 2007.

[78] W.-L. Lin, J.-Y. Yen, Y.-Y. Chen, K.-S. Cheng and M.-J. Shieh, "Specific Absorption Rate Ratio Patterns of Cylindrical Ultrasound Transducers for Breast Tumors," *Medical Physics,* vol. 6, pp. 1041-1048, 1998.

[79] H.-L. Liu, Y.-Y. Chen, J.-Y. Yen and W.-L. Lin, "Pilot Point Temperature Regulation for Thermal Lesion Control During Ultrasound Thermal Therapy," *Medical and Biological Engineering and Computing,* vol. 42, pp. 178-188, 2004.

[80] P. Prakash, X. Chen, J. Wooton, J. Pouliot, I.-C. Hsu and C. J. Diederich, "Patient Specific Optimization-Based Treatment Planning for Catheter-BasedUltrasound Hyperthermia and Thermal Ablation," in *International Society for Optics and Photonics: Energy-based Treatment of TIssue and Assessment V (Proceedings Volume),* 2009.

[81] W.-L. Lin, W.-C. Fan, J.-Y. Yen, Y.-Y. Chen and M.-J. Shieh, "A Theoretical Study of Cylindrical Ultrasound Transducers for Intracavitary Hyperthermia," *International Journal of Radiation Oncology Biological Physics,* vol. 46, no. 5, pp. 1329-1336, 2000.

[82] D. Schutt and H. D, "Effects of Variation in Perfusion Reates and of Perfusion

Models in Computational Models of Radio Frequency Tumor Ablation," *Medical Physics,* vol. 35, pp. 3462-3470, 2008.

[83] E. C. Burdette, "Patent #5391197: Ultrasound Thermotherapy Probe," 1995.

[84] S. Thuroff, C. Chaussy, G. Vallencien, W. Wieland, H. J. Kiel, A. Le Duc, F. Desgrandchamps, J. J. De La Rosette and A. Gelet, "High-Intensity Focused Ultrasound and Localized Prostate Cancer: Efficacy Results from the European Multicentric Study," *Journal of Endourology,* vol. 17, no. 8, pp. 673-677, 2003.

[85] T. Uchida, H. Ohkusa, H. Yamashita, S. Shoji, Y. Nagata, T. Hyodo and T. Satoh, "Five Years Experience of Transrectal High-Intensity Focused Ultrasound Using the Sonablate Device in the Treatment of Localized Prostate Cancer," *International Journal of Urology,* vol. 13, pp. 228-233, 2006.

[86] B. K. Bhuyan, "Kinetics of Cell Kill by Hyperthermia," *Cancer Reserach,* vol. 39, pp. 2277-2284, 1979.

[87] D. O'Neill, T. Peng and S. Payne, "Comparison of Two Mathematical Models for Hyperthermic Cell Death," in *IFMBE Proceedings*, Singapore, 2010.

[88] S. Bhowmick, D. J. Swanlund and J. C. Bischof, "Supraphysiological Thermal Injury in Dunning AT-1 Prostate Tumor Cells," *Journal of Biomedical Engineering,* vol. 122, pp. 51-59, 2000.

[89] L. P. Walsh, J. K. Anderson, M. R. Baker, B. Han, J.-T. Hsieh, Y. Lotan and J. A. Cadeddu, "In Vitro Assessment of the Efficacy of Thermal Therapy in Human Renal Cell Carcinoma," *Urology,* vol. 70, no. 2, pp. 380-384, 2007.

[90] D. Jiang, S.-Y. Zheng, J. Zhao, J.-F. Ge and H. Li, "The Research on the Effect of Hyperthermia on Growth of A549 and H1299 Lung Cancer Cells," in *International Conference on Future BioMedical Information Engineering,* Sanya, 2009.

[91] S. P. Tomasovic, M. Barta and J. Klostergaard, "Neutral Red Uptake and Clonogenic Survival Assays of the Hyperthermic Sensitization of Tumor Cells to Tumor Necrosis Factor," *Radiation Research,* vol. 119, pp. 325-337, 1989.

[92] N. A. Moussa, E. N. Tell and E. G. Cravalho, "Time Progression of Erythrocyte Populations Exposed to Supraphysiological Temperatures," *Journal of Biomedical Engineering,* vol. 101, pp. 213-217, 1979.

[93] MATLAB, "cart2pol," [Online]. Available: http://cens.ioc.ee/local/man/matlab/techdoc/ref/cart2pol.html. [Accessed 2012].

[94] D. R. Daum and K. Hynynen, "Theoretical Design of a Spherically Sectioned Phased Array for Ultrasound Surgery of the Liver," *European Journal of Ulrasound,* vol. 9, pp. 61-69, 1999.

[95] G. E. Dieter and L. C. Schmidt, Engineering Design, New York: McGraw-Hill Companies, Inc., 2009.

[96] MATLAB, "sph2cart," [Online]. Available: http://cens.ioc.ee/local/man/matlab/techdoc/ref/sph2cart.html. [Accessed 2012].

[97] A. Payne, R. Merrill and E. Minalga, "Design and Characterization of a Laterally Mounted Phased-Array Transducer Breast-Specific MRgHIFU Device with Integratedd 11-Channel Receiver Array," *Medical Physics,* vol. 39,

no. 3, pp. 1552-1560, 2012.

[98] L. A. Gloeckler Ries and M. P. Eisner, "Chapter 13: Cancer of the Female Breast," in *Cancer Survival Among Adults: U.S. SEER Program, 1988-2001*, Bethesda, National Cancer Institute, SEER Program, 2007, pp. 101-110.

[99] J. A. Pearce, "Relationship Between Arrjenius Models of Thermal Damage and the CEM 43 Thermal Dose," in *SPIE*, 2009.

[100] M. Lacroix and G. Leclercq, "Relevance of Breast Cancer Cell Lines as Models for Breast Tumours: an Update," *Breast Cancer Research and Treatment*, vol. 83, pp. 249-289, 2004.

[101] J. A. Aka and S.-X. Lin, "Comparison of Functional Proteomic Analyses of Human Breast Cancer Cell Lines T47D and MCF7," *Plos One*, vol. 7, no. 2, pp. 1-9, 2012.

[102] Grainger, Inc., "TEMPCO Strip Heater," 2012. [Online]. Available: http://www.grainger.com/Grainger/TEMPCO-Strip-Heater-6THL6. [Accessed 23 August 2012].

[103] F. P. Incropera and D. P. DeWitt, Fundamentals of Heat and Mass Transfer, New York: John Wiley & Sons, Inc, 2002.

[104] C. Thamire, *Lecture: Review of Statistics (Contd.)*, College Park: University of Maryland, College Park, 2012.